Topological Modes and Flatbands in Microcavity Exciton-Polariton Lattices

Dissertation zur Erlangung des

naturwissenschaftlichen Doktorgrades

der Julius-Maximilians-Universität Würzburg

vorgelegt von

Tristan H. Harder

aus Hamburg

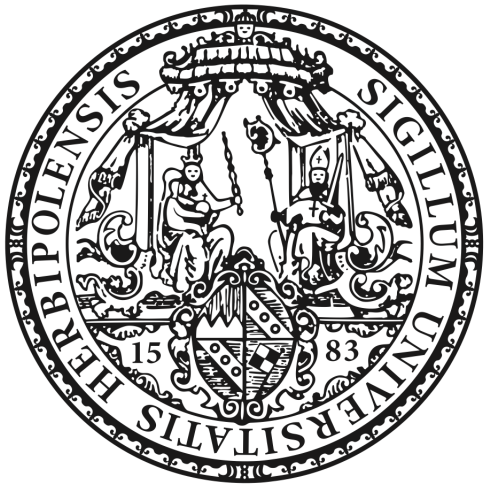

Würzburg 2022

This document is licensed under the Creative Commons Attribution-NonCommercial-NoDerivatives 4.0 International License (CC BY-NC-ND 4.0):
http://creativecommons.org/licenses/by-nc-nd/4.0 This CC license does not apply to third party material (attributed to another source) in this publication.

Eingereicht am: 17. März 2021
bei der Fakultät für Physik und Astronomie

1. Gutachter: Prof. Dr. Sebastian Klembt

2. Gutachter: Prof. Dr. Ronny Thomale

3. Gutachter: Prof. Dr. Alexander Szameit
der Dissertation

Vorsitzende(r): Prof. Dr. Karl Brunner

1. Prüfer: Prof. Dr. Sebastian Klembt

2. Prüfer: Prof. Dr. Ronny Thomale

3. Prüfer: Prof. Dr. Vladimir Dyakonov
im Promotionskolloquium

Tag des Promotionskolloquium: 16. Februar 2022

Doktorurkunde ausgehändigt am: .....

Contents

1 Introduction

Humanity is currently living in a digital era, in which all aspects of life, ranging from social interaction to economy and communication all the way to science, are heavily influenced and driven by microelectronics with continuously growing computational capabilities that support a rapidly evolving digital infrastructure. Today's big trends, such as *Industry 4.0*, the *Internet of Things* and autonomous driving, will spread the influence of digitisation even further across the realms of human life and interaction. One of the key discoveries at the base of this enormous progression is the first transistor that was developed by Shockley, Bardeen and Brattain in 1947 [BB48], who were later awarded the Nobel Prize for their work. Based on this discovery, Atalla and Kahng invented the metal-oxide-semiconductor field-effect-transistor (MOSFET) [Kah60] that represents the fundamental building block of today's silicon-based integrated circuits. With the following discovery of the functionality of semiconductor heterostructures, for which Kroemer and Alferov were awarded the Nobel Prize, the semiconductor success story reached optics, as these heterostructures represent the foundation for the development of opto-electronic devices such as light emitting diodes (LEDs), lasers and solar cells.

The driving motivation of the development of semiconductor electronics has long been to increase computational power by fabricating smaller transistors and increasing the number of transistors per chip [Moo06]. However, over the last decades, the prevailing challenge has evolved from computational power towards energy efficiency, as on a small scale the computational speed is limited by heating and on a global scale climate change has become one of the major challenges of our civilisation [Int14]. Information and communication technology already accounts for approximately 2 % of the global carbon emissions and its contribution to the global electricity demand is projected to double by 2030 and reach a daunting 20 % [AE15; Jon18]. To address this challenge, entirely new, innovative solutions are required. In particular, the concept of topological insulators that is based on the discovery of the quantum Hall effect by von Klitzing in 1980 [KDP80] has evolved as a new paradigm to control the flow of electric current. Starting in electronics, this concept has spread across large parts of solid-state physics and reached photonics as a new degree of freedom to control the propagation of light. This development is particularly exciting as photonics has evolved as a key player for the future development of our

digital infrastructure, where even optical integrated circuits and optical computing are envisioned.

Already, vertical-cavity surface-emitting lasers (VCSELs) that consist of two distributed Bragg reflectors (DBRs) surrounding a microcavity that contains quantum wells as a gain material are widely used in data communication. However, the physics that can be found in a vertical microcavity resonator goes far beyond photonic lasing, as Weisbuch and co-workers demonstrated in 1992 [Wei+92] with their first realisation of a regime of strong coupling between the cavity photons and the quantum well excitons. In this regime, the emission of a photon during the recombination of a quantum well exciton becomes reversible, as the photon remains in the cavity for long enough to be reabsorbed through the formation of an exciton. The system thus forms two new eigenstates that are part-matter and part-light in nature and are referred to as exciton-polaritons (polaritons). This unique composition results in an equally unique set of properties, as polaritons inherit a very low effective mass from the photonic fraction while still being able to interact with each other through the excitonic part. Additionally, the mature technological control over the gallium arsenide material platform, representing the foundation of VCSEL technology, allows for precise fabrication of polaritonic devices. The real beauty of polaritons, however, arises during their decay when a photon leaves the microcavity. This photon carries the phase, amplitude, momentum and energy information of the polariton and thus provides direct experimental access to the polaritonic states through photoluminescence (PL) spectroscopy techniques allowing to directly visualise the complex physical phenomena that can be realised in microcavities.

At the heart of this new field of polariton research was the idea of realising a Bose-Einstein condensate (BEC), motivated by the very small polariton mass on the order of 10^{-5} electron masses. The first demonstration of a BEC of polaritons that was reported by Kasprzak and co-workers in 2006 [Kas+06] was followed by a lively discussion on the physical nature of this state. In summary, such a BEC of polaritons does not represent a BEC in a strict sense, as it constitutes a driven-dissipative system that is far from equilibrium. In fact, the lifetime of the polaritons is on the same order as the relaxation time of polaritons towards the condensate and the condensate itself only represents a small portion of the overall polariton density [Dev12]. To address this distinction, the term *polariton condensate* is commonly used instead of *BEC of polaritons*.

Based on this understanding, the field of polaritonics evolved. First of all, experiments inspired by the research on atomic BECs were performed and effects such as superfluidity [Amo+09b; Amo+09a; Amo+11], vortices [Lag+08; Lag+09; San+10; Nar+11; Rou+11] and Josephson oscillations [Lag+10] were observed. Polaritons furthermore carry a spin that has attracted significant scientific interest [Kav+04; She+09]. Already in 1996,

Imamoglu and co-workers started the research direction of polariton light sources by suggesting to use the coherence of polariton condensates for the development of thresholdless lasers [Ima+96]. Of particular importance in the context of polaritons as light sources are the works on electrically driven polariton condensates [Sch+13; Bha+13] as well as the search for new active materials that support polariton condensation at room temperature [GB16]. Additionally to research on polariton condensates themselves, polaritons have evolved as a platform for a broad range of physical effects based, among others, on advanced potential landscapes serving as lattice simulators [Sch+16], polariton transistors pursuing optical integrated circuits [Bal+13; Zas+19] as well as polaritonic neural networks [Bal+20; Xu+20]. Additionally, the interplay of polaritons with topologically non-trivial effects has risen as a new research direction that directly links the field of polaritonics to the current challenges in electronics and computing, as polaritons can serve as a powerful platform to advance the understanding of the interplay of topology and non-Hermiticity as well as to explore new opportunities for the development of lasers based on topological protection. The progress of polariton research has been summarised in a number of excellent reviews of the field [DHY10; Dev12; CC13; BKY14; Kav+17].
The aim of this work is to advance the field of polariton lattice simulators and focusses particularly on the lasing properties of the latter. It is divided into the following six chapters:

In **chapter 2, *Fundamentals of polariton lattices*,** the basic physical concepts of light and its confinement in microcavities as well as quantum well excitons and the strong coupling between the two are introduced. Additionally, two-dimensional lattices and their band structure features are briefly explained, followed by an introduction into the concept of topological insulators.

In **chapter 3, *Experimental methods*,** a brief overview of the III-V semiconductor material platform as well as the fabrication process of polariton lattices is given. Afterwards, the spectroscopic techniques used to excite polaritons and study various properties of the photons emitted from these microcavities are introduced.

In **chapter 4, *Establishing lattice potentials for polaritons*,** a systematic study of the fundamental properties of polaritons in lattice potential environments that represent the foundation for the research presented in the following chapters is provided. In particular, the evolution from the discrete energy levels of individual polariton traps to a fully developed band structure of a polariton lattice, in analogy to the formation of band structures for electrons in crystals, as well as the excitation of polariton condensates within such a lattice are emphasised.

In **chapter 5, *Polaritons in flatbands*,** polaritonic lattices with geometries that evoke dispersionless flatbands are investigated. After demonstrating precise technological control over the remaining dispersiveness of these bands, the controlled excitation of polaritons and polariton condensates in flatbands is realised and used for an investigation of the influence of the unique properties of flatbands on the coherence of polariton condensates. Finally, the formation of vortex lattices as well as their relation to chiral edge transport is investigated.

In **chapter 6, *Topological polaritons and topological lasing*,** polaritons in topologically non-trivial lattice potential environments are studied. After the first demonstration of a two-dimensional polariton topological insulator, the lasing characteristics of a polariton condensate in a topological defect mode of a one-dimensional polariton chain are studied in detail. Finally, the protection of a propagating topological boundary mode is used to ensure coherent coupling of an array of VCSELs.

In **chapter 7, *Engineering of polaritonic band structures*,** technological efforts towards modifying polaritonic band structures and creating band gaps in the latter are summarised. These results represent a promising path for future experiments on polaritonic lattices, as they form the foundation for studies on for example the coupling of flatbands to dispersive bands as well as a topologically protected polariton quantum valley Hall insulator.

2 Fundamentals of polariton lattices

In this chapter, a summary of the physical background needed to understand this thesis is given. First, the description of light using electromagnetic waves to describe its properties, such as amplitude, frequency, wave vector, phase, polarisation and coherence, is summarised in section 2.1. In section 2.2, the physics of confined light and excitons in semiconductor microcavities and quantum wells as well as the interaction between the two are introduced. Subsequently, a summary of lattice potentials and the calculation of their band structures is provided in section 2.3. Here, two-dimensional lattices are emphasised and the two distinguished cases of vanishing and infinite effective band masses are presented. Finally, an introduction into topology as a new degree of freedom in solid-state systems is given in section 2.4.

2.1 The physics of light

This section is devoted to give a short summary of the aspects of the physical treatment of light that are relevant for this thesis and is based on the more elaborate descriptions that can be found in literature [ST91; Gol11; Dem13].
Our current understanding of light as an electromagnetic wave, in the context of classical physics, dates back to the set of equations published by Maxwell in 1865 [Max65] that describe the evolution of electric and magnetic field in space and time in vacuum. These equations can be extended to describe the propagation of light in matter,

$$\boldsymbol{\nabla} \cdot \boldsymbol{D} = \frac{\rho}{\varepsilon_0} \tag{2.1a}$$

$$\boldsymbol{\nabla} \cdot \boldsymbol{B} = 0 \tag{2.1b}$$

$$\boldsymbol{\nabla} \times \boldsymbol{E} = -\frac{1}{c}\partial_t \boldsymbol{B} \tag{2.1c}$$

$$\boldsymbol{\nabla} \times \boldsymbol{B} = \frac{1}{\varepsilon_0 c^2}\partial_t \boldsymbol{J} + \frac{1}{c^2}\partial_t \boldsymbol{D}, \tag{2.1d}$$

where ρ denotes the free electric charge density, ε_0 the vacuum permittivity, c the speed of light in vacuum, $\boldsymbol{J}$ the free current density and $\boldsymbol{B}$ the magnetic field. The electric

displacement field is given by

$$\boldsymbol{D} = \varepsilon_0 \boldsymbol{E} + \boldsymbol{P} = \varepsilon \boldsymbol{E}, \tag{2.2}$$

with the electric field $\boldsymbol{E}$ and the dielectric polarisation $\boldsymbol{P}$. The dielectric constant ε accounts for the influences of matter on light, such as reflection and absorption, and is related to the refractive index n through $n = \sqrt{\varepsilon/\varepsilon_0}$. In dielectric and semiconductor materials, as the materials relevant for this work, Maxwell's equations simplify as $\rho = 0$ and $\boldsymbol{J} = 0$ can generally be assumed.
The solution of Maxwell's equations is given by a linear combination of plane waves

$$\boldsymbol{E}(\boldsymbol{r}, t) = \boldsymbol{E}_0 \exp(i(\boldsymbol{k} \cdot \boldsymbol{r} - \omega t)), \tag{2.3}$$

with amplitude $\boldsymbol{E}_0$ and frequency ω. The propagation direction of such a plane wave is characterised by its wave vector $\boldsymbol{k}$ with an absolute value that is given by $k = n \cdot \omega/c$. The direction of the wave vector defines the polarisation of light. A transverse electromagnetic wave travelling along z-direction can consequently be written as

$$E_\mathrm{x}(z, t) = E_{0\mathrm{x}} \cos(\omega t - kz + \delta_\mathrm{x}) \tag{2.4a}$$

$$E_\mathrm{y}(z, t) = E_{0\mathrm{y}} \cos(\omega t - kz + \delta_\mathrm{y}) \tag{2.4b}$$

with the amplitudes $E_{0\mathrm{x,0y}}$ and phases $\delta_\mathrm{x,y}$. Therefore, to fully characterise a beam of light, one does not only need to consider its propagation direction but also the dynamical rotation of its electromagnetic field vector. The time-dependent orientation of the wave vector $\boldsymbol{k}$ is referred to as the *spin angular momentum* or *polarisation*, whereas the spatial distribution of the phase of a wave front is called *orbital angular momentum*.
The polarisation is determined by the differences in phases $\delta = \delta_\mathrm{y} - \delta_\mathrm{x}$ as well as amplitudes between the two components and is therefore in general given by an ellipse in the $(E_\mathrm{x}, E_\mathrm{y})$-plane. With this definition, three sets of distinguished polarisations can be identified. The horizontal (H) and vertical (V) linear polarisations are defined by $E_{0\mathrm{y}} = 0$ and $E_{0\mathrm{x}} = 0$, respectively. The diagonal (D) and anti-diagonal (A) linear polarisation directions are characterised by $E_\mathrm{y} = \pm E_\mathrm{x}$ with $\delta = 0, \pi$ and right (σ_+) and left (σ_-) circular polarisations occur for $E_{0\mathrm{x}} = E_{0\mathrm{y}}$ with $\delta = \frac{\pi}{2}, \frac{3\pi}{2}$. In most realistic scenarios, light is a superposition of multiple plane waves with partially randomly distributed phases and is thus partially

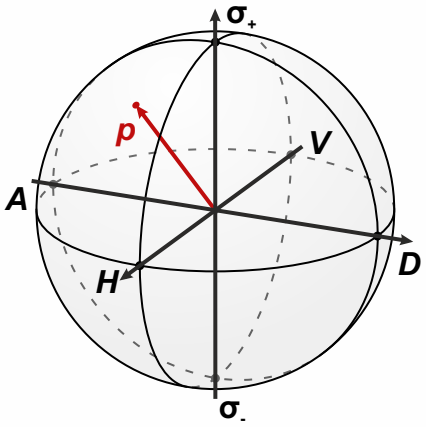

Figure 2.1: Schematic of the Poincaré sphere. Any given polarisation is characterised by a vector $\boldsymbol{p}$ starting from the centre of the sphere and pointing towards the polarisation direction. The degree of polarisation is encoded in the length of the vector and scales from $p=0$ to $p=1$, corresponding to fully unpolarised and fully polarised light, respectively.

unpolarised. The degree of polarisation is then given by the Stokes vector [Sto52]

$$\boldsymbol{S} = \frac{1}{S_0}\begin{pmatrix} S_0 \\ S_1 \\ S_2 \\ S_3 \end{pmatrix} = \frac{1}{I_\mathrm{H}+I_\mathrm{V}}\begin{pmatrix} I_\mathrm{H}+I_\mathrm{V} \\ I_\mathrm{H}-I_\mathrm{V} \\ I_\mathrm{D}-I_\mathrm{A} \\ I_{\sigma_+}-I_{\sigma_-} \end{pmatrix} \begin{matrix} \text{total light intensity} \\ \text{amount of } H\text{-}/V\text{-polarisation} \\ \text{amount of } D\text{-}/A\text{-polarisation} \\ \text{amount of } \sigma_+\text{-}/\sigma_-\text{-polarisation} \end{matrix} \tag{2.5}$$

with $I_\mathrm{H}, I_\mathrm{V}, I_\mathrm{D}, I_\mathrm{A}, I_{\sigma_+}$ and I_{σ_-} denoting the light intensities with the corresponding polarisation. For fully polarised light, the relation $S_0^2 = S_1^2 + S_2^2 + S_3^2$ must be fulfilled whereas for fully unpolarised light $S_1 = S_2 = S_3 = 0$ holds true. The total degree of polarisation can hence be calculated by

$$p = \frac{\sqrt{S_1^2 + S_2^2 + S_3^2}}{S_0}. \tag{2.6}$$

Furthermore, a given polarisation can be visualised as a vector in the Poincaré sphere that is schematically depicted in Fig. 2.1, where the type of polarisation is encoded in the orientation of the vector and the degree of polarisation is given by its length, scaling from $p=0$ to $p=1$ for fully unpolarised and fully polarised light, respectively.
The orbital angular momentum is commonly characterised by the phase difference acquired on a closed loop around the centre of the beam in a plane perpendicular to the propagation direction and is given by $\phi = m \cdot 2\pi$ with $m \in \mathbb{Z}$. A wavefront with a flat phase is characterised by $m=0$ whereas $m \neq 0$ corresponds to a helical wavefront with a vortex with topological charge m at its core.

Additionally to the importance of knowing the polarisation and orbital angular momentum of a certain emission, in realistic scenarios the statistics of the light emitters become significant. The most important quantity is coherence, which is defined as a fixed phase relation between waves. The most general origin of deviations from a fixed phase relation is a finite spread in frequency that leads to a range of phase differences. Such a frequency spread is common in any realistic emitter and occurs for example due to the finite time of emission that, through the uncertainty principle, directly links to a spread in frequency. Additional statistics is added to a system if multiple emitters have to be considered. As information can only be extracted from a signal if a fixed phase relation was maintained, the degree of coherence is a measure for the ability to gather information from a signal. Typically, this distance to the source is defined in two domains, space and time, leading to the definition of spatial and temporal coherence. The degree of coherence can be measured through interference of a signal with itself at a distance in either space or time, as only waves with a fixed phase relation will lead to a stationary interference pattern once the signal is superimposed with itself at an angle. This autocorrelation is used to quantify the first order degree of temporal coherence as

$$g^{(1)}(\tau, t) = \frac{\langle E^*(t)E(t+\tau)\rangle}{\langle |E(t)^2| \rangle} \tag{2.7}$$

for a time t and a time delay τ and analogously for space and a spatial separation. For a fully coherent signal, $g^{(1)} = 1$, and for a fully incoherent signal, $g^{(1)} = 0$. By Fourier transforming the commonly occurring exponential coherence decay of $g^{(1)}(\tau) \sim \exp(-\tau/\tau_{\text{coh}})$ into the frequency domain, one finds a Lorentzian line shape with a linewidth γ that is given by $\gamma = \frac{h}{\pi\tau_{\text{coh}}}$, known as the Wiener-Khintchine theorem [Wie30; Khi34].
When moving beyond the classical description of light towards a quantum picture that considers individual photons, higher degrees of coherence become meaningful. Most notably, correlating the detection of a photon at time t with the detection of another photon at time $t+\tau$ provides crucial information about the emitter. The probability of detecting this second photon is given by the second order coherence degree [Gla63a; Gla63b; Gla07]

$$g^{(2)}(t, \tau) = \frac{\langle E^*(t)E^*(t+\tau)E(t)E(t+\tau)\rangle}{\langle E^*(t)E(t)\rangle^2}. \tag{2.8}$$

If $E(t)$ and $E(t+\tau)$ are stationary but uncorrelated, $g^{(2)}(\tau) = 1$, implying that the relevant information is given by $g^{(2)}(0)$. For an emitter with a single mode, $g^{(2)}(0) = 2$ for a thermal emitter, referred to as photon bunching, $g^{(2)}(0) = 1$ for a coherent emitter and $g^{(2)}(0) = 1 - 1/n$ for a number state consisting of a fixed number of emitters, resulting in the characteristic anti-bunching behaviour of $g^{(2)}(0) = 0$ for a single photon source.

A technological approach to increasing the coherence of an emitter is *light amplification by stimulated emission of radiation*, in short LASER. In the most general description, a laser consists of three components, namely an active medium with at least three energy levels, a pump and a resonator. When the pump excites the active medium, a population inversion can be reached. A photon emitted spontaneously will now produce further identical photons through stimulated emission. This process is enhanced by keeping photons within the resonator. As multiple emitters now emit identical photons, the emission does not occur with a finite lifetime but continuously, thus decreasing the spread in frequency and increasing the degree of coherence. The key identifiers at the threshold from spontaneous light emission to lasing are therefore a non-linear increase in emission intensity, a decrease in linewidth and the build-up of coherence.

2.2 Semiconductor microcavities and quantum wells

In this section, the confinement of excitons in quantum wells as well as photons in microcavities are introduced, followed by a description of the interaction between these light and matter components. Here, a particular emphasis is put towards the regime of strong light-matter coupling that results in the formation of exciton-polaritons (polaritons). Finally, the properties of polaritons, such as their pseudospin, angular momentum, the formation and relaxation processes as well as their ability to form polariton condensates are elaborated. Further details on the introduction that is given in this section can be found in textbooks [Kit05; Dev06; YC10; Kli12; TS12; Kav+17] as well as review articles [Kav10; DHY10; Yu+19] on the topic.

2.2.1 Photonic confinement in microcavities

The key concept of an optical cavity is the confinement of light as a standing wave, which can most intuitively be achieved by an optical resonator formed by two planar mirrors, referred to as a *Fabry-Pérot resonator* [FP97]. In the realms of semiconductor physics, where a range of designs to realise optical confinement has been established [Vah03], the size of the optical cavities is commonly reduced to the order of the wavelength of the confined light, thus justifying the term *microcavity*. For this work, Fabry-Pérot microcavities consisting of two distributed Bragg reflectors (DBRs) separated by a cavity layer were investigated. A DBR consists of a stack of consecutive pairs of two materials with a difference in refractive index, causing light to reflect at every interface. The thicknesses d of the layers are determined by $n_1 d_1 = n_2 d_2 = \lambda_{\mathrm{DBR}}/4$, such that they fulfil the Bragg condition resulting in constructive interference of the reflected light from the

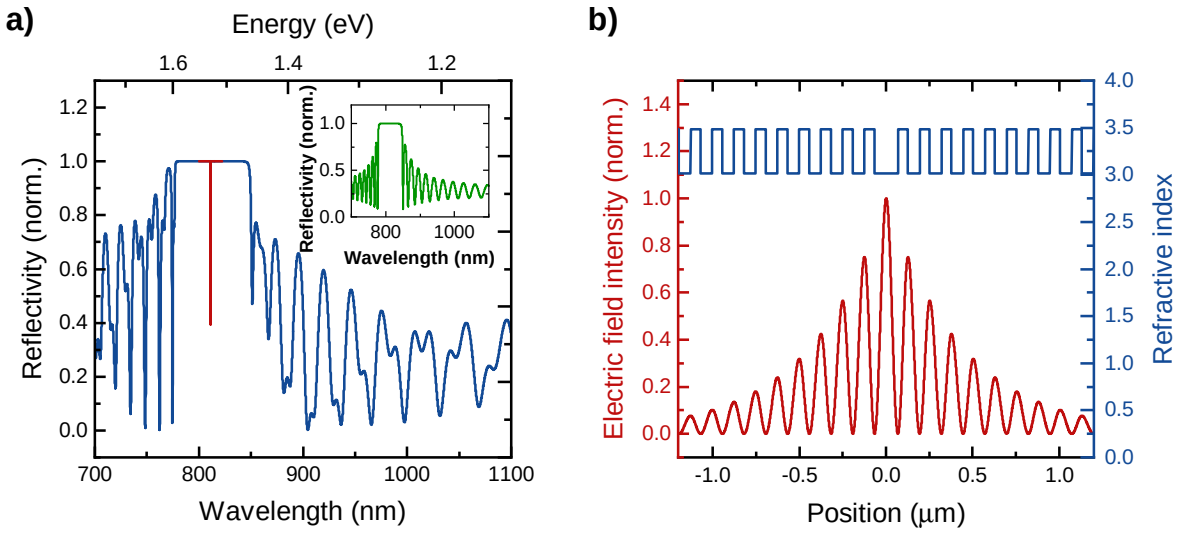

Figure 2.2: **a)** Transfer matrix simulation of the reflectivity spectrum of an AlAs cavity surrounded by $Al_{0.20}Ga_{0.80}As$/AlAs DBRs showing the characteristic cavity resonance, highlighted in red, at the centre of the stopband of the DBRs. A reflectivity spectrum of a single DBR is presented in the inset. **b)** Refractive index structure of the microcavity in blue and the corresponding electric field distribution featuring a maximum at the centre of the cavity in red.

individual interfaces. The reflectivity spectrum thus features a spectral range of high reflectivity, coined *stopband*, centred around λ_{DBR}. The reflectivity spectrum of a DBR can be calculated using the transfer matrix method [Hol21; Yu03] and is displayed in the inset of Fig. 2.2 a).

A Fabry-Pérot resonator can be formed by stacking two DBRs with a spacer layer, referred to as *cavity layer*, with an optical thickness of integer multiples of $\lambda_{\mathrm{C}}/2$ in between them. As depicted in Fig. 2.2 a), the resulting cavity resonance at $\lambda_{\mathrm{C}}/2$ is usually designed to be located at the centre of the DBR stopbands and therefore at the reflectivity maximum by obeying the condition $\lambda_{\mathrm{DBR}} = \lambda_{\mathrm{C}}$. The quality of such a microcavity is quantified by the quality factor

$$Q = \frac{\lambda_{\mathrm{C}}}{\gamma_{\mathrm{C}}} = \frac{E_{\mathrm{C}}\tau_{\mathrm{C}}}{h}, \tag{2.9}$$

with γ_{C} denoting the linewidth of the cavity resonance. The Q-factor can be understood as the average number of round trips a photon travels within the cavity before escaping through one of the mirrors and is therefore directly related to the lifetime τ_{C} of a cavity photon through the energy of the cavity resonance E_{C} and the Planck constant h. Experimentally, quality factors on the order of $Q = 10{,}000$, corresponding to lifetimes of $\tau_{\mathrm{C}} \approx 30\,\mathrm{ps}$, are routinely observed in linewidth measurements. Due to confining photons

into a two-dimensional plane, here set to be the x-y-plane, their dispersion relation is drastically changed. When expressing the photonic wave vector as $k^2 = k_\parallel^2 + k_\perp^2$ to reflect the symmetries of the system and approximating the component of the wave vector perpendicular to the cavity $k_\perp$ to be significantly smaller than the in-plane wave vector $k_\parallel = \sqrt{k_x^2 + k_y^2}$, the energy dispersion of a cavity photon can be approximated by

$$E_\mathrm{C} = \frac{\hbar c}{n_\mathrm{C}}\sqrt{k_\perp^2 + k_\parallel^2} \approx \frac{\hbar c}{n_\mathrm{C}} k_\perp \left(1 + \frac{k_\parallel^2}{2k_\perp^2}\right) = E_\mathrm{C}(k_\parallel = 0) + \frac{\hbar^2 k_\parallel^2}{2m_\mathrm{C}^*} \quad \text{with} \quad E_\mathrm{C}(k_\parallel = 0) = \frac{hc}{\lambda_\mathrm{C}} \tag{2.10}$$

where $\hbar$ corresponds to the reduced Planck constant. Strikingly, due to the confinement, the photonic dispersion changes from a linear to a quadratic dependency on the wave vector and can be described using an effective mass

$$m_\mathrm{C}^* = E_\mathrm{C}(k_\parallel = 0)\frac{n_\mathrm{C}^2}{c^2} \tag{2.11}$$

that, under the consideration of relativistic effects, is even predicted to be an actual inertial and gravitational mass [Ric19]. As the in-plane wave vector is directly linked to the emission angle θ by

$$k_\parallel = n_\mathrm{C}\frac{2\pi}{\lambda_\mathrm{C}} \tan\left(\sin^{-1}\left(\frac{\sin\theta}{n_\mathrm{C}}\right)\right) \approx \frac{2\pi}{\lambda_\mathrm{C}}\theta \quad \text{for} \quad k_\parallel \ll k_\perp, \tag{2.12}$$

the dispersion can be imaged through angular resolved spectroscopy. It is additionally important to note that, opposed to metallic mirrors, the electric field penetrates into the DBRs resulting in an effective cavity length

$$L_\mathrm{eff} = L_\mathrm{C} + L_\mathrm{DBR} \quad \text{with} \quad L_\mathrm{DBR} \approx \frac{\lambda_\mathrm{C}}{2n_\mathrm{C}}\frac{n_1 n_2}{|n_1 - n_2|} \tag{2.13}$$

for normal incidence and $\lambda_\mathrm{C} = \lambda_\mathrm{DBR}$, as depicted in Fig. 2.2 b). By mismatching the stopband centre ω_DBR and the cavity resonance ω_C, the penetration depth into the DBRs and therefore also the effective cavity length and thus the energy of the cavity resonance acquire a dependence on the polarisation, resulting in an energetic splitting between transverse electric (TE) and transverse magnetic (TM) polarised modes that is only zero at normal incidence and is given by

$$\omega^\mathrm{TM}(\theta) - \omega^\mathrm{TE}(\theta) \approx \frac{L_\mathrm{C} L_\mathrm{DBR}}{L_\mathrm{eff}^2}\frac{2\cos\theta_\mathrm{eff}\sin^2\theta_\mathrm{eff}}{1 - 2\sin^2\theta_\mathrm{eff}}\left(\omega_\mathrm{s}(0) - \omega_\mathrm{C}(0)\right) \tag{2.14}$$

with $\theta_{\text{eff}} \approx \arcsin\left(\frac{n_{\text{DBR}}}{n_{\text{C}}} \sin\theta\right)$ being the effective incidence angle in the cavity region with a refractive index of the first DBR layer of n_{DBR} [Pan+99]. The importance of this splitting will become apparent in section 2.2.4, as it can be viewed as an artificial gauge field comparable to spin-orbit interaction in the context of understanding polarisation as a pseudospin.

2.2.2 Excitonic confinement in quantum wells

A common approach towards treating excitations within a matter environment is to consider the ground state of this matter as the new quasivacuum to then be able to refer to the excitations as quasiparticles. One example of such a quasiparticle, named *exciton*, is an excited electron that is bound to a hole by Coulomb interaction. The binding energy and thus also the Bohr radius a_{B} depend on the dielectric screening of the environment, with strongly bound excitons termed *Frenkel excitons* [Fre31] and weakly bound excitons being referred to as *Wannier-Mott excitons* [Wan37]. While Frenkel excitons featuring binding energies on the order of 1 eV are commonly observed in organic semiconductors [Knu03], Wannier-Mott excitons with binding energies on the order of 1 meV are present inorganic semiconductors such as GaAs [Nam+76]. As excitons represent a dipole, they can interact with light with an interaction strength

$$f = \frac{2m_{\text{X}}^{*}\omega}{\hbar} \langle u_{\text{h}}|e\boldsymbol{r}|u_{\text{e}}\rangle^2 \frac{V}{\pi a_{\text{B}}^3}, \tag{2.15}$$

where m_{X}^{*} refers to the effective exciton mass, $|u_{\text{e,h}}\rangle$ are the electron and hole Bloch functions, $e\boldsymbol{r}$ the dipole operator and V the volume. The exciton pseudospin s_{X} is dictated by the electron spin $s_{\text{e}} = \pm 1/2$ and the light (heavy) hole pseudospin $s_{\text{h}} = \pm 1/2, (\pm 3/2)$, resulting in possible values of $s_{\text{X}} = \pm 1, \pm 2$. As momentum conservation allows only excitons with a pseudospin of $s_{\text{X}} = \pm 1$ to be directly optically accessed, excitons with a pseudospin of $s_{\text{X}} = \pm 1$ and $s_{\text{X}} = \pm 2$ are also referred to as bright and dark excitons, respectively.
Excitons can be confined by fabricating their host material as a thin layer of semiconductor with a band gap that is smaller than the band gap of the surrounding material and lies within the latter. These two-dimensional excitons interact significantly stronger with light, as only the in-plane wave vector needs to match with the exciting light and the Bohr radius is decreased, leading to an increase in interaction strength.
For this work, it is furthermore important to note that excitons that are placed in an external magnetic field B are subject to a diamagnetic shift

$$\Delta_{\text{dia}} = \kappa_{\text{X}} B^2, \tag{2.16}$$

given by the effective diamagnetic factor κ_{X} [Nas+89], and a Zeeman splitting [Zee97]

$$\Delta_{\mathrm{Z}} = g_{\mathrm{X}}(B)\mu_{\mathrm{B}}B \tag{2.17}$$

of the exciton pseudospins, with μ_{B} denoting the Bohr magneton and $g_{\mathrm{X}}(B)$ the effective exciton g-factor. As the exciton g-factor is influenced both by the electron and the hole, its dependence on the magnetic field is strongly nonlinear [Kot+01].

2.2.3 Light-matter interaction

A powerful scheme to realise high interaction strengths between light and matter is to place one or multiple quantum wells hosting excitons inside a microcavity. Here, the highest interaction is achieved by placing the quantum wells at the position of the anti-node of the electric field of the cavity resonance, which is usually designed to be at the centre of the cavity layer as introduced in Fig. 2.2 b). The coupling of excitons and photons is described by the Hamiltonian

$$\hat{H} = \begin{pmatrix} E_{\mathrm{C}} + i\hbar\gamma_{\mathrm{C}} & V \\ V & E_{\mathrm{X}} + i\hbar\gamma_{\mathrm{X}} \end{pmatrix}, \tag{2.18}$$

with V denoting the coupling strength between the two oscillators, γ_{C} the rate of photons leaving the cavity and γ_{X} the rate of non-radiative exciton decay.
The two eigenvalues

$$\begin{aligned} E_{\mathrm{UP,LP}}(k_{\parallel}) = &\frac{1}{2}\left(E_{\mathrm{C}}(k_{\parallel}) + E_{\mathrm{X}}(k_{\parallel}) + i\hbar(\gamma_{\mathrm{C}} + \gamma_{\mathrm{X}})\right) \\ &\pm \frac{1}{2}\sqrt{4V^2 + \left(E_{\mathrm{C}}(k_{\parallel}) - E_{\mathrm{X}}(k_{\parallel}) + i\hbar(\gamma_{\mathrm{C}} - \gamma_{\mathrm{X}})\right)^2} \end{aligned} \tag{2.19}$$

of this Hamiltonian are characterised by a vacuum Rabi splitting at a detuning of $\Delta_{\mathrm{E}} = E_{\mathrm{C}} - E_{\mathrm{X}} = 0$ given by

$$2\hbar\Omega_{\mathrm{R}} = E_{\mathrm{UP}}(k_{\parallel} = 0) - E_{\mathrm{LP}}(k_{\parallel} = 0) = \sqrt{4V^2 - \hbar^2\left(\gamma_{\mathrm{C}} - \gamma_{\mathrm{X}}\right)^2}. \tag{2.20}$$

The term *vacuum Rabi splitting* indicates the analogy to normal mode coupling between an atom and a cavity mode that is described by the Jaynes-Cummings model [JC63] and features an oscillation of the excitation between the atom and the photonic mode at the Rabi frequency. However, there are several major differences between the two systems, the most significant of which is the fact that an atom is a quantum mechanical two level system whereas excitons in a quantum well are most appropriately described as

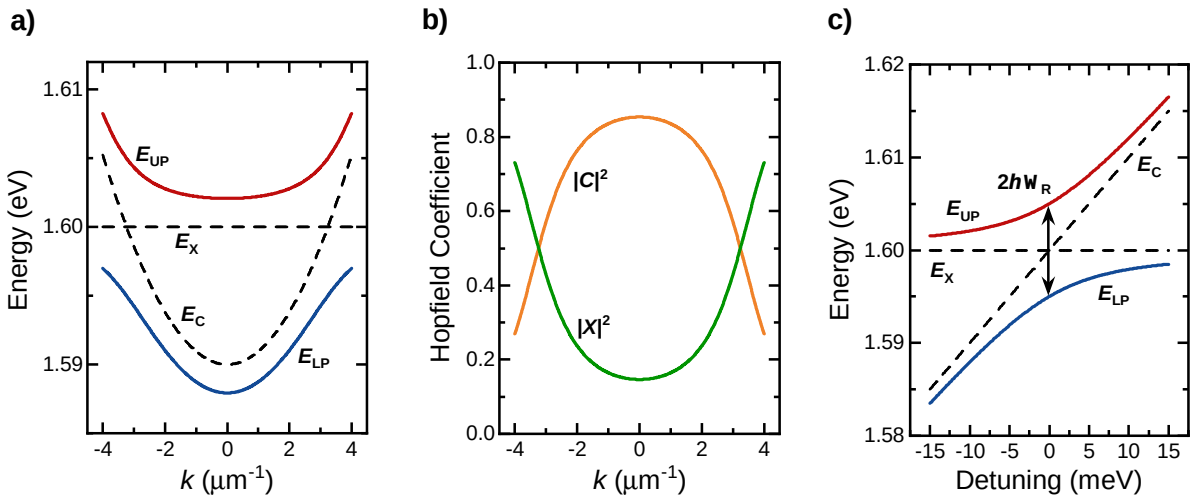

Figure 2.3: **a)** Dispersion relation of the lower and upper polariton branch for an exciton-photon detuning of $\Delta_{\mathrm{E}} = -10\,\mathrm{meV}$ and a Rabi splitting of $2\hbar\Omega_{\mathrm{R}} = 10\,\mathrm{meV}$. The uncoupled excitonic and photonic modes are represented by dashed lines. **b)** Hopfield coefficients for the excitonic ($|X|^2$) and photonic ($|C|^2$) components of the lower polariton. **c)** Polaritonic eigenenergies at $k_{\parallel} = 0$ as a function of the detuning visualising the anti-crossing behaviour of the new eigenmodes.

a harmonic oscillator [SFW98; HR06]. Using equations 2.19 and 2.20, the detuning can be expressed as

$$\Delta_{\mathrm{E}}(k) = \frac{4E_{\mathrm{LP}}(k_{\parallel})^2 - (2\hbar\Omega_{\mathrm{R}})^2 - 8E_{\mathrm{LP}}(k_{\parallel}) \cdot E_{\mathrm{X}} + 4E_{\mathrm{X}}^2}{4\left(E_{\mathrm{LP}}(k_{\parallel}) - E_{\mathrm{X}}\right)}. \tag{2.21}$$

For imaginary values of the square root in equation 2.20, the system is referred to as weakly coupled and excitons and photons remain the eigenmodes. However, for $V > \frac{\hbar}{2}\,|\gamma_{\mathrm{C}} - \gamma_{\mathrm{X}}|$, the two oscillators are strongly coupled resulting in new eigenmodes that are a combination of exciton and photon and are referred to as exciton-polaritons (polaritons). In this regime, that was first observed experimentally in 1992 by Weisbuch and co-workers [Wei+92], energy is coherently transferred between exciton and photon. Here, the Rabi splitting $2\hbar\Omega_{\mathrm{R}}$ corresponds to the experimentally observable energetic splitting between the two oscillators at a detuning of $\Delta_{\mathrm{E}} = 0$. Equation 2.19 describes the dispersions of the upper and the lower polariton branch, UP and LP, respectively, that are displayed in Fig. 2.3 a). These polaritons are part-light, part-matter quasiparticles with a composition

that is given by the Hopfield coefficients [Hop58]

$$\begin{aligned} \left|C(k_\parallel)\right|^2 &= \frac{1}{2}\left(1 - \frac{\Delta_\mathrm{E}(k_\parallel)}{\sqrt{\Delta_\mathrm{E}^2(k_\parallel) + (2\hbar\Omega_\mathrm{R})^2}}\right) \quad \text{and} \\ \left|X(k_\parallel)\right|^2 &= \frac{1}{2}\left(1 + \frac{\Delta_\mathrm{E}(k_\parallel)}{\sqrt{\Delta_\mathrm{E}^2(k_\parallel) + (2\hbar\Omega_\mathrm{R})^2}}\right) \end{aligned} \tag{2.22}$$

with photonic and excitonic fractions $|C|^2$ and $|X|^2$, respectively, and $|C|^2 + |X|^2 = 1$, as presented in Fig. 2.3 b). The most characteristic feature of such a strongly coupled system is the anti-crossing behaviour displayed in Fig. 2.3 c) that occurs when one of the underlying modes, namely the exciton or the photon, is tuned across the energy of the other mode. The unique composition of polaritons as a combination of excitons and photons constitutes a distinct set of properties including a very low effective mass, inherited from the photonic fraction, on the order of $m_\mathrm{P}^* \approx 10^{-5} m_\mathrm{e}$, with m_e denoting the electron mass, and the ability to interact and be susceptible to magnetic fields, inherited from the excitonic part. Due to the short lifetime of microcavity photons on the order of 10 ps, compared to excitonic lifetimes on the order of several 100 ps up to 1 ns, the decay of polaritons is dominated by photons that leave the microcavity. As these photons carry the phase, amplitude, momentum and energy information of the polariton, they provide direct experimental access to the polariton states by photoluminescence (PL) spectroscopy. It is this set of properties that has driven the development of an active field of research in the pursuit of potential optoelectronic applications, where in particular the development of platforms such as organic semiconductors [Lid+98; Lid+99], II-VI semiconductors [Sab+01] as well as GaN-based microcavities [Taw+04; But+06] that open the path towards room temperature operation is worth mentioning.
For an even higher interaction strength between excitons and photons, on the order of the coupling strength of the excitons, a regime of very strong coupling leading to a hybridisation with higher orbital excitons was predicted [Khu01; CK03] and realised experimentally [Bro+17].

2.2.4 Properties and excitation of polaritons

Polariton pseudospin and orbital angular momentum

The polariton pseudospin is a powerful concept to describe the interplay of the excitonic pseudospin and the photonic polarisation as well as their evolution under various conditions [Kav+04; She+09]. The excitonic pseudospin and the photonic polarisation are intertwined, as light with a circular polarisation of $S_3 = \pm 1$ excites bright excitons with

a pseudospin of $s_\mathrm{X} = \pm 1$, respectively, whereas linearly polarised light excites a linear combination of the two excitonic pseudospin orientations. Analogously to projecting the photonic polarisation onto the Poincaré sphere (s. Fig. 2.1), the polariton pseudospin is mapped onto the Bloch sphere simply by replacing the horizontal and vertical, diagonal and anti-diagonal and left and right circular polarisations with the spin components $s_\mathrm{x}, s_\mathrm{y}, s_\mathrm{z} = \pm 1/2$. The pseudospin of a polariton therefore becomes apparent in the emission of polarised light.

Whereas the polariton pseudospin can be experimentally accessed by measuring the Stokes parameters of the polarised emission, the orbital angular momentum of the polaritonic state translates into the orbital angular momentum of the light emitted from the cavity. For a coherent state with a fixed phase relation, the orbital angular momentum therefore becomes apparent in a spatial phase map which can be measured through interference techniques.

For a range of phenomena, the coupling of motion and spin of a particle, referred to as spin-orbit coupling, is of key importance. Such a spin-orbit coupling can be defined for polaritonic systems as well and is achieved by realising a coupling between the polariton pseudospin and its orbital angular momentum [Sal+15]. Here, a thorough understanding of the dynamics of the polariton pseudospin is essential and has thus evolved to be a complex area of research. The pseudospin can decay through relaxation of the excitonic pseudospin, which is governed mainly by spin-flip exchange interaction of electrons and holes [PB71; MAS93; She+09], or a loss of coherence of the photonic component. Furthermore, its interplay with internal and external magnetic fields leads to a rich set of effects. In particular, the TE-TM splitting of the cavity mode, which was introduced in section 2.2.1, plays a major role as it lifts the degeneracy of the polarised photonic modes and can, in the pseudospin picture, be described as an internal magnetic field analogously to the Rashba field that is used to describe spin-orbit interaction for electronic systems. A comparison of the two fields

$$\boldsymbol{B}_\mathrm{eff}^\mathrm{Rashba}(\boldsymbol{k}_\parallel) \sim (\boldsymbol{e}_\mathrm{x}\cos(\phi) + \boldsymbol{e}_\mathrm{y}\sin(\phi)) \tag{2.23a}$$

$$\boldsymbol{B}_\mathrm{eff}^\mathrm{TE\text{-}TM}(\boldsymbol{k}_\parallel) \sim (\boldsymbol{e}_\mathrm{x}\cos(2\phi) + \boldsymbol{e}_\mathrm{y}\sin(2\phi)) \tag{2.23b}$$

demonstrates the similarity, as the only difference in the dependence on the wave vector of the two fields is a factor of two in the winding number. This unique dependence on the wave vector, however, leads to peculiar effects such as the optical spin Hall effect [KMG05; Ley+07], polarisation-dependent patterns [Lan+07] as well as polarisation and phase vortices [LKS07]. The polariton pseudospin is furthermore susceptible to external magnetic fields as they lift the degeneracy of the excitonic pseudospin components through the Zeeman effect, as will be discussed later on.

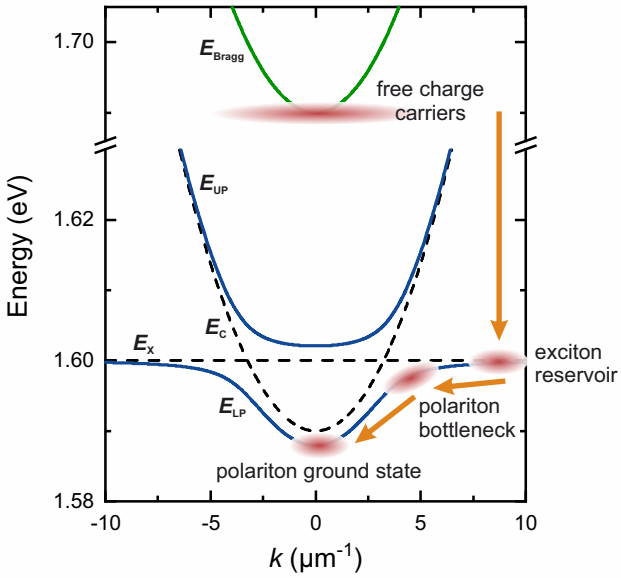

Figure 2.4: Schematic of the relaxation processes that lead to a population of the polariton ground state through non-resonant excitation. This figure was adapted from reference [Kas+06].

Polariton excitation

This section provides a brief description of the prevailing methods to create a polariton population from a theoretical viewpoint, whereas a description of the technological aspects of realising these excitation schemes can be found in section 3.2. The most common approach towards creating a polariton population is schematically depicted in Fig. 2.4 and features a non-resonant scheme in which free charge carriers are excited at an energy above the exciton energy by tuning a laser to a high-energy reflection minimum of the stopband of the upper DBR, referred to as *Bragg minimum* E_{Bragg}. An electrical injection of free charge carriers is technologically achievable as well [Tis+05; Tsi+08] and can be treated analogously. These free charge carriers dissipate energy to the lattice and form an exciton reservoir. Through spontaneous emission of photons and the coupling process described in section 2.2.3, polaritons occupying predominantly the lower polariton branch at high wave vectors and thus with a high excitonic fraction and lifetime are formed. Efficient scattering with phonons, other excitons and polaritons allows further cooling until the photonic influence becomes significant, resulting in a steeper dispersion and shorter lifetime, where scattering with phonons becomes inefficient [Lag+03; Doa+05]. At this so-called bottleneck, polariton-polariton scattering is the predominant scattering mechanism to create a polariton population at the energy minimum of the dispersion at $k_{\parallel} = 0$ [Das+02; Per+05].

Alternatively to non-resonant excitation schemes, a polariton population at a determinis-

tic position of the dispersion can be created through resonant excitation by matching the wave vector and the energy of the desired state with the excitation laser. In particular, the incidence angle and energy of the excitation laser can be carefully tuned to coincide with the lower polariton branch such that parametric scattering results in a polariton population in the ground state as well as a population at correspondingly higher energy and wave vector [Bau+00]. This excitation scheme is consequently referred to as an *optical parametric oscillator*. It is important to note that, in contrast to non-resonant excitation, the phase and polarisation of the excitation laser is imprinted on the resonantly excited polariton population. Finally, a quasi-resonant excitation by tuning the laser resonantly to the exciton reservoir is feasible.

Polariton condensation

The phenomenon of spontaneously occurring coherence, known for example from the laser introduced in section 2.1, has motivated ongoing research for decades. Another phase that is characterised by a macroscopic coherence forming at a threshold is the Bose-Einstein condensate (BEC) [PS03]. Based on Bose's formulation of the statistics for bosonic particles [Bos24], Einstein developed the idea that a gas of non-interacting bosons should, at a certain critical density of equivalently at a certain critical temperature, be able to undergo a phase transition to the macroscopic occupation of a single, coherent ground state [Ein24], referred to as *Bose-Einstein condensate* BEC. The criterion to reach this phase transition can be understood as a density that is high enough for the wavefunctions to overlap and is given by

$$n\lambda_{\mathrm{D}}^3 = 2.62 \quad \text{with} \quad \lambda_{\mathrm{D}} = \sqrt{\frac{2\pi\hbar^2}{mk_{\mathrm{B}}T}}, \tag{2.24}$$

for density n, de Broglie wavelength λ_{D}, Boltzmann constant k_{B} and temperature T. This phase transition leads to the appearance of a macroscopic condensate wavefunction $\psi(\boldsymbol{r})$ with non-zero mean value

$$\langle\psi(\boldsymbol{r})\rangle = \sqrt{n(\boldsymbol{r})}e^{i\theta(\boldsymbol{r})}, \tag{2.25}$$

where the real part is given by the square root of the density and the imaginary part describes the specific phase ϕ that arises at the threshold and represents the appearance of phase coherence.

As polaritons consist of excitons, which are bosonic as long as their wavefunctions do not overlap, and photons, which are bosons as well, they follow bosonic statistics at low densities. Furthermore, their effective mass is very low due to the photonic component, rendering them good candidates to achieve Bose-Einstein condensation at elevated

temperatures. It is thus not surprising that, when increasing the excitation power, the relaxation processes described above lead to an increase in occupation of the lowest-energy state which, as soon as a threshold density is reached, leads to stimulated scattering into the lowest energy state and the formation of a condensate. However, due to long wavelength thermal fluctuations, long-range order and thus a BEC should be inhibited in two-dimensional systems [Hoh67]. This argument can be overcome by limiting the system to a finite size given by a box with length L, which can reasonably be assumed for any experimental system, resulting in a criterion for condensation given by

$$n = \frac{2}{\lambda_{\mathrm{D}}^2} \ln\left(\frac{L}{\lambda_{\mathrm{D}}}\right). \tag{2.26}$$

As BECs represent a macroscopically occupied, coherent state, polariton condensates where soon theoretically considered for lasing applications [Ima+96; Mal+03], as they would not require the population inversion that is critical for photonic lasers [Den+03]. The following experimental efforts [Ric+05] resulted in the first realisation of a polariton condensate 2006 by Kasprzak and co-workers [Kas+06]. As the field developed further, the size of the condensates was increased [Bal+17], the operating temperature of polariton lasers was extended to room temperature [GB16] based on the organic, II-VI and GaN semiconductor material platforms and even an electrically injected polariton laser was realised [Sch+13; Bha+13]. As one of the defining characteristics of polariton condensation is the build-up of coherence, significant efforts were directed towards the theoretical [PT03; WE09] and experimental investigation of the spatial [Den+07; Spa+12] and temporal [Kas+08; Hau+12; Adi+15] coherence properties of polariton condensates. Furthermore, the influence of reducing the condensate dimensionality [Zha+14; Fis+14; Kla+18] as well as the prevailing decoherence mechanisms [Lov+08; Kle+18] were studied, resulting in the establishment of a coherent polariton laser [Kim+16]. Linked to the coherence properties of polariton condensates is their well-defined pseudospin which has motivated work on the control of the pseudospin [Ask+16; Kla+19] as well as the implementation of a chiral polariton laser [Car+19].

A major difference between polaritons and an ideal gas is the finite lifetime which, to reach a BEC at thermal equilibrium, needs to be larger than the thermalisation time. In this ongoing field of research [DHY10; CC13; BKY14], currently the three terms *polariton BEC*, *polariton laser* and *photon laser* are distinguished. A *polariton BEC* describes a condensate in thermodynamic equilibrium, whereas a macroscopic occupation of a single state without thermalisation is commonly achieved experimentally and is referred to as a *polariton laser*. The experimental observables of this condensation are a non-linear increase in intensity, a drop in linewidth correlated to the build-up of coherence and an

energetic blueshift due to the increased interaction of polaritons resulting from the higher densities. Furthermore, the macroscopic occupation of one pseudospin degree of freedom leads to linearly polarised emission. Owing to its emission characteristic, this type of driven-dissipative, non-equilibrium condensate is referred to as a *polariton laser*. Both the polariton BEC and the polariton laser are covered by the comprehensive term *polariton condensate*. At an even higher excitation power, the Mott density, given in the simplest approximation by $n_{\mathrm{M}} = a_{\mathrm{X}}^{-3}$ [Kli12] with a_X denoting the exciton Bohr radius, is reached. At this density, the excitons decay into an electron-hole plasma due to overlap of their wave functions and the microcavity behaves as a *photon laser*, or more specifically a vertical-cavity surface-emitting laser (VCSEL). The main difference between a polariton laser and a photon laser is the origin of the coherence. In a polariton laser, the coherence is generated through stimulated scattering into a single state resulting in a coherent active medium that emits through spontaneous emission, while a photon laser emits coherently through stimulated emission from an incoherent active medium. Due to the strong coupling to excitons, the polariton laser can be distinguished from a photon laser by the blueshift of the condensate with increasing excitation power and through its susceptibility to external magnetic fields.

Inspired by the close link between Bose-Einstein condensation and superfluidity, prominently featuring frictionless transport, polariton research has also directed its attention towards a description of polariton condensates as *quantum fluids of light* [CC13]. Polaritonic superfluids were investigated in experiments [Amo+09a; Ler+17] and theory [WC10]. Motivated by the vision of answering open questions regarding for example a Berezinskii-Kosterlitz-Thouless (BKT) transition, votices and vortex pairs in polariton superfluids have been studied [Lag+08; Nar+11; Rou+11], manifesting the potential of polaritonic simulators due to the combination of their unique properties with excellent experimental access.

2.3 Lattice potentials

The main constituents of this thesis are polaritons confined in lattice potentials. Following the introduction into polariton physics in the previous section, this section therefore provides an overview of the formation of band structures in lattice potentials. After a general introduction of band structure calculation and the concept of an effective mass in the context of a band structure, the two extreme cases of a vanishing effective mass in Dirac cones as well as an infinite effective mass in flatbands are highlighted.

2.3.1 Band structure calculation

When trying to understand the formation of a band structure in solid-state physics [Kit05; AM12], one intuitively starts by describing individual atoms that are characterised by discrete energy levels. By coupling two atoms together, these atomic energy levels split into molecular orbitals, with each atomic orbital resulting in one molecular orbital. Consequently, when coupling multiple atoms, the energy levels split further and form a band structure of states that are available for the electrons. The most important characteristic of these bands is their momentum dependence, given by the dispersion relation $E(\boldsymbol{k})$. Analogously to electrons in atoms, polaritons can be confined into micropillars resulting in discrete energy levels. A detailed introduction on the technological implementation of creating trapping potentials for polaritons is provided in section 3.1.2. When coupling these micropillars together by placing them close to each other in a lattice geometry, polaritonic band structures that closely resemble the electronic band structures known from crystalline materials can be formed.
The simplest theoretical description of such a band structure is the tight binding approach that treats the lattice Hamiltonian

$$H = \sum_i H_{\mathrm{at}}(\boldsymbol{r} - \boldsymbol{R}_i) + \Delta U(\boldsymbol{r}) \tag{2.27}$$

as a sum of the Hamiltonians H_{at} of the individual atoms at positions $\boldsymbol{R}_i$ with an energy deviation $\Delta U(\boldsymbol{r})$ describing the influence of the lattice potential. Due to the translational symmetry of a lattice, the wave function solving this Hamiltonian needs to satisfy the Bloch theorem which would intuitively motivate a linear combination of plane waves. However, such plane waves would neglect the orbital nature of the atomic states, thus motivating an approach based on Bloch functions, where the Bloch function $\phi_j(\boldsymbol{k}, \boldsymbol{r})$ of a

sub-band is constructed as a linear combination of atomic orbitals (LCAO) [SDD98]

$$\phi_j(\boldsymbol{k}, \boldsymbol{r}) = \frac{1}{\sqrt{N}} \sum_{\boldsymbol{R}}^{N} e^{i\boldsymbol{k}\boldsymbol{R}} \varphi_j(\boldsymbol{r} - \boldsymbol{R}), \tag{2.28}$$

where φ_j denotes the orbital wavefunction of the jth atom of the lattice unit cell and $\boldsymbol{R}$ corresponds to the lattice vector in a lattice composed of N unit cells. The eigenfunctions of the lattice are then expressed as linear combinations of these Bloch functions as

$$\psi_j(\boldsymbol{k}, \boldsymbol{r}) = \sum_{k=1}^{n} c_{jk}(\boldsymbol{k}) \phi_k(\boldsymbol{k}, \boldsymbol{r}) \tag{2.29}$$

and the energy eigenvalues are given by

$$E_j(\boldsymbol{k}) = \frac{\langle \psi_j | H | \psi_j \rangle}{\langle \psi_j | \psi_j \rangle}. \tag{2.30}$$

The elements of the Hamiltonian can be calculated by

$$H_{jk}(\boldsymbol{k}) = \langle \phi_j | H | \phi_k \rangle \,. \tag{2.31}$$

Each discrete energy level of a site results in one band with a bandwidth determined by the coupling strength. Furthermore, as the orbital nature of the underlying states needs to be considered [Ma+19], its nomenclature, such as S, P and D orbitals, is transferred to the resulting bands. In analogy to the formation of a band structure for atomic crystals, this nomenclature is used for bands of artificial lattices as well. Furthermore, as each site in the unit cell contributes one state per band, the number of sub-bands in a band is given by the number of sites in the unit cell.

The tight binding method allows to get a quick estimate of the bands, including the dispersion relations, that are to be expected for a given lattice. However, some deviations to experimentally determined band structures are expected for polaritonic systems due to rather shallow confinement potentials, the influence of mode hybridisation and deviations from the real space mode patterns. A more accurate description can be obtained by an alternative approach based on calculating the full Bloch modes consisting of excitonic and photonic components and a realistic real space potential environment, thus representing the experimental conditions far more accurately [Kle+17].

2.3.2 Effective mass in band structures

The motion of a particle in a lattice potential environment is significantly altered compared to the motion in vacuum. This deviation is commonly described by assigning an effective band mass defined as

$$m^*_{\text{band}} = \hbar^2 \left(\frac{\partial^2 E(\boldsymbol{k})}{\partial \boldsymbol{k}^2} \right)^{-1} \tag{2.32}$$

to particles in a lattice reflecting the influence of the dispersion relation $E(\boldsymbol{k})$. In particular, the two distinct cases of a vanishing effective mass, achieved for linear dispersions at Dirac points, and the infinitely large effective mass, achieved in flatbands where the energy is constant independently of $\boldsymbol{k}$, have attracted significant scientific interest.
In the first case, the vanishing effective mass at linear dispersions results in relativistic transport of particles described by the Dirac equation [Dir28] and has thus provoked such dispersions to be referred to as Dirac cones. Due to the relativistic transport, these Dirac cones are ideally suited to study phenomena such as the Klein paradox of perfect transmission of relativistic particles through a tunnel barrier [Kle29]. Additionally, band touching points at Dirac points have attracted significant interest in the context of opening topological band gaps [Hal88]. The most prominent example of a two dimensional lattice hosting Dirac cones is the honeycomb lattice geometry of graphene [Cas+09] that, next to research on graphene, has spurred the development of numerous platforms for artificial lattices [Pol+13].
In contrast to Dirac cones, flatbands are characterised by an infinite effective mass corresponding to fully localised states with a vanishing group velocity $\boldsymbol{\nabla}_{\boldsymbol{k}} E(\boldsymbol{k})$ that are referred to as *compact localized states (CLSs)* [AAM96]. The first predictions of lattices featuring such a flatband where the dice lattice proposed by Sutherland [Sut86] and the Lieb lattice [Lie89]. These first discoveries where generalised by Mielke and Tasaki in the context of flatband ferromagnetism that occurs if the flatband is the lowest energy band [Mie91; Tas92; Tas08]. Mielke replaced the links of a given lattice with sites, so called line graphs, to generate lattices that host flatbands, whereas Tasaki fine-tuned the interplay of nearest and next-nearest neighbour coupling. While finely tuning system parameters has unveiled a broad range of flatband lattices, a general theory is still lacking. Therefore, nowadays an approach based on assuming the existence of a CLS and then constructing compatible Hamiltonians is used not only to generate new geometries that support flatbands but also to advance a more general understanding of the latter [Mai+17; LAF18]. Notably, the localisation in flatbands does not arise through a local deformation of the potential, but rather through a combination of phase frustration and geometric symmetry considerations. While there has been ongoing theoretical interest in flatband systems since their first description in the 1980s, experimental studies that use the peculiar nature

of flatbands to investigate for example the magnetic ordering, the enhanced inter-particle interaction or the sensitivity to disorder have only recently evolved, in particular in the context of artificial flatband systems [LF18; LAF18].

2.3.3 Two-dimensional lattices

In two dimensions, there are five Bravais lattices, namely the oblique, square, rectangular, centred-rectangular and hexagonal lattices. In the following, the square and the hexagonal lattices as well as lattices derived from these base lattices will be introduced, since polaritonic implementations of these lattices are studied within this work.
The square lattice is a valuable model system due to its simple geometry which is displayed in Fig. 2.5 b). Its real space geometry defines the high-symmetry points Γ, X and M of the Brillouin zone that is displayed in Fig. 2.5 a) and results in a square symmetry of the energy dispersion of the S band, calculated using the tight binding approach and given by

$$E(\boldsymbol{k}_{\parallel}) = 2t\left(\cos(k_{\mathrm{x}}a) + \cos(k_{\mathrm{y}}a)\right) \tag{2.33}$$

with nearest neighbour coupling t and nearest neighbour distance a that is displayed in Fig. 2.5 c). An important lattice derived from the square lattice is the Lieb lattice featuring the square unit cell with three sites that is presented in Fig. 2.5 d). Owing to its square geometry, it shares the same high-symmetry points of the Brillouin zone. The energy dispersion of the S band, as given by a tight binding model, can be expressed as

$$E(\boldsymbol{k}_{\parallel}) = 0; \pm 2t\sqrt{\cos^2\left(k_{\mathrm{x}}a\right) + \cos^2\left(k_{\mathrm{y}}a\right)} \tag{2.34}$$

with nearest neighbour coupling t. It features a flatband that intersects with a Dirac point at the M-point of the Brillouin zone, as can be observed in Fig. 2.5 e).
Similarly to the square lattice, the hexagonal lattice, that is also referred to as triangular lattice, is a valuable model system and represents the base for interesting derived lattices. Its Brillouin zone with high-symmetry points Γ, K, K' and M and the real space geometry are presented in Figs. 2.6 a) and b). As the hexagonal lattice features only one site per unit cell, the K and K' points are equivalent. The dispersion relation of its S band, determined by a tight binding model, is given by

$$E(\boldsymbol{k}_{\parallel}) = 2t\left(\cos\left(k_{\mathrm{x}}a\right) + 2\cos\left(\frac{1}{2}k_{\mathrm{x}}a\right)\cos\left(\frac{\sqrt{3}}{2}k_{\mathrm{y}}a\right)\right) \tag{2.35}$$

and is displayed in Fig. 2.6 c). Historically, the most famous, derived lattice of the hexagonal lattice is the honeycomb lattice, as it is the lattice geometry of graphene [Cas+09].

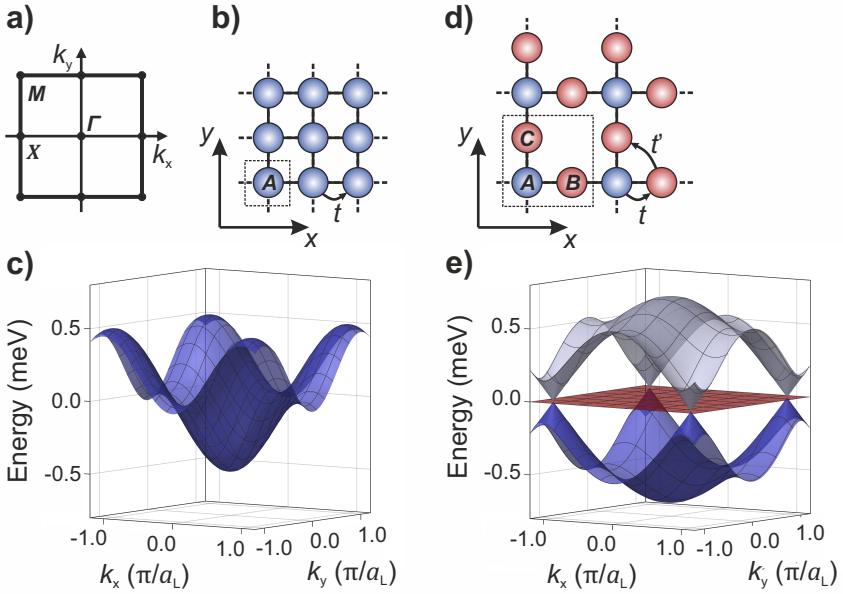

Figure 2.5: **a)** Brillouin zone of the square and Lieb lattices, characterised by the high-symmetry points Γ, X and M. **b)** Real space geometry of the square lattice and the corresponding dispersion of the S band in **c)**, with a_L denoting the lattice constant. **d)** Real space geometry of the Lieb lattice with three sites in the unit cell and its S band dispersion relation featuring a flatband (red) intersecting with the dispersive bands at the Dirac point at the M point of the Brillouin zone in **e)**.

Its geometry featuring a hexagonal lattice with two sites in the unit cell is presented in Fig. 2.6 d). Here, it is important to note that the edge terminations on the top and bottom are referred to as armchair edges, whereas the left and right edges are called zigzag edges. In artificial honeycomb lattices, a third edge termination featuring an additional site in front of the outermost sites of the zigzag-edge, referred to as bearded edge, can be realised. Furthermore, lattices featuring a unit cell with two sites, such as the honeycomb lattice, are commonly referred to as *bipartite* lattices. The Brillouin zone of the honeycomb lattice features the same geometry as the Brillouin zone of the hexagonal lattice that is depicted in Fig. 2.6 a), with the important difference of the K and K' points being nonequivalent. Whereas at the K point, the valence (conduction) band originates from atomic orbitals of the A (B) site, the opposite holds true for the K' point. The S band dispersion obtained by tight binding calculation

$$E(k) = \pm t\sqrt{3 + f(k)} - t' f(k) \tag{2.36a}$$

$$\text{with} \quad f(k) = 2\cos\left(\sqrt{3}k_\mathrm{y}a\right) + 4\cos\left(\frac{\sqrt{3}}{2}k_\mathrm{y}a\right)\cos\left(\frac{3}{2}k_\mathrm{x}a\right) \tag{2.36b}$$

with nearest neighbour coupling t and next-nearest neighbour coupling t' is displayed in Fig. 2.6 e). It famously features two Dirac points at the touching points of the two S sub-bands, located at the K and K' points of the Brillouin zone, and was first described by Wallace in 1947 [Wal47]. Another important derived lattice of the hexagonal geometry is the Kagome lattice which is named after the woven pattern of a Japanese bamboo basket [Mek03] that shares the same geometry. The Kagome lattice was introduced to the realms of physics in the context of magnetism [Syo51] and can be constructed as the line graph of the honeycomb lattice by building a lattice of sites located at the connections between adjacent sites of the honeycomb lattice [Mie91; Mie92]. Its geometry, characterised by a hexagonal lattice with three sites in the unit cell, is displayed in Fig. 2.6 f) and therefore also shares the Brillouin zone with the high-symmetry points Γ, K, K' and M with the hexagonal lattice. Within the tight binding approximation, the dispersion of the S band is given by

$$E(\boldsymbol{k}_{\parallel}) = 2t; -t \pm 2t\cos\left(\sqrt{3}k_{\mathrm{x}}a + 2k_{\mathrm{y}}a\right)\sqrt{3 + 4\cos\left(\sqrt{3}k_{\mathrm{x}}a\right)\cos\left(k_{\mathrm{y}}a\right) + 2\cos\left(2k_{\mathrm{y}}a\right)}. \tag{2.37}$$

As can be observed in Fig. 2.6 g), the Kagome lattice inherits the lowest two sub-bands of the S band from the honeycomb lattice and features and additional flatband on top of these two sub-bands. It is important to note that, by changing the sign of the hopping term and thereby switching to an attractive coupling, the flatband becomes the lowest energy band and thus the ground state of the lattice.

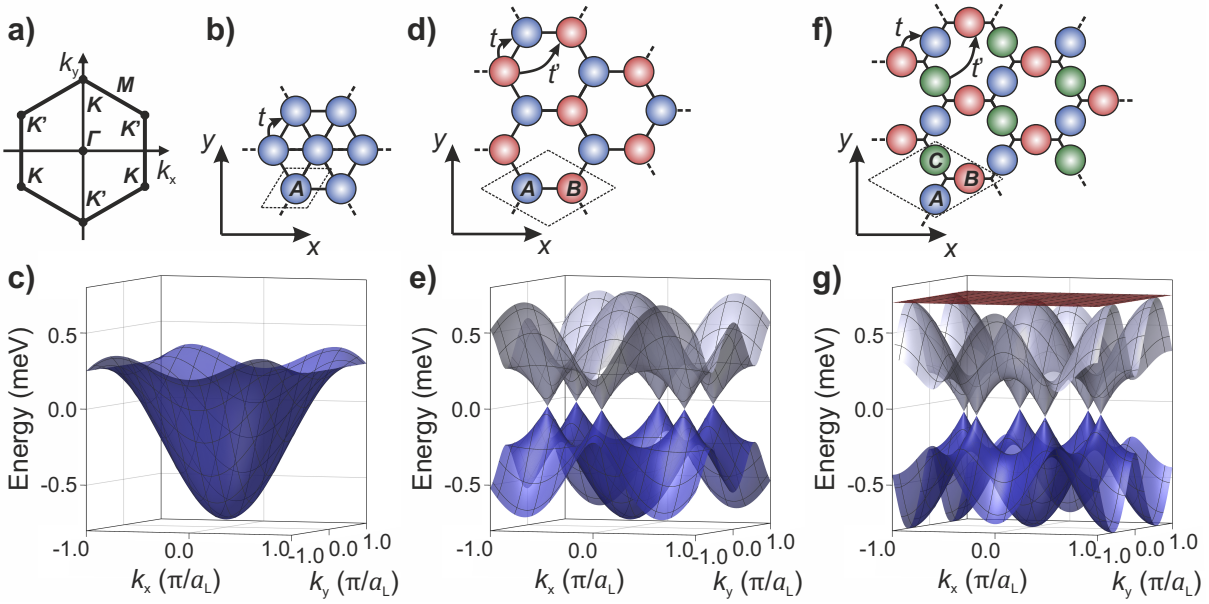

Figure 2.6: **a)** Brillouin zone of the hexagonal, honeycomb and Kagome lattices, characterised by the high-symmetry points Γ, K, K' and M. **b)**, **d)** and **f)** Real space geometries of the hexagonal, honeycomb and Kagome lattices with one, two and three sites in the unit cell, respectively. **c)**, **e)** and **g)** Corresponding S band dispersion relations considering only nearest neighbour coupling, with a_L denoting the lattice constant.

2.4 Topological physics

One of the defining paradigms of solid-state physics of the recent decades has been the classification of various phases by their topological order. In this section, a short introduction to this concept as well as a description of two particular geometries, namely the one-dimensional Su-Schrieffer-Heeger chain and the two-dimensional honeycomb lattice, are given. Extensive summaries of the field can be found in literature [Nak05; DCN10; HK10; QZ11; BH13; AOP16].

2.4.1 Transferring topology from mathematics to solid-state physics

In mathematics, the term *topology* refers to the characterisation of surfaces. Here, an important classification is the Euler characteristic g which is defined by

$$\frac{1}{2\pi}\int_S K\,dA = 2\,(1-g), \tag{2.38}$$

where the left side of the equation represents an integration over the curvature K of a surface S. It is important to note that this curvature is a local property of the surface which is therefore dependent on the coordinate system and changes for example when transforming a cube into a sphere by changing from a cartesian to a polar coordinate system. The Euler characteristic, however, is a global property corresponding to the number of holes of the surface and thus remains unchanged during modifications of the coordinate system.

Analogously to the Euler characteristic, in solid-state physics a bulk band structure, defined by the Hamiltonian of a system, can be viewed as a surface. In the common case of a Hamiltonian with energy gaps between individual bands, this surface is characterised by the Berry phase [Ber84]

$$\gamma(L) = \oint_L \boldsymbol{A}(\boldsymbol{k})d\boldsymbol{k} \tag{2.39}$$

which is defined as an integral over a closed loop L of the Berry connection

$$\boldsymbol{A}(\boldsymbol{k}) = i\,\langle\psi(\boldsymbol{k})|\boldsymbol{\nabla}_{\boldsymbol{k}}\psi(\boldsymbol{k})\rangle\,. \tag{2.40}$$

The Berry phase is a geometric phase that is accumulated additionally to the phase that is acquired during the time evolution of a state and depends only on the path of the loop in reciprocal space. The Berry connection can be understood as the vector potential of a magnetic field

$$\boldsymbol{\Omega}(\boldsymbol{k}) = \boldsymbol{\nabla}_{\boldsymbol{k}} \times \boldsymbol{A}(\boldsymbol{k}) \tag{2.41}$$

which is referred to as the Berry curvature of a band structure. Finally, the analogon to the Euler characteristic of this curvature can be calculated as

$$C = \frac{1}{2\pi} \int_{BZ} \boldsymbol{\omega}(\boldsymbol{k}) d\boldsymbol{S} \tag{2.42}$$

by integrating over a band across the entire Brillouin zone. The integer quantity C is a topological invariant that remains unchanged as long as no band gap is closed or opened and is referred to as *Chern number*. For $C = 0$, an insulator is referred to as trivial, whereas $C \neq 0$ represents an insulator with a non-trivial topology. As the Chern number can only change when closing a band gap, robust edge states protected by the topology of the bulk materials appear at the interface of a topologically trivial and a non-trivial phase [RH02]. The Chern number corresponds to the number of edge states [Tho+82]. This relation of edge states forming as a result of the bulk band structure is summarised by the term *bulk-boundary correspondence*.

Historically, what is today a major field of research stretching across numerous fields of solid-state physics started with the discovery of the quantum Hall effect by von Klitzing [KDP80], where a magnetic field applied to a two-dimensional electron gas results in a quantised Hall resistance and chiral edge modes. It was this discovery that led to the introduction of topological order as an entirely new approach of classification [Tho+82; Wen95]. In the further progress, the quantum Hall effect was demonstrated not only at cryogenic temperatures but also at room temperature [Nov+07]. Furthermore, with the quantum anomalous Hall effect, non-trivial topology was predicted and demonstrated without the presence of an external magnetic field by using ferromagnetic materials [Yu+10; Che+14a]. These effects can both be characterised by a non-zero Chern number where broken time reversal symmetry results in chiral edge modes and are summarised as $\mathbb{Z}$ topological insulators. In parallel to advancing the understanding of materials in this topological class, the concept of topology was extended to a $\mathbb{Z}_2$ topological class featuring the characteristic two counter-propagating edge states of the quantum spin Hall effect [KM05a; KM05b]. In the $\mathbb{Z}_2$ topological class, a magnetic field is not required and time reversal symmetry remains preserved. The quantum spin Hall effect can be visualised as two copies of the quantum Hall effect with opposite magnetic field orientations for the two electron spin components and was first experimentally realised in HgTe quantum wells [BHZ06; Kön+07]. Above a certain critical thickness, these quantum wells feature an inverted band gap, as the orbitals at the origin of the valence and conduction band are inverted with respect to a trivial insulator band gap. As time reversal symmetry is preserved in the quantum spin Hall effect, a classification using an overall Chern number is no longer feasible. However, Kane and Mele found that the edge states of the two spin

sub-systems are still topologically protected and can be classified by topological invariants that include the two sub-systems [KM05a]. Recently, in the field of topological quantum chemistry, a bottom up approach towards topologically non-trivial materials was found. In this approach, all feasible trivial bands are constructed from atomic orbitals in a given spatial symmetry. A topological phase in this picture is defined as a state that cannot be written in terms of exponentially localised orbitals that respect the symmetries of the system [Bra+17]. The major stronghold of this approach lies in the fact that knowledge of the system Hamiltonian is no longer required allowing to determine the topology purely from the real space orientation of the involved atomic orbitals.

2.4.2 Su-Schrieffer-Heeger model

The Su-Schrieffer-Heeger (SSH) model [SSH79] is the simplest example of a one-dimensional topological system that, due to its simple geometry, has evolved to be an ideal starting point to study topological effects in various experimental platforms. The following short introduction was adapted from [AOP16]. The SSH model consists of a dimerised linear chain characterised by two coupling strengths t_1 and t_2 for the intra- and inter-unit cell couplings, respectively, as is schematically depicted in Fig. 2.7 a). As the topology is defined through the bulk band structure, it is worthwhile to start by assuming a chain with periodic boundary conditions. In this case, the Bloch theorem applies and the tight binding Hamiltonian in Fourier space reads

$$H(k) = \begin{pmatrix} 0 & t_1 + t_2 e^{-ik} \\ t_1 + t_2 e^{ik} & 0 \end{pmatrix}. \tag{2.43}$$

The eigenvalues

$$E(k) = \pm\sqrt{t_1^2 + t_2^2 + 2t_1 t_2 \cos k} \tag{2.44}$$

of this Hamiltonian feature a band gap with a size that is determined by the difference $|t_1 - t_2|$ between the two coupling strengths and that is visualised in the spectra plotted in Figs. 2.7 b)-d) for the three cases $t_1 = 2.0\, t_2$, $t_1 = t_2$ and $t_1 = 0.5\, t_2$. In analogy to the definition of the Chern number as an integral over a closed loop of the Berry phase, the topological invariant

$$\gamma = \frac{1}{\pi} \int_{-\pi}^{\pi} i \langle u_\mathrm{k} | \frac{\partial u_\mathrm{k}}{\partial k} \rangle \, dk = \begin{cases} 0 & \text{for} \quad t_1 > t_2 \\ 1 & \text{for} \quad t_1 < t_2 \end{cases} \tag{2.45}$$

of a one-dimensional SSH chain is defined as the integral over a closed loop of the Zak phase [Zak89].

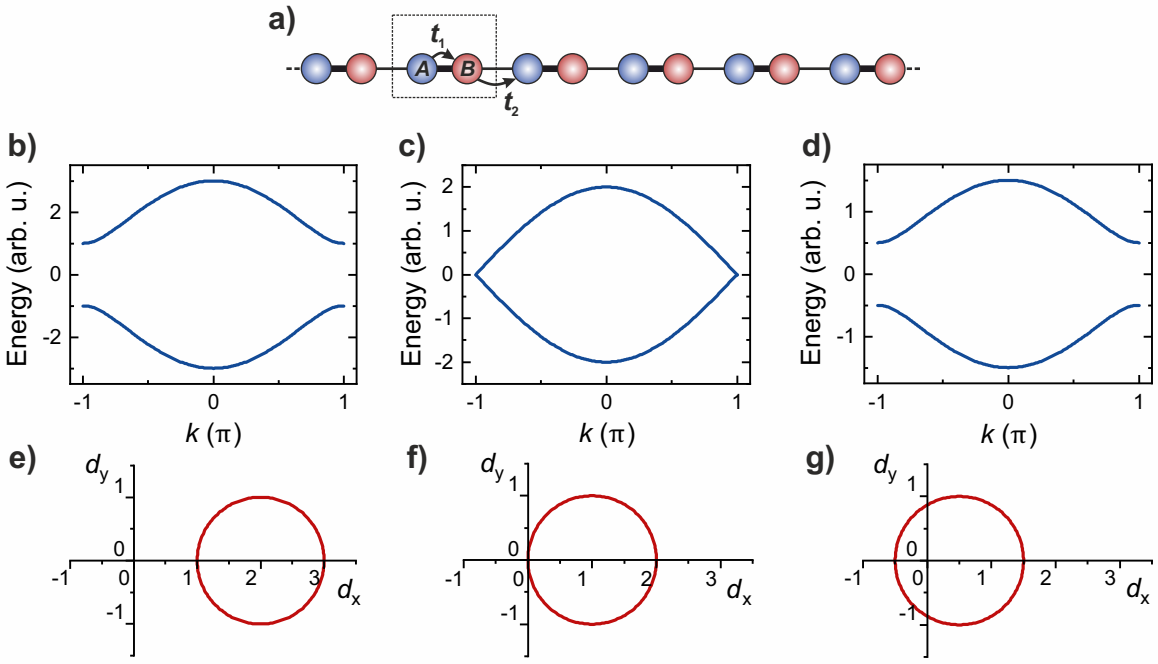

Figure 2.7: a) Schematic of the one-dimensional SSH model featuring two sites in the unit cell and intra- and inter-unit cell couplings t_1 and t_2, respectively. **b)-d)** Dispersion relations for $t_2 = 1.0$ and $t_1 = 2.0$, 1.0 and 0.5, respectively. **e)-g)** Corresponding plots of the vector $\boldsymbol{d}$ used to express the SSH Hamiltonian with respect to the Pauli matrices to visualise the topological phase transition as a change of the winding number. This figure is based on reference [AOP16].

To visualise this invariant, it is fruitful to express the Hamiltonian with respect to the Pauli matrices $\sigma_{0,\mathrm{x,y,z}}$ as

$$H(k) = d_0(k)\hat{\sigma}_0 + d_x(k)\hat{\sigma}_\mathrm{x} + d_y(k)\hat{\sigma}_\mathrm{y} + d_z(k)\hat{\sigma}_\mathrm{z} \quad \text{with} \quad d_0(k) = 0, \quad \boldsymbol{d}(k) = \begin{pmatrix} t_1 + t_2 \cos k \\ t_2 \sin k \\ 0 \end{pmatrix}. \tag{2.46}$$

On a closed loop from $k = 0$ to 2π in the Brillouin zone, this vector forms the circles that are presented in Figs. 2.7 e)-g). The topological invariant can now be understood as the winding number of this vector, which is 1 if the circle encloses the origin and 0 if it does not. A phase transition is required to change between the topologically trivial regime of $t_1 > t_2$ in Figs. 2.7 b) and e) and the topologically non-trivial regime of $t_1 < t_2$ in Figs. 2.7 d) and g). Therefore, the band gap closes for $t_1 = t_2$ in Figs. 2.7 c) and f). Analogously, the band gap has to close at the interface between a topologically non-trivial bulk and the topologically trivial vacuum, leading to topologically protected edge states. To study these edge states, a suitable starting point is the real space Hamiltonian of a

chain with finite length, such as the exemplary Hamiltonian

$$\hat{H} = \begin{pmatrix} 0 & t_1 & 0 & 0 \\ t_1 & 0 & t_2 & 0 \\ 0 & t_2 & 0 & t_1 \\ 0 & 0 & t_1 & 0 \end{pmatrix} \tag{2.47}$$

of a chain with two unit cells. In Fig. 2.8 a), the energy eigenvalues of a chain with ten unit cells are plotted with respect to the intra-cell coupling t_1 while maintaining a constant inter-cell coupling strength of $t_2 = 1.0$. One can clearly observe that a topological state centred in the band gap arises for $t_1 < t_2$. The corresponding probability density of the eigenvector of this state for $t_1 = 0.3$, as marked by the red dot in Fig. 2.8 a), is presented in Fig. 2.8 b). For better visibility, the propability density is coloured in green for states on sub-lattice A and in orange for states on sub-lattice B. One can clearly observe that localised edge states arise on the outermost sites of the chain. These topological defect states are exponentially localised and feature a non-zero probability density only on one of the sub-lattices.

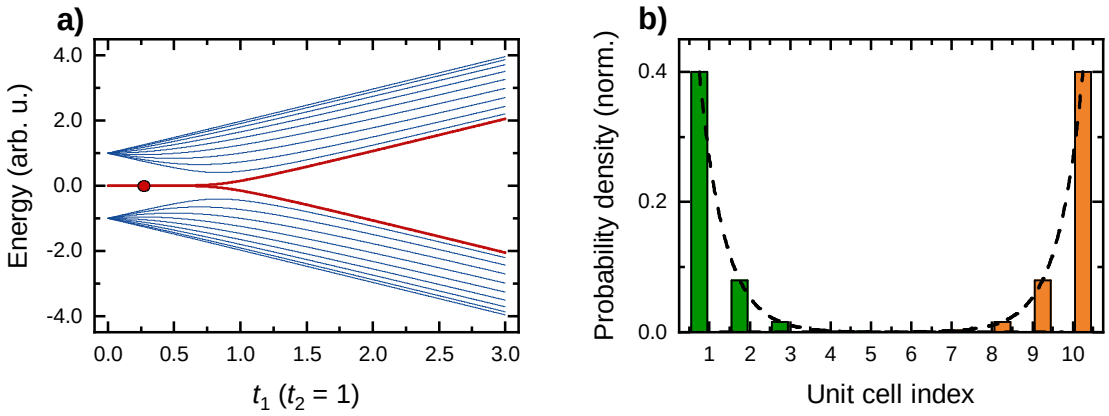

Figure 2.8: a) Energy eigenvalues of an SSH-chain consisting of ten unit cells with respect to the intra-cell coupling strength t_1 for a fixed inter-cell coupling strength $t_2 = 1$. A topologically protected state at the centre of the band gap arises for $t_1 < t_2$. **b)** The probability density of a topological state at $t_1 = 0.3$, highlighted by a red dot in a), visualises that the topological states are exponentially localised to the edges and, at each edge, populate only sites from one sub-lattice.

2.4.3 Topology of the honeycomb lattice

Throughout the development of research on topology, the honeycomb lattice has played a crucial role. As introduced in section 2.3.3, a mono-atomic honeycomb lattice is a semi-metal with two sub-bands in the S band touching in the two Dirac points that are protected by time reversal symmetry and spatial symmetries. Therefore, models converting a system based on a honeycomb lattice into a topological insulator are based on breaking one of these two symmetries in a way that opens a topologically non-trivial gap at the Dirac points.

The most intuitive way to open a band gap at the Dirac points was described by Semenoff in 1984 [Sem84] and is based on breaking the inversion symmetry of the lattice by unbalancing the eigenenergies of the two sites of the unit cell, which in the context of atomic lattices would imply creating a honeycomb lattice consisting of two types of atoms. However, the band gap opened by this approach is topologically trivial. The first model that realises a quantum Hall state in a lattice geometry is the Haldane model [Hal88] that adds a complex next-nearest neighbour hopping term to Semenoff's model to break time reversal symmetry. In this context, Kane and Mele's model of the quantum spin Hall effect, that was introduced above and originally considered graphene as an experimental platform [KM05a; KM05b], can be understood as a combination of two copies of Haldane's model, one for each spin component.

Another approach towards studying topological effects in a Semenoff lattice focuses on investigating only a subset of the band structure and harnesses that the K and K' points

are not equivalent. While the Chern number of the entire bands are zero, the Chern number calculated for one half of the Brillouin zone including only one of the valleys at either the K or K' point is non-trivial. Therefore, as long as only one of the valleys is populated, topological propagation is possible. As one can translate the valley index of a given state into a pseudospin picture, this effect resembles a quantum spin Hall effect. This propagation is, however, not topologically protected against backscattering as protection is only present as long as scattering between the valleys is inhibited. This type of protection is referred to as valley protection, resulting in the related effects being referred to as quantum valley Hall effects [DYN07].

It is important to note that, even though photons are neutral bosons and can thus not show a quantum Hall effect in an external magnetic field, they can still exhibit topologically protected edge modes in lattice based models that do not require external magnetic fields [HR08]. Based on this realisation, the field of topological photonics has evolved [RH08], starting, among others, with the realisation of a topological insulator consisting of photonic waveguides [Rec+13a]. A more elaborate introduction to topological photonics is given in chapter 6. The higher degree of flexibility over the lattice geometry that can be achieved using artificial lattices has led to the discovery of a more advanced approach towards breaking the spatial symmetries of the honeycomb lattice that leads to a topologically non-trivial band gap and is referred to as *crystalline topological insulator* [WH15]. In this model, the unit cell is extended to include the artificial analogon of a benzene ring that consists of six sites. Next, this benzene ring is either compressed or stretched within each unit cell, resulting in the real space lattice geometry that is depicted in Fig. 2.9 d). This lattice is now characterised by the coupling strengths $t_{\mathrm{i}}^{\mathrm{c}}$ and $t_{\mathrm{e}}^{\mathrm{c}}$ as well as $t_{\mathrm{i}}^{\mathrm{s}}$ and $t_{\mathrm{e}}^{\mathrm{s}}$ within a unit cell (internal, i) and between adjacent unit cells (external, e) for the compressed (c) and stretched (s) domains, respectively, and an additional coupling strength t_{b} at the boundary between the two domains. The band structure calculations of the two domains as well as the unmodified honeycomb lattice that are presented in Figs. 2.9 a)-c) were reprinted from reference [WH15] and demonstrate that a band gap opens at the Dirac points in both the compressed and the stretched domains. Here it is important to note that, due to the expansion of the unit cell, both the K and K' points are projected onto the Γ point. In Figs. 2.9 a)-c), the contributions of the P and D modes of the benzene rings that constitute the unit cells are highlighted by the colour scale. It is important to note that, while each band of the compressed lattice is comprised of the corresponding band of the benzene rings, the bands of the stretched lattice are inverted at the band gap with respect to the benzene origin. This colour-coding therefore directly visualises that the compressed lattice features a topologically trivial gap while the stretched lattice is characterised by a topologically non-trivial gap featuring a band

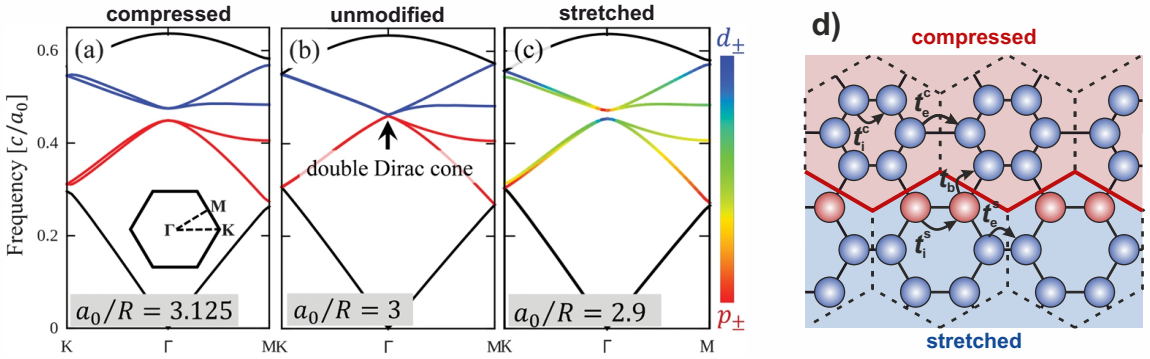

Figure 2.9: a)-c) Band structure calculations for the internally compressed, unmodified and internally stretched honeycomb lattices, respectively. Here, a_0 denotes the lattice constant and and R corresponds to the distance between adjacent sites within a unit cell. The colour scale marks the contributions from the P and D sub-bands of the units cells. a)-c) were reprinted from reference [WH15]. **d)** Schematic of the crystalline topological insulator (CTI) lattice geometry. The interface between a compressed (red background) and a stretched (blue background) honeycomb lattice is marked in red. As the stretched lattice features a topologically non-trivial band gap, a topological boundary mode is expected on the interface sites that are marked in red. The new unit cells of the modified lattices are marked with dashed lines.

inversion. Consequentially, analogously to the inverted band structure that is used to realise a quantum spin Hall effect, a topologically protected edge mode is expected at the interface between the stretched and the compressed domains.

The models introduced so far consider Bloch's band theory to create topological states. Another approach towards breaking time reversal or spatial symmetries of the honeycomb lattice that has proven to be particularly powerful in the field of topological photonics appears in the context of Floquet theory. Here, contrary to Bloch theory that is based on spatial periodicity, a Hamiltonian that is periodic in time is considered [LRG11]. Such systems therefore involve either periodic driving or a projection of time onto a propagation axis where in the latter time reversal symmetry can be broken by breaking inversion symmetry in the propagation direction.

3 Experimental methods

Following the introduction into the theoretical foundation of this thesis, this chapter focuses on the experimental techniques used to obtain the results that are presented in the subsequent chapters. The predominant experimental platform used in this work is based on III-V semiconductor microcavities featuring strong coupling between the cavity resonance and quantum well excitons to form polaritons. Additionally, a lattice potential landscape is engineered for these polaritons. In section 3.1, short introductions into the III-V semiconductor material platform, the microcavity growth by molecular beam epitaxy as well as the different approaches for implementing a potential landscape are given, followed by a description of the Fourier photoluminescence spectroscopy techniques used to study the polariton lattices in section 3.2.

3.1 Polariton lattice fabrication

3.1.1 III-V material system and microcavity growth

The combinations of one of the elements of aluminium (AL), gallium (Ga) or indium (In) from the third group of the periodic table with either phosphorus (P) or arsenic (As) from group V result in crystalline semiconductor materials with a variation in refractive indices and band gaps, while maintaining a similar lattice constant. This allows for homoepitaxial growth of semiconductors with more than two compounds as well as interfaces of different material combinations with excellent crystal quality. For this work, in particular the two semiconductors GaAs and AlAs are of key importance. They both feature a zinc blende crystal structure with a difference in lattice constant of less than 0.15 % at room temperature [Ada85]. The difference between the band gaps of $E_\mathrm{g} = 1.519\,\mathrm{eV}$ and $E_\mathrm{g} = 2.249\,\mathrm{eV}$ for GaAs and AlAs at $T = 4\,\mathrm{K}$, respectively [Iof20], allows to create electronic confinement in quantum wells and, as GaAs features a direct band gap at the Γ point of the Brillouin zone, the electronic transition across the band gap is directly optically accessible. Furthermore, the difference in refractive index in the wavelength range corresponding to the band gap of GaAs of $n = 3.67$ and 3.00 for GaAs and AlAs, respectively [Pol17], enables to fabricate structures for optical confinement. The ternary component $\mathrm{Al_xGa_{1-x}As}$ can

be used to realise parameters between pure GaAs and AlAs, whereas adding Indium to a GaAs quantum well reduces its band gap and, due to the 34 times larger electron g-factor of InAs compared to GaAs [Wim+94], drastically increases the susceptibility to an external magnetic field. This set of properties renders the GaAs material platform ideal to fabricate devices for the investigation of light-matter interaction.
The polariton lattices studied in this work are based on GaAs-based microcavities that were fabricated using molecular beam epitaxy (MBE). MBE is a powerful technique to fabricate high quality, crystalline semiconductor materials that was initially developed by Cho and collaborators [CA75] and has been optimised and extended ever since [HS13]. In particular, MBE allows for fast switching between the materials and thus enables homoepitaxial growth of layered structures of different material composition with precisely controlled thicknesses and interfaces. First, a cleaned, heated GaAs wafer that serves as growth substrate is mounted onto a rotating sample holder in the ultra-high vacuum chamber of the MBE. The group-V element arsenic is provided as a gaseous background pressure of As_4 and the elements from group III of the periodic table are provided by solid source effusion cells. The flux of these effusion cells is controlled by their temperature and switched on and off using shutters. This allows epitaxial growth of the desired layers with precise control over the layer thicknesses. It is additionally important to note, that this fabrication technique naturally results in a radial thickness gradient as the growth rate decreases from the centre of the wafer towards the edge. For microcavities, this influences predominantly the photonic modes and results in a blueshift of the cavity resonance. This radial energy shift allows to perform experiments at a desired exciton-photon detuning by selecting the corresponding radial position on the wafer.
To increase the Mott density as well as the Rabi splitting, multiple quantum wells are included in the anti-nodes of the electric field of the cavity mode at the centre of the cavity as well as in the first mirror pairs adjacent to the cavity. For experimental studies requiring the susceptibility to an external magnetic field as well as for experiments using resonant excitation in transmission geometry, samples with $In_xGa_{1-x}As$ quantum wells are used. For studies on polariton propagation, GaAs quantum wells have proven to be more suitable.

3.1.2 Polariton confinement techniques

By the design of the cavity, polaritons are inherently confined into the x-y-plane, perpendicular to the growth direction. Additional lateral confinement can be achieved by a variety of techniques that create potential landscapes for the excitonic component, the photonic component or a combination of both [Sch+16]. As the band gap of semiconduc-

tors and therefore also the exciton energy depend on the distance between the atoms, the exciton can be confined using local, mechanical strain [Bal+07] or surface acoustic waves [Lim+06; Cer+10], where the latter effects mainly the exciton but also causes a non-negligible effect on the photonic mode. Another approach towards excitonic confinement is based on proton implantation that results in intermixing of the quantum well material with the surrounding barrier [Tan+96]. Furthermore, excitons are susceptible to electric fields and can thus be influenced by electrostatic potentials [Fis+96; But+02; Ges+14]. A remarkably versatile method that has recently attracted increasing attention is based on creating local potential barriers through the interaction-induced blueshift that occurs for high polariton densities. As the polariton occupation can be directly controlled by shaping the pattern of the excitation laser, this technique provides high flexibility over the potential landscape [Tos+12b; Tos+12a; Ask+13; Dal+14; Oha+17; Aly+20]. Finally, the quantum wells themselves can be replaced by a low-dimensional active material such as quantum dots [Rei+04; Yos+04; Pet+05]. Combined with the technological progress on site-controlled quantum dot growth [Sch+09] and the quantum nature of the emission of quantum dots [Hen+07; Pre+07; Far+08], this approach could represent a promising path to investigate quantum effects in polariton lattices.

In this work, a confinement of the photonic component based on lithography and etching processes was used. The first micropillars fabricated using such a process were etched into a planar cavity in 1996 [Gér+96], resulting in discrete polariton modes [Gut+98; Nar+09]. The first attempts towards a periodic potential landscape were based on metal stripes placed on top of the cavity [Lai+07; Kim+11]. These stripes result in a local shift of the potential environment that is, however, limited to the order of µeV. Therefore, techniques based on the electron beam lithographical definition of lattice structures with a subsequent etching step were advanced [Jac+14]. A scheme of a *fully-etched* honeycomb lattice as well as a corresponding scanning electron microscopy image are presented in Figs. 3.1 a) and b), respectively. Here, coupling between individual micropillars is ensured by an overlap between the pillars. To avoid defects in the cavity and quantum well layers induced by the etching process, the etch depth can be adjusted such that the micropillars are etched only into the top DBR, as depicted in Figs. 3.1 c) and d). These lattices are commonly referred to as *half-etched*. The advantages of these two techniques are a large confinement potential for the photonic component as well as the opportunity to optimise the etching process post growth by iterating on small pieces of a large microcavity wafer. However, the range of coupling strengths between the pillars is limited by the requirement of overlap between pillars and the confinement potential is not tuneable. To overcome these limitations, an additional approach based on a locally elongated cavity layer at the position of the lattice sites that results in an energetic redshift of the

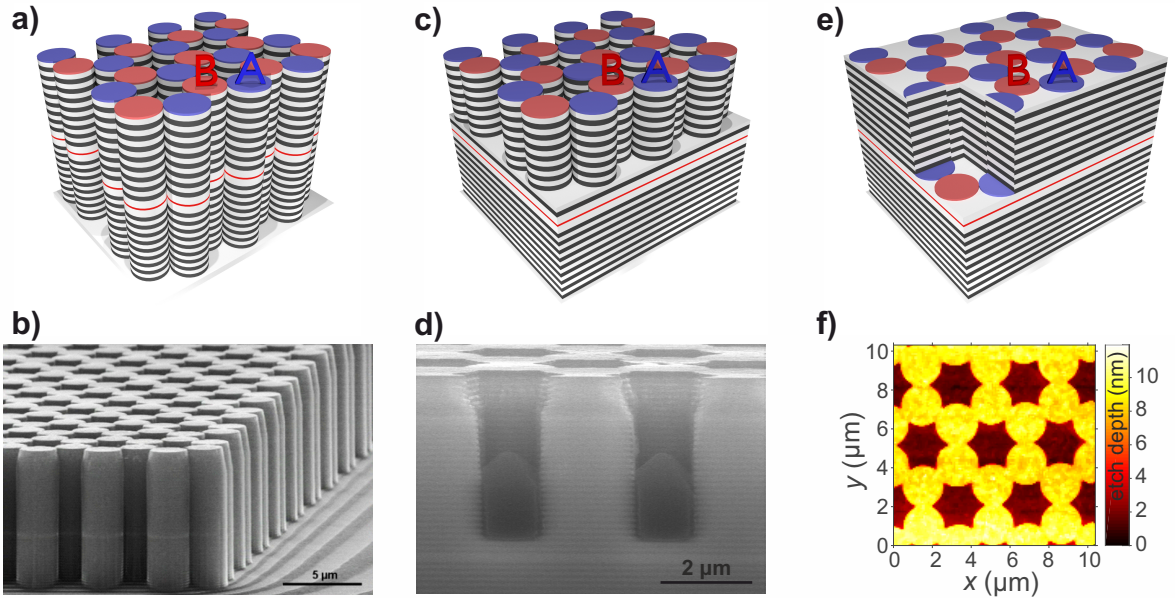

Figure 3.1: **a)**, **c)** Schematics of a fully-etched and a half-etched polaritonic honeycomb lattice and corresponding scanning electron microscopy images in **b)** and **d)**. **e)** Schematic of an etch-and-overgrowth (EnO) polaritonic honeycomb lattice. **f)** Atomic force microscopy image of the structured surface of the cavity layer of an EnO honeycomb lattice prior to the growth of the top DBR.

cavity resonance and a consequent confinement potential was introduced by El Daïf and co-workers [El +06] and advanced by Winkler and co-workers [Win+15; Win+16]. To achieve such a local elongation of the cavity layer, the epitaxial growth is interrupted after the cavity layer is completed. Subsequently, the lattice structure is defined by electron beam lithography and the areas surrounding the lattice sites are etched to a depth of approximately 10 nm, resulting in a confinement potential on the order of 10 meV that can be finely tuned by adjusting the etch depth. After a cleaning procedure, the wafer is remounted in the MBE growth chamber and the top DBR is grown, motivating the term *etch-and-overgrowth* EnO for this confinement technique. A schematic representation of such an EnO lattice as well as an atomic force microscopy image of the structured cavity layer are displayed in Figs. 3.1 e) and f), respectively. Using this method not only provides control over the confinement potential, but also allows to tune the coupling strength over a larger scale since EnO microtraps couple even if they are designed without overlap. In contrast to half- or fully-etched lattices, EnO lattices are not susceptible to deviating etching rates towards the edge of a lattice and thus have a very uniform potential landscape across an entire lattice. Furthermore, there is semiconductor material in the holes of a lattice that suppresses direct emission from the quantum wells and thus simplifies spectroscopy close to zero detuning. Additionally, etching holes with a large

aspect ratio d_e/d_h, with d_e and d_h denoting the etch depth and the hole diameter, respectively, represents a major challenge that has so far inhibited the realisation of for example Kagome lattices by a half- or fully-etched approach. The EnO technique offers a pathway to overcome this challenge, as the very shallow etch depth decreases the aspect ratio of etched holes by approximately three orders of magnitude, from having to etch several micrometers to an etch depth on the order of 10 nm. Finally, EnO lattices are robust towards mechanical stress enabling to polish the backside of a wafer to allow excitation in transmission geometry. However, as the fabrication of EnO lattices involves a high technological effort, both the fully- and half-etched as well as the EnO approach are valuable techniques towards defining lattice potential environment for polaritons. A summary of all relevant parameters characterising the microcavities studied in this work is provided in Table 3.1. Here, the microcavities were labelled based on the composition of the active material of either $In_xGa_{1-x}As$ (In) or GaAs (Ga) and the fully-etched (FE), half-etched (HE) or etch-and-overgrowth (EnO) technique to achieve photonic confinement. Further details on the characterisation measurements leading to these parameters can be found in the appendix in section A.1.

Sample name	**In-FE1**	**In-FE2**	**In-HE1**	**In-EnO1**	**Ga-EnO1**
Active material	QD	QD	QW	QW	QW
QW / QD material	$In_{0.30}Ga_{0.70}As$	$In_{0.30}Ga_{0.70}As$	$In_{0.04}Ga_{0.96}As$	$In_{0.04}Ga_{0.96}As$	GaAs
QW thickness (nm)	-	-	16	16	7
Number of QWs	-	-	3	3	8
E_X (eV)	1.3212	1.3218	1.4770	1.4844	1.6106
γ_X (meV)	34.84	16.75	1.29	0.92	4.77
Δ_Z at 5 T (μeV)	-	-	540	355	-
Cavity material	GaAs	GaAs	GaAs	GaAs	AlAs
Cavity thickness	λ	λ	λ	λ	$\lambda/2$
DBRs ($Al_xGa_{1-x}As$/AlAs)	$x = 0.00$	$x = 0.00$	$x = 0.10$	$x = 0.10$	$x = 0.20$
MPs in bottom/top DBRs	33.5/29	33.5/29	35.5/30	33.5/27	37/32
γ_C (meV)	0.15	0.16	0.10	0.33	0.22
Q	8,500	8,200	14,800	4,500	7,400
max. $\Delta_{TE/TM}$ (μeV)	-	-	600	650	-
$2\hbar\Omega_R$ (meV)	-	-	4.3	4.5	11.4
Confinement technique	fully-etched	fully-etched	half-etched	EnO	EnO
Confinement potential (meV)	-	-	-	11.5	6.7

Table 3.1: Summary of the basic parameters characterising the samples studied in this work. The exciton depends on the active material that can be comprised of either quantum dots (QDs) or quantum wells (QWs) and, in the latter case, of the thickness as well as the number of quantum wells and is characterised by the emission energy E_X, the linewidth γ_X and the Zeeman splitting Δ_Z. The photonic resonance depends on the cavity material and thickness, the DBR composition as well as the number of mirror pairs (MPs) in each DBR and is characterised by the linewidth γ_C, the Q factor and the TE/TM-splitting $\Delta_{TE/TM}$. The polaritons that arise from strong coupling between photons and excitons feature a Rabi-splitting $2\hbar\Omega_R$ and are confined by either an etching or the EnO approach.

3.2 Photoluminescence spectroscopy

One of the most valuable physical property of microcavities is the direct link between the emission angle of photons escaping from the microcavity and the wave vector of the polaritonic state they originate from that was introduced in section 2.2.1, as it allows not only to image the mode distribution in real space but also provides access to the dispersions across the full Brillouin zone. In this section, the technique of photoluminescence Fourier spectroscopy used to perform these measurements is introduced, followed by a brief description of correlation measurements providing access to coherence information. Finally, the spatial light modulator is introduced as a powerful tool to convert any arbitrary gray scale image into an excitation laser pattern.

3.2.1 Fourier spectroscopy

A Fourier spectroscopy setup can be deconstructed into three major parts, namely the cryostat in which the sample is mounted and cooled to cryogenic temperatures, the injection path used to illuminate the sample with a white light source or a laser and the detection path used to study the reflected light or PL emission from the sample. A schematic of such a setup is presented in Fig. 3.2.
For the experiments performed in this work, two liquid Helium flow cryostats enabling to evacuate the sample space to a pressure on the order of $p = 1 \times 10^{-6}$ mbar and operating at a temperature of $T = 4$ K were available. Whereas one cryostat, a Janis ST-500, was operated purely in reflection geometry, the other cryostat, an Oxford Instruments MicrostatMO, provides the additional options of excitation in transmission geometry as well as applying external magnetic fields of up to $B = 5$ T in Faraday geometry. To avoid the distortion of measurements with long integration times due to oscillations and drift, the position of the Janis ST-500 was actively stabilised. Additionally, both cryostats provide the ability to heat the sample for measurements at elevated temperatures.
In reflection geometry, the injection and the detection path share the same microscope objective and are separated by a beam splitter placed in front of the objective. Here, two infinity-corrected objectives with twentyfold and fiftyfold magnifications and numerical apertures (NAs) of 0.40 and 0.42, respectively, that were fabricated by Mitutoyo were used. In transmission geometry, a lens with a focal length of $f = 150$ mm was used to focus the laser onto the backside of the sample. Illumination of the sample was provided through a white light source for reflection measurements and orientation on the sample as well as two Ti:sapphire lasers, an M Squared SolsTiS tuneable continuous wave (cw) laser and a Spectra-Physics Tsunami tuneable pulsed laser with a pulse length of 10 ps and a repetition rate of 82 MHz, used to perform PL spectroscopy. The excitation power was monitored with a calibrated photodiode power meter. The injection path is furthermore

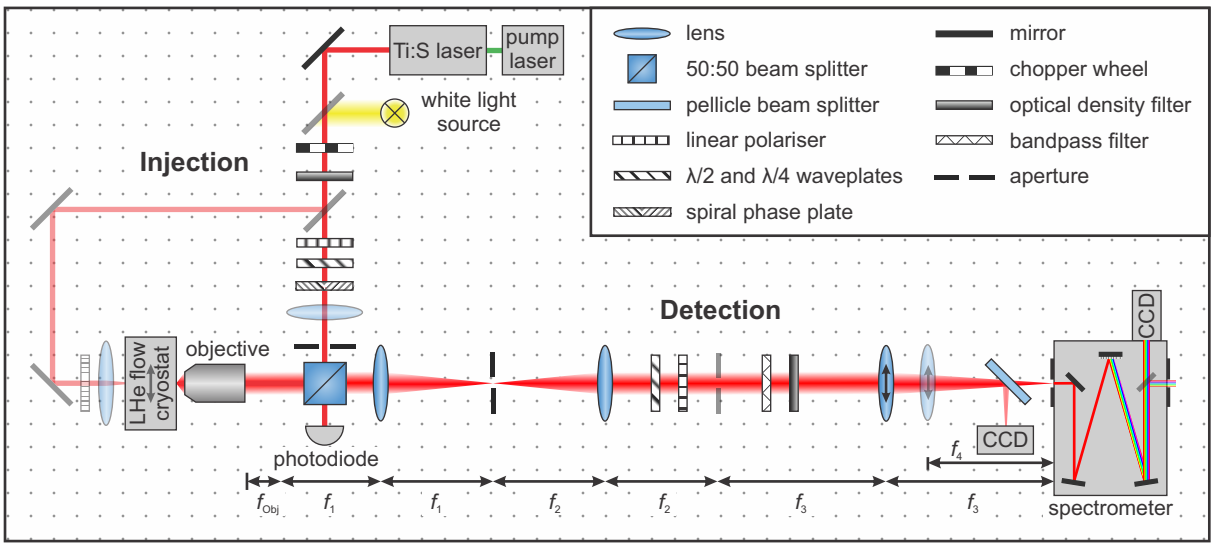

Figure 3.2: Schematic of a photoluminescence Fourier spectroscopy setup consisting of an injection path featuring a laser and a white light source to illuminate the sample that is mounted in a liquid Helium flow cryostat, either in reflection or transmission geometry. The PL emission is collected with a microscope objective and imaged onto a CCD camera as well as the entrance slit of a spectrometer through three or four lenses for real space or Fourier space imaging, respectively.

equipped with a chopper wheel to reduce sample heating and a variable optical density (OD) filter to adjust the laser excitation power. The excitation lasers emit linearly polarised light with a small elliptical component that can be eliminated by a linear polariser. Subsequently, the polarisation can be fixed to any point on the Pointcaré sphere with a $\lambda/2$ and a $\lambda/4$ waveplate. To adjust the angle of these waveplates to realise a desired polarisation, a polarisation analyser by Schäfter + Kirchhoff was used. When illuminating the entire back focal plane of the objective and thus using the entire available NA, the laser is focused to a spot size of approximately $d = 2\,\mu\text{m}$. The spot size can be increased by reducing the effective NA of the objective, which can be achieved by either using a lens, commonly called expander lens, that focuses the laser to the back focal plane of the objective, or by introducing an aperture that reduces the diameter of the laser beam. The use of an expander lens ensures minimal loss of laser power whereas an aperture provides a continuously tuneable spot size. The shape of the laser can be adjusted by replacing the expander lens with a cylindrical lens resulting in a laser spot that is elongated along one direction or by using a spiral phase plate enabling to create a ring-shaped spot characterised by a vortex with topological charge $m = 2$ in the linear polarisation domain. Full flexibility over the geometry of the laser excitation can be achieved by using a spatial light modulator (SLM), as described in section 3.2.3.

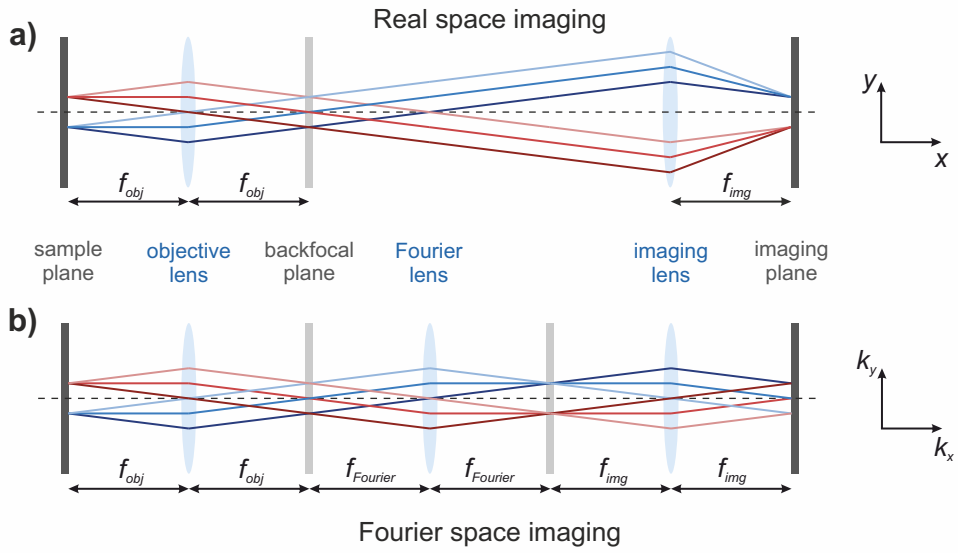

Figure 3.3: Schematics of the optical beam paths for real space imaging in **a)** and Fourier space imaging in **b)**. Emission from two different positions on the sample are distinguished by colour, whereas the emission angle is encoded in the brightness gradient from dark to bright.

The light emitted from the sample is collected using the microscope objective and imaged using two complementary lens configurations that are schematically presented in Fig. 3.3, where red and blue beams correspond to two different emission positions and the emission angle is encoded in the gradient from dark to bright. In Fig. 3.3 a), a real space image is created using the objective and a single imaging lens. The objective lens furthermore performs a two-dimensional, spatial Fourier transform of the emitted light into the back focal plane which motivates the term *Fourier spectroscopy* [Ric+05; Goo17]. Each point in this plane corresponds to light emitted from the sample at a certain angle, which is linked to a certain wave vector of polaritons in the microcavity through equation 2.12. Therefore, in Fig. 3.3 the beams are sorted by brightness rather than colour in the back focal plane. By introducing another lens, labelled *Fourier lens*, the back focal plane can be imaged.

Both in real and Fourier space imaging configuration, an image is created on a charge coupled device (CCD) camera, an Andor Clara, that is Peltier-cooled to $T = -20\,°\mathrm{C}$, as well as the entrance slit of a Czerny-Turner spectrometer. Here, an Andor Shamrock 750 spectrometer equipped with three gratings with 150, 600 and 1200 lines per millimetre and a CCD camera (Andor iKon-M) that was Peltier-cooled to $T = -70\,°\mathrm{C}$ were used. The highest energy resolution achievable with this spectrometer, determined by the size of the entrance slit, the line spacing on the grating, the length of the spectrometer and

the pixel spacing of the camera, is approximately 20 µeV at an energy of 1.470 eV. When imaging either real space or Fourier space onto the entrance slit, one cross section of the image is selected and an energy-resolved image, either $E(x)$ or $E(k_x)$, is obtained along this direction. The other dimension can be acquired by automated scanning routines that scan the image across the slit by moving the last imaging lens. From this dataset, the full information on real space mode distribution $E(x, y)$, referred to as *mode tomography*, or dispersion relations across the full Brillouin zone $E(k_x, k_y)$, termed *hyperspectral imaging*, can be reconstructed. As depicted in Fig. 3.2, an additional telescope in the detection path provides further control over the image magnification as well as image planes of both real and Fourier space that can be used to block parts of the emission in either of these planes. Furthermore, the detection path is equipped with optical density filters to prevent camera saturation as well as polarisation optics, namely a $\lambda/2$ and a $\lambda/4$ waveplate followed by a linear polariser. By rotating the $\lambda/2$ waveplate, the degree of linear polarisation can be measured, whereas evaluating the intensity I in dependence of the angle of the $\lambda/4$ waveplate φ gives access to all Stokes parameters [Kih94] by

$$I(\varphi) = \frac{1}{2}\left(S_0 + S_1 \cos^2 2\varphi + S_2 \sin 2\varphi \cos 2\varphi + S_3 \sin 2\varphi\right). \tag{3.1}$$

For the data analysis of a range of measurements performed for this thesis, such as excitation power, polarisation and detuning series, hyperspectral images including tight binding fits, mode tomographies as well as the techniques to measure correlation that are described in the following section, an analysis software package including a graphical user interface for interactive data analysis was implemented using MathWorks MATLAB.

3.2.2 Interferometry

Next to energy-resolved real and Fourier space information, the knowledge of first order as well as higher order degrees of coherence can provide valuable insight on the physical phenomena occuring in a microcavity. Experimentally, the coherence properties of a signal can be accessed through autocorrelation experiments, in which the signal is superimposed with itself. In the following, the Michelson and the Mach-Zehnder interferometers used for measurements of first order coherence as well as the Hanbury Brown-Twiss interferometer providing access to second order coherence are introduced.

A schematic of the Michelson interferometer, which owes its name to A. A. Michelson who invented it for the famous Michelson-Morley experiment [MM87], is depicted in Fig. 3.4 a). It consists of a 50:50 beam splitter dividing the signal into two arms. In both arms, the signal is reflected back towards the beam splitter, once by a mirror and once by a corner cube retroreflector that additionally flips the image both in x and y direction. The two

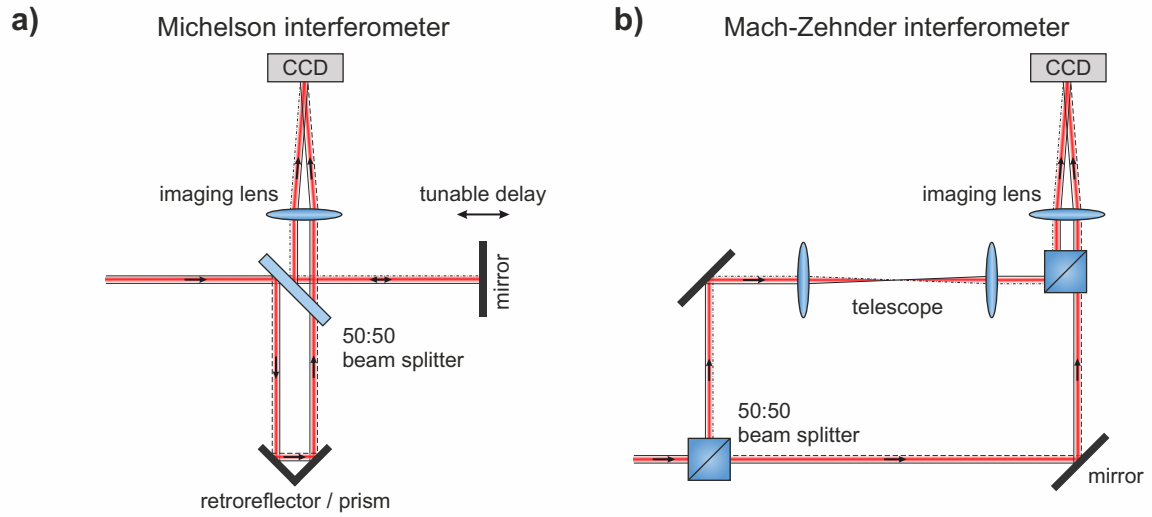

Figure 3.4: Schematics of a Michelson interferometer in **a)** and a Mach-Zehnder interferometer in **b)**, both providing access to first order coherence information by dividing the signal into two arms and then superimposing the two images again onto a CCD camera. While the focus of the Michelson interferometer lies on the spatial and temporal decay of coherence, the Mach-Zehnder interferometer is ideally suited to extract spatial phase maps.

images are then recombined by the beam splitter and imaged using a lens. Introducing an offset between the two parallel beams causes an angle between the beams behind the lens and thus enables to tune the fringe periodicity and direction of the interference pattern. As one of the images is flipped in the retroreflector, the light superimposed on a certain point of the camera with a distance d to the centre of the image corresponds to light from two positions on the sample at a distance of $2d$. Therefore, evaluating the coherence across a Michelson interferogram gives access to the spatial decay of first order coherence. Alternatively to using a retroreflector, a prism can be mounted in one of the arms of the interferometer to flip the image only along one axis and provide spatial coherence information with respect to the distance to the mirror axis. Additionally, the temporal distance τ between the two superimposed images can be tuned by moving one of the mirrors and thus delaying the image from one of the arms. The degree of first order temporal coherence $g^{(1)}(\tau)$ can be extracted from such a measurement by evaluating the fringe contrast as a function of delay, given by

$$I(x,\tau) = I_1(x) + I_2(x) + 2|g^{(1)}(\tau)|\sqrt{I_1(x)I_2(x)}\cos\left(\frac{2\pi\theta}{\lambda_0}x + \varphi\right) \tag{3.2}$$

for light with a wavelength λ_0, phase difference φ, an angle θ between the two beams and intensities $I_1(x)$ and $I_2(x)$ of the two individual images, obtained by blocking the other arm.

Another interferometry configuration, the Mach-Zehnder interferometer [Zeh91; Mac92], is presented in Fig. 3.4 b). Again, the image is divided into two arms using a beam splitter. However, the two images are not recombined in the same beam splitter, but rather in a second beam splitter and thus do not pass through the same path twice. This allows to place a telescope consisting of two lenses within one of the arms. If two lenses with the same focal length are chosen, the image is flipped in both directions and the first order spatial coherence can be measured. Additionally, by selecting two lenses with a difference in focal lengths, the image in one arm can be magnified to superimpose only a small part of the image with the entire image from the other arm. This small fraction of the image is used as a constant phase reference and enables to generate a spatial phase map. Additionally, this technique allows to identify vortices, as a phase vortex superimposed with a magnified, coherent image as phase reference results in a fork dislocation within the fringe pattern. For the aim of evaluating the phase of the emitted light, a two-dimensional Fourier transform is applied to the fringe pattern, the coherent part of the image is extracted and finally transformed back using the inverse Fourier transform. The imaginary part of the resulting image represents a spatial phase map.
As described in section 2.1, the second order coherence can provide valuable additional information to first order coherence measurements due to its dependency on the process of light generation. Experimentally, the second order coherence function is measured using a Hanbury Brown-Twiss (HBT) interferometer [HT56] dividing the image into two arms, both of which are equipped with avalanche photo diodes (APDs) by ID Quantique for single photon counting. The intensities obtained from the two APDs are subsequently correlated. A schematic of this interferometer is presented in Fig. 3.5. As imaging is not required to measure second order coherence, this interferometer is commonly implemented using fibre optics. For this experiment, the sample is excited with the pulsed laser and thus emits light in pulses separated by 12 ns. A timer is started once a photon is detected in one of the arms and stopped as soon as a photon is detected in the other arm. As the signal of the second arm is delayed by approximately 50 ns and the APDs count photons over a time interval of 100 ns, the central peak corresponds to photons generated by the same laser pulse, whereas the photons resulting in all other peaks originate from different laser pulses and are thus uncorrelated. The correlation is performed by a Becker & Hickl SPC-130 time-correlated single photon counting module. For the analysis, the photons within each peak are integrated. The degree of second order coherence characterises the mechanism of light generation within the light source and is given by $g^2(0) = 1$ for uncorrelated photons. The side peaks are hence used for normalisation. The APDs feature a time resolution of 40 ps that is considerably longer than the laser pulse width of approximately 10 ps and the characteristic time scales of the polariton dynamics on the order of 10 ps, thus resulting

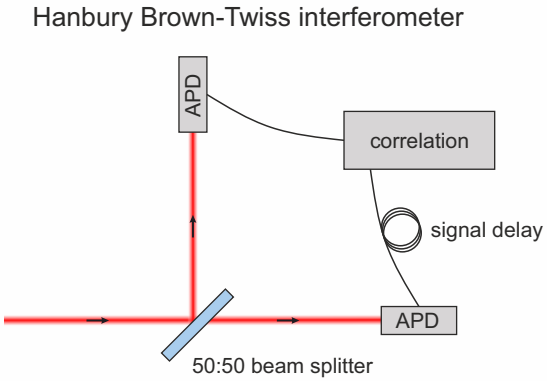

Figure 3.5: Schematic of the Hanbury Brown-Twiss interferometer that is used to measure second order coherence and thus provides valuable information on the mechanism of light generation in the source. The signal is divided into two arms that are each equipped with an APD capable of single photon counting. The signal of one of the APDs is delayed by approximately 50 ns on the way to the computer performing the correlation analysis.

in a measurement of the second order coherence function $\bar{g}^{(2)}$ averaged over the duration of the pulse. Furthermore, the HBT interferometer is mounted behind the spectrometer at the second exit slit, marked on the right side of the spectrometer in Fig. 3.2, allowing to measure the second order coherence of a single, energetically separated mode.

3.2.3 Spatial light modulator

In section 3.2.1, the general operating scheme of a Fourier spectroscopy setup including beam shaping optics such as an expander lens or an elliptical lens was introduced. However, for a range of experiments, more complex laser patterns are required for the excitation of the microcavity. For this aim, a SLM represents an ideal solution, as it offers an extensive degree of flexibility and allows to use almost any grey scale image as a laser excitation pattern. SLMs are comprised of an array of pixels, each of which modifies either the amplitude, the phase or both of the incoming laser light. For excitation schemes in Fourier spectroscopy, phase-only SLMs are preferred as they provide superior resolution and efficiency over amplitude-modulating SLMs [RL13]. As part of this work, a HOLOEYE Photonics GAEA-2 phase-only SLM with a resolution of 4160×2464 pixels based on liquid crystal display technology [YW15] was added to the spectroscopy setup and software to generate phase patterns and operate the SLM was implemented using MathWorks MATLAB.

The operating scheme of an SLM capable of modulating the phase of a laser beam is based upon the fact that a lens performs a two-dimensional, spatial Fourier transform of the

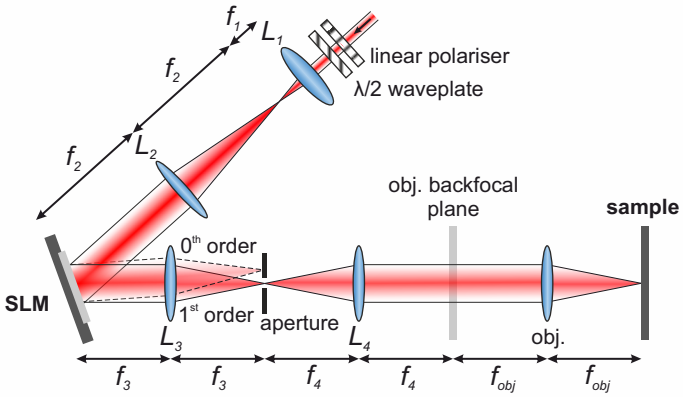

Figure 3.6: Schematic of the beam path used to operate a phase-only SLM. Each pixel of the SLM modulates the phase of the linearly polarised, expanded laser beam. The desired laser pattern is obtained by Fourier transformation with the objective lens. A telescope is used to adjust the magnification and enables to suppress zero order reflections with an aperture.

incoming light field, which is used to transform the phase modulation imprinted by the SLM into an amplitude modulation of the laser excitation. In Fig. 3.6, a schematic of the optical path used to operate the SLM is presented. First, the axis of linear polarisation of the excitation laser needs to be aligned with the SLM, as only one polarisation orientation is modulated. Next, a telescope consisting of lenses L_1 and L_2 is used to expand the laser beam such that is covers the entire SLM display, which acts as a mirror in which each pixel can imprint a phase shift between 0 and 2π onto the laser light. The objective then performs a Fourier transform of the phase-modulated laser beam resulting in the desired amplitude-modulated laser pattern on the sample surface. A second telescope is used to tune the magnification as well as to suppress zero-order reflections originating from the inactive area between the pixels of the SLM, residual light in a polarisation that is not aligned with the SLM display, imperfections in the SLM calibration as well as residual reflections of the pixels. Using this telescope, the SLM plane is imaged onto the back focal plane of the objective.

Once installed, the key challenge in operating the SLM lies in the generation of the phase patterns to imprint on the laser beam to achieve the desired laser patterns on the sample. For a few tasks, analytically determined phase patterns are available. The most prominent examples are shifts of the laser spot in the sample plane using gratings, shifts along the optical axis using a lens as well as axicon ring excitations created by a vortex phase pattern. Of the latter, gratings are particularly valuable, as they can be used to spatially offset the desired laser pattern from the zero order reflection spot [Zha+09a], which can subsequently be blocked by the aperture depicted between lenses L_3 and L_4 in Fig. 3.6. Alternatively, a strategy based on destructive interference can be used to eliminate this

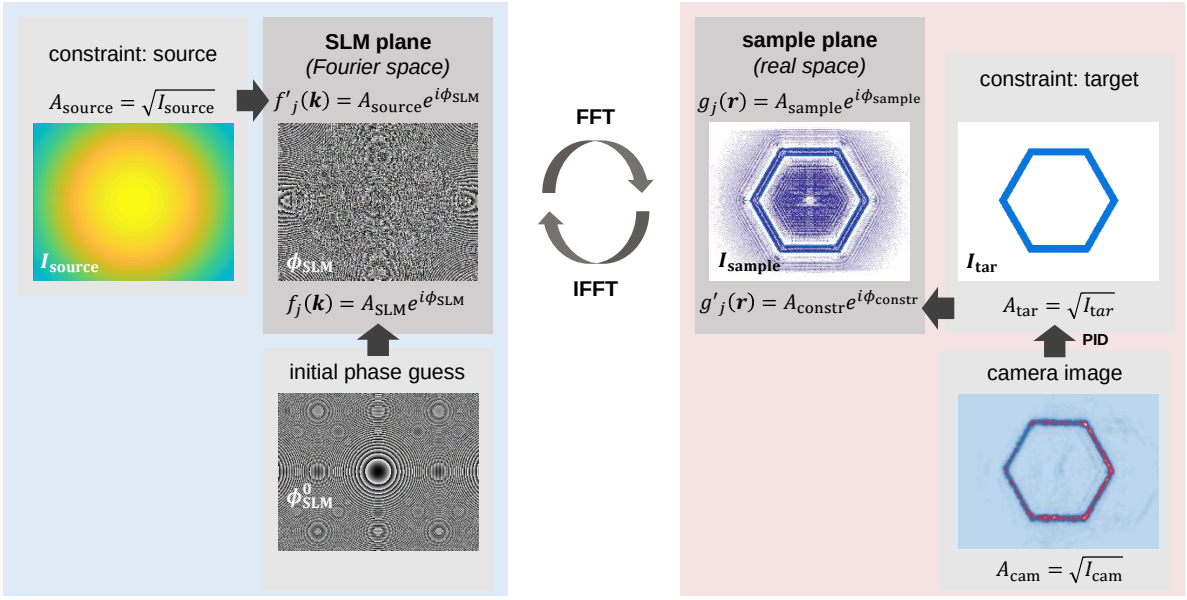

Figure 3.7: Schematic of the iterative Fourier algorithm that is used to calculate the phase patterns to display on the SLM to achieve the desired laser pattern on the sample surface. The light fields at the SLM and the sample planes are linked through a two-dimensional fast Fourier transform (FFT). Phase retrieval algorithms commonly start with an initial phase guess, perform iterative Fourier transformations and apply constraints to the light field in the SLM and Fourier planes. Additionally, feedback from a camera image of the actual laser pattern can be included.

undesired zero order reflection [MEB07; PD07]. However, in general, an analytical solution for the phase pattern of a desired laser pattern, referred to as *phase retrieval problem* [Fie78; Fie82; Els03], does not exist and has to be derived through iterative algorithms. For this work, iterative Fourier algorithms were used to obtain the phase patterns, also referred to as kinoforms, that are imprinted onto the laser by the SLM. A schematic of the operating principle of these algorithms is depicted in Fig. 3.7. The light field

$$f_j(\boldsymbol{k}) = A_{\mathrm{SLM}} e^{i\phi_{\mathrm{SLM}}} \tag{3.3}$$

in iteration j of the algorithm with amplitude A_{SLM} and phase ϕ_{SLM} in the SLM plane in Fourier space is linked to the light field

$$g_j(\boldsymbol{r}) = A_{\mathrm{sample}} e^{i\phi_{\mathrm{sample}}} \tag{3.4}$$

in the sample plane in real space by an objective which is represented by a two-dimensional fast Fourier transform (FFT) and an inverse fast Fourier transform (IFFT). In the SLM plane, the light field is constrained by the Gaussian intensity distribution $I_{\mathrm{source}} = A^2_{\mathrm{source}}$

of the excitation laser, resulting in the constrained light field

$$f'_j(\boldsymbol{k}) = A_{\text{source}} e^{i\phi_{\text{SLM}}}, \tag{3.5}$$

whereas the light field in the sample plane is constrained by the desired target intensity pattern $I_{\text{tar}} = A_{\text{tar}}^2$ and the light field is described by

$$g'_j(\boldsymbol{r}) = A_{\text{constr}} e^{i\phi_{\text{sample}}}. \tag{3.6}$$

Both in the SLM and the sample plane, further constraints on the phase can be applied. However, this was not necessary for this work. The iterative algorithm to obtain the phase pattern that is required to generate the desired target pattern is comprised of the following steps:

1. Select a target amplitude pattern A_{tar}.
2. Construct an initial light field at the SLM plane consisting of the intensity profile of the excitation and an initial phase guess ϕ^0_{SLM}.
3. Apply a Fourier transform to the light field at the SLM plane to obtain the light field at the sample plane.
4. Apply the constraints at the sample plane. Usually, an arbitrary phase is allowed and only the amplitude is constrained to the desired target distribution.
5. Propagate the constrained light field back to the SLM plane by an inverse Fourier transform.
6. Apply the constraints in the SLM plane. Again, commonly only the amplitude is constrained by the intensity distribution of the excitation laser whereas the phase can be arbitrarily modulated using the SLM.
7. In each iteration, calculate a merit function to quantify the deviation between the amplitude of the obtained light field and the target distribution. Repeat steps 3 to 6, until the deviation is smaller than a pre-defined threshold value.

The quality of the results of this algorithm depends strongly on the initial phase guess. Here, the prevailing incentive is to maximise the overlap between the amplitude of the light field obtained by the first Fourier transformation and the target amplitude distribution [Lea+06] by selecting a combination of a lens and gratings. However, the largest potential for optimisation of both quality and efficiency of the algorithm is comprised in the

application of the constraints to the light field in the sample plane. In the following, the two algorithms used in this work, namely modified versions of the *Gerchberg-Saxton (GS)* [GS72] algorithm and the *mixed-region amplitude freedom (MRAF)* [PD08] algorithm, are described. For descriptions of several further algorithms that have been developed for this purpose the reader is referred to a review in literature [Ket04].
The GS algorithm provides the most straightforward approach towards constraining the light field in the sample plane, as the amplitude is simply replaced by the target amplitude distribution to obtain the new light field

$$g'_{j+1} = A_{\mathrm{tar}} e^{i\phi_{\mathrm{sample}}}. \tag{3.7}$$

However, this algorithm tends to stagnate in local minima and is therefore commonly modified [Fie80; GLS15], such that the new light field

$$g'_{j+1} = (1-\beta) g_j + \beta A_{\mathrm{tar}} \left(2e^{i\phi_{\mathrm{sample}}} - e^{i\phi_{\mathrm{constr},j}}\right) \tag{3.8}$$

contains a contribution from the amplitude obtained by Fourier transformation. The mixing ratio is given by the factor β.
The MRAF algorithm applies the amplitude constraint only in a signal region *SR* that is defined as an area around the target pattern while the amplitude is allowed as an additional degree of freedom for the algorithm in the surrounding noise region *NR*. The new light field

$$g'_{j+1} = \left(m A^{SR}_{\mathrm{tar}} + (1-m) A^{NR}_{\mathrm{sample}}\right) e^{i\phi_{\mathrm{sample}}} \tag{3.9}$$

is governed by the mixing parameter m balancing the trade-off between signal quality ($m \ll 1$) and efficiency ($m \approx 1$). Conceptually, the SLM redistributes the intensity of the laser beam from a Gaussian profile to the desired pattern by balancing out interference conditions. Due to the boundary conditions of, among others, the finite number of pixels as well as the finite numerical aperture of the objective, parts of the intensity cannot be redirected correctly. It is therefore useful to provide a noise region that serves as a dump for this redundant intensity. Additionally, adding a small offset to the target pattern [GH12] to avoid pixels with zero intensity significantly reduces the number of vortices in the calculated phase patterns [SWS05].
Next to a graphical user interface providing interactive control for the definition of the source and target patterns, the algorithm parameters and analytical phase patterns, the software implemented as part of this work further includes the ability to stabilise a laser pattern based on feedback from a camera image through a proportional–integral–derivative (PID) controller as well as a tool to calibrate the phase shift of

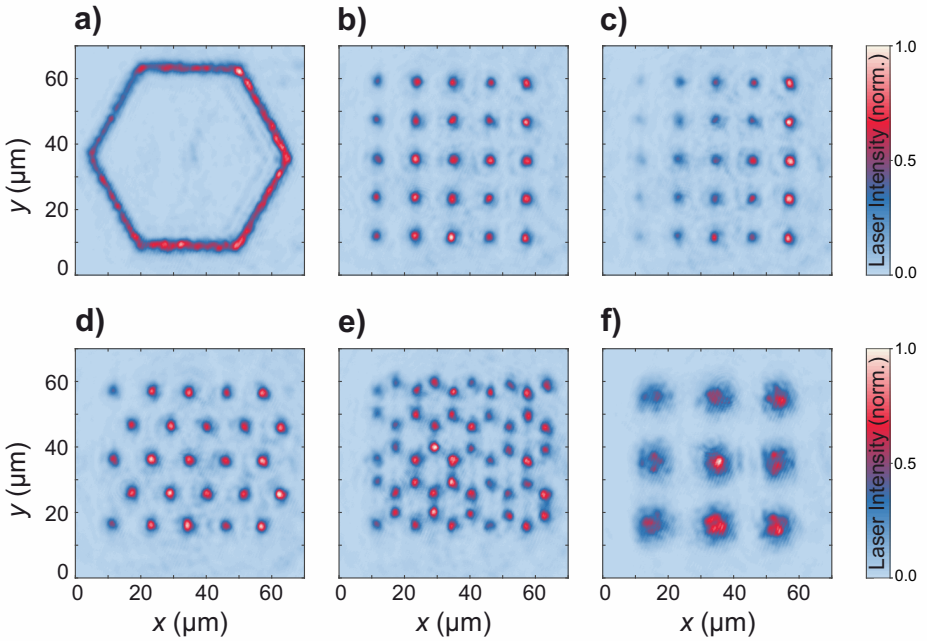

Figure 3.8: Exemplary laser patterns generated with an SLM. The hexagon in **a)** features a width of approximately 2.5 µm. The square lattice in **b)**, the square lattice with an intensity gradient in **c)** as well as the hexagonal and honeycomb lattices in **d)** and **e)**, respectively, consist of laser spots with diameters of approximately 3.0 µm. The square lattice in **f)** features laser spots with diameters of approximately 7.0 µm. The remaining intensity inhomogeneity is predominantely caused by an inhomogeneous reflectivity of the microcavity surface.

the SLM pixels with respect to the applied voltage [LC19]. A selection of laser patterns generated with this software are presented in Fig. 3.8, demonstrating the versatility of an SLM to modulate the laser excitation. The remaining intensity inhomogeneity arises due to an inhomogeneous reflectivity of the microcavity surface. This inhomogeneity as well as an additional inhomogeneity caused, among others, by imperfections in the Gaussian beam profile, the beam alignment as well as the phase calibration of the SLM can be compensated using feedback from the imaging camera. While these laser patterns fulfil the requirements of the experiments performed as part of this work, the development of software for SLMs remains an open field of research including for example evolutionary strategies to optimise iterative algorithms [Bir+00], advanced strategies towards compensating a variety of imperfections of the SLM display itself [Ket+04; XC04; Pus+20] as well as improving overall algorithm efficiency [LT02; WCT15; Bow+17].

4 Establishing lattice potentials for polaritons

Solid-state physics has evolved around the description of electrons in crystalline structures and their dispersion relations. As part of this development, two-dimensional systems, such as graphene, surface-states or layered structures, have led to a range of key discoveries. However, electronic systems can be hard to access and their geometries are often limited to the crystalline structures that occur in nature. Therefore, a range of artificial lattice platforms, so called quantum simulators [GAN14], have been developed to complement the research efforts on lattice potential environments and their physical phenomena. Especially the honeycomb lattice, known from graphene, has proven to be particularly valuable and has hence been realised in a range of platforms [Pol+13]. Among the most prominent lattice simulators are ultra-cold gases of atoms trapped in optical lattices [Blo05; WD08; BDZ08] and photonic lattices [Pel+07; Ang17]. For the latter, various platforms that commonly consist of either optical cavities, as introduced in section 3.1, or waveguides [Lon09] and provide control over the coupling strength between individual sites have been established. These photonic lattice simulators cover a broad range of wavelength regimes, from microwave to visible light. The interest in such lattices justifies itself in the easy and controlled initiation of a wave packet in a certain state as well as extensive access to information on the states through imaging and spectroscopy techniques measuring for example amplitudes, polarisation, phase and coherence. Furthermore, nonlinearities, gain and loss can be added and enhance the capabilities of lattice simulation. Through operating photonic lattices with single photon sources, quantum effects such as boson sampling were investigated [Bro+13; Spr+13; Til+13], whereas research on lattices using classical light has, over the recent years, pointed its focus towards topological phases. The research field of topological photonics is based upon the insight that the topological classification of Hamiltonians is not limited to fermionic systems but can be transferred to bosonic systems and even classical waves as well [HR08; RH08]. Based upon this idea, the first demonstrations of topologically non-trivial phases for photons were realised in magneto-optic photonic crystals in the microwave regime [Wan+08; Wan+09]. In the following development of the field, various concepts to circumvent the necessity of magneto-optic

materials and implement non-trivial topology for photons in the infrared and visible spectrum were conceived [Haf+11; Rec+13a; Haf+13]. These achievements constitute the foundation of the diverse range of platforms that represents the field of topological photonics today [Oza+19]. A more detailed introduction to this research area is provided in chapter 6.

For this work, photonic lattice potentials were realised in a microcavity platform that hosts polaritons by using the technological approaches introduced in section 3.1.2. By adding an excitonic matter component to the eigenstates of the photonic system, such polaritonic lattice simulators combine the advantages of photonic lattices with the ability to study lattice Hamiltonians of interacting particles with gain and loss [AB16]. As introduced in section 3.1.2, the development of polaritonic lattices was driven by the technological progress in fabricating etched micropillars that feature discrete modes [Gér+96; Nar+09], based on which coupling between two pillars resulting in a photonic molecule was achieved by designing the individual pillars with overlap [Bay+98; Mic+11]. Having established control over the coupling of two micropillars, linear chains of pillars resulting in the formation of a one-dimensional band structure were implemented [Bay+99; Tan+13]. Furthermore, the flexibility in designing the geometry of artificial lattices of micropillars was demonstrated by fabricating one-dimensional Lieb lattices [Bab+16] as well as Fibonacci quasicrystals [Bab+17]. One of the milestones in these developments was the implementation of a two-dimensional honeycomb lattice in which the characteristic band structure of graphene was reproduced for polaritons [Jac+14]. Complementary to etched lattices, the maturing technological control over the fabrication of GaAs-based microcavities enabled the fabrication of one-dimensional chains [Win+16] as well as two-dimensional square lattices [Win+15] using the EnO approach. Furthermore, research on polaritonic lattices was extended by optically inducing lattices of polariton condensates [Oha+16; Oha+17; Ber+17; Oha+18; Pic+20; Töp+21; Pie+21] as well as developing lattices in new material platforms such as perovskites [Su+20] and organics [Dus+20].

This chapters aims to provide a foundation of the physics of polaritonic lattices, in particular fabricated using the EnO approach, on which the subsequent chapters are based. At first, a detailed investigation of the formation of a band structure with a particular focus on the transition from molecular orbitals to a continuous dispersion relation is given in section 4.1. In the following section 4.2, polariton condensation in these lattice potentials is studied. For the understanding of the data presented in this work, it is important to note that all lattices are characterised by the diameters d of the underlying EnO microtraps or etched micropillars and the reduced trap or pillar distance $v = a/d$, with a denoting the centre-to-centre distance of adjacent lattice sites.

4.1 Band structure formation

Two-dimensional polaritonic lattices can be used to emulate and simulate a broad range of physical phenomena. The underlying principle of these simulators is the formation of a band structure from the discrete energy levels of multiple coupled micropillars or micro-traps. The concept of a band structure is based on the translational symmetry of a lattice that allows the description using Bloch states, which are defined for an infinitely large lattice or, equivalently, under periodic boundary conditions. However, while individual micropillars and molecules with discrete energy levels as well as one- and two-dimensional polaritonic lattices with continuous dispersion relations have been demonstrated, the transition from discrete modes to a fully formed band structure of a lattice with a size large enough to neglect any remaining discretisation has not been studied in detail. A thorough understanding of the formation of band structures is, however, indispensable for the investigation of more advanced phenomena occurring in lattice potential environments. In particular in the realms of topological photonics and topological lasing, the edges and interfaces of lattice domains have attracted increasing attention. As topological edge modes are a result of a topologically non-trivial bulk band structure, understanding the lower size constraints for a lattice domain to form a bulk band structure becomes essential. Furthermore, ribbons of polariton lattices are predicted to feature fascinating effects such as antichiral edge states that are not accessible in large lattices [MGL19]. This section is therefore devoted to investigate the band structure formation of EnO lattices from single traps over molecules and small lattices of a few unit cells to large lattices with fully evolved band structures. All structures investigated in this section were processed on sample Ga-EnO1 and feature traps with diameters of $d = 2.0\,\mu\text{m}$ and a reduced trap distance of $v = 1.00$, corresponding to touching traps. The excitation was provided by a non-resonant, continuous wave laser that was tuned to a high-energy Bragg minimum of the top DBR and expanded to cover multiple unit cells of the investigated lattice.

The foundation of the EnO lattices studied in this work is a single trap. The spectra in Fourier and real space of such a single trap with a diameter of $d = 2\,\mu\text{m}$ that are displayed in Figs. 4.1 a) and b), respectively, clearly show the expected discrete energy levels of the S and P modes. While the real space spectrum corresponds to a cross section through the centre of the trap along the x-axis, the Fourier space spectrum was integrated over k_y to enhance the contrast. Furthermore, the iso-energy cuts obtained from a tomography of these two modes presented in Figs. 4.1 c)-e) reveal the characteristic real space mode distribution. The highest intensity of the S mode is located at the centre of the trap and the mode is rotationally symmetric. As reported in literature [Nar+09], the two-fold degenerate P mode is highly susceptible to small disorder in the confinement potential

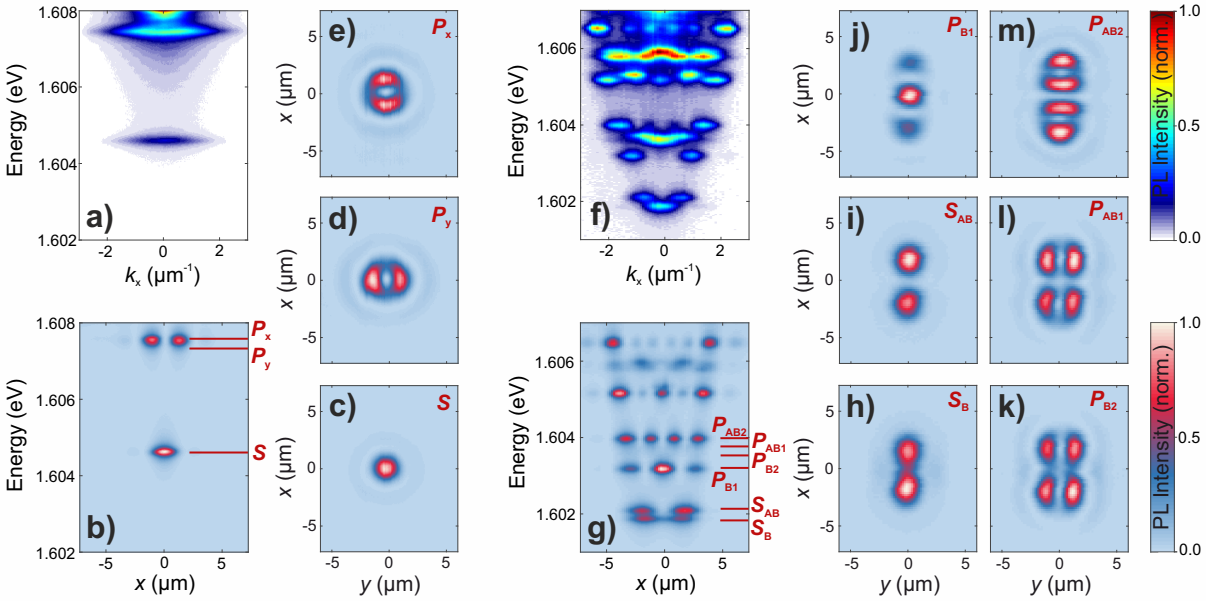

Figure 4.1: a)-b) Fourier and real space spectra of a polariton trap with a diameter of $d = 2.0\,\mu m$, respectively. **c)-e)** Real space images of the S, P_y and P_x modes. **f)-m)** The Fourier and real space spectra of two touching, coupled traps as well as real space images of the molecular S and P modes.

due to the lack of rotational symmetry. Thus, the degeneracy is lifted and the two characteristic dumbbell-shaped modes can be observed at a slight energy difference.

The first step in studying the coupling of individual polariton traps is a molecule consisting of two touching traps. The formation of the energy levels of a polaritonic molecule can be described in analogy to the formation of the orbitals of atomic molecules, where each energy level of the contributing atoms leads to one molecular orbital. The S mode therefore splits into two sub-modes that are referred to as bonding (B) and anti-bonding (AB) modes, as observed in the Fourier and real space spectra presented in Fig. 4.1 f) and g). Again, the Fourier space spectrum was integrated along k_y for better visibility while the real space spectrum represents a cross section along the x-axis through the centre of the molecule. The nomenclature of bonding and anti-bonding modes is based on the high probability density of the lower sub-mode between the sites, motivating the term *bonding*, compared to the high probability density localised to the individual sites of the upper sub-mode that is thus named *anti-bonding*. Real space images at the energies of the two S sub-modes are displayed in Fig. 4.1 h) and i). The P band is based upon the two P modes of each trap and consequently splits into four sub-modes whose real space mode patterns are presented in Figs. 4.1 j)-m). Analogously to the S-modes, it is worth noting that the two bonding modes P_{B1} and P_{B2} are characterised by a higher probability density between the sites than the two anti-bonding modes P_{AB1} and P_{AB2}. Furthermore,

it is important to note that in particular the higher modes extend significantly into the surrounding material as well as neighbouring traps, resulting in a larger effective trap diameter as well as a larger coupling strength between the traps. This larger coupling strength reveals itself in the larger bandwidth of the P modes compared to the S modes. Additionally it is important to note that, due to the lack of rotational symmetry of the characteristic dumbbell shape of P modes, the coupling strength acquires an additional directional dependence.

To observe the transition from the discrete energy levels of a single trap or a molecule to the continuous band structure of a lattice, the honeycomb lattice geometry was chosen due to its well-known and characteristic band shape featuring two Dirac cones at the intersection of the bonding and the anti-bonding S sub-bands. To study the band structure formation, a series of honeycomb ribbons with varying widths were fabricated. In Figs. 4.2 a)-e), real space images at the energy of the anti-bonding S sub-band of ribbons with a width of $N = 1$, 2, 3, 6 and 10 unit cells, respectively, are presented. Due to the anti-bonding nature of this mode, the probability density is localised to the centre of the individual traps allowing to image the lattice geometry. In Figs. 4.2 f)-j), Fourier space images, reconstructed from hyperspectral imaging scans by selecting an iso-energy cross section at the energy at which the Dirac points are expected, are displayed. Fourier space spectra along k_x, thus along the short axis of the ribbons, at $k_\mathrm{y} = 0$ as well as at $k_\mathrm{y} \approx 1\,\mu\mathrm{m}^{-1}$, cutting through a Dirac cone, are presented in Figs. 4.2 k)-o) and Figs. 4.2 p)-t), respectively.

The narrowest ribbon of a honeycomb lattice, corresponding to a width of one unit cell, is a single zigzag chain with angles of $\varphi = 120°$ between adjacent traps. Such a chain features two sites per unit cell resulting in two S sub-bands along the chain. Due to the width of only two sites of this chain, a cross section perpendicular to the chain resembles the spectrum of the polaritonic molecule introduced in Fig. 4.1 f) that is characterised by discrete energy levels. With an increasing width of the ribbons, more energy levels are added to each sub-band. This effect can be particularly clearly observed in the anti-bonding S sub-band in a spectrum through the Γ point, corresponding to Figs. 4.2 k)-o), where the number of energy levels corresponds precisely to the width of the ribbon in numbers of unit cells. For a width of $N = 3$ unit cells, the energy splitting between the modes in the bonding S sub-band is already too small to be resolved with respect to the linewidth, while the anti-bonding sub-band still consists of clearly separated, discrete modes. For a width of $N = 10$ unit cells, the band structure is fully evolved and no remaining discretisation is observed. Corresponding to the band structure formation at $k_\mathrm{y} = 0$, the formation of a Dirac cone is observed in the spectra at $k_\mathrm{y} \approx 1\,\mu\mathrm{m}^{-1}$ presented in Figs. 4.2 p)-t). Already at a ribbon width of $N = 6$ unit cells, the Dirac cone is fully evolved, corresponding to

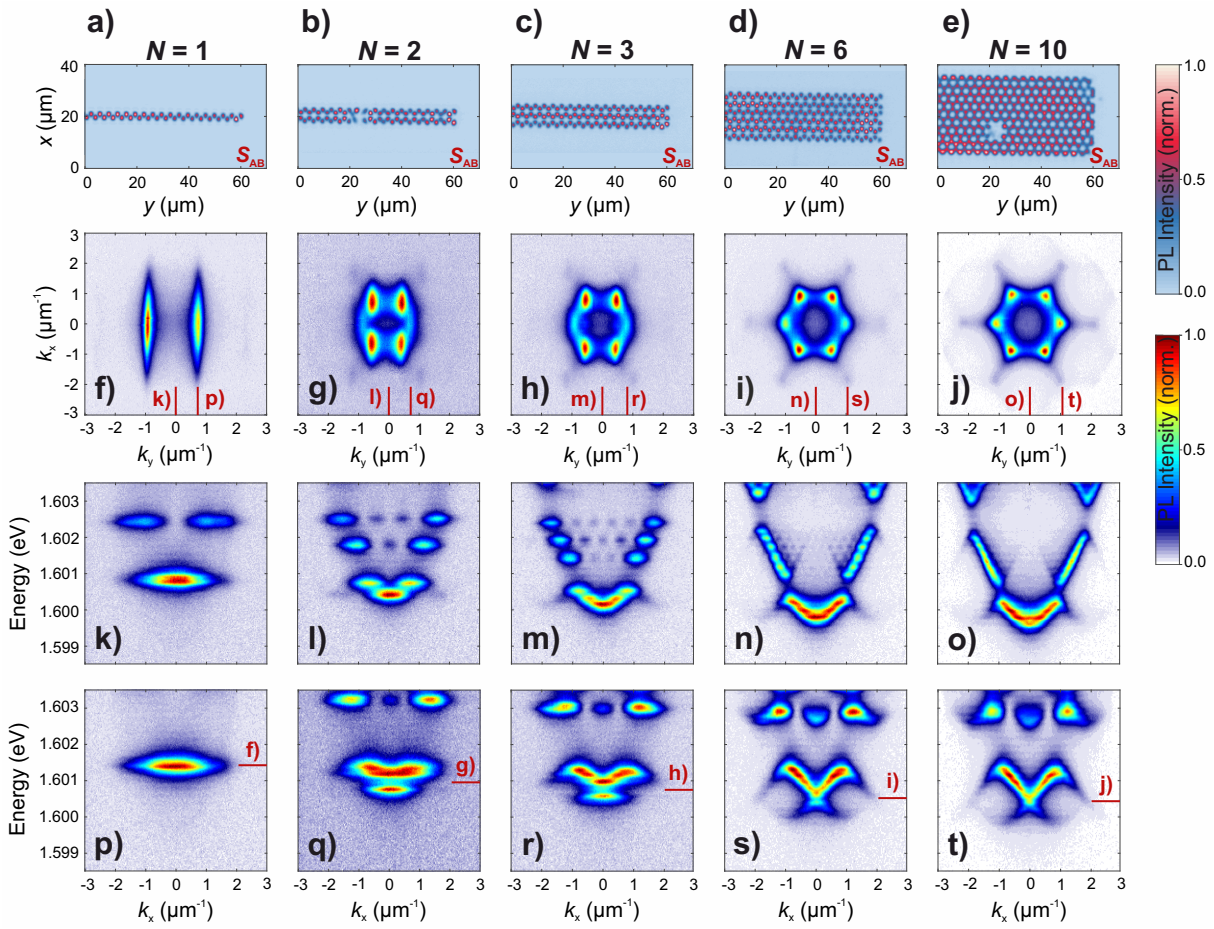

Figure 4.2: **a)-e)** Real space images at the energy of the anti-bonding S sub-band of honeycomb ribbons with widths of $N = 1$, 2, 3, 6 and 10 unit cells, respectively. **f)-j)** Corresponding Fourier space images at the energy of the Dirac cones. **k)-o)** and **p)-t)** Fourier space spectra along the short axis of the ribbons through the Γ point as well as through a Dirac point, respectively.

a degree of translational as well as C_3 symmetry that is large enough to simulate the band structure of graphene. This result is of significant importance for the design of more advanced lattice geometries containing different domains, as it sets a lower bound on the size of the individual domains that is required for a lattice to be viewed as a region with a continuous band structure rather than a molecular structure with discrete energy levels. Finally, spectroscopic results on a honeycomb lattice with a size of 30×30 unit cells, thus considerably larger than the excitation spot, are presented in Fig. 4.3. Here, all lattice symmetries are fully evolved resulting in a continuous band structure. Selected cuts along the K-Γ-K', M-Γ-M and K-K directions of the Brillouin zone are presented in Figs. 4.3 a)-c) and reveal the well-known band structure of graphene featuring the two Dirac points at the K and K' points of the Brillouin zone. An iso-energy Fourier space image at the energy of the Dirac points that highlights the high-symmetry points of the Brillouin zone is presented in Fig. 4.3 e). In Figs. 4.3 a) and b), no PL emission is detected from the anti-bonding S sub-band in the first Brillouin zone. This effect is commonly observed for a number of bands in polaritonic lattices and is attributed to destructive interference in the far field [Jac+14]. It is therefore worthwhile to study the band structure in the reduced zone scheme representation that is depicted in Fig. 4.3 d). Here, the PL intensity of the dispersions of the first as well as the back-folded bands from one of the adjacent second Brillouin zones were averaged such that the full S band dispersion becomes apparent. The intensity maxima extracted from the hyperspectral imaging scan for each subband at every $k_{\mathrm{x,y}}$ value are plotted as blue data points in a three-dimensional $E(k_{\mathrm{x}}, k_{\mathrm{y}})$ graph in Fig. 4.3 f). Furthermore, the band structure is accurately reproduced across the full Brillouin zone by a tight binding model considering nearest and next-nearest neighbour couplings t and t', respectively, represented by red lines in Figs. 4.3 a)-d) and a surface plot in Fig. 4.3 f). This tight binding model allows to evaluate coupling strengths of $t = 356\,\mu\mathrm{eV}$ and $t' = 44\,\mu\mathrm{eV}$ and demonstrates the benefit of a tight binding model. Despite its simplicity, it is able to reproduce all major features of the band structure with only two fitting parameters that are directly linked to the overlap between adjacent sites and thus allow a direct feedback from the theoretical model to the technological implementation of new lattices. However, while it provides a fast and direct opportunity to evaluate the quality of a lattice, the agreement is not perfect. The remaining deviations between the data and the model arise due to the assumption of the tight binding model that the modes are highly localised with coupling strengths that are significantly smaller than the confinement potential. In particular for higher bands, this assumption is no longer valid. Additionally, the overlap between adjacent traps results in deviations of the mode shapes from atomic orbitals and thus from the tight binding assumption. These deviations lead to discrepancies between model and experiment in

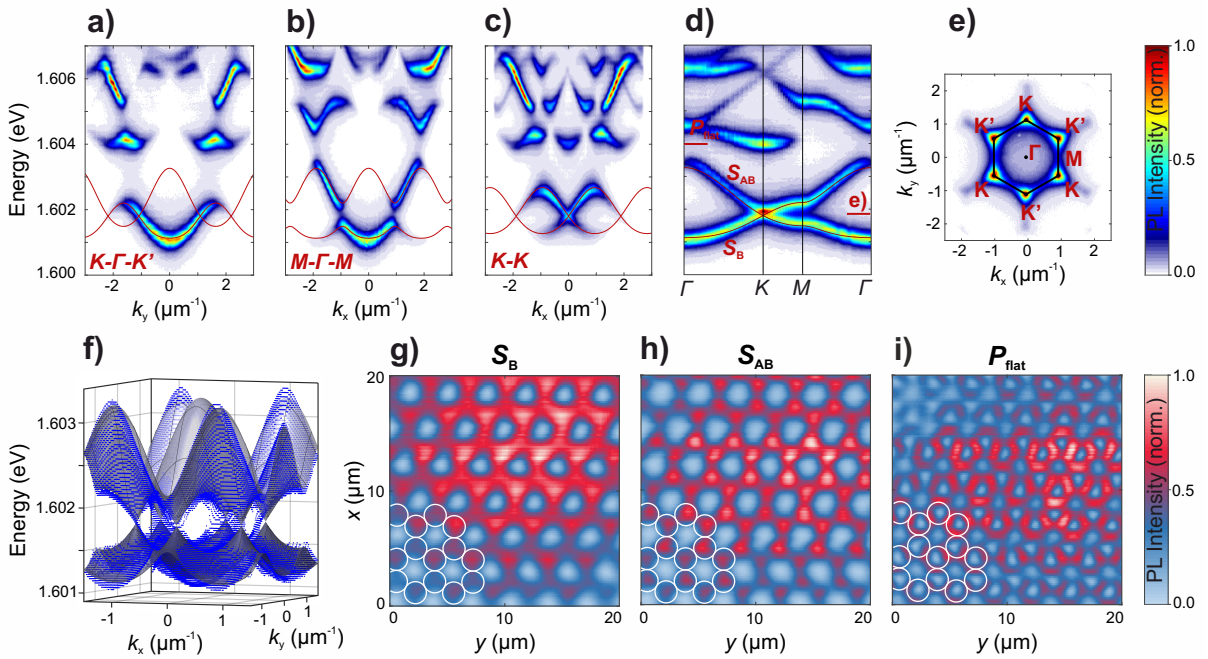

Figure 4.3: a)-c) Fourier space spectra along the K-Γ-K', M-Γ-M and K-K directions of the Brillouin zone of a polaritonic honeycomb lattice. **d)** Reduced zone scheme representation averaged over the first and one adjacent, second Brillouin zone. **e)** Fourier space image at the energy of the Dirac cones. **f)** Reconstruction of the S bands (blue data points) and a tight binding model (surface). **g)-i)** Real space images of the bonding and anti-bonding S sub-bands as well as the lowest P sub-band.

particular for higher bands as these modes extend further beyond the boundaries of the physical traps [Pan+19]. Finally, for high coupling strengths, the individual bands start to hybridise. To include these effects in the theoretical description, the tight binding model was extended to a full Bloch mode description by Dr. Oleg Egorov, the details on which can be found in references [Kle+17] and [Har+20].

The bonding and anti-bonding nature of the two S sub-bands of the honeycomb lattice becomes apparent in the real space mode distributions presented in Figs. 4.3 g) and h), respectively. Additionally, it is interesting to note that the highest probability densities of the lowest P sub-band, a flatband, are localised between the traps. This sub-band is presented in Fig. 4.3 i) and thus features the geometry of a Kagome lattice.

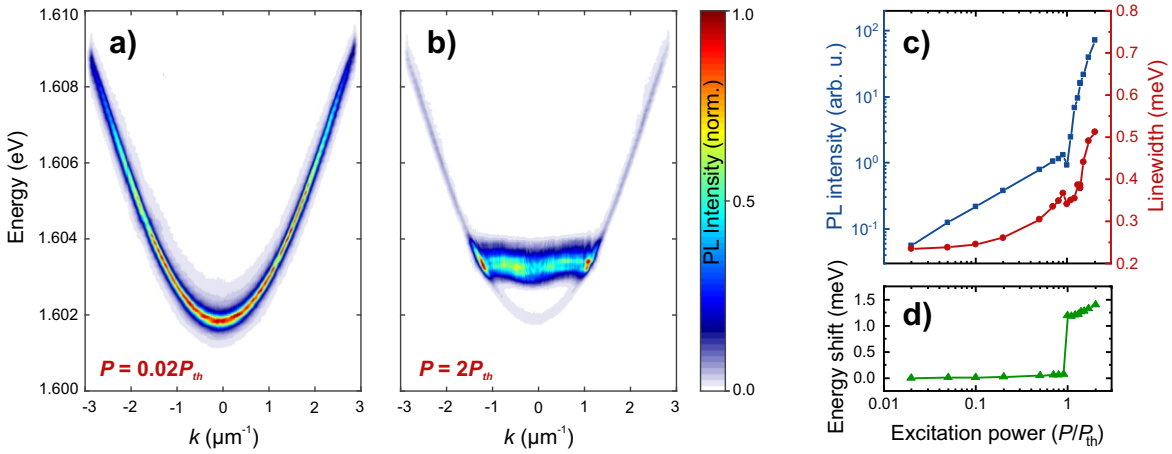

Figure 4.4: Polariton dispersion of a planar microcavity below and above the condensation threshold in **a)** and **b)**, respectively, and the corresponding input-output characteristic and linwidth in **c)** as well as the energy shift in **d)**.

4.2 Polariton condensation in lattice potentials

Research on polaritons is closely intertwined with experiments on polariton condensation, as introduced in section 2.2.4. In particular, polariton condensates constitute a promising path towards realising experiments that harness the inherent non-linearity of the system as the high occupation numbers in condensates enhance the effects of interaction. Following the first experimental realisation of a polariton condensate in a planar microcavity [Kas+06], polariton condensates were realised in confined structures such as micropillars [Baj+08] and molecules [Gal+12] as well. In the following development, polariton condensates were realised in one-dimensional [Tan+13; Bab+16; Win+16] as well as two-dimensional [Win+15; Mil+18] lattices.

As polariton condensation, in particular in EnO lattices, is crucial for this work, this section is devoted to give a systematic investigation of the latter. Furthermore, a thorough understanding of polariton condensation is indispensable for future developments towards technological applications based on polariton lasing, in particular when keeping in mind the recent progress on electrical injection into polariton lattices [Suc+18]. The experiments in this section were performed on sample Ga-EnO1 under excitation with an enlarged laser spot with a diameter of approximately 30 µm. Before studying the condensation within a lattice potential environment, the characteristics of polariton condensation are confirmed on a planar cavity region of the sample at a detuning of $\Delta_E = -4.9\,\mathrm{meV}$ under pulsed laser excitation. In Fig. 4.4 a) and b), exemplary Fourier space spectra below and above the condensation threshold of $P_{\mathrm{th}} = 1.2\,\mathrm{mW}$, respectively, are presented. The input-output characteristic, linewidth and energy shift displayed in Figs. 4.4 c) and

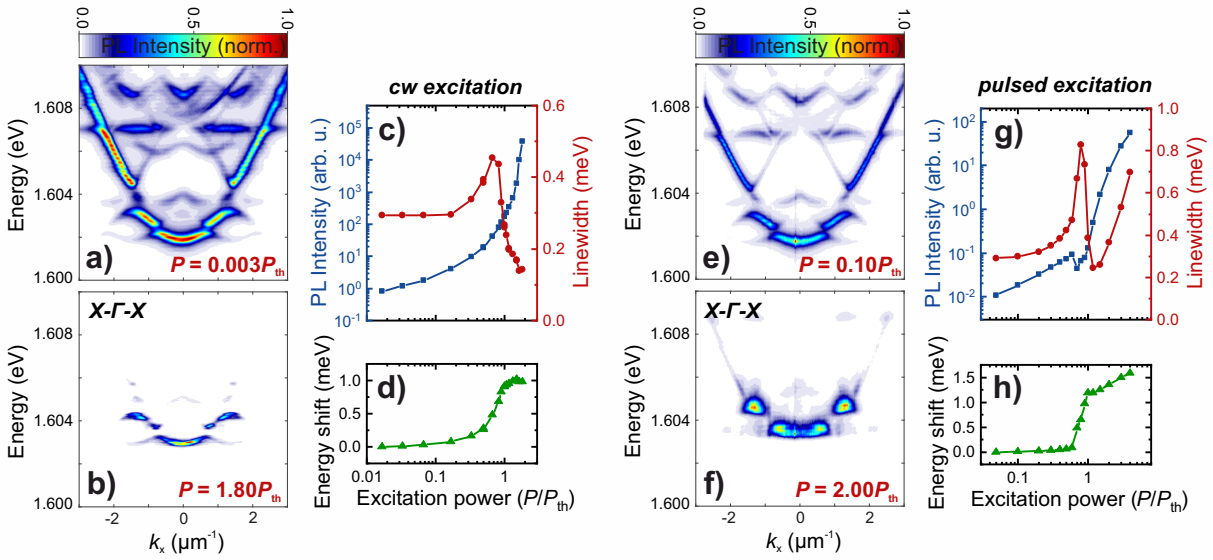

Figure 4.5: Polariton dispersion of a polariton Lieb lattice along the X-Γ-X-direction below and above the condensation threshold under cw excitation in **a)** and **b)**, respectively, and the corresponding input-output characteristic and linewidth in **c)** as well as the energy shift in **d)**. **e)**-**h)** Analogous dataset obtained under pulsed excitation.

d) feature clear evidence of polariton condensation, as the non-linear increase in intensity is accompanied by a drop in linewidth due to the build-up of coherence and an energetic blueshift induced by the increased interaction between polaritons.

Next, condensation in Lieb lattices with trap diameters of $d = 2.0\,\mu\text{m}$ is studied under both pulsed and cw excitation as well as with respect to the detuning, the reduced trap distance and the excitation power. In Fig. 4.5 a), a Fourier space spectrum along the X-Γ-X direction of the Brillouin zone of a Lieb lattice with a reduced trap distance of $v = 1.00$, corresponding to touching traps, obtained under cw excitation with an excitation power well below the condensation threshold is presented. The lattice features a moderately negative exciton-photon energy detuning of $\Delta_E = -5.0\,\text{meV}$ evaluated for the lowest S sub-band of polaritons confined in the lattice potential. With increasing excitation power, the occupation of certain bands increases until polariton condensates form at a threshold power of $P_\text{th} = 36.0\,\text{mW}$, resulting in the spectrum displayed in Fig. 4.5 b). The input-output characteristic, linewidth and energy shift corresponding to the lowest S sub-band presented in Figs. 4.5 c) and d) feature the characteristics of polariton condensation. It is important to note that, analogously to polariton condensation in single micropillars [Kri+09], condensates can form in multiple bands of a lattice simultaneously. In Figs. 4.5 e)-h), analogous data obtained on the same lattice under pulsed excitation are presented. Again, the characteristics of polariton condensation are observed with

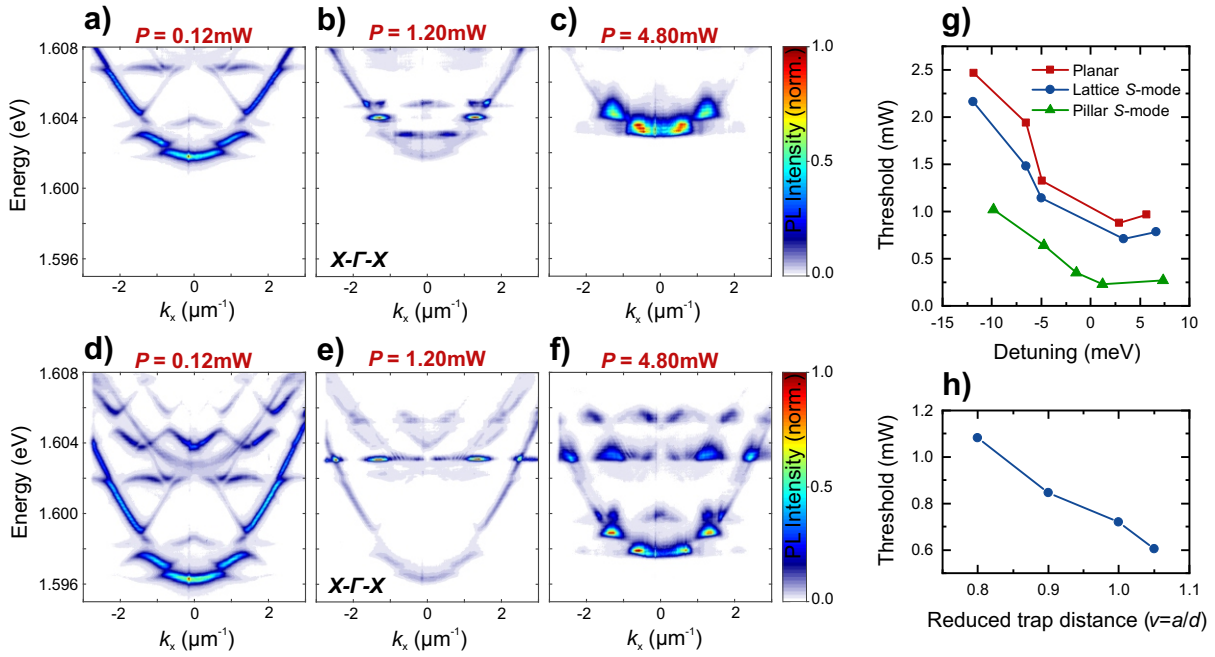

Figure 4.6: **a)-f)** Fourier space spectra of two Lieb lattices along the X-Γ-X direction at detunings of $\Delta_E = -5.0\,\mathrm{meV}$ and $\Delta_E = -12.0\,\mathrm{meV}$, respectively, for three different excitation powers. **g)** Evaluation of the condensation threshold with respect to the detuning for planar microcavities, Lieb lattices and single traps. **h)** Condensation threshold of the lower S band of Lieb lattices with a variation in reduced trap distance.

a threshold power of $P_{\mathrm{th}} = 1.2\,\mathrm{mW}$. The advantages of a pulsed laser for condensation experiments are its high peak power as well as the ability to perform time resolved measurements. However, as the system undergoes the entire condensation process from an occupation of the linear band structure to the formation of a blue-shifted condensate within each pulse, a broader linewidth is observed. In contrast, a cw laser emits constantly over time and thus enables to measure the very narrow linewidth of a condensate. Its disadvantages are the considerably lower maximal power that is available as well as stronger heating effects within the sample as more energy is transferred into the system.
Next, the influence of the detuning on the condensation in an EnO polariton lattice is studied. In Figs. 4.6 a)-c) and d)-f), Fourier space spectra along the X-Γ-X direction of two Lieb lattices with reduced trap distances of $v = 1.00$ at detunings of $\Delta_E = -5.0\,\mathrm{meV}$ and $\Delta_E = -12.0\,\mathrm{meV}$, respectively, at pulsed excitation powers of $P = 0.12$, 1.20 and 4.80 mW are presented. While both lattices emit in the linear regime for an excitation power of $P = 0.12\,\mathrm{mW}$ and condensates have formed in the lowest S band of both lattices at $P = 4.80\,\mathrm{mW}$, it becomes apparent that for an excitation power of $P = 1.20\,\mathrm{mW}$, a condensate has already formed in the lowest S band of the lattice at a detuning of $\Delta_E = -5.0\,\mathrm{meV}$, whereas the lowest S band of the lattice at a detuning of $\Delta_E = -12.0\,\mathrm{meV}$

is still in the linear regime. A more detailed evaluation of this dependence of polariton condensation on the detuning is presented in Fig. 4.6 g) and clearly reveals a decrease of the condensation threshold towards zero detuning. Furthermore, power dependent measurements under the same excitation conditions on a planar region of the microcavity as well as a single polariton trap with a diameter of $d = 2.0\,\mu\text{m}$ feature the same dependence. This decrease of the condensation threshold is commonly attributed to enhanced phonon scattering and a longer polariton lifetime due to the increasing excitonic contribution [DHY10]. Additionally, in Fig. 4.6 g) a systematic decrease of the condensation threshold between a planar microcavity and a single trap due to the increased polariton density in a confined potential is observed. As expected, the condensation threshold of a lattice that provides a higher confinement with respect to a planar microcavity, however less confinement than a single pillar due to the coupling between adjacent sites, is found to be between these two distinct cases. Additionally, the condensation threshold was studied for Lieb lattices at a detuning of $\Delta_E \approx -5.0\,\text{meV}$ featuring reduced trap distances of $v = 0.80$, 0.90, 1.00 and 1.05, as presented in Fig. 4.6 h). In agreement with the comparison to a planar microcavity and a single trap, the condensation threshold decreases with increasing distance and thus reduced coupling between the traps.

Finally, a comparison of the excitation power dependent polariton occupation in the two lattices presented in Figs. 4.6 a)-c) and d)-f) reveals that varying the combination of detuning and excitation power allows to control into which band condensation occurs preferably. Here, the definition of an effective detuning is valuable. While the detuning of a lattice is given by the energy of the lowest S band with respect to the exciton energy through equation 2.21, the effective detuning is calculated for each band individually using the PL emission energy of that band. For the lattice corresponding to the spectra presented in Figs. 4.6 d)-f), the considerably smaller effective negative detuning of the P flatband of $\Delta_E = -4.7\,\text{meV}$ compared to the detuning of $\Delta_E = -12.0\,\text{meV}$ of the lowest S band results in polaritons to condensate into the P flatband first. For higher excitation powers and thus occupations, the relaxation processes become more efficient and a condensate forms in the S band.

In summary, this detailed investigation of the polariton condensation behaviour in EnO lattices allows to adjust the detuning, lattice parameters and excitation conditions adequately to ensure the optimal polariton condensation required for the specific aim of an experiment, such as the selective condensation into flatbands that is presented in the following chapter.

5 Polaritons in flatbands

The interest in flatband systems started in theoretical physics and is based on the initial works by Sutherland [Sut86] and Lieb [Lie89], who discovered that in certain lattice geometries, dispersionless bands with an energy that is independent of the wave vector arise. In these bands, the group velocity vanishes, resulting in fully localised states that are commonly referred to as compact localized states (CLSs) [AAM96].
The starting point of both theoretical and experimental research on flatband systems was the magnetic ordering in flatband ground states, which is studied predominantly in electronic systems. The study of the effect of flatbands on magnetism remains an active area of research [MT93; Ram94; LMM11] that has very recently gained additional pace through the observation of flatbands in the antiferromagnetic Kagome lattice compound FeSn [Kan+20; Lin+20; GM20]. Additionally, the research interest was soon extended as a connection between electronic flatbands and superconductivity was discovered [VMD98; Igl+14]. One peculiarity in this context are the CuO_2 planes in cuprate high temperature superconductors. These planes are organised in a Lieb lattice structure and the resulting flatbands are believed to play an important role in explaining the high critical temperature. Additionally, the recent burst in research on two-dimensional materials has spurred the discovery of flatbands in multilayer silicene [Li+18b] as well as bilayer graphene [Mar+18], which are studied in particular in the context of the superconductivity of graphite and graphene [Esq+14; Vol18] and were motivated further by the observation of superconductivity in magic-angle graphene [Cao+18a; Cao+18b].
Nowadays, the scientific interest in flatbands has spread across a broad range of fields, focussing for example on the high sensitivity to disorder that is induced by the lack of dispersiveness, as even a weak perturbation can define the dominant energy scale [Bod+14; BM18]. In experimental systems, however, this sensitivity also results in flatbands not being perfectly flat along all directions of the Brillouin zone. Therefore, commonly an extended definition including partially flat bands that are only flat along certain directions of Fourier space is used. Next to disorder, flatbands are also used to study strongly interacting systems, as the interaction between individual particles is enhanced through the localisation in flatbands [DRM15]. This research direction has in particular gained theoretical interest in the context of interacting topological phases [PRS13; BL13; Ma+20a].

Accompanying the increased theoretical efforts, the development of new experimental platforms based on artificial lattices further accelerated the research field [LAF18]. Here, the most prominent, two-dimensional lattices that host flatbands are the Lieb and Kagome lattices. Even though some of the artificial lattice implementations focus on the magnetic properties of flatbands in metamaterials [Gar+18], the overwhelming amount of experiments is based on the localisation to CLSs, the sensitivity to disorder, the increased inter-particle interaction as well as the combination of flatbands and topology. Up to today, flatbands have been realised using lattices of ultra-cold atoms [She+10; AHM10; Tai+15; Oza+17; Leu+20], electronic surface states [Slo+17b] as well as plasmonic metamaterials [Nak+12]. Complementary, progress in realising a Kagome lattice of atoms on a surface was achieved [Sun+20]. Furthermore, photonic realisations of Lieb [Guz+14; Muk+15; Vic+15; Xia+16; Die+16; Pol+17] and Kagome [Zon+16] lattices have evolved to powerful simulators of flatband physics [LF18]. One of the unique features of photonic implementations is the ability to introduce gain and loss, thus opening up the path towards studying the interplay of flatbands and non-Hermiticity. In particular in the realm of lasing, it remains an open question how flatbands effect the coherence of both a single laser as well as long range correlations between lasers [Nix+13; Lon19].

In polaritonic microcavities, the first attempt towards realising a band structure featuring a flatband was a Kagome lattice defined by a lithographically designed metal film on top of the cavity [Mas+12]. However, due to the very small confinement potential, no experimental evidence of a flatband was observed. Following the technological development of confinement techniques, the following realisations of one-dimensional [Bab+16; Gob+19] and two-dimensional [Kle+17; Whi+18] Lieb lattices were based on coupled, etched micropillars. In particular the two-dimensional Lieb lattice implementations were able to provide valuable insight into the destructive interference mechanism that leads to the localisation and thus the formation of a flatband. Furthermore, flatbands were realised in the P band of a honeycomb lattice [Jac+14; Mil+19].

In this chapter, a detailed investigation of flatbands in polaritonic Lieb and Kagome lattices in EnO microcavities is presented. First, in section 5.1, precise control over the remaining dispersiveness of the flatbands is demonstrated. In particular the realisation of flatbands in Kagome lattices should be emphasised, as this lattice has not yet been realised in etched lattices due to the challenges in etching holes with the required large aspect ratios that were described in section 3.1.2. In section 5.2, the controlled excitation of polaritons in flatbands as well as selective condensation into CLSs are demonstrated. Building upon this technological control, the influence of the localisation in flatbands on the coherence properties of polariton condensates is investigated in section 5.3. Finally, an investigation of vortex lattices as well as superfluid, chiral edge transport of polariton condensates in Kagome lattices is presented in section 5.4.

5.1 Engineering polariton flatbands

Before investigating the characteristics of polariton condensates in flatbands, a thorough understanding of these flatbands as well as the influence of lattice parameters on their dispersion is required. Therefore, this section is devoted to a systematic investigation on the controlled engineering of polariton flatbands by adjusting the lattice design parameters.

Among the first lattices identified to host a flatband is the Lieb lattice [Lie89] hosting an S flatband which features the additional peculiarity of intersecting with the two dispersive sub-bands at Dirac cones at the M-points of the Brillouin zone. Fourier space spectra along the high-symmetry directions X-Γ-X, M-X-M and M-Γ-M of a Lieb lattice on sample Ga-EnO1 with trap diameters of $d = 2.0\,\mu\text{m}$ and a reduced trap distance of $v = 1.05$ located at a detuning of $\Delta_\text{E} = -4.7\,\text{meV}$ and excited by an enlarged Gaussian, cw laser spot with a diameter of approximately $30\,\mu\text{m}$ are presented in Figs. 5.1 a)-c). The data were accurately reproduced by a tight binding model including nearest and next-nearest neighbour coupling. In the model, the S and P flatbands are highlighted in red. While the Dirac cones can be best identified in Figs. 5.1 b) and c), the dispersionless nature of the flatbands is best observed along the M-X-M direction displayed in Fig. 5.1 b). The lattice geometry as well as the high-symmetry points of the Brillouin zone are visualised in the Fourier space image at the energy of the S Dirac points presented in Fig. 5.1 f). As a consequence of a non-zero next-nearest neighbour coupling in polaritonic lattices, a remaining dispersiveness of the flatbands is observed along the other directions of the Brillouin zone. Analogously to the experimentally obtained spectra of a honeycomb lattice presented in Fig. 4.3, no emission is observed in the first Brillouin zone from certain bands due to destructive interference in the farfield [Jac+14]. To overcome this limitation, emission from an adjacent second Brillouin zone was back-folded and averaged with the emission from the first Brillouin zone to generate the reduced zone scheme representation depicted in Fig. 5.1 d). This representation further visualises that the flatbands remain perfectly dispersionless between the X and M points. A full reconstruction of the S sub-bands from the hyperspectral imaging scan is plotted as blue dots in Fig. 5.1 e) and reinforces the good agreement of the tight binding model with the data. To get further insight on the nature of the bands, it is fruitful to study the real space mode distributions that were obtained from a mode tomography and are presented in Figs. 5.1 g)-j). As introduced in chapter 4, the lattice geometry can be clearly observed from the anti-bonding S sub-band. A real space image at the energy of the latter is presented in Fig. 5.1 i). In contrast, the influence of the square lattice that is the origin of the Lieb lattice dictates the mode distribution of the bonding S sub-band plotted in Fig. 5.1 g). Of particular

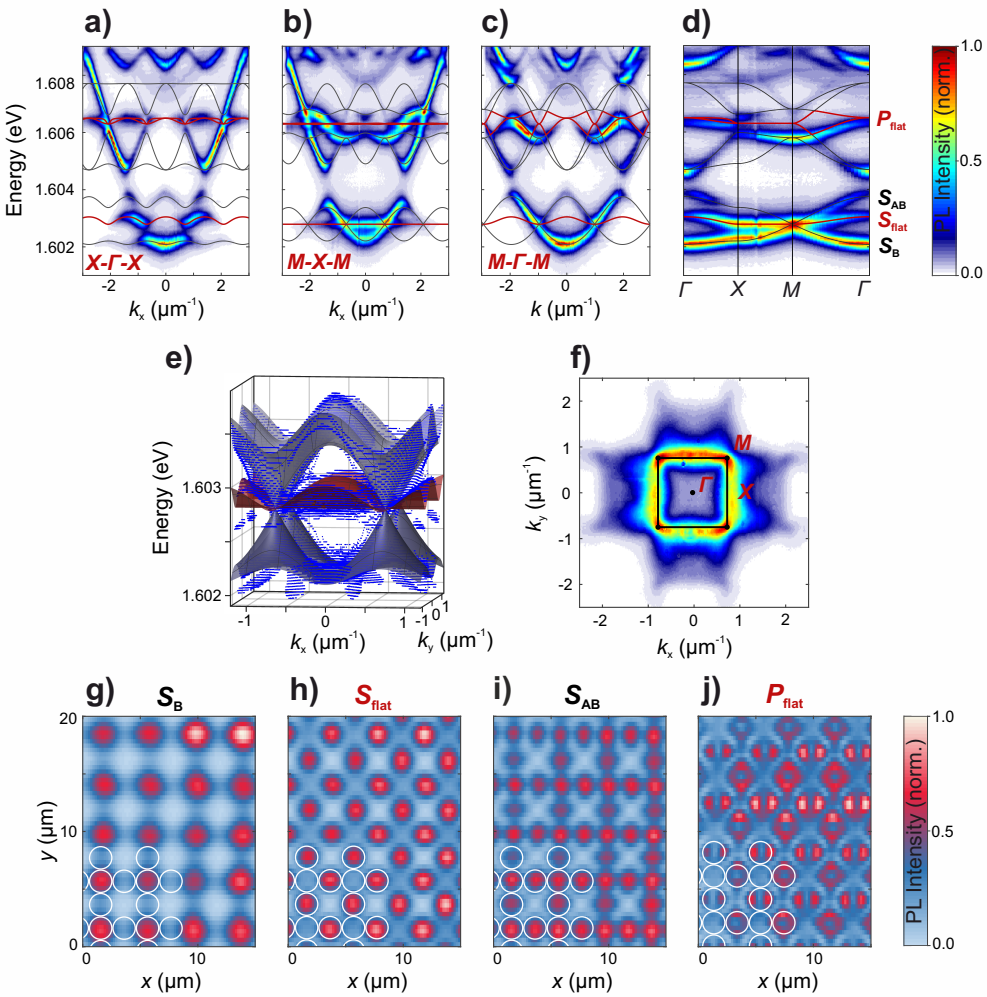

Figure 5.1: **a)-d)** Fourier space spectra of an EnO Lieb lattice with trap diameters of $d = 2.0\,\mu\text{m}$ and a reduced trap distance of $v = 1.05$ along the X-Γ-X, M-X-M and M-Γ-M directions as well as in the reduced zone scheme representation, respectively. The data are reproduced well by a tight binding model that includes nearest and next-nearest neighbour coupling. The S and P flatbands are highlighted in red. **e)** Reconstructed S bands (blue dots) including a tight binding fit. **f)** Fourier space image at the energy of the Dirac points of the S band. **g)-j)** Real space images at the energies of the bonding S sub-band, the S flatband, the anti-bonding S sub-band and the P flatband, respectively.

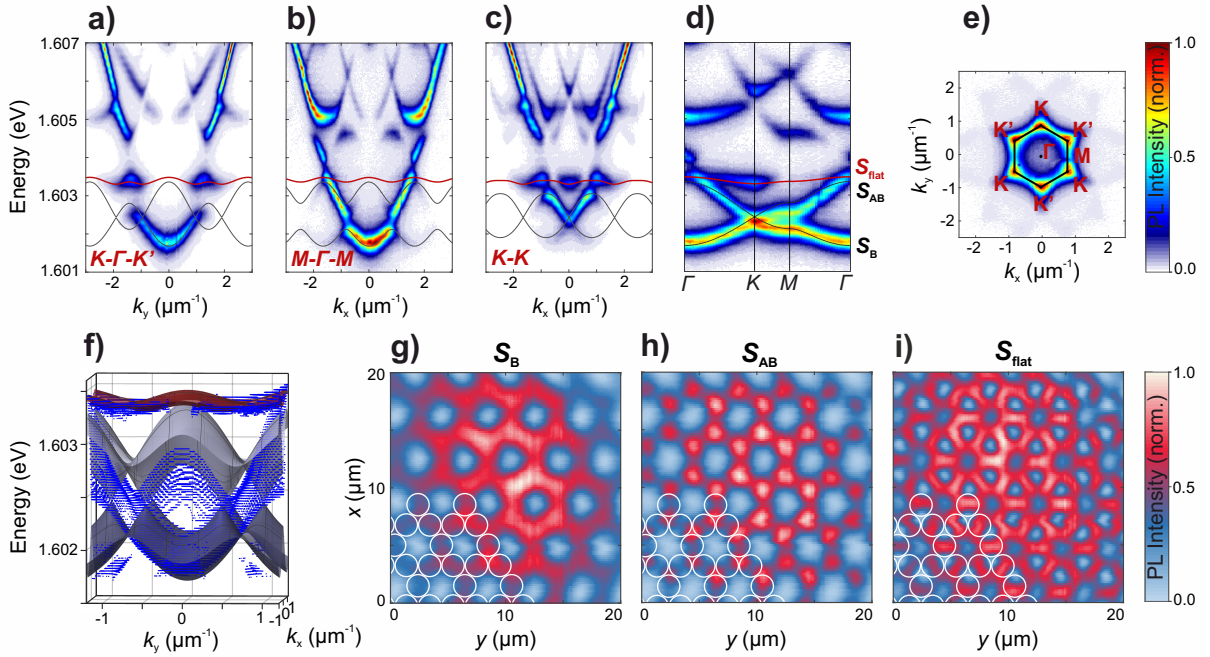

Figure 5.2: a)-d) Fourier space spectra of an EnO Kagome lattice with trap diameters of $d = 2.0\,\mu\text{m}$ and a reduced trap distance of $v = 1.05$ along the K-Γ-K', M-Γ-M and K-K directions as well as in the reduced zone scheme representation, respectively. The data are reproduced well by a tight binding model that includes nearest and next-nearest neighbour coupling. The S flatband is highlighted in red. **e)** Fourier space image at the energy of the Dirac points of the S band. **f)** Reconstructed S bands (blue dots) including a tight binding fit. **g)-j)** Real space images at the energies of the bonding and anti-bonding S sub-bands as well as the S flatband, respectively.

interest is the mode pattern of the flatbands in Figs. 5.1 h) and j) featuring emission only from the B and C sites of the unit cell. This mode pattern is termed Lieb diamond and reveals the flatband formation due to destructive interference of polaritons on the A sites that originiated from the B and C sites [Kle+17; Whi+18]. The polariton population thus localises to the Lieb diamond and forms a CLS.

The second important lattice for flatband studies is the Kagome lattice. Fourier space spectra along the high-symmetry directions K-Γ-K', M-Γ-M and K-K of a Kagome lattice on sample Ga-EnO1 with trap diameters of $d = 2.0\,\mu\text{m}$ and a reduced trap distance of $v = 1.05$ located at a detuning of $\Delta_E = -5.1\,\text{meV}$ and excited with a large Gaussian, cw laser spot are depicted in Figs. 5.2 a)-c). The data are accurately reproduced by a tight binding model including nearest and next-nearest neighbour coupling. To understand these spectra it is valuable to remember that the Kagome lattice can be described as the line graph of the honeycomb lattice. It is therefore not surprising that the lower two S sub-bands of the Kagome lattice are inherited from the honeycomb lattice. The prevail-

ing characteristics of these two sub-bands are the two Dirac cones connecting the two sub-bands at the K and K' points. The linear dispersion of such a Dirac cone is clearly visible in Fig. 5.2 c). On top of these two sub-bands, a flatband touching the upper dispersive S sub-band at the Γ-points appears and is highlighted in red in Figs. 5.2 a)-d). The high-symmetry points are visualised in the Fourier space image at the energy of the Dirac points presented in Fig. 5.2 e). Analogously to the Lieb lattice, a non-zero next-nearest neighbour coupling results in a remaining dispersiveness of the flatband. Additionally to the Fourier space spectra along high-symmetry directions, a representation in the reduced zone scheme, averaged over the first and an adjacent, second Brillouin zone, as well as a full reconstruction including a tight binding fit reproducing the characteristic shape of the S band are presented in Figs. 5.2 d) and f), respectively. In particular in the three-dimensional representation of the S sub-bands across the full Brillouin zone, the striking resemblance with the honeycomb band structure becomes unequivocal. Furthermore, the honeycomb origin of the lower two S sub-bands does not only become apparent in Fourier space spectra but also dictates the mode distribution in real space presented in Figs. 5.2 g) and h), as the two sub-bands share the identical patterns with the honeycomb lattice introduced in Fig. 4.3. The geometry of the Kagome lattice can clearly be observed in the mode distribution of the S flatband depicted in Fig. 5.2 i).

In the polaritonic implementations of both Lieb and Kagome lattices introduced above, the strength of next-nearest neighbour interaction is the key parameter determining the remaining dispersiveness of the flatbands. Control over this parameter is therefore crucial to flatten the flatbands and thus increase localisation as far as possible. Additionally, this control offers the opportunity of studying the effects of transitioning from a dispersive band to a flatband. The coupling strength of two traps decreases rapidly as soon as there is a physical separation between the traps, therefore allowing to decrease next-nearest neighbour coupling significantly while maintaining a reasonable nearest neighbour coupling strength to form a band structure. To realise such a separation, characterised by a reduced trap distance of $v > 1$, the EnO approach is particularly valuable as an overlap between traps is not required to ensure coupling. Fourier space spectra of Lieb lattices with trap diameters of $d = 2.0\,\mu\text{m}$ and reduced trap distances of $v = 0.80$, 0.90 and 1.05 along the high-symmetry directions X-Γ-X, M-Γ-M and M-X-M are displayed in Figs. 5.3 a)-c), e)-g) and i)-k), respectively. Schematics elucidating the directions in the Brillouin zone are provided in Figs. 5.3 d), h) and l). As the dispersiveness of the flatbands is not only limited by a next-nearest neighbour contribution to the coupling but also through deviations of the mode profiles due to the small confinement potential and overlap between the modes, more accurate band structure calculations were performed by Dr. Oleg Egorov using a Bloch mode approach that is described in detail in reference

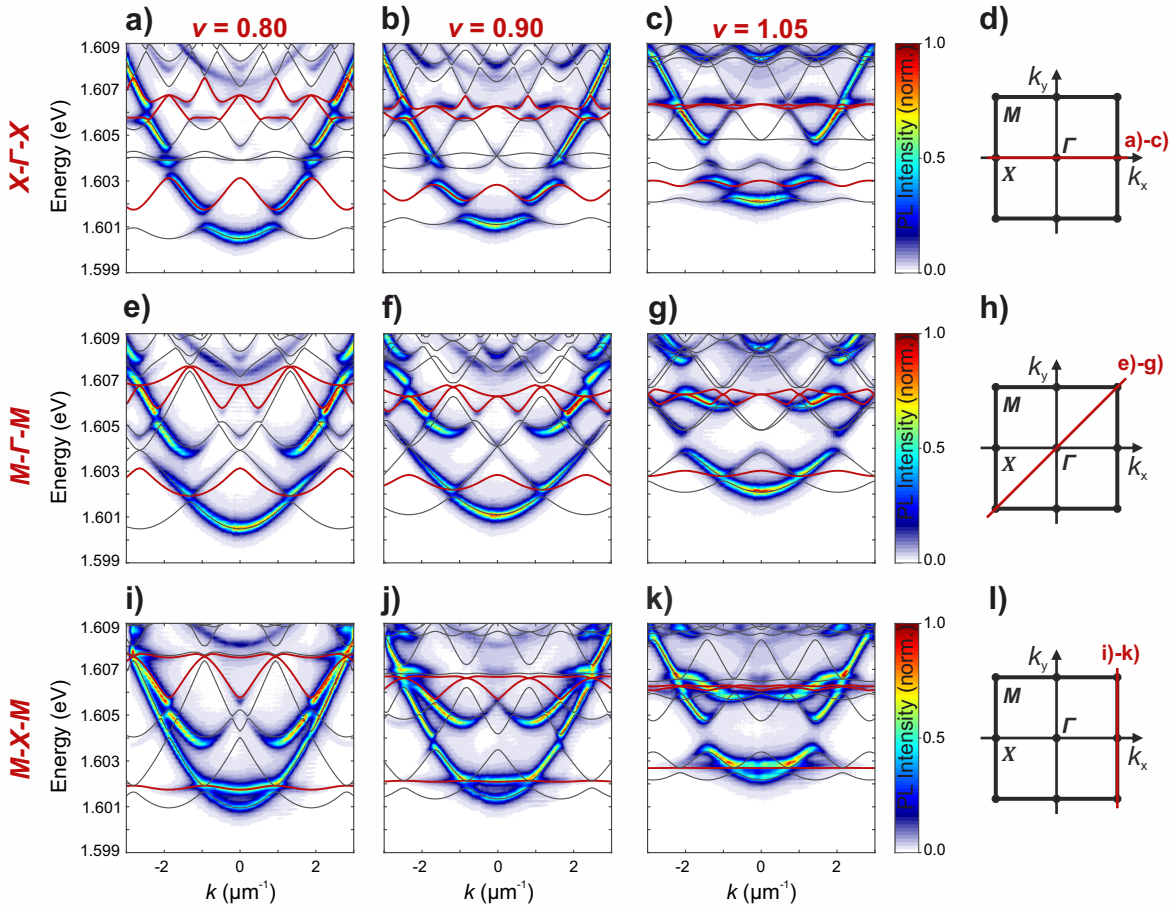

Figure 5.3: **a)-c)** Fourier space spectra along the X-Γ-X direction of Lieb lattices with trap diameters of $d = 2.0\,\mu m$ and reduced trap distances of $v = 0.80$, $v = 0.90$ and $v = 1.05$, respectively. In the Bloch mode calculations that accurately reproduce the data, the S and P flatbands are highlighted in red. **e)-g)** and **i)-k)** Corresponding spectra along the M-Γ-M and M-X-M directions, respectively. **d)**, **h)** and **l)** Schematics visualising the directions in Fourier space.

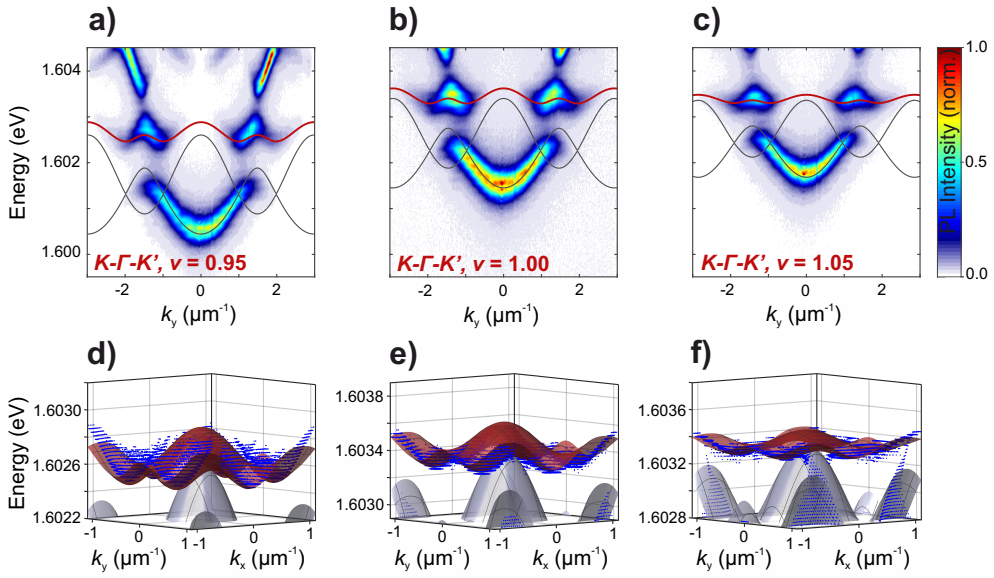

Figure 5.4: a)-c) Fourier space spectra along the K-Γ-K' direction of a Kagome lattice with trap diameters of $d = 2.0\,\mu\text{m}$ and reduced trap distances of $v = 0.95$, $v = 1.00$ and $v = 1.05$, respectively. The S flatband is highlighted in red in the tight binding model. **d)-f)** Reconstructions of the S flatband from the hyperspectral imaging scans (blue dots) including tight binding fits.

[Har+20]. The resulting band structures reproduce the experimentally obtained Fourier spectra perfectly and are plotted in Fig. 5.3 as well, with the flatbands highlighted in red. Along the M-X-M direction presented in Figs. 5.3 i)-k), the P flatband exhibits the highest dispersiveness. When increasing the reduced trap distance and thus decreasing the influences of both next-nearest neighbour coupling as well as deviations of the mode profile due to overlapping traps, its bandwidth decreases drastically. The S flatband, however, exhibits the lowest remaining dispersiveness along this direction and thus does not change significantly with respect to changes of the reduced trap distance. In contrast, the S flatband shows significant remaining dispersiveness along the X-Γ-X direction. Analogously to the P flatband, its bandwidth can be reduced significantly by increasing the reduced trap distance v.

Comparably to the Lieb lattice, a variation of the reduced trap distance was performed for Kagome lattices with trap diameters of $d = 2.0\,\mu\text{m}$. Fourier space spectra along the K-Γ-K' direction of Kagome lattices with reduced trap distances of $v = 0.95$, 1.00 and 1.05 are displayed in Figs. 5.4 a)-c). The corresponding reconstructions of the S flatband from the hyperspectral imaging scans, represented by the blue dots, that were reproduced by a tight binding model are presented in Figs. 5.4 d)-f). Again, the transition from flatbands with significant remaining dispersiveness to almost perfectly flat flatbands is observed.

An evaluation of the bandwidths of the S and P flatbands of the Lieb lattices including

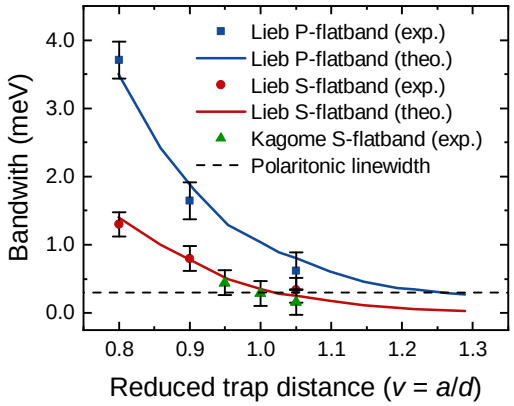

Figure 5.5: Evaluation of the bandwidth, that represents a measure for the dispersiveness, of the flatbands in polaritonic Lieb and Kagome lattices with respect to the reduced trap distance v. For the Lieb lattices, the experimental data were accurately reproduced by a Bloch mode calculation. For comparison, the polaritonic linewidth of the flatbands is highlighted by the dashed line.

the results obtained from the Bloch mode calculations as well as a bandwidth evaluation of the S flatband of the Kagome lattices is plotted in Fig. 5.5. Of particular importance is a comparison between the remaining dispersiveness of the flatbands and the polaritonic linewidth of the latter. For the S flatband of the Kagome lattice with a reduced trap distance of $v = 1.05$, the bandwidth of 160 µeV is significantly smaller than the polariton linewidth of $\gamma_P \approx 300$ µeV. In the following experiments, this flatband can thus be treated as almost perfectly flat. For the S and P flatbands of the Lieb lattice characterised by a reduced trap distance of $v = 1.05$, bandwidths of 340 µeV and 620 µeV were achieved. Again, the bandwidth of the S flatband is on the order of the linewidth, while the P flatband remains dispersive compared to the linewidth. This effect is expected, as the P modes extend further beyond the boundaries of the individual traps and thus couple stronger. However, the overall bandwidth of the band structure is still large enough to resolve all important features, thus motivating to fabricate lattices with traps that are located even further apart in future work. The weaker effect of next-nearest neighbour coupling of the Kagome lattice compared to the Lieb lattice can intuitively be explained by the larger distance a_{NN} between next-nearest neighbours that is given by $a_{NN} = \sqrt{3}a$ for the Kagome lattice and $a_{NN} = \sqrt{2}a$ for the Lieb lattice.

In conclusion, deterministic control over the bandwidths of the flatbands in polaritonic Lieb and Kagome lattices was demonstrated by adjusting the reduced trap distance. In particular for the Kagome lattice, a bandwidth well below the polaritonic linewidth was achieved. Before harnessing this control in experiments on the influence of the dispersiveness of a flatband on the coherence properties of a polariton condensate, a variety

of experimental methods for the controlled excitation of flatband states is introduced in the following section. The systematic evaluation of the dispersiveness of the flatbands in polaritonic Lieb lattices presented in this section was published in reference [Har+20].

5.2 Controlled excitation of flatband states

In the previous section, the fabrication of polaritonic lattices featuring flatbands that are nearly perfectly flat across the entire Brillouin zone was demonstrated. To address specific aspects of these flatbands such as CLSs, disorder effects or non-Hermitian physics experimentally, a controlled excitation of polaritons and polariton condensates in flatbands is crucial. An overview of the excitation schemes described in this section is presented in Fig. 5.6.

To harness the increased inter-particle interaction of polaritons in flatbands as well as for research towards flatband lasers, polariton condensates both stretching across multiple unit cells as well as in a single CLS are promising platforms. In Fig. 5.6 a), the excitation of a large condensate with a Gaussian spot that covers multiple unit cells is schematically depicted. A real space image of the polariton condensate in the S flatband of a Lieb lattice characterised by trap diameters of $d = 2.0\,\mu\text{m}$ and a reduced trap distance of $v = 1.05$ located at a detuning of $\Delta_\text{E} = -3.9\,\text{meV}$ on sample Ga-EnO1 is presented in Fig. 5.6 b). The excitation with a cw, Gaussian excitation spot with a diameter of approximately 30 µm results in a homogeneous condensate covering multiple unit cells. However, the real space spectrum presented in Fig. 5.6 c) reveals that further condensates have formed in other bands. The input-output characteristics as well as Fourier space spectra corresponding to the real space data presented here can be found in Fig. 4.5.

Sun and co-workers proposed to excite a polariton condensate in a single CLS rather than a large scale condensate by using a Laguerre-Gaussian laser spot with the motivation that, in future experiments, these localised condensates could form the basis for network computations [Sun+18]. In Fig. 5.6 d), the excitation with a ring-shaped laser spot created using a spiral phase plate is schematically depicted. Using a cw laser shaped to a ring with a diameter of approximately 4.0 µm that is centred at the Lieb diamond, this excitation geometry results in a polariton condensate localised to a single Lieb diamond, thus forming a single CLS, and is presented in Fig. 5.6 e). Additionally, the real space spectrum presented in Fig. 5.6 f) further reveals that polariton condensation occurred selectively into the S flatband, leaving all other bands below the condensation threshold. These experiments were, analogously to the excitation of a large condensate, performed on Lieb lattices with trap diameters of $d = 2.0\,\mu\text{m}$ and a reduced trap distance of $v = 1.05$, corresponding to the largest available distance between the traps and therefore the flat-

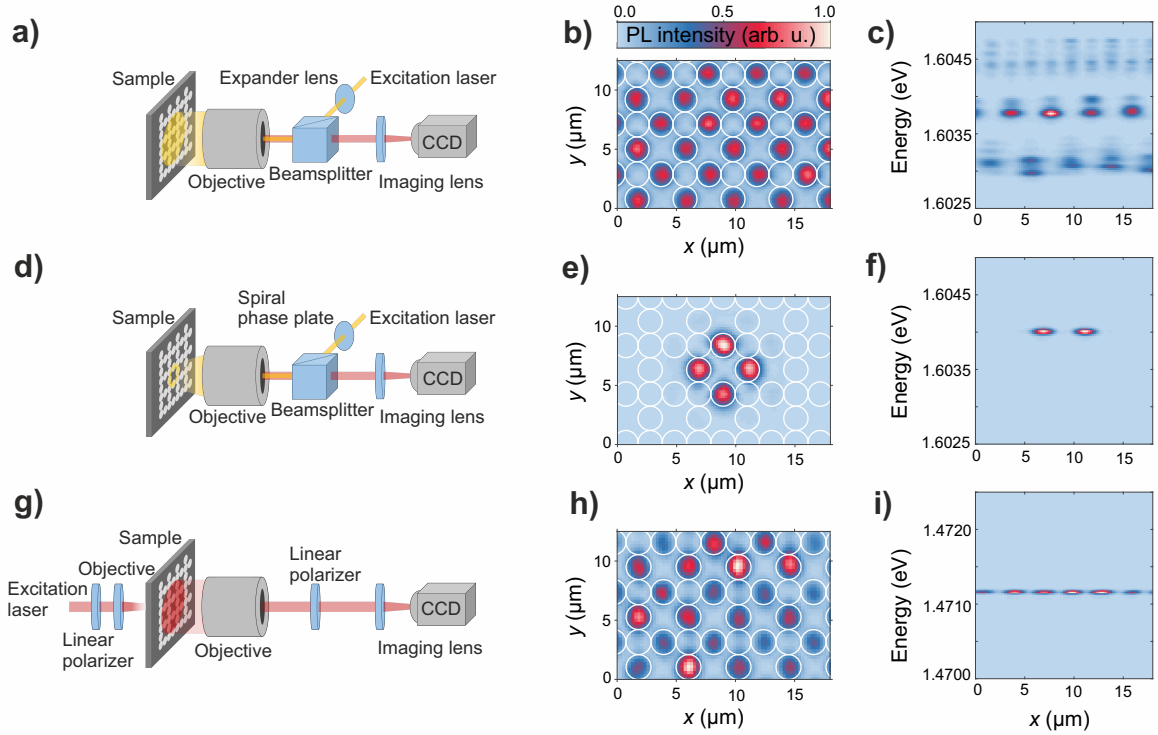

Figure 5.6: **a)** Schematic of the non-resonant excitation of the large polariton condensate in a Lieb lattice in **b)** as well as a real space spectrum above the condensation threshold in **c)**. **d)** Schematic of the non-resonant, ring excitation using a spiral phase plate to create the polariton condensate in a single CLS in **e)** as well as a corresponding real space spectrum. **g)** Schematic of the resonant excitation in transmission geometry of polaritons in the S flatband of a Lieb lattice as presented in **h)** as well as the corresponding real space spectrum in **i)**.

bands with the least remaining dispersiveness. Based on this selective excitation of a polariton CLS and the capability of a spatial light modulator to create multiple ring-shaped excitation spots, experiments on networks of CLS condensates can be envisioned. Next to using flatbands to host polariton condensates, flatbands themselves offer open research opportunities such as their sensitivity to disorder [LAF18] and the coupling between flatbands and dispersive bands [GLN18]. Both of the latter are important aspects when considering flatband states for example for the distortion free storage of information in a CLS. To investigate these effects in polaritonic lattices, the need for a controlled excitation of a polariton population at a well-defined energy and wave vector motivates the development of resonant excitation techniques. Here, the resonant excitation scheme in transmission geometry that was introduced in section 3.2 and is schematically depicted in Fig. 5.6 g) was used to excite polaritons in the S flatband of a Lieb lattice with trap diameters of $d = 2.0\,\mu\text{m}$ and a reduced trap distance of $v = 1.00$ at a detuning of $\Delta_\text{E} \approx -14.5\,\text{meV}$. As described in section 3.2, for experiments in transmission geometry samples with $In_xGa_{1-x}As$ quantum wells are used as their excitonic resonance lies within the band gap of the GaAs substrate which is hence transparent for the excitation laser. Here, a Lieb lattice on sample In-EnO1 with a polished backside was used. Details on the backside polishing process can be found in the appendix in section A.2. The resulting real space mode distribution under excitation with a cw laser with a spot diameter of approximately 30 µm at a wave vector of $k_\parallel = 0$ and an energy of 1.4711 eV, in resonance with the S-flatband, is displayed in Fig. 5.6 h). Again, the characteristic Lieb diamond pattern is reproduced. Additionally, an intensity fluctuations arising due to inhomogeneities in the laser excitation and the transmission properties of the sample are observed. These intensity fluctuations represent a further manifestation of the flatband properties, as the localisation of the polaritons in the flatband inhibits propagation that could compensate the inhomogeneous occupation. The real space spectrum presented in Fig. 5.6 i) further visualises the energetic selectivity achieved with a resonant, transmission excitation scheme.

In summary, three complementary schemes towards exciting polaritons in the S flatband of Lieb lattices were demonstrated. The implementation of these schemes allows to specifically address different aspects of polariton flatbands and design spectroscopic experiments specifically for the desired investigation. Generally, most experiments on polaritonic lattices that were performed so far across the research community have started at negative detunings with high photonic fractions, since the photonic linewidth is usually much smaller than the excitonic linewidth. Furthermore, the bandwidth is determined by the photonic fraction, as the coupling between sites is a predominantly photonic effect. However, it is the excitonic fraction that provides access to non-linear regimes and

separates polaritonic from photonic lattices. Transitioning towards excitonic detunings is thus a major challenge of the entire community. In this context, the excitation schemes presented in this section represent an important step, as in particular the resonant excitation does not rely on polariton relaxation mechanisms that can prove to be complicated in particular towards positive detunings. Polariton flatbands thus represent a well-controlled platform, both from the perspective of lattice design as well as polariton excitation that is in the following section used to study the influence of the localisation in flatbands on the coherence properties of polariton condensates.

5.3 Coherence of flatband condensates

Following the results on the controlled engineering and excitation of polaritons in flatbands described in the previous sections, the aim of this section is to use this platform for a detailed investigation of the coherence properties of flatband polariton condensates. In this respect, both a large condensate as well as a condensate localised to a single CLS are of interest.

As a starting point and following the demonstration of the controlled excitation of polaritonic flatbands in Lieb lattices described in the previous section, the excitation of a large condensate in the S flatband of a Kagome lattice with trap diameters of $d = 2.0\,\mu\text{m}$ and a reduced trap distance of $v = 1.00$ with an enlarged, Gaussian, cw laser spot is presented in Fig. 5.7. In Figs. 5.7 a) and b), exemplary Fourier space spectra at excitation powers below and above the condensation threshold of $P_{\text{th}} = 36.0\,\text{mW}$, respectively, are presented. Here, selective condensation into the flatband was achieved. The experimentally obtained dispersion relations were reproduced by Dr. Oleg Egorov using a full Bloch mode calculation. The real space mode distribution of the flatband condensate presented in Fig. 5.7 c) reveals the expected mode pattern of the Kagome flatband that was introduced in Fig. 5.2. Furthermore, the input-output characteristics presented in Figs. 5.7 d) and e) confirm the formation of a polariton condensate. Establishing selective excitation of a large flatband condensate offers the opportunity to study the degree of first order spatial coherence, $g^{(1)}(r)$, of the latter by autocorrelation measurements.

In section 5.1, control over the remaining dispersiveness of the flatband through a variation in the reduced trap distance was demonstrated. This control enables to investigate the degree of spatial coherence along the transition from a dispersive band to a flatband. In Figs. 5.8 a) to c), Michelson interferograms of polariton condensates, excited by an enlarged, Gaussian, cw laser spot, in the flatbands of Kagome lattices with trap diameters of $d = 2.0\,\mu\text{m}$ and reduced trap distances of $v = 0.95$, $v = 1.00$ and $v = 1.05$ located at a detuning of $\Delta_{\text{E}} \approx -6\,\text{meV}$ on sample Ga-EnO1 are presented. In these interference pat-

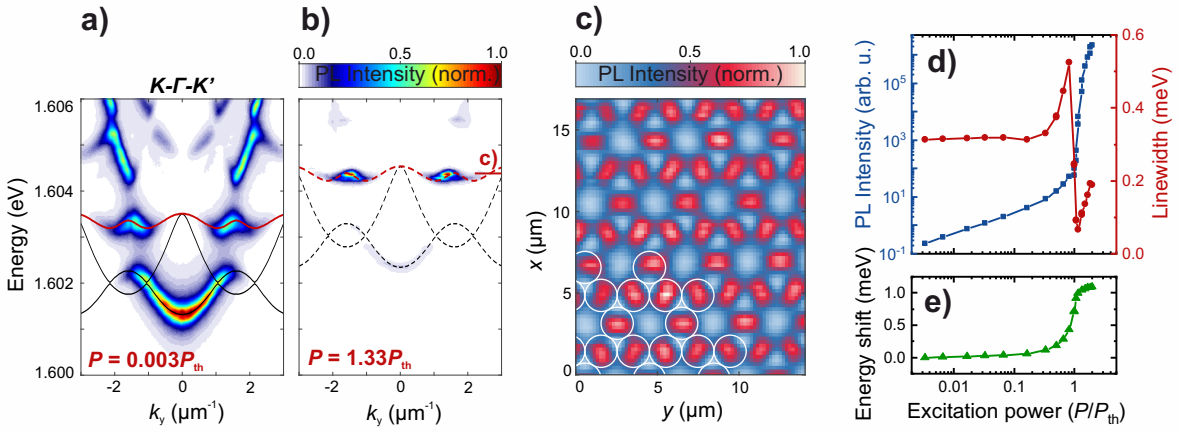

Figure 5.7: a)-b) Fourier space spectra of a Kagome lattice with trap diameters of $d = 2.0\,\mu\text{m}$ and a reduced trap distance of $v = 1.00$ at excitation powers below and above the condensation threshold, respectively. The dispersion relations were reproduced bz a full Bloch mode calculation. **c)** Real space image of the flatband polariton condensate. **d)-e)** Input-output characteristics of the flatband polariton condensate.

terns it is important to note that, to avoid artefacts in the subsequent coherence analysis, the interferometer was meticulously aligned to ensure consistent fringe periodicity and orientation across the three measurements. As described in section 3.2.2, one arm of the Michelson interferometer can be equipped with a retroreflector flipping the image in x- and y-direction. Consequently, the distance between the emission from traps superimposed in the interferogram increases twofold when moving radially from the centre towards the outside of the interferogram. The radial decay of the fringe pattern thus contains information on the spatial coherence length of the polariton condensate. To visualise the spatial coherence, the interferograms are Fourier transformed, the coherent part of the image is extracted and an inverse Fourier transform is applied. The real part of the resulting image can be understood as a map of spatial coherence. These spatial coherence maps are presented in Figs. 5.8 d)-f). In Fig. 5.8 d), one can observe that, for a Kagome lattice with a reduced trap distance of $v = 0.95$, the coherence length is considerably longer than the size of a CLS. However, when increasing the reduced trap distance and thus reducing the dispersiveness of the flatband, the degree of localisation increases resulting in a condensate that is only coherent within a single CLS. In Fig. 5.8 f), corresponding to a reduced trap distance of $v = 1.05$, only the charactersitic six lobes of a Kagome CLS are observed in the spatial coherence map, impressively demonstrating the effect of the almost perfectly flat flatband on the propagation dynamics of the polaritons. Furthermore, the numerical simulations based on a modified Gross-Pitaevskii model that were provided by Dr. Oleg Egorov and are presented in Figs. 5.8 g)-i) accurately reproduce the experimental results. Further details on these theoretical results can be found in reference [Har+21b].

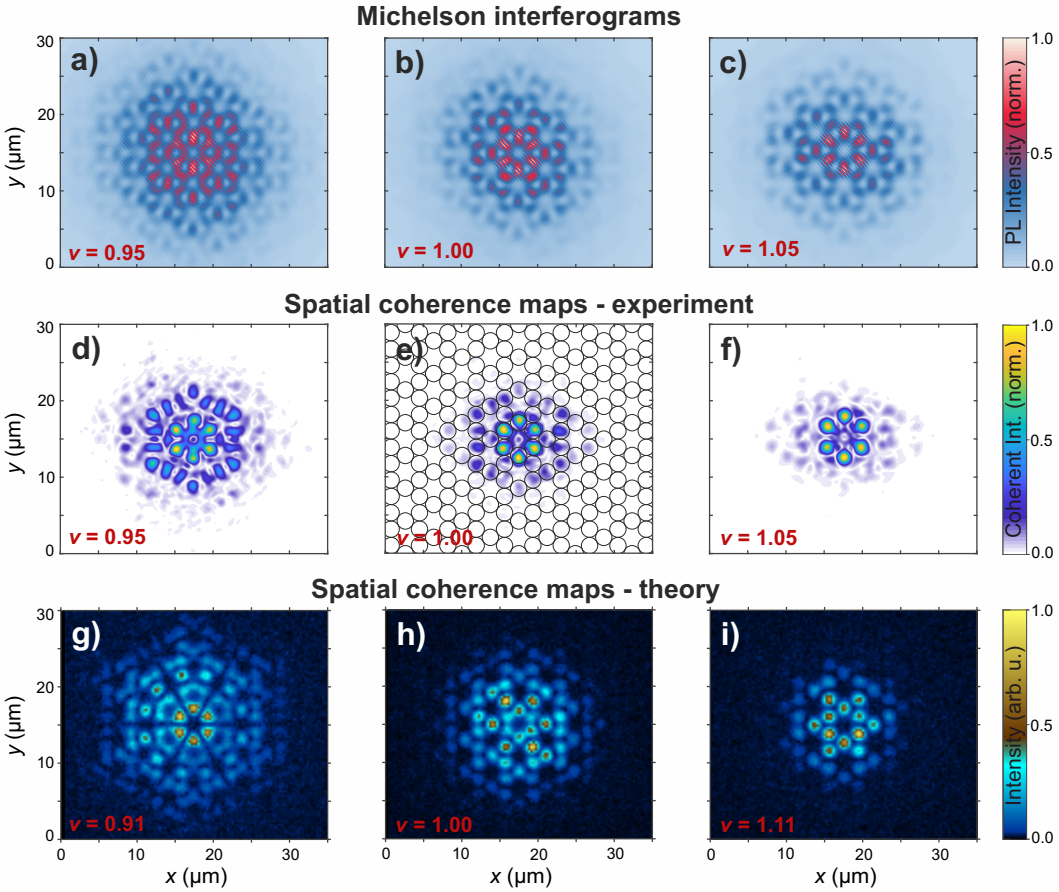

Figure 5.8: a)-c) Michelson interferograms of polariton condensates in the flatbands of Kagome lattices with trap diameters of $d = 2.0\,\mu\text{m}$ and reduced trap distances of $v = 0.95$, $v = 1.00$ and $v = 1.05$, respectively. **d)-f)** Corresponding spatial coherence maps obtained by two-dimensional Fourier transformation, selection of the coherent part and inverse Fourier transformation, where d) includes a schematic of the lattice geometry visualising the localisation to a CLS. **g)-i)** Corresponding spatial coherence profiles obtained from numerical simulations, adapted from reference [Har+21b].

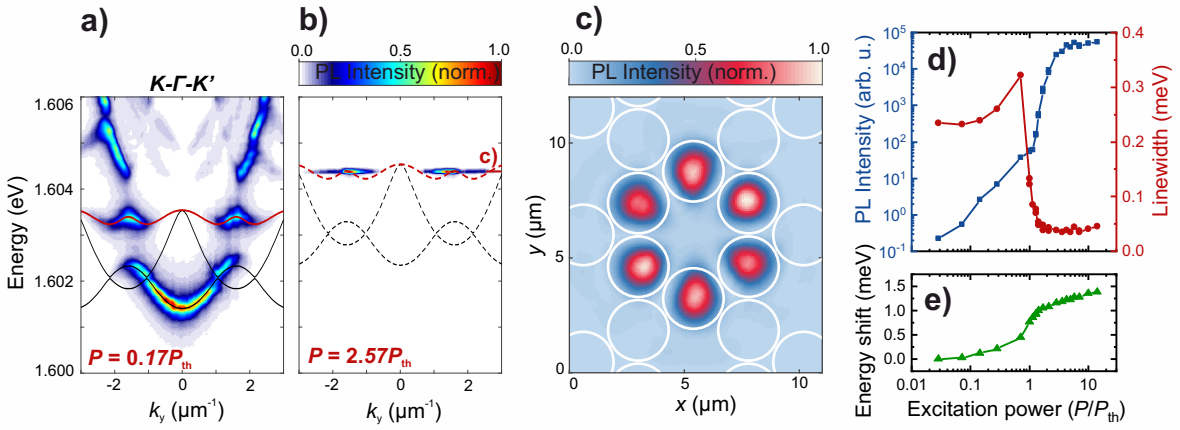

Figure 5.9: a)-b) Exemplary Fourier space spectra obtained on a Kagome lattice with trap diameters of $d = 2.0\,\mu\text{m}$ and a reduced trap distance of $v = 1.05$ by exciting with a small laser spot centred on a CLS at excitation powers below and above the polariton condensation threshold, respectively. **c)** Corresponding real space image of the CLS polariton condensate. **d)-e)** Input-output characteristics of the CLS polariton condensate.

Next, polariton condensation into a single CLS is realised by exciting a Kagome lattice with trap diameters of $d = 2.0\,\mu\text{m}$ and a reduced trap distance of $v = 1.05$ using a small, cw laser spot centred between the six lobes of the CLS. In Figs. 5.9 a) and b), Fourier space spectra below and above the condensation threshold of $P_{\text{th}} = 7.0\,\text{mW}$, respectively, are presented. In these spectra, in particular the very high degree of selectivity of condensation into the flatband should be emphasised. The real space image displayed adjacently in Fig. 5.9 c) confirms that the condensate features the characteristic mode pattern of a Kagome CLS. Again, the input-output characteristics plotted in Figs. 5.9 d) and e) confirm the formation of a polariton condensate, as the non-linear increase in emission intensity is accompanied by a decrease in linewidth as well as a continuous blueshift of the emission energy. Most notably, a linewidth of just 37 µeV, limited by the resolution of the spectrometer, was measured for the CLS polariton condensate.

Based on the excitation of a polariton condensate in a single CLS, the phase as well as the degree of first order temporal coherence, $g^{(1)}(\tau)$, can be investigated. To extract the phase pattern of the CLS polariton condensate, Mach-Zehnder interferometry in the configuration introduced in section 3.2.2 was performed. The interferometry patterns obtained by interfering a CLS condensate with a single, magnified lobe of the condensate that is used as a phase reference is displayed in Fig. 5.10 a). This fringe pattern was analysed using the same Fourier analysis method introduced above, by applying a two-dimensional Fourier transformation to the fringe pattern. From the transformed image, the coherent emission of the condensate is extracted and transformed back using an inverse Fourier transforma-

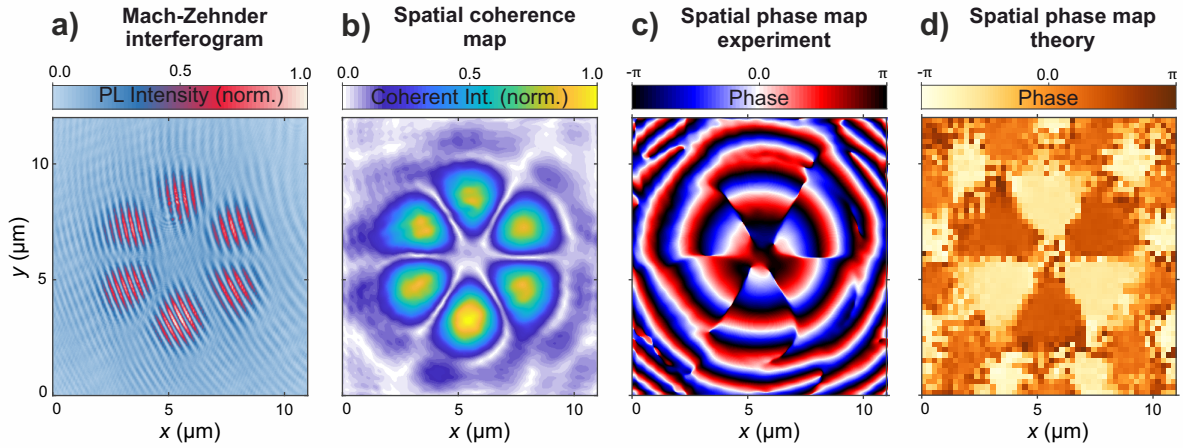

Figure 5.10: **a)** Mach-Zehnder interferogram of a CLS polariton condensate, obtained by interfering the emission of the CLS polariton condensate with the magnified image of one of the six lobes. After Fourier transforming, selecting the coherent part and inverse Fourier transforming, the real part of the image represents a map of coherence, presented in **b)**, while the imaginary part represents a phase map, presented in **c)**. **d)** Calculated spatial phase map, adapted from reference [Har+21b].

tion. The real part of the resulting image is displayed in Fig. 5.10 b) and represents a real space image of coherence that again highlights the localised nature of the CLS condensate. The imaginary part of the back-transformed image is presented in Fig. 5.10 c) and represents a spatial phase map. Here, a π phase shift between adjacent sites of the CLS condensate is revealed. This phase shift represents the origin of the localisation leading to the formation of the flatband, as it ensures destructive interference of polaritons on sites adjacent to the CLS. Again, the experimental result is confirmed by the numerical simulation presented in Fig. 5.10 d) [Har+21b]. These phase maps thus further highlight the capabilities of a polariton lattice simulator, as direct access to all quantities required to understand the physical mechanism occurring in such a lattice is granted.

Finally, the degree of first order temporal coherence, $g^{(1)}(\tau)$, is measured by exciting a CLS polariton condensate and moving the mirror in one arm of the Michelson interferometer to tune the delay between the two images that are superimposed on the camera. From the interferograms and the two individual images superimposed to generate the inferferogram, the coherence function $g^{(1)}$ can be evaluated from the fringe contrast using equation 3.2. In Fig. 5.11 a), an exemplary image of a Michelson interferogram of a CLS polariton condensate in a Kagome lattice with a reduced trap distance of $v = 1.05$ is depicted. A line spectrum extracted from the area marked by the black box in Fig. 5.11 a) including a fit of the fringe contrast based on equation 3.2 is presented in Fig. 5.11 b). In Fig. 5.11 c), the coherence function is plotted as a function of the delay between the two superimposed

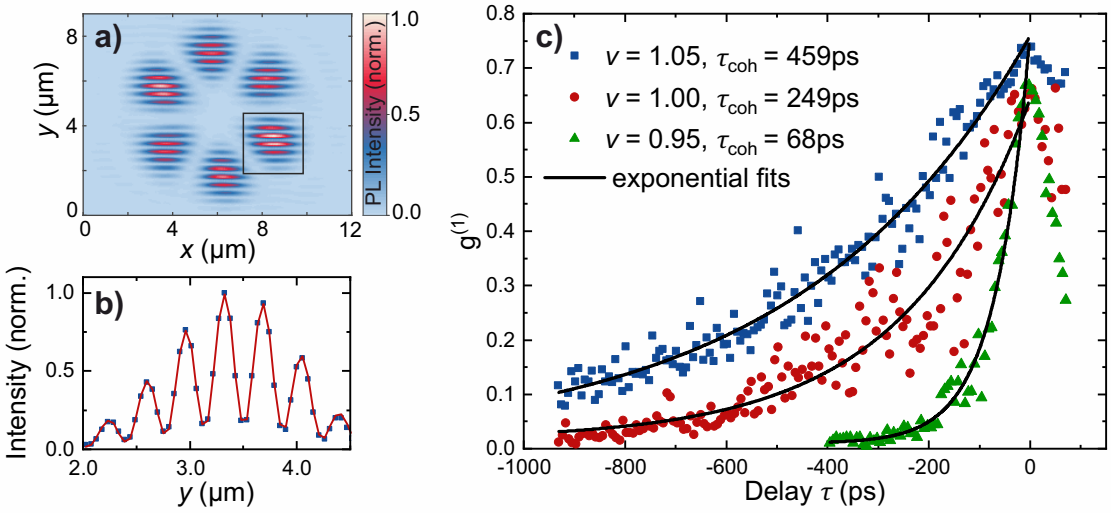

Figure 5.11: **a)** Exemplary Michelson interferogram of a CLS polariton condensate in a Kagome lattice with a reduced trap distance of $v = 1.05$. **b)** Line spectrum of the area marked with the black box in a) including a fit of the fringe contrast based on equation 3.2 and the individual two images that, when superimposed, create the interference pattern. **c)** Evaluation of the degree of first order temporal coherence $g^{(1)}$ as a function of delay, realised by moving one of the mirrors in a Michelson interferometer and extracting the fringe contrast from every interferogram.

images for Kagome lattices with trap diameters of $d = 2.0\,\mu\text{m}$ and reduced trap distances of $v = 0.95$, $v = 1.00$ and $v = 1.05$. For all three condensates, the decay of temporal coherence can be described accurately by an exponential function $g^{(1)}(\tau) \sim \exp(\tau/\tau_{\text{coh}})$, where the coherence time is denoted by τ_{coh}. This single-exponential decay is a good indicator for a single-mode condensate in which the coherence time is limited by intrinsic dephasing [Kim+16]. Most notably, the coherence time increases from $\tau_{\text{coh}} = (68 \pm 3)\,\text{ps}$ for a reduced trap distance of $v = 0.95$ to $\tau_{\text{coh}} = (249 \pm 18)\,\text{ps}$ for $v = 1.00$ and finally reaches $\tau_{\text{coh}} = (459 \pm 30)\,\text{ps}$ for $v = 1.05$.

This astonishingly high degree of first order temporal coherence is an important quantity for the quality of a laser that focusses on the properties of the emitted light. Complementary to the coherence time, knowledge of the second order temporal coherence function represents an important aspect focussing predominantly on the characteristics of the light source. Here, a value of $g^{(2)}(\tau = 0) = 1$ is anticipated for a laser, with any deviations towards the value of $g^{(2)}(0) = 2$ that characterises a thermal light source corresponding to deviations from a single-mode laser. Therefore, to complement the $g^{(1)}(\tau)$ measurements, Hanbury Brown-Twiss (HBT) interferometry, using the configuration introduced in section 3.2.2, was performed on polariton condensates in single CLSs of the same three Kagome lattices. Exemplary HBT correlation measurements performed on a Kagome

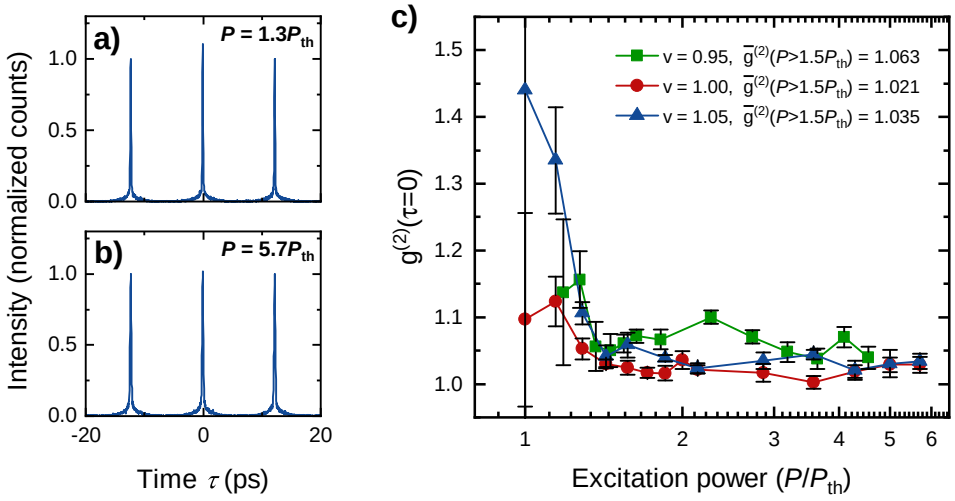

Figure 5.12: a)-b) Exemplary second order correlation measurements performed using a Hanbury Brown-Twiss interferometer at excitation powers of $P = 1.3P_{\mathrm{th}}$ and $P = 5.7P_{\mathrm{th}}$, respectively. **c)** $g^{(2)}(\tau = 0)$ evaluated from the correlation measurements and plotted as a function of the excitation power for CLS polariton condensates in Kagome lattices with reduced trap distances of $v = 0.95$, 1.00 and 1.05.

lattice with a reduced trap distance of $v = 1.05$ at excitation powers of $P = 1.3P_{\mathrm{th}}$ and $P = 5.7P_{\mathrm{th}}$ using the pulsed laser are presented in Fig. 5.12 a) and b), respectively. In these measurements, a timer is started when a first photon is detected in one of detectors and stopped by the detection of a photon by the second detector. By delaying the signal obtained by the second detector, the peak corresponding to photons that originate from the same laser pulse is centred in the detection time interval. Furthermore, photons originating from different laser pulses are uncorrelated and the corresponding peaks can thus be used to normalise the correlation measurement. The excitation power dependent second order temporal coherence function $g^{(2)}(0)$ that was evaluated from these correlation measurements is displayed in Fig. 5.12 c), including error bars derived from the standard deviation of the fluctuation of the peaks corresponding to photons generated during different laser pulses. The Corresponding input-output characteristics used to evaluate the threshold power P_{th} can be found in the appendix in Fig. A.7.

Close to the condensation threshold, the coherence time is smaller than the jitter of the detectors, resulting in a higher value of $g^{(2)}(0)$ that is commonly observed [Jin+94; Kim+16; Kla+18]. At higher excitation powers, however, the coherence of the polariton condensate builds up and the coherence function approaches the value of $g^{(2)} = 1$ expected for an ideal single-mode laser. By averaging the coherence function for excitation powers of $P > 1.5P_{\mathrm{th}}$, values of $\bar{g}^{(2)}(0) = 1.0628 \pm 0.0065$, 1.0210 ± 0.0029 and 1.0354 ± 0.0042

were evaluated for Kagome lattices with reduced trap distance of $v = 0.95$, 1.00 and 1.05, respectively. Again, the lasing properties of the polariton condensates are improved by reducing the dispersiveness of the flatbands, as a larger value of $\bar{g}^{(2)}(0)$ is observed for a lattice with $v = 0.95$. For the lattices with $v = 1.00$ and $v = 1.05$, the remaining differences between the values of $\bar{g}^{(2)}(0)$ can most likely be attributed to uncertainties of the measurement. Polariton condensates in single CLSs are highly susceptible to small deviations of the excitation conditions, in particular to changes in the position of the excitation laser. Without an active stabilisation of the position of the cryostat, $g^{(2)}(0)$ measurements of small polaritonic structures are not feasible at all [Adi+17]. However, even though the position of the cryostat was actively stabilised during the measurements presented here, the remaining small deviations of the position of the excitation spot can cause the observed fluctuations of the $\bar{g}^{(2)}(0)$ value. Nevertheless, the observed values of $\bar{g}^{(2)}(0)$ underline the excellent lasing properties of flatband condensates.

In summary, the localisation to a CLS in a Kagome flatband facilitated the observation of highly coherent polariton lasing with a coherence time of up to $\tau_{\mathrm{coh}} = (459 \pm 30)\,\mathrm{ps}$. This coherence time is particularly striking when compared to the values between 50 ps [Kim+16] and 150 ps [Lov+08] that are typically observed in literature for polaritonic systems under non-resonant excitation. In these high-quality microcavities, the exciton reservoir represents the prevailing limitation of the coherence time. Therefore, attempts on increasing the coherence time have focussed on avoiding an excitonic reservoir by implementing either an optical parametric oscillator configuration, resulting in a coherence time of approximately 500ps [Kri+06], or a spatial separation between the polariton condensate and the exciton reservoir through the use of an annulus pump spot. In the latter, a coherence time of up to 2.7 ns was achieved [Ask+19]. It is interesting to note that the configuration of a CLS polariton condensate excited with a small spot can be viewed as the inverse geometry to an annulus pump, as the highest reservoir density is located between the six lobes of the CLS condensate. Kagome flatbands thus combine the enhancement of the coherence time through the localisation and consequent reduction of the dispersiveness provided by the flatband with a separation of the exciton reservoir from the polariton condensate. The results presented in this section were published in reference [Har+21b].

5.4 Kagome vortex lattices and superfluid, chiral edge propagation

In the previous sections, polariton condensates in flatbands were established as a well-controlled platform that was used for an in-depth investigation of the influence of the localisation and the consequent vanishing dispersiveness on the lasing properties. In this section, the formation of vortices in these condensates is emphasised.
The formation of vortices is one of the most distinct properties of superfluids. Furthermore, the orbital angular momentum of light that can feature a vortex phase distribution is one of the key characteristics of any light emitter. It is therefore not surprising that research efforts were devoted to investigate the formation of vortices in photonic microcavities as well, in particular in the regime of polariton condensation that features superfluid properties. These efforts have resulted in the demonstration of chiral lasing emission [Car+19; Ma+20b] as well as the formation of ordered vortex patterns in lattice potential environments [Tos+12a; Gao+18] and optically induced potential landscapes [Bou+16; Pan+21]. In Kagome lattices, the formation of vortex lattices was particularly emphasised in theoretical work, where the effect of spontaneous symmetry breaking between two possible vortex lattice orientations was predicted to lead to superfluid, chiral edge transport [Bar+16; SLL17]. Comparably, a link between an interaction driven, spontaneous symmetry breaking and a quantum anomalous Hall phase was predicted for electronic systems [Zhu+16].
The starting point of the investigations presented here is a polariton condensate that was excited with an enlarged, cw, Gaussian laser spot in the flatband of a Kagome lattice on sample Ga-EnO1 characterised by trap diameters of $d = 2.0\,\mu m$ and a reduced trap distance of $v = 1.00$. In Fig. 5.13 a), a Mach-Zehnder interferogram of such a condensate, obtained by enlarging one trap in one of the arms of the interferometer to cover the entire condensate when superimposed with the image of the second arm, is presented. In this configuration, the enlarged image of one trap serves as a constant phase reference, thus allowing to study the phase profile and in particular the presence of vortices. The schematic representation of the excitation geometry displayed in Fig. 5.13 b) highlights that the excitation intensity is reasonably homogeneous across the analysed condensate area marked by the black box. Kagome lattices feature three sites in the unit cell surrounding a small hole. In Figs. 5.13 c)-h), the phase profiles at the centre of the six threefold trap groups marked in Fig. 5.13 a) are presented. In each group, a vortex with a charge of $m = \pm 1$ is found. The vortex charges alternate between adjacent groups and compensate each other. Therefore, no vortex is observed in the phase pattern of the centre of the large hole between the six groups presented in Fig. 5.13 i). This vortex lattice

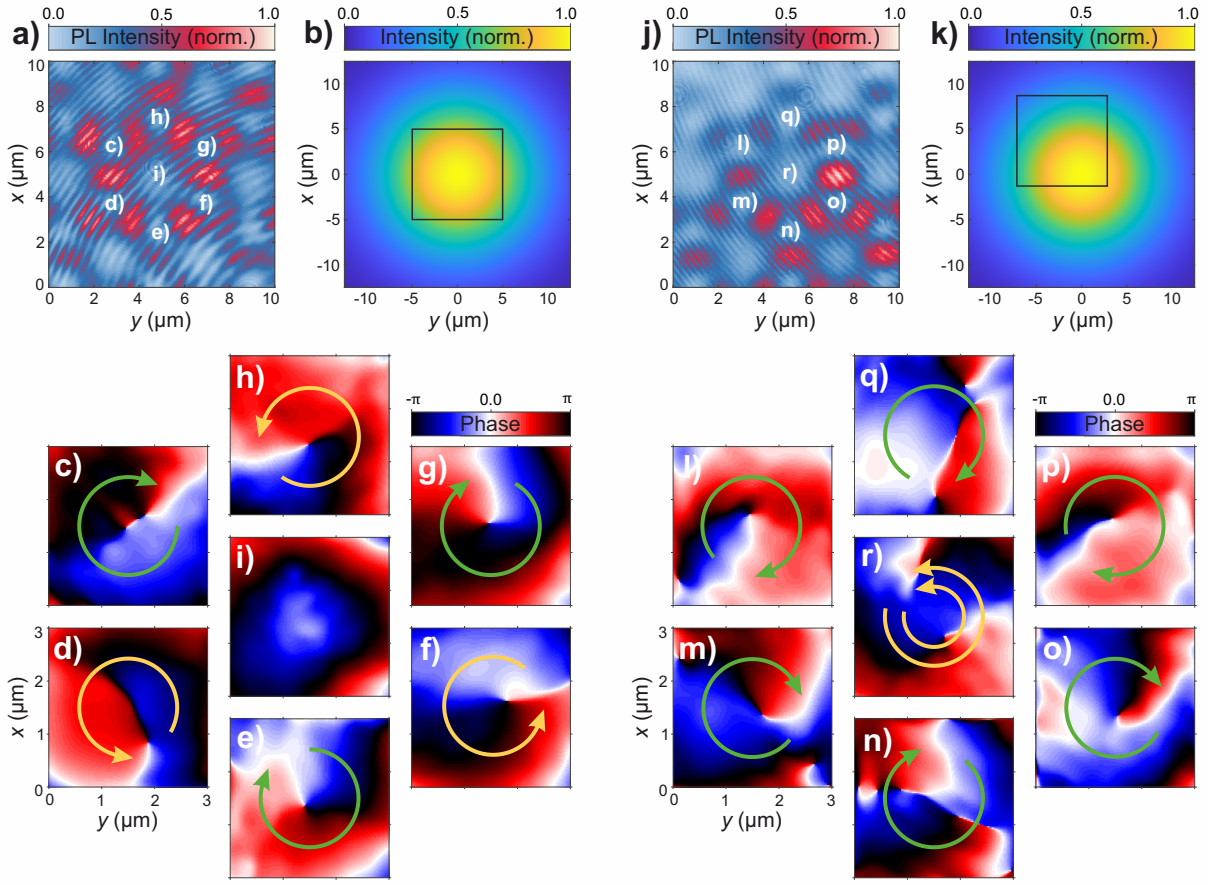

Figure 5.13: **a)** Mach-Zehnder interferogram of a polariton condensate in a Kagome flatband excited with an enlarged, Gaussian laser spot. **b)** Schematic visualising the position of the interferogram in a) with respect to the excitation spot. **c)-h)** Phase maps evaluated from the interferogram at the centre of the six unit cells that are marked in a). The yellow and green arrows highlight the vortex orientations. **i)** Phase map at the centre of the six unit cells. **j)-r)** Corresponding analysis performed at a position with an offset to the centre of the excitation spot.

was found to be stable with respect to switching the excitation on and off as well as changing the excitation power. The observed configuration thus appears to be energetically favourable compared to the opposite orientation due to small imperfections in the potential landscape. When exciting a polariton condensate with an enlarged laser spot covering a CLS and the surrounding sites, the high polariton densities result in outward radial flow of the polariton superfluid. This flow is guided by the potential landscape of the Kagome lattice, plausibly resulting in the observed vortex lattices. Furthermore, the investigation of the phase profile at a position that is offset with respect to the centre of the excitation spot and thus features a larger intensity gradient revealed an entirely different vortex lattice. The Mach-Zehnder interferogram that was analysed as well as a schematic highlighting the location with respect to the excitation spot are presented in Figs. 5.13 j) and k). Again, an analysis of the vortices in six adjacent trap groups was performed and six vortices with aligned orientation were found in the phase patterns presented in Figs. 5.13 l)-q). To ensure that no overall vortex charge remains, an opposite vortex with a charge of $|m| = 2$ is expected at the centre between the six unit cells. Indeed, this vortex can be observed in the phase pattern depicted in Fig. 5.13 r). It should be mentioned that this phase configuration appears to be considerably less stable, as it was only observed in a specific excitation configuration. Nevertheless, this vortex lattice provokes interest for further investigations, as the vortex charges do not compensate each other at the lattice edge. Sigurdsson and co-workers therefore predicted that spontaneous symmetry breaking should lead to the manifestation of one of the two orientations of this vortex configuration, which should result in chiral transport of the polariton superfluid at the lattice edge [SLL17].

Motivated by this prediction, polariton condensates were excited at the edge of the Kagome lattice using a small, cw laser spot. In Figs. 5.14 a)-c), real space spectra along the lattice edge at excitation powers of $P \approx 0.03 P_{\mathrm{th}}$, $P \approx 1.25 P_{\mathrm{th}}$ and $P \approx 7.50 P_{\mathrm{th}}$, respectively, are presented. While the spectrum is symmetric below the condensation threshold, uni-directional propagation is clearly observed at excitation powers above the threshold. In particular the condensate at the lowest energy, corresponding to the S band of the lattice, propagates over a distance of nearly 25 µm, as is confirmed by the real space image at the energy of this condensate that is presented in Fig. 5.14 d), corresponding to an excitation power of $P \approx 5.00 P_{\mathrm{th}}$. For this measurement, the excitation laser was aligned with one site of the lattice edge, as is schematically depicted by the red dot in Fig. 5.14 e). In Figs. 5.14 f)-i), corresponding measurements under the excitation of the adjacent trap are presented. Interestingly, uni-directional transport in the opposite direction is observed. To understand this effect, it is important to note that two adjacent sites at the lattice edge of a Kagome lattice are not equivalent. On the contrary, the

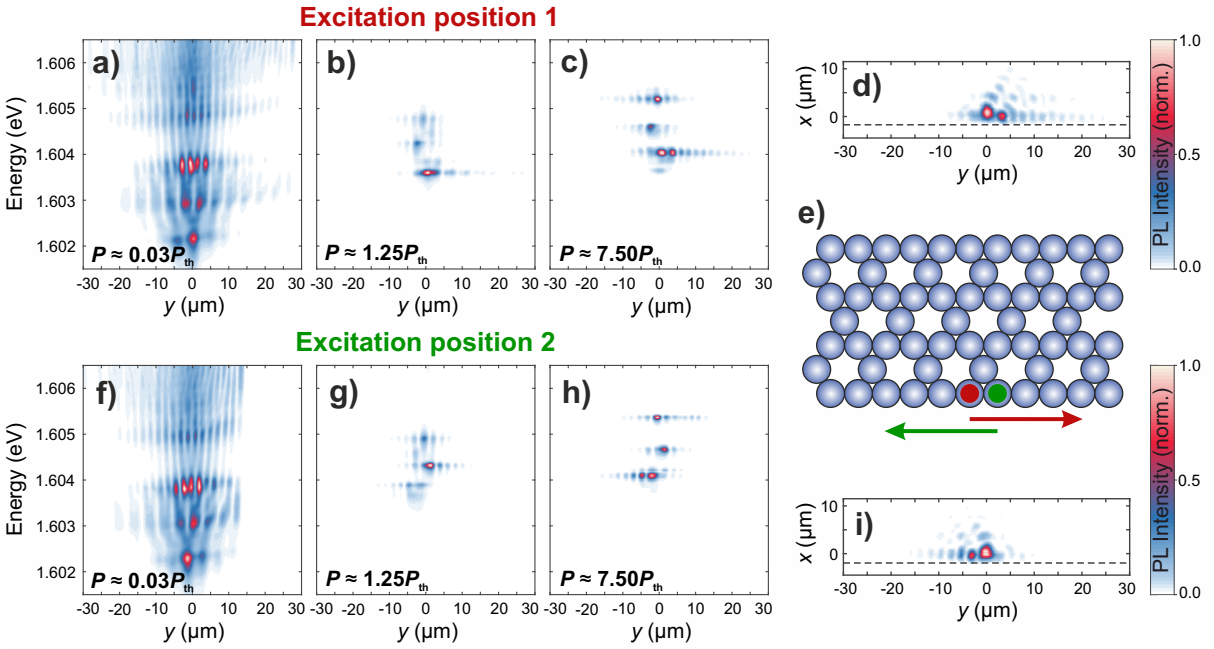

Figure 5.14: **a)-c)** Real space spectra along the edge of a Kagome lattice under the excitation with a small spot at excitation powers of $P \approx 0.03P_{\mathrm{th}}$, $P \approx 1.25P_{\mathrm{th}}$ and $P \approx 7.50P_{\mathrm{th}}$, respectively. The position of the excitation spot is marked by the red dot in e). **d)** Real space image at the energy of the lowest condensate at an excitation power of $P \approx 5.00P_{\mathrm{th}}$. The dashed line marks the lattice edge **e)** Schematic visualising the excitation configuration. **f)-i)** Corresponding dataset obtained by exciting an adjacent lattice site, marked by the green dot in e).

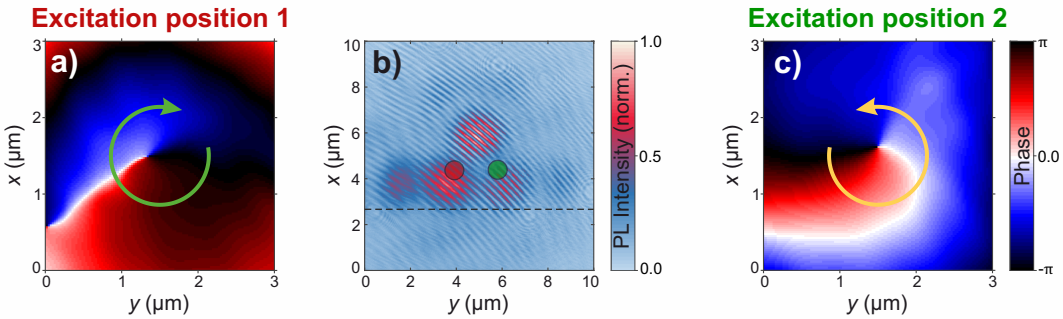

Figure 5.15: a) Phase pattern of a unit cell at the lattice edge under the excitation of the site marked by the red dot in b). The green arrow highlights the vortex orientation. **b)** Corresponding Mach-Zehnder interferogram. The dashed line highlights the lattice edge. **c)** Phase pattern of the same unit cell under excitation at the position of the adjacent trap, marked by the green dot in b).

third site of the unit cell, located one row further towards the bulk of the lattice, provides an additional propagation option and thus biases the potential environment towards one direction. One can thus envision that this asymmetry in the potential environment causes the polariton condensate to propagate in one direction only.

To relate the uni-directional transport observed here to the theoretical work in reference [SLL17], the phase of the vortex in the unit cell of the site that was excited was measured. In Fig. 5.15 b), a Mach-Zehnder interferogram of this unit cell under the excitation with a small laser spot at the position marked by the red dot is presented. In Figs. 5.15 a) and c), the phase patterns of the unit cell for the excitation of a polariton condensate at the position of the red and green dots, respectively, are presented. Indeed, the orientation of the vortex changes with respect to the position of the excitation spot and thus with the change of the propagation direction of the condensate. In conclusion, the peculiar phenomenon of uni-directional edge transport that was observed here can most likely be explained by the influence of the intrinsic asymmetry of the potential landscape of a Kagome lattice on the superfluid flow. In previous theoretical works such as reference [SLL17], a large condensate that forms a vortex lattice was investigated and the symmetry breaking was achieved by a small perturbation of this large condensate. While the excitation with a small spot that was performed here leads to uni-directional edge transport and a change in the vortex orientation at the edge as well, the connection to these theoretical results remains to be investigated. These results thus motivate further studies of polariton condensates in Kagome lattices in particular as well as the propagation of polariton condensates in lattice potential environments in general. The theoretical explanation of the results presented in this section is part of the ongoing process in preparation for publication.

6 Topological polaritons and topological lasing

The discovery of the quantum Hall effect in 1980 [KDP80] started the development of topology as a new fundamental concept in solid-state physics at the base of the rapidly evolving research field of topological insulators that was introduced in section 2.4. Another milestone followed in 2008, when Haldane and Raghu realised that the idea of topological classification and the associated observable effects are not limited to fermionic electrons but apply to bosons as well [HR08; RH08]. Based on the ideas of thinking of topology as a broader concept and using lattice potentials to generate band gaps and edge modes as observables for topologically non-trivial modes, implementations with ultra-cold atoms were developed [Ata+13; Jot+14]. A more elaborate review of the following development of this field that for example found paths towards directly observing the anomalous velocity caused by the Berry phase [Aid+15] can be found in literature [CDS19].
In the further progress of the field, it was realised that one implication of Haldane's and Raghu's work [HR08] is that the concept of topology cannot only be transferred from electrons to bosons, but that it does not even require the underlying states to have a quantum nature. On the contrary, a topological classification and the creation of topologically non-trivial states, including the well-known observables such as robust edge transport, can be realised based on classical waves and their interference. With this understanding in mind, topology spread across an even broader range of platforms and research fields, including mechanical systems [Nas+15; SH15; Hub16], acoustics and phonons [Yan+15; MKW15; Kha+15], electronic surface states [Dro+17], electric circuit networks [AGJ15; Nin+15; Lee+18; Imh+18; Hel+19; Hof+19] and even a description of equatorial waves in the Earth's atmosphere and oceans [DMV17]. One of the most important and versatile platforms based on artificial, topologically non-trivial lattices that has evolved in recent years is photonics. Here, the traditional degrees of freedom that were available to study light, such as frequency, amplitude, phase, wave vector and polarisation, were extended by topology as a new pathway towards controlling the propagation of light. Up to now, a significant range of the electromagnetic spectrum, from radio frequency [Yve+17; Slo+17a] over microwaves [Wan+08; Wan+09] to the infrared

and visible [Haf+11; Rec+13a; Haf+13], was covered and experimental platforms were developed. The following short overview of topological photonics is based on recent reviews of the field [LJS14; LJS16; KS17b; MDH18; Oza+19].

Analogously to the development of topological insulators that started with quantum Hall states based on broken time-reversal symmetry and then evolved to quantum spin Hall states characterised by time-reversal invariance, photonic topological systems can be classified into systems with broken and preserved time-reversal symmetry. Intuitively following the mechanism of the quantum Hall effect for electrons, magneto-optic photonic crystals in which time-reversal symmetry can be broken with an external magnetic field were considered [RH08] and implemented [Wan+09]. However, while this approach is well suited for the microwave regime, an extension to optical frequencies was hindered by the lack of magneto-optic materials in this frequency range. Therefore, time-reversal preserving approaches based on breaking either a field symmetry for a pseudospin or a spatial symmetry of a lattice were developed to open topologically non-trivial band gaps in photonic lattices. It is important to note, however, that in contrast to the spin of an electron, polarisation is not a protected spin and thus backscattering into a state of opposite polarisation is possible in the presence of for example TE-TM splitting. Therefore, systems that introduce a non-trivial topology by inducing a polarisation chirality are not rigorously topologically protected against backscattering. Nevertheless, topology was successfully brought to the realms of optics in time-reversal invariant systems based on silicon photonics operating in the infrared [Haf+11; Haf+13; Mit+14; Mit+16] and microwave metamaterials [Kha+13; Che+14b].

A complementary approach of combining topology and optics is based on Floquet's theorem [Flo83], which can be understood as an analogon of Bloch's theorem for Hamiltonians that are not periodic in space but in time. Such a Hamiltonian is consequently not characterised by a periodic band structure in momentum but rather by a periodic energy structure. Common approaches towards experimentally realising Floquet Hamiltonians involve either a periodic excitation or a projection of time onto a propagation axis with a periodic design. In particular in the latter, it is important to notice that breaking time reversal symmetry is translated into breaking inversion symmetry of the propagation axes and can thus be achieved without external magnetic fields. Photonic implementations of Floquet physics are based on coupled waveguides [Sza+06; Del+07; SN10] and topologically non-trivial structures were proposed [OA09; LRG11; FYF12; Rud+13] and realised experimentally [Rec+13a; Plo+14; Mac+17; Muk+17] by several groups. Recently, this approach even facilitated the implementation of a photonic topological insulator in the $\mathbb{Z}_2$ class [Mac+20a]. Building on the success of photonic Floquet systems, similar Hamiltonians were implemented for ultra-cold atoms [Flä+16] and acoustics [FKA16] as well.

In section 2.4.3, the particular importance of the honeycomb lattice in the development of topological physics was highlighted and several approaches to open topologically non-trivial band gaps at the Dirac points were introduced. As these approaches do not rely on electrons subject to the Kramers degeneracy as the underlying eigenstates, photonic topological honeycomb lattice implementations creating a topological band gap were developed as well. Over the past years, several approaches such as a valley Hall effect [MS16; Don+17; Noh+18a; Sha+19] based on different eigenenergies of the two sites of the lattice unit cell, a spin Hall effect [Kha+13] based on different effective fields for pseudospin components and band gaps based on breaking spatial symmetries [WH15; Yve+17; Noh+18a; Bar+18; Gor+18] have been implemented.

One of the key motivations driving the development of topological photonics is the vision of ground-breaking technological applications such as optical delay lines, light propagation in waveguides that are topologically protected against backscattering and non-reciprocal devices. Another potential application that is particularly relevant to this work is topological lasing [Bah+17; Ban+18; Har+18], which could provide an entirely new approach towards improving the lasing characteristics of an individual laser as well as coupling multiple individual lasers to one coherent and single-mode laser based on the propagation of a topologically protected mode. Furthermore, over the recent years the inherent ability to add gain, loss and non-linear effects to artificial lattice simulators has evolved to a major stronghold of the field providing access to non-Hermitian and non-linear topological physics [Ota+20; Smi+20; Hel+20; Mac+20b].

The work presented in this chapter is focussed on the combination of polaritonics and topological physics. The motivation for this combination is twofold: Firstly, the inherent gain and loss in combination with the ability of polaritons to interact with each other opens up a path towards studying non-Hermitian and non-linear topological effects in a lattice simulator environment from a fundamental perspective. Secondly, the individual pillars forming a polariton lattice can be understood as vertically emitting lasers, thus representing an array of coupled VCSELs in which the influence of topology on the coupling of these lasers can be studied. Despite the mature technological control, coherent coupling of extended arrays of VCSELs remains a major contemporary challenge. In section 6.1, the first demonstration of a two-dimensional, polariton topological insulator is presented. In the following section 6.2, the convincingly simple and well understood one-dimensional SSH model is implemented in a chain of polariton microtraps to study the lasing properties of a topological mode in detail. Finally, in section 6.3, the first implementation of a two-dimensional topological insulator array of VCSELs, in which non-trivial topology is achieved through geometric symmetry breaking rather than a magnetic field, is presented.

6.1 Exciton-polariton topological insulator

The recent development of photonics has been inspired by the concept of topology that provides an entirely new degree of freedom to control the propagation of light. Here, polaritonics offers the potential of taking topological photonics beyond the linear regime by strongly coupling photons to excitons and thus implementing inter-particle interaction. The first demonstration of a polaritonic system with non-trivial topology was a one-dimensional SSH chain of coupled micropillars that features a zero-dimensional, topological defect and was realised by St-Jean and co-workers in 2017 [St-+17]. However, such an inherently localised defect cannot propagate, thus motivating the implementation of a two-dimensional, topological lattice simulator with one-dimensional edge modes. The intuitive starting point for the development of such a simulator is the honeycomb lattice, as it is well established for polaritons [Jac+14; Mil+15; Mil+17] and, as introduced in section 2.4.3, offers multiple approaches towards opening a topologically non-trivial band gap. Based on these general ideas, specific proposals for a polariton topological insulator were developed [Kar+15; Bar+15; NSM15].

To understand the idea of these proposals, it is worthwhile to remember that polaritons consist of two components, namely excitons and photons. Therefore, to open a topologically non-trivial band gap, symmetries need to be broken for both components. For the photonic component that forms the honeycomb band structure, the proposals follow the ideas of Kane and Mele [KM05a; KM05b] on the quantum spin Hall effect emerging due to spin-orbit interaction in graphene. In microcavities, a splitting between the polarisations and thus the pseudospin components can be obtained by an energetic offset between the cavity resonance and the stopband centre of the DBRs that results in TE-TM splitting. This splitting leads to an optical spin Hall effect [KMG05] and can be described by an artificial gauge field resembling the Rashba field used to describe spin-orbit interaction in electronic systems [Nal+15; Sal+15]. Whereas in atomic graphene, the topological gap is limited to approximately 10 µeV as it is induced by the effect of the spin-orbit interaction of carbon of approximately 4 meV on the coupling between next-nearest rather than nearest neighbours [Min+06; Yao+07], polaritonic graphene is artificially engineered and the energetic splitting is tuneable by adjusting the TE-TM splitting. For the excitonic component of the polaritonic eigenstates, time reversal symmetry is broken by an external magnetic field resulting in a Zeeman splitting of the quantum well resonance [Kot+01; Rah+11]. The overall polaritonic honeycomb lattice with TE-TM and Zeeman splitting thus features a broken time reversal symmetry placing it in the $\mathbb{Z}$ topological insulator class that features chiral edge modes. It should additionally be noted that the combination of TE-TM and Zeeman splitting on its own renders any polaritonic band, including in par-

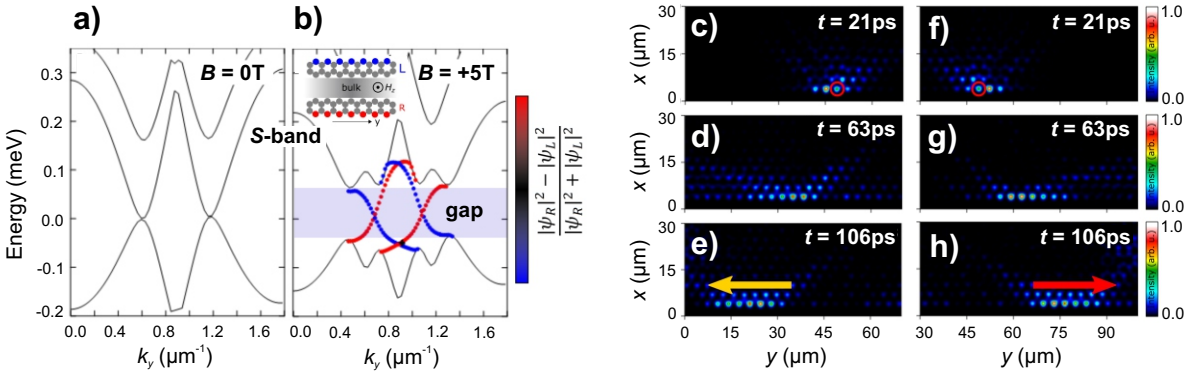

Figure 6.1: Band structure calculation for a polariton honeycomb lattice with TE-TM splitting and an external magnetic field of $B = 0\,\mathrm{T}$ in **a)** and $B = 5\,\mathrm{T}$ in **b)**. The edge states that appear in the topological band gap are marked in red and blue, corresponding to the front and rear edges of the lattice. The propagation dynamics of these edge modes at $B = -5\,\mathrm{T}$ and $B = 5\,\mathrm{T}$ are presented in **c)-e)** and **f)-h)**, respectively. This figure was adapted from reference [Kle+18].

ticular a planar cavity dispersion, topologically non-trivial [Ble+18; Gia+20]. However, a honeycomb lattice potential provides easier access to observables, such as a topological band gap and edge states, and potentially allows to control polariton propagation within such an edge mode. The work presented here closely follows the proposal by Nalitov and co-workers [NSM15], was started during my Master's project and finalised during the PhD project.

In Figs. 6.1 a) and b), calculated dispersion relations of a polariton honeycomb lattice along the K-Γ-K' direction at external magnetic fields of $B = 0\,\mathrm{T}$ and $B = 5\,\mathrm{T}$, respectively, and including TE-TM splitting are presented. Introducing TE-TM splitting to the honeycomb lattice results in a non-zero effective mass at the Dirac points, but only in the presence of an additional external magnetic field, a topological band gap opens. Within the gap, edge states marked in red and blue, corresponding to the front and rear side of the lattice, arise. In Figs. 6.1 c)-e) and f)-h), numerical simulations of the dynamics of a polariton wave package that is injected into one of these edge states at $B = -5\,\mathrm{T}$ and $B = 5\,\mathrm{T}$, respectively, are presented. Here, the chirality of the topological mode becomes unambiguous. Furthermore, the propagation direction is flipped under the inversion of the magnetic field. The topological nature of this mode becomes apparent in its protection against scattering at defects or at the corners of the lattice. Further details on the theoretical modelling that was performed by Dr. Oleg Egorov can be found in reference [Kle+18].

The key parameter for the sample optimisation towards a polariton topological insulator is the size of the expected band gap with respect to the linewidth of the polaritonic

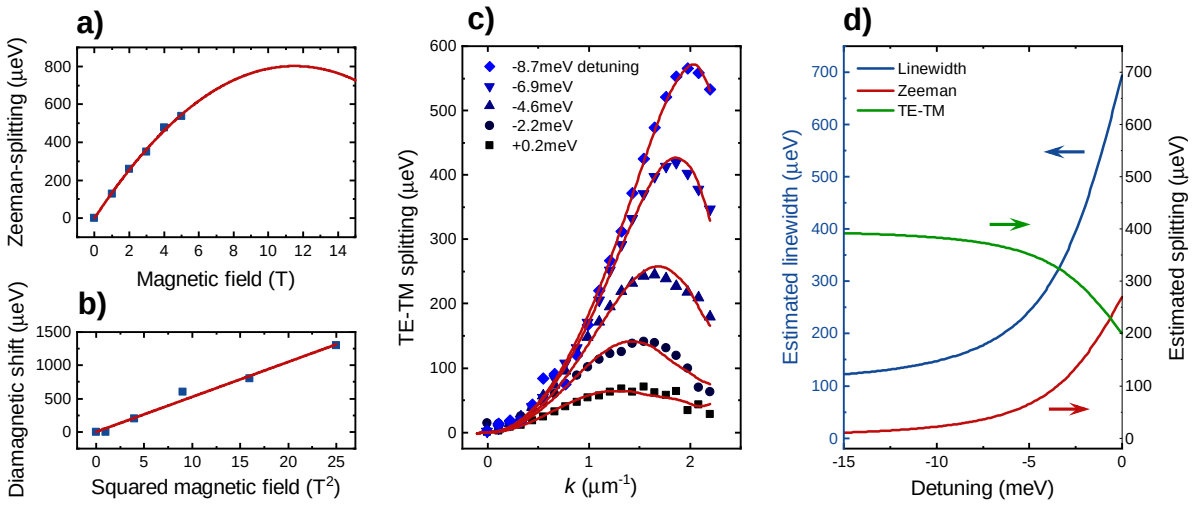

Figure 6.2: Summary of the key parameter optimisations of sample In-HE1. **a)** Zeeman splitting including an extrapolated, second order polynomial fit. **b)** Diamagnetic shift including a fit based on equation 2.16. **c)** TE-TM splitting for various exciton-photon detunings including fits based on equation 2.14 multiplied with the Hopfield coefficients. **d)** Expected polariton linewidths as well as Zeeman and TE-TM splitting as functions of the detuning, estimated using the data presented in a) and c) as well as the Hopfield coefficients.

eigenmodes. To increase this parameter, several optimisations in the fabrication of the underlying polaritonic microcavities were performed. A summary of the relevant parameters of sample In-HE1, which was selected for the experiments presented in this section, is presented in Fig. 6.2. Firstly, for the quantum wells, a large Zeeman splitting in combination with a narrow linewidth is desirable. To increase the Zeeman splitting, indium is introduced into the quantum wells to increase the effective exciton g-factor. In previous works in the research group, an optimal Zeeman splitting to linewidth ratio was determined for quantum wells with $In_{0.04}Ga_{0.96}As$ composition. It is furthermore important to note that, due to different g-factors and magnetic field dependencies of the electron and the hole that constitute an exciton, the Zeeman splitting does not scale linearly with increasing magnetic field and can even return to zero when the g-factors of electron and hole compensate each other. The Zeeman-splitting obtained for the excitons in sample In-HE1, including an extrapolated second order polynomial fit visualising the non-linear dependency on the magnetic field, is presented in Fig. 6.2 a). Secondly, the TE-TM splitting is increased by increasing the offset between the cavity resonance and the stopband centre of the DBRs. However, the reflectivity of the DBRs decreases towards the edge of the stopband, thus reducing the quality factor of the cavity resonance and increasing its linewidth. Additionally, the TE-TM splitting increases with higher emission angles and therefore for polariton states with higher wave vectors. Hence, the use of lattices with

smaller lattice constants, achieved by using smaller micropillars with large overlaps, in which the Dirac points are located at higher wave vectors, is preferable. Based on this consideration, honeycomb lattices with pillar diameters of $d = 2.0\,\mu m$ and a reduced trap distance of $v = 0.85$ were processed using the half-etching technique that was introduced in section 3.1.2. The experimentally obtained TE-TM splittings for a range of detunings that are presented in Fig. 6.2 are well described by equation 2.14, multiplied with the photonic Hopfield coefficients. In a realistic scenario, the TE-TM splitting is larger than the Zeeman splitting, leaving the Zeeman splitting as the limiting factor for the size of the expected band gap. Lastly, both the Zeeman and the TE-TM splitting can, in a first approximation, be scaled by the Hopfield coefficient for the excitonic and photonic components, respectively, for a given polaritonic state, resulting in the estimated splittings and linewidths that are presented in Fig. 6.2 d). In this graph it becomes apparent that, while the Zeeman splitting can be increased by selecting a device at a more excitonic detuning, the linewidth increases as well due to the larger linewidth of the exciton compared to the photon. As the linewidth scales with the excitonic Hopfield coefficient as well, the ratio between the expected Zeeman splitting and the polaritonic linewidth does not improve. Therefore, a lattice at a moderately negative detuning of $\Delta_E = -11.5\,meV$, corresponding to Hopfield coefficients of $|C|^2 = 0.96$ and $|X|^2 = 0.04$, where the band structure is clearly observable, was selected for the following experiments.

Ideally, to investigate the transition from a gapless graphene band structure without an external magnetic field to a gapped, topologically non-trivial band structure under the influence of a magnetic field, one would like to observe the opening of a band gap in Fourier space. In Figs. 6.3 a)-c), Fourier space spectra along the high-symmetry direction *K*-Γ-*K'* at low excitation powers and external magnetic fields of $B = -5\,T$, $0\,T$ and $5\,T$, respectively, of the selected lattice are presented. While a band gap is predicted to open in the theoretical calculation, provided by Dr. Oleg Egorov, that is based on the actual sample parameters and is plotted as dashed lines in Figs. 6.3 a)-c), no clear evidence of a topological gap is observed. However, this predicted band gap is small compared to the polariton linewidth. Furthermore, based on the TE-TM splitting of $\Delta_{TE\text{-}TM} = 400\,\mu eV$ of the planar cavity at a wave vector corresponding to the Dirac cones of the lattice, a TE-TM splitting of $\Delta^P_{TE\text{-}TM} \approx 384\,\mu eV$ is expected for polaritons at the wave vector and energy of the Dirac cones. Analogously, the Zeeman splitting of the quantum wells of $\Delta_Z = 540\,\mu eV$ translates into a Zeeman-splitting of $\Delta^P_Z \approx 22\,\mu eV$ for the polaritons at the Dirac point. It is therefore not surprising that, even though the spectra reveal some indication of a changes to the band structure at the Dirac cones, a band gap cannot be observed unambiguously in the linear regime in Fourier space. Additionally, as a large area of the lattice was illuminated, fluctuations of the potential environment across the

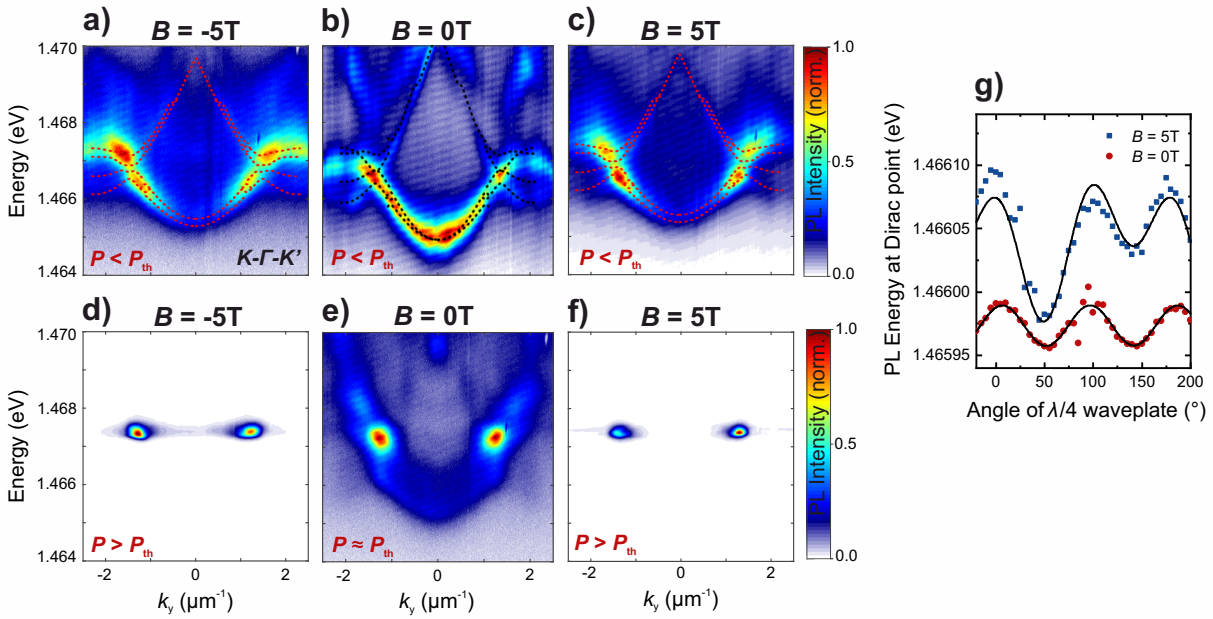

Figure 6.3: **a)-c)** Fourier space spectra along the K-Γ-K' direction for external magnetic fields of $B = -5\,\mathrm{T}$, $0\,\mathrm{T}$ and $5\,\mathrm{T}$, respectively, at excitation powers in the linear regime. The data is reproduced by the dispersion relations obtained from theory that are plotted in dotted lines. **d)-f)** Corresponding Fourier space spectra for excitation powers above the condensation threshold. **g)** Energetic position of the PL intensity maximum at the Dirac point with respect to the circular polarisation.

lattice further decrease the visibility of a band gap. However, as the states below and above the gap feature opposite circular polarisations, tracking the energetic position of the intensity maximum at the Dirac point with respect to the angle of a $\lambda/4$ waveplate in the detection path, as is depicted in Fig. 6.3 g), allows to estimate a gap of $E_\mathrm{g} \approx 108 \pm 32\,\mu\mathrm{eV}$. Motivated by the decrease in linewidth at the threshold of polariton condensation, further measurements of Fourier space dispersions were obtained above the condensation threshold. The resulting dispersion relations are presented in Figs. 6.3 d)-f). While the linewidth has narrowed, a clear observation of a gap mode is hindered by a combination of the remaining linewidth and a non-vanishing spatial inhomogeneity across the lattice. However, a clearly observable band gap is not the only characteristic observable of a topologically non-trivial state, as the most prominent feature are protected edge states. Therefore, real space tomographies were obtained above the polariton condensation threshold. A microscope image of the lattice area that was excited using a Gaussian, pulsed laser spot with a diameter of approximately $40\,\mu\mathrm{m}$ is presented in Fig. 6.4 g). In Figs. 6.4 a)-c), real space spectra perpendicular to the lattice edge that were recorded for external magnetic fields of $B = 0\,\mathrm{T}$, $-5\,\mathrm{T}$ and $5\,\mathrm{T}$, respectively, are presented. In all three spectra, a polariton condensate in the bulk S band is observed. The real space images at the

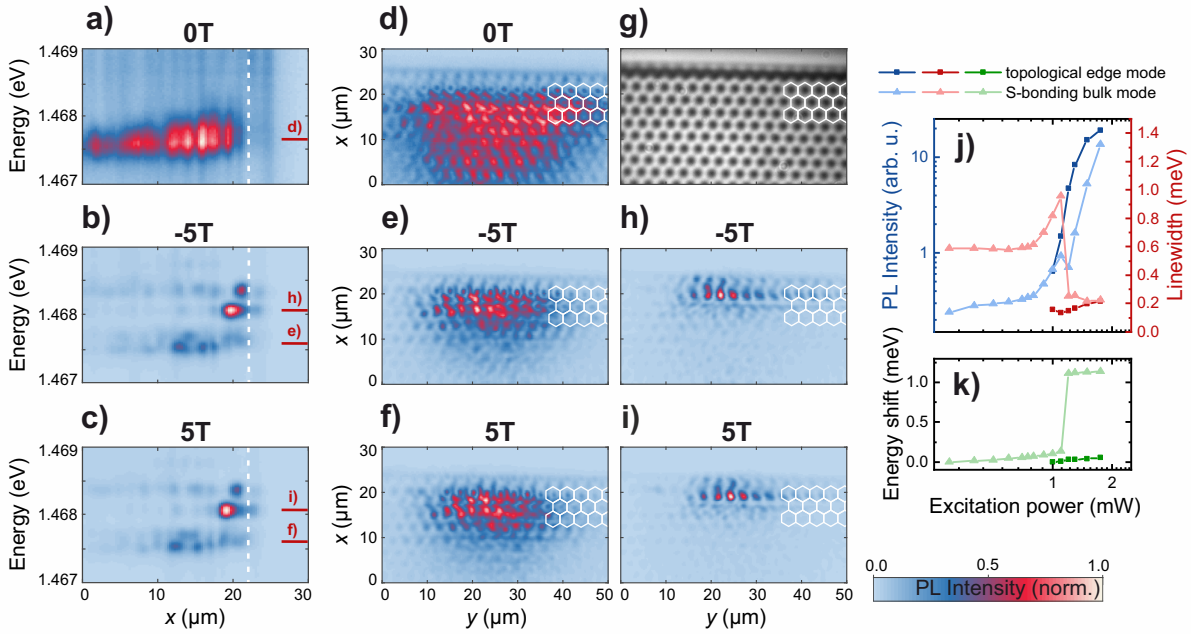

Figure 6.4: **a)-c)** Real space spectra perpendicular to the zigzag lattice edge for external magnetic fields of $B = 0\,\mathrm{T}$, $-5\,\mathrm{T}$ and $5\,\mathrm{T}$, respectively, obtained at excitation powers above the condensation threshold. The white dashed lines mark the edge of the lattice. **d)-f)** Real space images at the energy of the bulk condensates. **g)** Microscope image of the zigzag edge. **h),i)** Real space images at the energy of the topological edge mode. **j)**, **k)** Input-output characteristics of the bulk condensate (light colours) as well as the topological edge mode (dark colours).

energy of these bulk condensates that are displayed in Figs. 6.4 d)-f) further visualise, that the condensates stretch over a large bulk lattice area. Additionally to the bulk condensates, in the spectra in Figs. 6.4 b) and c) corresponding to measurements at magnetic fields, an additional mode that is localised to the lattice edge is observed above the bulk condensates. The real space images at the energy of this mode presented in Figs. 6.4 h) and i) confirm the localisation to the lattice edge. Furthermore, the energy of this mode coincides perfectly with the energetic position of the expected topological band gap, rendering this mode an ideal candidate for a topological edge mode. At this point it is worth confirming that the observed PL emission actually originates from polariton condensates by studying the input-output characteristic depicted in Figs. 6.4 j) and k). As the combination of a non-linear increase in intensity, a decrease in polariton linewidth and an energetic blueshift is observed both for the bulk as well as the edge mode, polariton condensation can be confirmed. It is worth noting that the edge mode cannot be identified below the condensation threshold, whereas due to the drastic decrease of the linewidth at the condensation threshold, the modes are separated in energy once the condensates have formed.

Now that a candidate for the topological edge mode has been identified, the topological nature of this mode needs to be investigated. Firstly, while there are trivial edge modes at the zigzag edge of a honeycomb lattice [YYN09; Mil+15; Mil+17], no trivial edge modes exist at the armchair edge [Fuj+96]. A real space image at the energy of the edge mode that was extracted from a mode tomography obtained at the armchair edge of the lattice at a magnetic field of $B = -5\,\mathrm{T}$ is presented in Fig. 6.5 a). The area of the mode tomography is visualised by the microscope image presented in Fig. 6.5 d). The edge mode is again unambiguously observed, thus confirming that it is indeed the expected topological edge mode. Next, the robustness against backscattering of this topological edge mode is studied by investigating the behaviour of the mode at a corner of the lattice, presented in Fig. 6.5 b), as well as at an artificial defect generated by leaving out one pillar at the edge of the lattice, displayed in Fig. 6.5 c). Microscope images corresponding to these lattice areas are presented in Figs. 6.5 e) and f). Both at the lattice corner as well as at the artificial defect, no scattering into the bulk is observed, providing further evidence for the topological nature of the edge mode.

Finally, the chirality of this topological edge mode is investigated. Ideally, one would like to locally excite a polariton condensate in the edge mode and observe its propagation in one direction, with the propagation direction being determined by the polarity of the external magnetic field. However, due to the small band gap, this experiment has not been possible so far. Therefore, the chirality of the mode is studied in Fourier space. As the edge mode condensate cannot be separated from the bulk condensate in Fourier space,

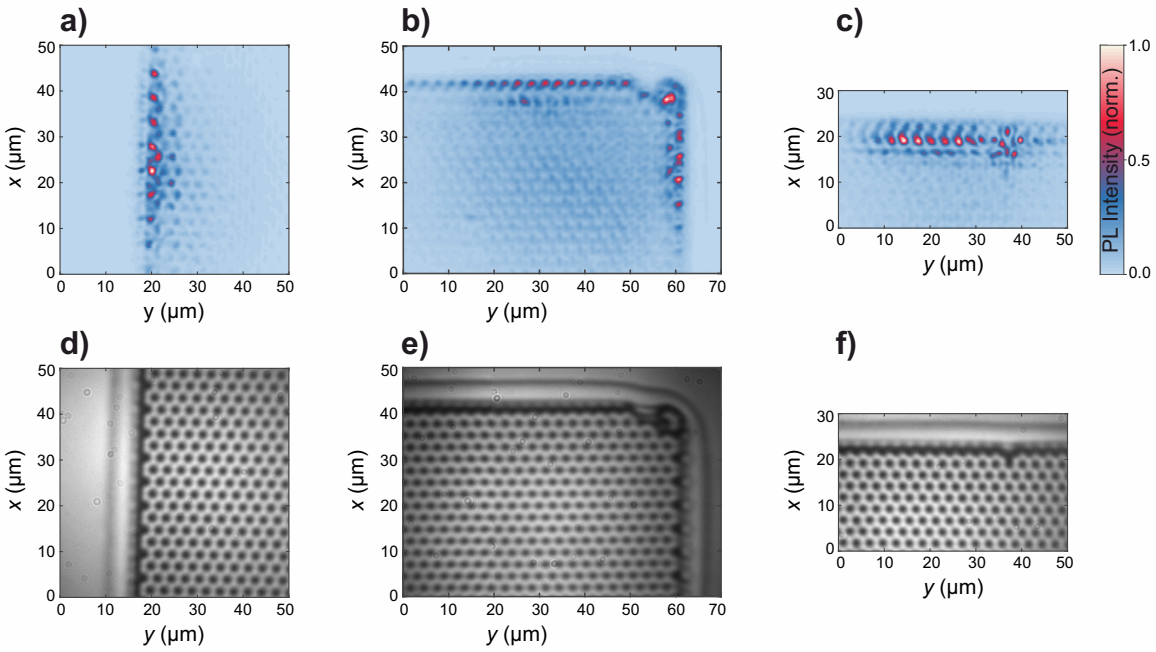

Figure 6.5: Real space images of polariton condensates at magnetic fields of $B = -5\,\mathrm{T}$ in the topological edge mode revealing its existence at the armchair edge of the lattice in **a)** as well as its protection against scattering into bulk modes at a lattice corner in **b)** and at an artificial defect in **c)**. **d)-f)** Microscope images corresponding to the areas of the lattice that are depicted in a)-c).

the intensity is integrated over both condensates, resulting in the Fourier space images presented in Figs. 6.6 a)-c). An intensity imbalance between the condensates at the K and K' points can be observed in these images and even more clearly in the evaluation of the intensity ratio between the K and K' points that is plotted in Fig. 6.6 d). The change of this imbalance between the hyperspectral imaging scans at $B = -5\,\mathrm{T}$ and $B = 5\,\mathrm{T}$ serves as an indication for a change in propagation direction and thus for a chirality of the topological edge mode.

In summary, the combination of evidence for a gap in Fourier space, a clear demonstration of an edge mode that exists at the zigzag and the armchair edge of the lattice and does not scatter at defects or the lattice corner and an indication of chirality observed in Fourier space constitutes a proof for the first realisation of a two-dimensional exciton-polariton topological insulator. The results presented in this section were published in reference [Kle+18].

This first implementation opens the path towards a range of proposed experiments that extend the polariton topological insulator to the honeycomb P band [ZWZ19] as well as other two-dimensional lattices such as the Lieb [Li+18a] and Kagome [Gul+16] lattices. Furthermore, harnessing the inherent non-linearity of polariton condensates which

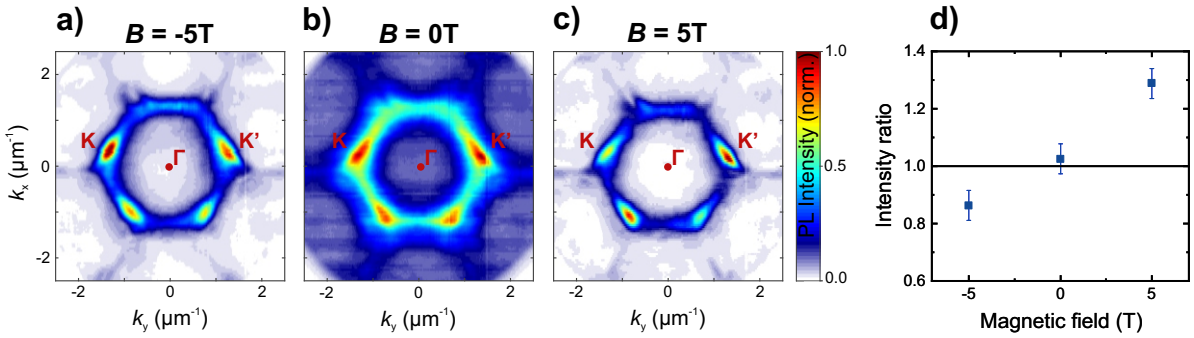

Figure 6.6: a)-c) Fourier space images integrated over the entire S band condensates at external magnetic fields of $B = -5\,\mathrm{T}$, $0\,\mathrm{T}$ and $5\,\mathrm{T}$, respectively. **d)** Intensity ratios of the intensity maxima at the K and K' points in a)-c).

should manifest itself for example in solitons in topological insulators [Lum+13; KS16] as well as bistabilities [KS17a] and should have a signifcant influence on the topology itself [BSM16] offers the potential to study the interplay of topology and non-linearity [Rac18]. In this context it is important to note that the exciton-polariton topological insulator demonstrated represents a truly polaritonic effect, as it relies not only on influencing the photonic band structure but also requires a Zeeman splitting of the excitonic component. Additionally and comparably to the evolution of electronic topological insulators, extending the polaritonic topological insulator to approaches that do not rely on external magnetic field, such as a $\mathbb{Z}_2$ topological insulator [BMS18] or a symmetry-protected topological mode [WH15] would be particularly valuable on the way towards technological applications. Potential applications include for example optical isolators [SBM18] and topological lasers [Bah+17; Ban+18; Har+18; KS19]. In this work, the starting point for studies towards a topological laser based on polaritonic microcavities is the systematic investigation of the lasing properties of the topological defect that occurs in a one-dimensional SSH chain which follows in the next section.

6.2 Polariton lasing from Su-Schrieffer-Heeger defect states

One of the key motivations of the field of topological photonics is the study of the interplay of topological physics and lasing [Bah+17; Ban+18; Har+18]. With future technological applications in mind, a vertically emitting system would be particularly favourable to enable compact devices as well as convenient collection of the emission. As polaritonic microtraps emit vertically and, as soon as a polariton condensate has formed, coherently as well, they represent an ideal platform for the study of topological lasing. In the previous

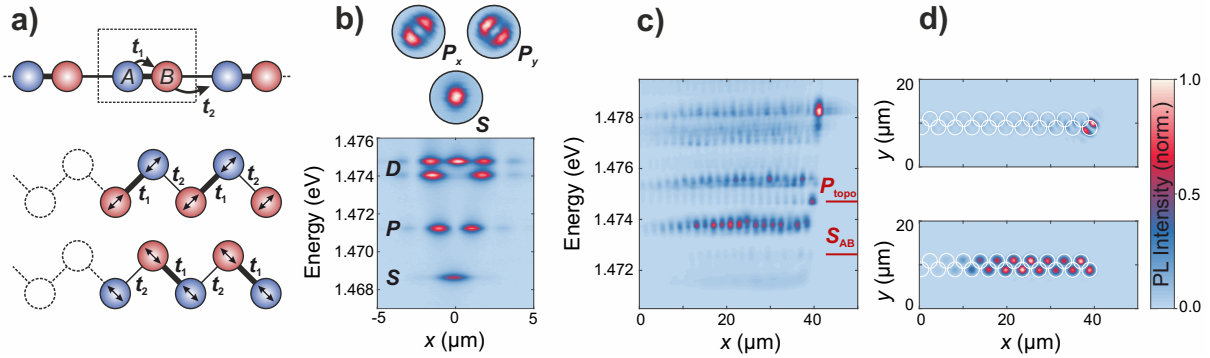

Figure 6.7: a) Schematics of the linear and the orbital SSH models, described by the two coupling strengths t_1 and t_2. The orientations of the P sub-modes of the orbital SSH model are marked with black arrows. **b)** Real space spectrum of a single microtrap with a diameter of $d = 3.5\,\mu\text{m}$ as well as real space images at the energies of the S, P_x and P_y modes. **c)** Real space spectrum along an orbital SSH chain with trap diameters of $d = 3.5\,\mu\text{m}$ and a reduced trap distance of $v = 0.80$. **d)** Real space images at the energies of the topological SSH edge mode (top) as well as the anti-bonding S sub-band (bottom).

chapter, the first demonstration of a two-dimensional, polaritonic topological insulator was presented. However, due to the small band gap and the necessity of an external magnetic field, this system is not ideally suited for an investigation that focusses on the lasing properties of the topological mode. Therefore, the SSH model introduced in section 2.4.2 was selected to achieve the latter. The SSH model serves as an ideal model system due to its convincingly simple geometry in combination with the comparably large achievable band gaps that have allowed precise experimental control in numerous experimental platforms, such as cold atoms [Ata+13], photonic waveguides [Bla+16] and plasmonics [Sin+15; Fed+19], as well as a detailed theoretical description. In photonics as well as electric circuit networks, the availability of gain and loss has led to a thorough investigation of non-Hermitian topology, both from a theoretical [RL09; Sch13; HKA16; Lie18; Lan+18] as well as an experimental perspective [Zeu+15; Wei+17; Kru+19; Ste+21]. Furthermore, lasing from the topological defect of the SSH model [Par+18; Ota+18] as well as gap solitons [Per+21] were realised. Very recently, these efforts were complemented by the implementation of an optically induced polaritonic SSH chain [Pie+21].

As introduced in section 2.4.2 and displayed in Fig. 6.7 a), the SSH model consists of a linear chain with two sites in the unit cell and is characterised by two coupling strengths t_1 and t_2. The size of the band gap is determined by the difference between these two coupling strengths. In a polaritonic system, this model can be implemented by a linear chain of micropillars, in which the two coupling strengths are realised by two different pillar overlaps. While this approach opens band gaps in all bands of the linear chain, the

band gaps remain comparably small due to the boundary conditions that pillars should be close enough to not decouple them entirely and should not overlap as much that they form a single, elliptical pillar. To overcome this limitation, a more elegant approach referred to as orbital SSH model was developed by Solnyshkov and co-workers [SNM16].
In Fig. 6.7 b), a real space spectrum as well as images at the energies of the S and P modes of a single polariton microtrap with a diameter of $d = 3.5\,\mu\text{m}$ on sample In-EnO1 are displayed. While the S mode is rotationally symmetric, the P mode is composed of two sub-modes, referred to as P_x and P_y, that are highly asymmetric. In the orbital SSH model, the microtraps are arranged in a zigzag chain with 90° angles between the connecting lines of neighbouring sites rather than a linear chain. The distances between the microtraps are identical for all sites. Due to the asymmetry of the P mode, this chain represents a twofold implementation of the SSH model, one for each sub-mode. In Fig. 6.7 a), these two implementations are schematically presented, with the orientation of the P sub-modes marked by the black arrows. If two arrows point towards each other, the mode overlap between the two sites and thus the coupling is large, while two parallel arrows results in a small mode overlap and a weak coupling. It is important to note that the last site of such a chain is therefore always strongly bound in one of the SSH model implementations and weakly bound in the other implementation. A topological edge defect mode is thus always expected for one of the P sub-modes.
The first experimental realisation of the polaritonic, orbital SSH model was achieved by St-Jean and co-workers [St-+17] who focussed on the topological nature of the mode. Lasing was achieved as well but not characterised in detail. Another realisation by Whittaker and co-workers [Whi+19] focused on the influence of spin-orbit interaction, engineered through TE-TM splitting, on the topological defect mode. In the work presented here, the lasing properties, in particular the coherence, of the topological edge mode are emphasised. Additionally, this work represents the first implementation of the orbital SSH model using the etch-and-overgrowth platform.
The data presented in this section was obtained on a variation of zigzag chains on sample In-EnO1 with trap diameters of either $d = 2.0\,\mu\text{m}$ or $d = 3.5\,\mu\text{m}$ and varying lengths. The chains are characterised by a moderately negative detuning of $\Delta_\text{E} \approx -12\,\text{meV}$ and were excited by a pulsed laser with an elliptical spot of approximately $30 \times 3\,\mu\text{m}^2$. In Fig. 6.7 c), a real space spectrum along a zigzag chain with trap diameters of $d = 3.5\,\mu\text{m}$, a reduced trap distance of $v = 0.80$ and a length of $N = 45$ traps that was obtained under low excitation power is presented. In the P band, a band gap hosting the topological SSH edge mode can be observed as expected. The real space image at the energy of this edge mode presented in the top panel of Fig. 6.7 d) confirms the localisation of this mode to the last trap of the chain as well as the expected orientation of the P_y sub-mode. The

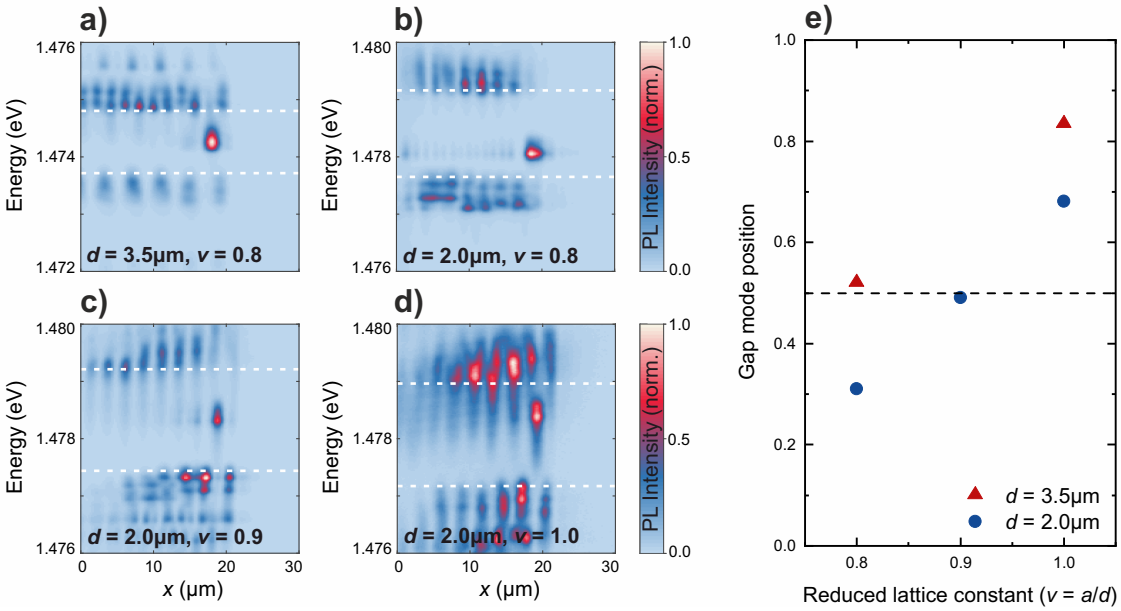

Figure 6.8: Real space spectra along zigzag chains with trap diameters of $d = 3.5\,\mu m$ and a reduced trap distance of $v = 0.80$ in **a)** as well as trap diameters of $d = 2.0\,\mu m$ and reduced trap distances of $v = 0.80$ in **b)**, $v = 0.90$ in **c)** and $v = 1.00$ in **d)**. The gap in the P band is visualised by the white dashed lines. **e)** Evaluation of the energetic position of the topological edge mode with respect to the band gap with 0.5 corresponding to the centre of the gap.

image at the energy of the anti-bonding S sub-mode that is presented below visualises the geometry of the chain as well as the size of the pump spot.

At first, the influence of a variation of the trap overlap, given by the reduced trap distance, on the topological edge mode is investigated. In Figs. 6.8 a)-d), real space spectra along zigzag chains with trap diameters of $d = 3.5\,\mu m$ and a reduced trap distance of $v = 0.80$ as well as trap diameters of $d = 2.0\,\mu m$ and reduced trap distances of $v = 0.80$, $v = 0.90$ and $v = 1.00$, respectively, are presented. From these spectra it becomes apparent that the energetic position of the topological mode within the gap can be controlled by changing the overlap between adjacent traps. The evaluation of the mode position with respect to the gap presented in Fig. 6.8 e), where 0.0 and 1.0 correspond to the lower and upper limits of the band gap and the centre of the gap is denoted by 0.5, confirms this observation. Indeed, the topological mode can be shifted across the band gap systematically by changing the trap overlap. For chains with either trap diameters of $d = 3.5\,\mu m$ and a reduced trap distance of $v = 0.80$ or trap diameters of $d = 2.0\,\mu m$ and a reduced trap distance of $v = 0.90$, the topological edge mode is perfectly centred in the gap. Therefore, the following experiments were performed on zigzag chains characterised by these sets of parameters.

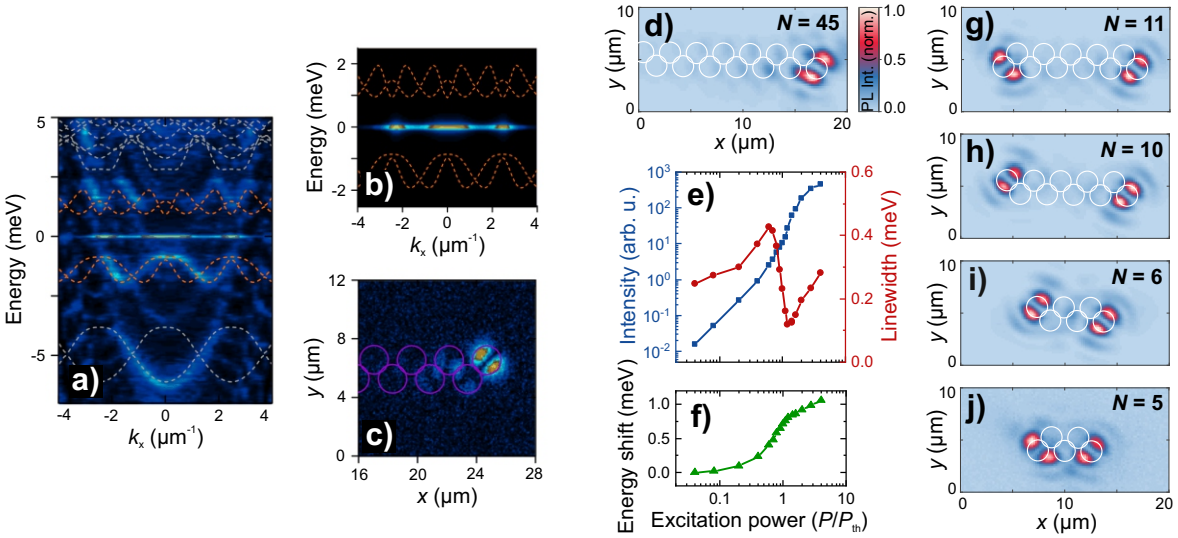

Figure 6.9: **a)** Fourier space spectrum of a polariton zigzag chain generated by a modified Gross-Pitaevskii model, including the result of a Bloch mode calculation (dashed lines). The P band is highlighted in orange. A Fourier space dispersion in **b)** and a real space image in **c)** reveal that at high polariton densities, a polariton condensate forms in the topological edge mode. Figs. a)-c) were adapted from reference [Har+21a]. **d)** Real space image at the energy of a polariton condensate in the topological edge mode of a chain with trap diameters of $d = 2.0\,\mu\text{m}$, a reduced trap distance of $v = 0.90$ and a length of $N = 45$ traps. **e)-f)** Input-output characteristic of the topological edge mode presented in d). **g)-j)** Real space images at the energies of the polariton condensates in zigzag chains with lengths of $N = 11$, 10, 6 and 5 traps.

Next, polariton lasing from the topological edge mode is investigated in detail. In order to obtain a thorough understanding of the system, a theoretical description using a modified version of the generalised Gross-Pitaevskii model was established. The resulting band structure in Fourier space is presented in Fig. 6.9 a), including a Bloch mode calculation based on the actual sample parameters that is plotted in dashed lines. The two models agree perfectly and reveal a band gap in the P band, marked in orange, including a topological mode at its centre. The modified Gross-Pitaevskii model is then used to investigate polariton condensation within the zigzag chain. In the Fourier space spectrum at high polariton densities that is presented in Fig. 6.9 b), a robust polariton condensate in the topological gap mode is observed. The real space image of this mode is displayed in Fig. 6.9 c) and confirms the localisation to the last site of the chain. A chain of microtraps hosting polaritons therefore represents an ideal candidate for an investigation of the properties of a topological lasing mode. A detailed description of this model that was developed by Dr. Oleg Egorov can be found in reference [Har+21a].

These theoretical findings are in excellent agreement with the experimental results, as indeed a polariton condensate forms in the topological edge mode under high excitation powers. A real space image of the condensate in a zigzag chain with trap diameters of $d = 2.0\,\mu m$, a reduced trap distance of $v = 0.90$ and a length of $N = 45$ traps is displayed in Fig. 6.9 d). Again, the characteristic mode pattern of the topological edge mode of the orbital SSH model is observed. The input-output characteristic of this mode that is presented in Figs. 6.9 e) and f) confirms the formation of a polariton condensate, as the non-linear increase in emission intensity is accompanied not only by a distinct drop in linewidth but also by a continuous blueshift of the emission energy.

One of the most important concepts of topological physics if the bulk-boundary correspondence, as it manifests that topological edge modes do not arise due to the specific properties of the edge but rather due to the topologically non-trivial nature of the bulk. Furthermore, when envisioning technological applications of topological lasers, a large boundary-to-bulk ratio would be favourable. It is therefore an interesting question, how large the bulk has to be to support lasing from topological edge modes. In Figs. 6.9 g)-j), real space images at the energies of the polariton condensates in zigzag chains with trap diameters of $d = 2.0\,\mu m$, reduced trap distances of $v = 0.90$ and lengths of $N = 11$, 10, 6 and 5, respectively, are depicted. Remarkably, even a bulk of merely three sites is sufficient to ensure polariton lasing from a topological edge mode.

As a bulk of three sites is sufficient to ensure polariton condensation in the topological edge mode, the following detailed study of the lasing properties was performed on a zigzag chain with trap diameters of $d = 3.5\,\mu m$, a reduced trap distance of $v = 0.80$ and a length of $N = 5$ traps. A real space image of the lasing emission from the topological edge mode is presented in the inset of Fig. 6.10 a). First, it is confirmed that the observed laser-like emission originates from a polariton condensate rather than a photon laser. While the lasing mode of a photon laser does not react to an external magnetic field, an energetic splitting between the circularly polarised components of the emission of a polariton condensate is induced by the Zeeman splitting of the excitonic component. This splitting should, in a first approximation, be determined by the Zeeman splitting of the uncoupled excitons, which was determined at $\Delta_Z = 355\,\mu eV$ for sample In-EnO1, multiplied by the excitonic fraction of the polariton, which is given by the Hopfield coefficient of $|X|^2 = 0.06$ for the topological edge mode. Therefore, at a magnetic field of $B = 5\,T$, a Zeeman splitting of the polariton condensate emission on the order of $22\,\mu eV$ is expected. Importantly, an external magnetic field does not change the topological properties of the SSH mode and, in this section, serves exclusively to distinguish polariton condensation from photon lasing. In Fig. 6.10 a), the Zeeman splitting with respect to the applied magnetic field, obtained from rotating a $\lambda/4$ waveplate in the detection path, is plotted. The Zeeman

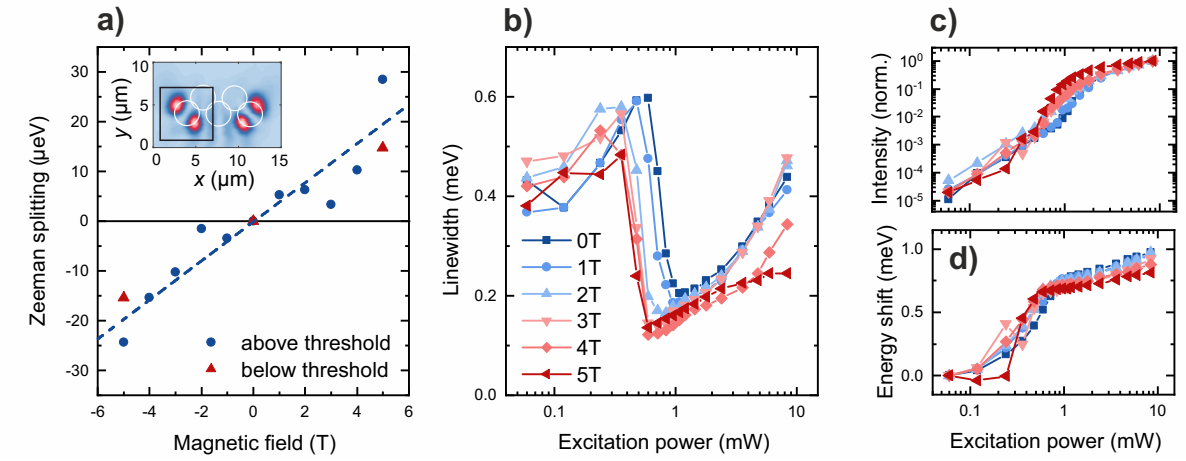

Figure 6.10: a) Zeeman splitting of the topological edge mode as a function of the applied magnetic field, obtained on the edge mode marked by the black box in the real space image in the inset. **b)-d)** Input-output characteristics of the topological edge mode for magnetic fields between $B = 0\,\mathrm{T}$ and $B = 5\,\mathrm{T}$.

splitting of approximately $\Delta_{\mathrm{Z}}^{\mathrm{P}} \approx 19.6\,\mu\mathrm{eV}$ at $B = 5\,\mathrm{T}$ that was extracted from the linear fit agrees well with the estimated splitting, thus confirming that the emission indeed originates from a polariton condensate. Additionally, a decrease of the condensation threshold with increasing magnetic field strength is observed in the linewidth decrease at the condensation threshold presented in Fig. 6.10 b). The same systematic trend is observed in the corresponding input-output characteristics as well as energetic blueshift presented in Figs. 6.10 c) and d). This effect is commonly attributed to a combination of a favourable change in detuning, an enhanced relaxation due to stronger exciton-exciton scattering as well as an increased excitonic oscillator strength [Rou+17; Kla+19] and further substantiates that the laser-like emission originates from a polariton condensate.

Finally, the temporal coherence of the condensate emission is investigated because, as introduced in section 2.1, coherence is the defining characteristic of a laser [Gla63a; Gla63b]. In particular, for coherent laser emission, the second order temporal coherence degree is given by $g^{(2)}(\tau = 0) = 1$. To measure $g^{(2)}(\tau = 0)$, correlation measurements were performed as a function of the excitation power using a Hanbury Brown-Twiss interferometer. Exemplary correlation measurements at excitation powers of $P = 3.0\,\mathrm{mW}$ and $P = 0.7\,\mathrm{mW}$, corresponding to $P \approx 4.3 P_{\mathrm{th}}$ and $P \approx P_{\mathrm{th}}$, are presented in Figs. 6.11 a) and b), respectively. From these correlation measurements, $g^{(2)}(\tau = 0)$ can be evaluated by integrating over all detected photons at $\tau = 0$ and subsequent normalisation using the side peaks that correspond to photons originating from different laser pulses and are thus uncorrelated. The result of this evaluation is presented in Fig. 6.11 c), including error bars derived from the fluctuation between the side peaks. In the grey area, corresponding to excitation

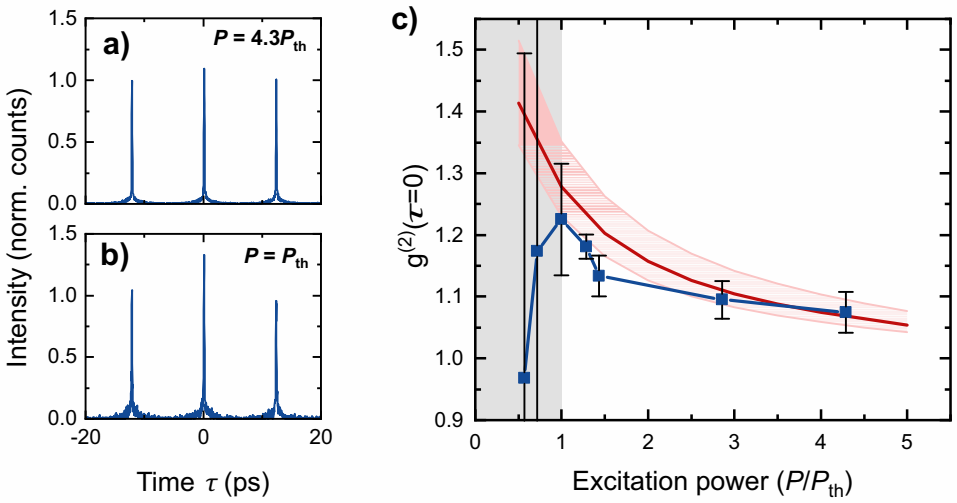

Figure 6.11: a)-b) Exemplary correlation measurements performed with a Hanbury Brown-Twiss interferometer at excitation powers of $P \approx 4.3P_{\mathrm{th}}$ and $P \approx P_{\mathrm{th}}$, respectively. **c)** $g^{(2)}(\tau = 0)$ evaluated from correlation measurements and plotted as a function of the excitation power (blue). The theoretical model (red) was calculated in the Lindblad master equation framework.

powers below the condensation threshold, the coherence time is smaller than the jitter of the detectors, resulting in a commonly observed overshoot of the experimentally determined value of $g^{(2)}(\tau = 0)$ [Jin+94; Kim+16; Kla+18]. For higher excitation powers, the coherence function approaches $g^{(2)}(\tau = 0) = 1$. For the topological edge mode investigated here, a value of $g^{(2)}(\tau = 0) \approx 1.07$ is reached for an excitation power of $P \approx 4.3P_{\mathrm{th}}$. This value is most likely limited from reaching $g^{(2)}(\tau = 0) = 1$ by scattering processes such as polariton-polariton interaction [Den+02; Kim+16]. However, when compared to literature [Kla+18], a value of $g^{(2)}(\tau = 0) \approx 1.07$ is an excellent result for a microlaser with a diameter of only $d = 3.5\,\mu\mathrm{m}$. Fig. 6.11 c) furthermore includes a theoretical model that is based on the Lindblad master equation framework [BP09] and reproduces the experimental results well for excitation powers above the condensation threshold. A detailed explanation of this model that was implemented by Meng Sun and Prof. Ivan Savenko can be found in reference [Har+21a], where the work presented in this section was published. In summary, a polariton condensate emitting highly coherent, laser-like light was excited in the topological edge mode of an orbital SSH chain. Markedly, a chain length of merely five sites proved to be sufficient to host polariton condensates in SSH defects. The ability to vary the chain length and therefore the distance between the SSH defects at the two ends of a chain allows to envision further experiments on the interaction of the two polariton condensates, for example in the context of weak lasing [AAR12]. Furthermore, the relative simplicity of the SSH model allowed a detailed investigation of this laser-like

emission, both experimentally as well as theoretically. This result therefore represents a valuable step towards a better understanding of the interplay of topological insulators and lasers. Based on these findings, a more complicated system hosting a one-dimensional, propagating topological boundary mode rather than a localised, zero-dimensional topological defect mode is studied in the following section.

6.3 Topological insulator vertically-emitting laser array

A potential application of topological photonics involving a strong non-linearity unfolds itself in the coupling of multiple lasers through a propagating, topologically protected mode. Generally, the process of coupling two oscillators to one frequency with a fixed phase relation is referred to as *injection locking*, where the frequency of one oscillator is imprinted on a neighbouring oscillator. Realising injection locking for a large array of lasers remains an ongoing challenge of significant importance, as it could combine the excellent emission characteristics, compact size and convenient geometry for light collection of individual VCSELs with the capability of coherent emission with high powers. Here, a topological mode provides several advantages. Firstly, its non-local nature dictates that it has to propagate and therefore favours injection locking over localised lasing domains. Furthermore, the protection resulting from the non-trivial topological has been predicted to suppress the influence of disorder and defects on both the slope efficiency [Har+18] as well as the coherence [AC20]. Additionally to potential technological applications, the combination of topology with an inherently non-linear regime is interesting from a fundamental perspective [BS18]. In a non-linear system, such as a laser, that is governed by loss, gain and gain saturation, quantities such as the energy are not conserved. Therefore the fundamental principles of defining topological invariants based on the Hamiltonian and observing phase transitions through the opening and closing of band gaps can no longer be applied and even the bulk boundary correspondence can break down [Wei+20]. In such a system, topological protection represents an important observable.
First demonstrations of two-dimensional, topological lasers were achieved by Bahari and co-workers, based on breaking time reversal symmetry by applying a magnetic field to gyromagnetic materials [Bah+17], as well as Bandres and co-workers, based on ring resonators with spatially offset links that induce phase shifts [Ban+18; Har+18]. Based on these impressive achievements, one can think further towards a technological application of topological lasers. Here, a system of coupled VCSELs with a topological mode arising without an external magnetic field would be preferable, as VCSELs represent a mature technology that is already widely used in commercial products [Yu03]. To avoid the necessity of an external magnetic field, approaches inspired by the quantum spin Hall

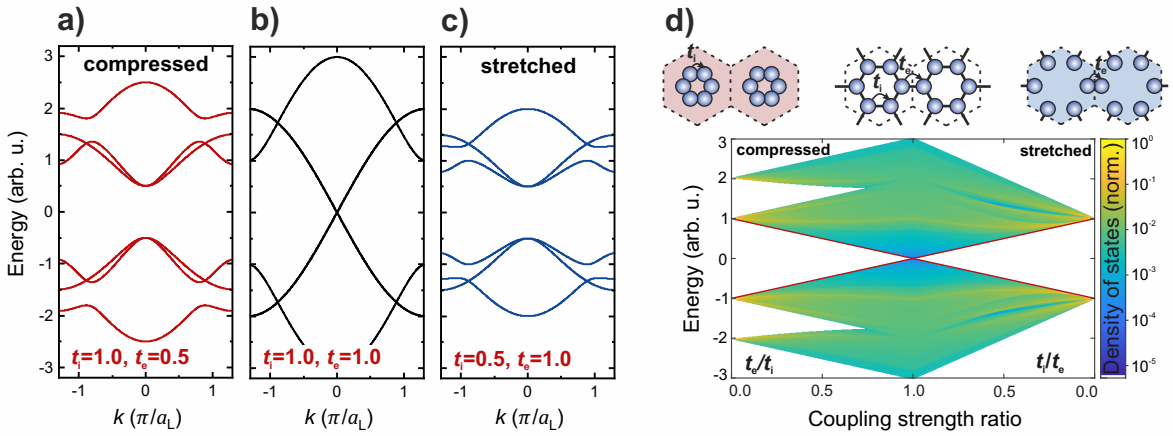

Figure 6.12: a)-c) Exemplary dispersion relations along the K-Γ-K' direction for a compressed crystalline topological insulator (CTI) lattice, an unmodified honeycomb lattice and a stretched CTI lattice, respectively. **d)** Density of states with respect to the ratio between the coupling strengths t_i within a unit cell and t_e between sites of adjacent unit cells. The band gap that opens at the Dirac points is highlighted in red and the three distinct cases of an array of uncoupled benzene rings, an unmodified honeycomb lattice and an array of uncoupled molecules are visualised by the schematics above.

effect are commonly used. These approaches are based on systems that are time reversal invariant but consist of two spin sub-systems each featuring non-trivial topology. In artificial lattices, instead of considering the spin of an electron, a system parameter is mapped to the two orientations of a pseudospin. In the quantum valley Hall effect, for example, the two valley degrees of freedom at the K and K' points serve as pseudospins. Here, a more sophisticated approach based on a recent proposal by Wu and Hu [WH15] that has proven to be working well for photonic crystals [Bar+20] and was introduced in section 2.4.3 is used. This approach is referred to as *crystalline topological insulator* (CTI) and is based on extending the unit cell of a honeycomb lattice to include six sites that form the artificial analogon of a benzene ring. In each unit cell, this benzene ring is then either stretched or compressed, with both of these modifications resulting in a band gap opening up at the Dirac points. To get a better understanding of the band structures that are to be expected in CTI lattices, a tight binding model based on nearest neighbour coupling was implemented. In Figs. 6.12 a)-c), three exemplary dispersion relations for a compressed CTI lattice, an unmodified honeycomb lattice and a stretched CTI lattice are depicted. It is important to note that, by extending the unit cell, the K and K' points of the honeycomb lattice are projected onto the Γ point of the new Brillouin zone. For clarity, the notation of the high-symmetry points of the honeycomb lattice that represents the foundation of the deformed lattices is used in the following. In the dispersion relations, the band gap that opens at the Dirac point can be clearly

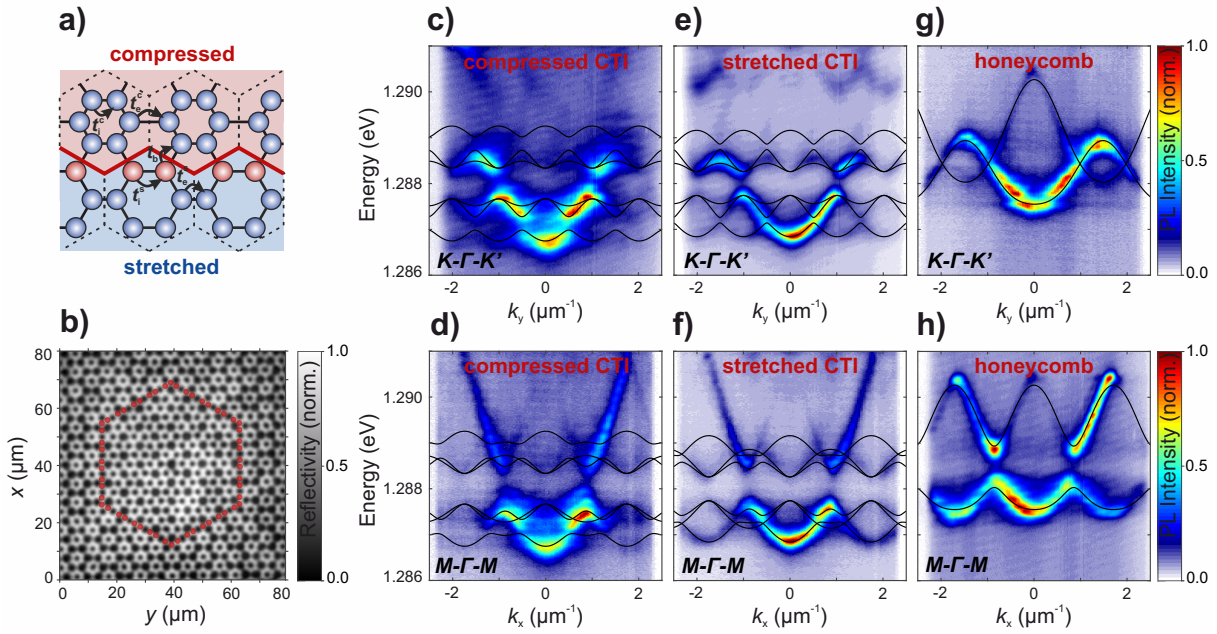

Figure 6.13: **a)** Schematic of the CTI lattice geometry featuring a domain wall (red) between the compressed (top) and stretched (bottom) domains. A topological boundary mode is expected on the interface sites marked in red. **b)** Microscope image of a CTI lattice consisting of a hexagonal, stretched domain that is surrounded by a compressed domain. Fourier space spectra along the K-Γ-K' and M-Γ-M directions of the compressed and stretched domains in **c)**-**d)** and **e)**-**f)**, respectively, including tight binding fits. **g)**-**h)** Corresponding Fourier space spectra of an unmodified honeycomb lattice.

observed. A systematic variation of the ratio between the two coupling strengths t_i and t_e, corresponding to coupling between sites within one unit cell (internal, i) and of adjacent unit cells (external, e), respectively, is presented in Fig. 6.12 d). Additionally, the three distinct cases of uncoupled benzene rings, characterised by $t_\mathrm{e} = 0$, an unmodified honeycomb lattice featuring $t_\mathrm{i} = t_\mathrm{e}$ and uncoupled molecules, characterised by $t_\mathrm{i} = 0$, are schematically visualised. In the illustration of the density of states, the evolution of the band structure from the four discrete energy levels of a benzene ring over the gapless band structure of the honeycomb lattice to the two discrete energy levels of a molecule can be observed. The band gaps opening at the Dirac points in the compressed and stretched domains are highlighted in red. As introduced in section 2.4.3 and analogously to the quantum spin Hall effect in HgTe quantum wells, these band gaps can be distinguished by an inversion of the band gap in the stretched domain with respect to the compressed domain. For the CTI lattice geometry, this band inversion is defined by the contribution of the bands of the benzene-like unit cells to the overall lattice band structure, rendering the stretched domain topologically non-trivial.

The geometry of a CTI lattice is depicted in Fig. 6.13 a), where the interface between the

compressed domain in the top and the stretched domain in the bottom is highlighted in red. Due to the topologically non-trivial band gap in the stretched domain, a topologically protected gap mode is expected on the interface sites marked in red. In Fig. 6.13 b), a microscope image of a CTI lattice that was fabricated on sample In-FE1 and features a hexagonally shaped, stretched domain surrounded by a compressed domain is presented. The interface sites are highlighted in red. Instead of quantum wells, the active material of sample In-FE1 is comprised of an ensemble of quantum dots. This sample was selected as the quantum dot ensemble does not couple strongly to the photonic mode and therefore, instead of reaching the more complex regime of polariton lasing, features pure photonic lasing above the threshold excitation power.

Each lattice is characterised by two reduced pillar distances, the internal reduced pillar distance v_i for the distances within each benzene ring and the external reduced pillar distance v_e for the distance between pillars of adjacent unit cells. In Figs. 6.13 c) and d), Fourier space spectra along the K-Γ-K' and M-Γ-M directions, respectively, of a compressed CTI lattice with pillar diameters of $d = 2.5\,\mu\mathrm{m}$ and reduced pillar distances of $v_\mathrm{i}^\mathrm{c} = 0.78$ and $v_\mathrm{e}^\mathrm{c} = 0.98$ are presented. The corresponding Fourier space spectra of a stretched CTI lattice with reduced pillar distances of $v_\mathrm{i}^\mathrm{s} = 0.91$ and $v_\mathrm{e}^\mathrm{s} = 0.72$ are depicted in Figs. 6.13 e) and f). For comparison, Fourier space spectra of an unmodified honeycomb lattice with pillar diameters of $d = 2.5\,\mu\mathrm{m}$ and a reduced pillar distance of $v = 0.90$ that was fabricated on the same sample are provided in Figs. 6.13 g) and h). All Fourier space spectra include tight binding models that agree well with the data. In both the compressed and the stretched CTI lattices, band gaps opening at the Dirac points are clearly observed.

Before advancing towards an investigation of the lasing properties of CTI interface modes, a systematic study and optimisation of the lattice design parameters was performed. For this aim, three lattice variations, named L1, L2 and L3, of reduced pillar distances v_i and v_e were designed such that the overall difference $\Delta v = |v_\mathrm{i} - v_\mathrm{e}|$ increases from variation L1 to variation L3. As the coupling strength between adjacent pillars is directly linked to the pillar overlap, the difference in reduced pillar distances represents the key parameter in opening a band gap in CTI lattices. A summary of the design parameters of these three lattice variations is provided in Fig. 6.14 b). The band gaps of the compressed and stretched domains of CTI lattices with pillar diameters of $d = 2.0\,\mu\mathrm{m}$, $2.5\,\mu\mathrm{m}$ and $3.0\,\mu\mathrm{m}$, each fabricated in all three lattice variations, are presented in Fig. 6.14 a). Details on the band gap evaluation can be found in the appendix in section A.4. First of all, a systematic increase of the band gap with decreasing pillar diameter is observed. This effect can be attributed to a higher mode overlap between adjacent pillars that results in overall higher coupling strengths. For lattices with pillar diameters of $d = 2.5\,\mu\mathrm{m}$ and $d = 3.0\,\mu\mathrm{m}$, the

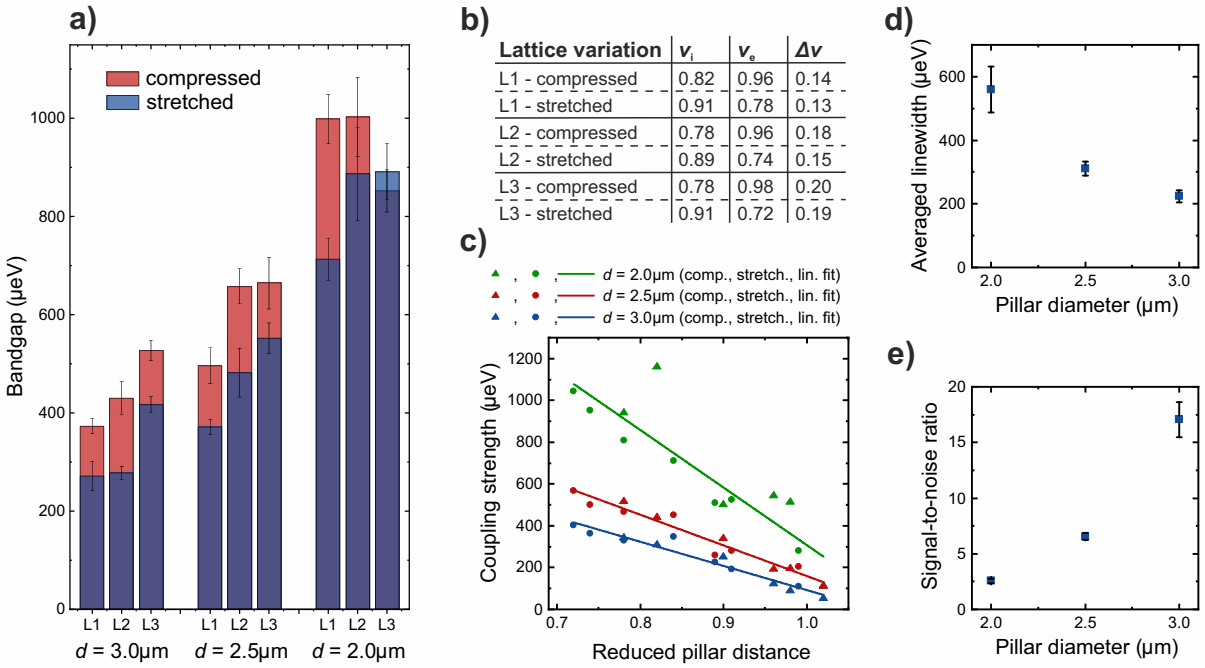

Figure 6.14: **a)** Band gap evaluation of compressed and stretched CTI lattices in three parameter variations L1, L2 and L3, each fabricated with pillar diameters of $d = 2.0\,\mu\text{m}$, $2.5\,\mu\text{m}$ and $3.0\,\mu\text{m}$. **b)** Table of the reduced pillar distances within a unit cell (v_i) and between adjacent unit cells (v_e) as well as the difference $\Delta v = |v_\text{i} - v_\text{e}|$. **c)** Coupling strengths with respect to the reduced pillar distances, evaluated from the bandwidth of the S sub-bands below the band gap and the size of the band gap under the assumption of a tight binding model considering nearest neighbour coupling. Photonic linewidth and signal-to-noise ratio with respect to the pillar diameter in **d)** and **e)**, respectively.

expected systematic increase of the band gap with respect to the difference in reduced pillar distances Δv is observed. For lattices with pillar diameters of $d = 2.0\,\mu\text{m}$, however, lattice variation L3 appears to be too extreme, as a decrease in the quality of the etch process that is observed for this set of parameters manifests itself in a decrease of the band gap compared to lattice variation L2.

From the tight binding model that was introduced above, the bandwidth E_b of the S sub-band below the band gap and the size of the band gap E_g can be related to the internal and external coupling strengths t_i and t_e, within a unit cell and between adjacent unit cells, respectively, through

$$\begin{aligned} E_\text{g} &= 2 \cdot |t_\text{i} - t_\text{e}| \quad \text{and} \\ E_\text{b} &= 2t_\text{i} + t_\text{e} - \frac{E_\text{g}}{2}. \end{aligned} \tag{6.1}$$

Using these relations, the coupling strengths that are plotted in Fig. 6.14 c), including linear fits, were evaluated. Particularly for lattices with pillar diameters of $d = 2.5\,\mu\text{m}$ and $d = 3.0\,\mu\text{m}$, a linear decrease of the coupling strengths between reduced pillar distances of $v = 0.72$ and $v = 1.02$ is observed. This clear dependency thus represents a calibration enabling to deterministically design the coupling strengths and thus band gaps of CTI lattices. For lattices with pillar diameters of $d = 2.0\,\mu\text{m}$, the fluctuations are considerably higher. Again, the deviations observed for pillar diameters of $d = 2.0\,\mu\text{m}$ can be explained by a decrease in the structural quality of these lattices arising due to difficulties with the etching process for these very small pillar sizes. This decrease in lattice quality is also reflected in the increase in linewidth depicted in Fig. 6.14 d) as well as the decrease in signal-to-noise ratio presented in Fig. 6.14 e). In conclusion, a trade-off between the size of the band gap and the lattice quality was found in the systematic band gap evaluation. Furthermore and analogously to the band gap considerations regarding the exciton-polariton topological insulator that were described in section 6.1, the most important figure of merit is the visibility of a topological mode within the band gap that is determined by the size of the band gap with respect to the linewidth. As a result, a CTI lattice with the parameters of lattice variation L3 and pillar diameters of $d = 2.5\,\mu\text{m}$ was selected for the lasing experiments that are presented in the following.

Conceptually, to evoke lasing from the topological interface mode, the sites that comprise the interface need to be excited such that lasing occurs selectively from the desired mode. As the topological boundary mode is by definition not localised but propagates, it should then ensure coherent coupling between the individual VCSELs that should be enhanced further as the interface was as a closed loop forming a ring cavity. The pulsed excitation laser was thus shaped into a hexagon, depicted in Fig. 6.15 a), using the SLM and precisely aligned and matched with the interface. From the cross section through the excitation hexagon, a width of approximately $2.9\,\mu\text{m}$ can be determined. Even though the SLM enables to create a laser hexagon with high quality, a finely tuned combination of lattice parameters, the size and width of the hexagon as well as the alignment between the excitation laser and the lattice interface is crucial, as is exemplified in the real space spectra and corresponding images of the lasing modes in Figs. 6.15 c)-e) and f)-h), respectively. Minor deviations from ideal excitation conditions can cause multi-mode lasing, presented in Figs. 6.15 c) and f), non-homogeneous lasing from parts of the topological mode, depicted in Figs. 6.15 d) and g) or lasing from non-topological modes, displayed in Figs. 6.15 e) and h).

However, after careful optimisation of the excitation conditions, single-mode lasing from the topological boundary mode consisting of 54 VCSELs was achieved. In Fig. 6.16 a), a real space spectrum at an excitation power of $P = 0.03 P_{\text{th}}$, well below the lasing threshold

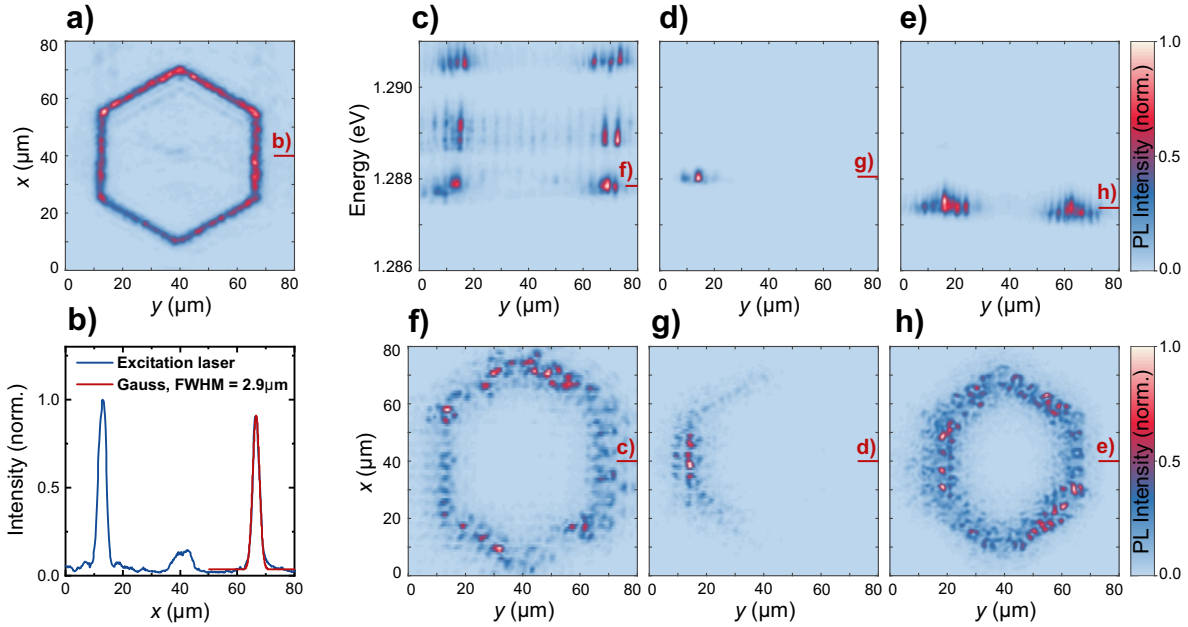

Figure 6.15: **a)** Hexagonal excitation laser shaped using an SLM. **b)** Cross section through the laser hexagon revealing a witdth of approximately 2.9 µm. **c)-e)** Real space spectra cutting through the hexagonal interface obtained above the lasing threshold to demonstrate that small deviations from ideal excitation conditions result in multi-mode lasing, inhomogeneous intensity distributions or lasing from bulk modes. **f)-h)** Corresponding real space images of the lasing modes that are marked by red lines in c)-e).

of $P_{\mathrm{th}} = 35.0\,\mathrm{mW}$, is presented. In the real space image at the energy of the bulk band gap depicted in Fig. 6.16 b), the topological boundary mode that arises at the interface between the stretched and the compressed domains is clearly observed. It should be noted that the slight distortion of this image can be attributed to a spatial drift of the sample during the mode tomography. The intensity that is observed towards the edge of the lattice arises due to deviations in the potential environment caused by an increased etch depth towards the lattice edge. Nevertheless, the real space spectrum as well as the real space image of the topological lasing mode at an excitation power of $P = 2.14 P_{\mathrm{th}}$ displayed in Figs. 6.16 c) and d) confirm single-mode and homogeneously distributed lasing from the hexagonal interface. The input-output characteristics presented in Figs. 6.16 e) and f) confirm the lasing threshold, as a non-linear increase in emission intensity combined with a decrease in linewidth due to the build-up of coherence is observed. As the topological interface mode cannot be separated unambiguously from the bulk modes below threshold, the intensity of a bulk mode was evaluated below the lasing threshold. Furthermore, the integrated emission spectrum across the entire area presented in Fig. 6.16 d) reveals that no emission from bulk modes occurs. In Fig. 6.16 h), emission spectra at the twelve posi-

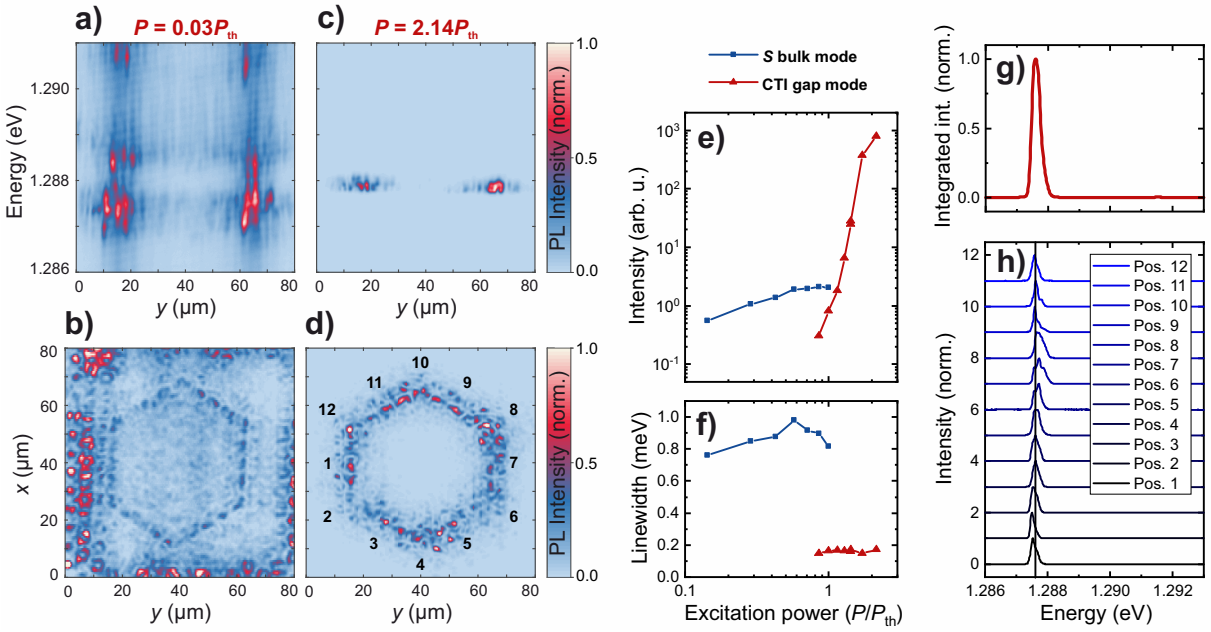

Figure 6.16: **a)-b)** Real space spectra of the CTI interface under excitation with a laser hexagon at excitation powers of $P = 0.03P_{\mathrm{th}}$ and $P = 2.14P_{\mathrm{th}}$, respectively. **c)-d)** Corresponding real space images of the topological boundary mode. **e)-f)** Input-output characteristic of the lasing threshold of the topological boundary mode. **g)** Emission spectrum of the topological lasing mode, integrated over the entire area of the image in d). **h)** Individual emission spectra at the twelve positions marked in d). The central energy of the integrated emission spectrum is marked by the black line.

tions marked in Fig. 6.16 d) are presented. Here, small deviations of the emission energy that are on the order of the linewidth are observed.

The topological protection of the lasing mode as well as the fact that it is a propagating mode are predicted to enhance coherent coupling between the lasers constituting the interface. Therefore, the coherence of the topological lasing mode is investigated. However, the configuration of the Michelson interferometer used in the previous chapter, where one arm is equipped with a retroreflector, is unsuitable here, as only VCSELs with maximal distance in the interface would be superimposed. Therefore, the retroreflector was exchanged by a prism flipping the image only along one axis, as introduced in section 3.2.2. In this configuration, an emitter located on the mirror axis is superimposed with itself, while the distance between two emitters superimposed at a distance s to the mirror axis of the interferogram is given by $2s$. In Figs. 6.17 a) and b), Michelson interferograms obtained by flipping the image in one arm along the mirror axis marked in red are presented. In Fig. 6.17 a), the distance between superimposed VCSELs increases starting from the centre of an edge of the hexagon, whereas in Fig. 6.17 b) a corner of the hexagon is located at the mirror axis. To elucidate the interferometry configuration, two the dis-

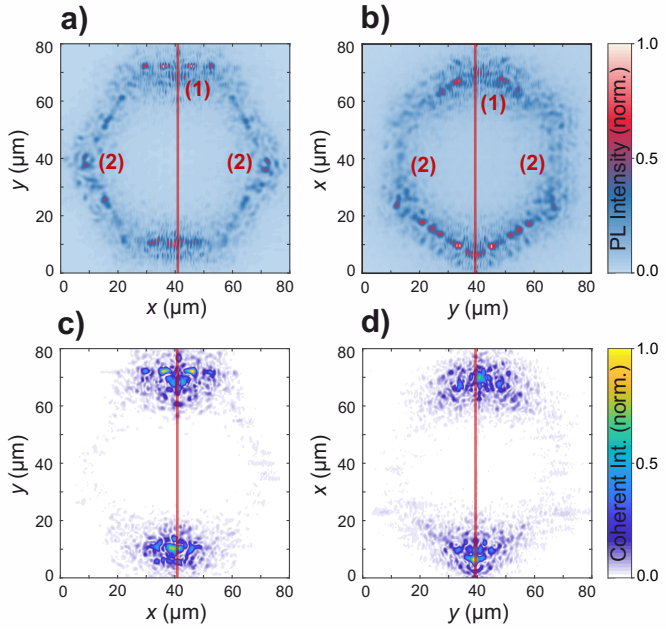

Figure 6.17: a)-b) Interferograms obtained for two orientations of the hexagonal CTI interface using a Michelson interferometer equipped with a prism in one arm that flips the image along the mirror axis marked in red. A VCSEL at position (1) is superimposed with itself, while the emission superimposed in position (2) originates from two VCSELs on opposite sides of the interface. **c)-d)** Corresponding spatial coherence maps.

tinct positions (1) and (2) were highlighted in the interferograms. At position (1), the emission originating from one VCSEL is superimposed with itself, while the superimposed emission at position (2) originates from two VCSELs on opposite sides of the interface. In Figs. 6.17 c) and d), the corresponding spatial coherence maps are presented. In the interferogram centred at an edge and presented in Figs. 6.17 a) and c), coherent emission from all ten lasers of one edge is revealed. Furthermore, the interferogram that is centred at a corner and is displayed in Figs. 6.17 b) and d) confirms that coherence is maintained around a corner of interface. However, coherent coupling along the entire interface was not achieved, as disorder across the lattice results in localisation of the lasing modes. Furthermore, the coherence length is limited by the propagation length within the interface mode.

Following these promising first results, sample In-FE2 was processed on a wafer with a microcavity that is nominally identical to the wafer used to process sample In-FE1. One conclusion obtained from the systematic investigation of the influence of lattice parameters on the topological band gaps presented in Fig. 6.14 is that the further increase of the coupling difference between lattice variations L2 and L3 did not result in a significant increase in the band gap for lattices with diameters of $d = 2.5\,\mu\text{m}$. However, the larger

difference in overlaps and the consequently larger difference in hole sizes causes more defects during the etching process. Therefore, lattices with pillar diameters of $d = 2.5\,\mu\text{m}$ and reduced pillar distances of $v_\text{i}^\text{c} = 0.80$, $v_\text{e}^\text{c} = 0.98$, $v_\text{i}^\text{s} = 0.92$ and $v_\text{e}^\text{s} = 0.74$, corresponding to parameters between lattice variations L2 and L3 of sample In-FE1, were processed. The size of the interface was decreased from 54 to 30 sites to reduce the influence of fluctuations of the lattice potential across the wafer. Furthermore, the length of an interface with 30 sites is closer to the propagation length within the topological mode and therefore enhances the possibility of the formation of a closed ring cavity which should enhance the lasing properties. It is important to note that for an interface with 30 sites, the bulk of the stretched lattice domain surrounded by this interface still consists of 84 sites. A comparison to the investigation of the band structure formation in honeycomb ribbons presented in Fig. 4.2 confirms that the bulk is still sufficiently large to support a fully evolved band structure. In Figs. 6.18 a) and c), Fourier space spectra along the K-Γ-K' direction of the compressed and stretched domains, respectively, are presented. The data are reproduced with tight binding models and topological band gaps of 553 µeV and 565 µeV, respectively, were evaluated. In Fig. 6.18 b), a Fourier space spectrum obtained on the interface between the two domains is presented. Here, the topological mode that stretched across the band gap is highlighted by a red ellipse. The dashed lines correspond to the tight binding model used to reproduce the spectrum that was obtained on the stretched domain. Optical and electron microscopy images visualising the lattice geometry can be found in the appendix in Fig. A.9.

The first step towards the investigation of the lasing properties of this topological mode is a measurement of the lasing threshold. The input-output characteristic as well as linewidth of the topological interface mode presented in Fig. 6.18 d) confirm that the lasing threshold was reached at an excitation power of $P_\text{th} \approx 17.5\,\text{mW}$. For these experiments, the SLM was operated using the modified MRAF algorithm that was introduced in section 3.2.3 and resulted in the hexagonal shape presented in the inset of Fig. 6.18 d). As this algorithm directs some of the laser intensity into a noise region and the photodiode used to measure the laser excitation power cannot distinguish between the signal and noise regions, the threshold power obtained from the input-output measurement should only be understood as an estimate. Nevertheless, a lasing threshold was observed unambiguously. The 30 VCSELs constituting this topological laser can be seen in the real space images at the energy of the topological mode depicted in Figs. 6.18 e) and f), corresponding to excitation powers below and above the lasing threshold, respectively.

While the image below the lasing threshold was obtained under excitation with a large, Gaussian spot, the excitation laser was shaped into a hexagon using an SLM and meticulously aligned with the topological mode for the measurement of the input-output char-

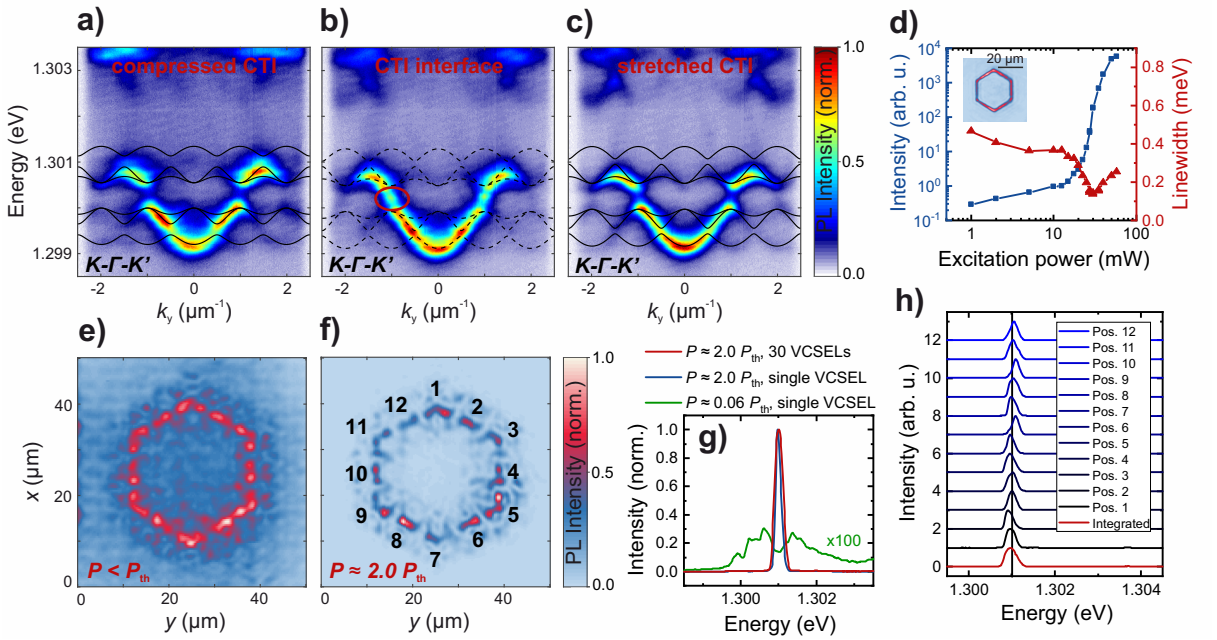

Figure 6.18: **a)-c)** Fourier space spectra obtained on the compressed domain, the interface as well as the stretched domain. The topological interface mode is marked by a red ellipse. **d)** Input-output characteristics of the lasing threshold of the interface mode. An image of the excitation laser is provided in the inset. **e)-f)** Real space images at the energy of the interface mode obtained for excitation powers below and above the lasing threshold, respectively. **g)** Energy spectra of the emission of a single VCSEL below and above the threshold as well as the integrated emission spectrum of the full interface. **h)** Spectral analysis of the lasing mode along the interface at the positions marked in f).

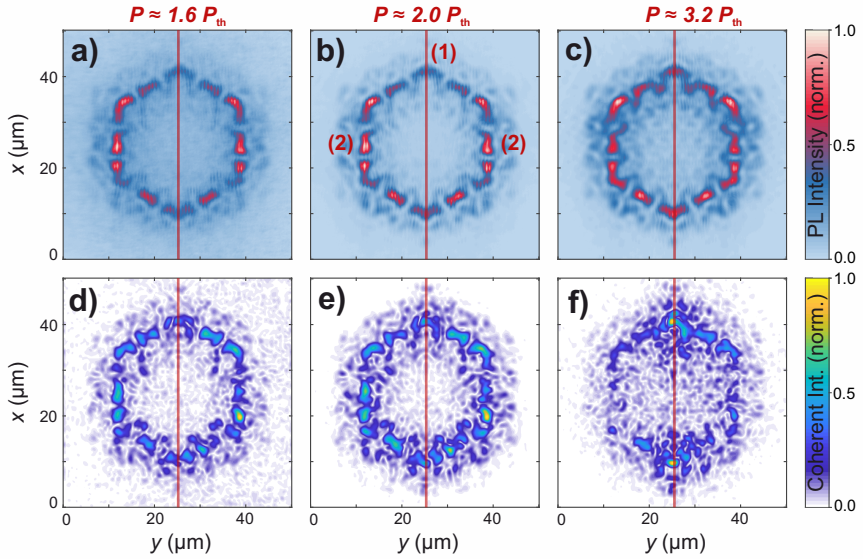

Figure 6.19: a)-c) Michelson interferograms of the topological lasing mode at excitation powers of $P \approx 1.6P_{\mathrm{th}}$, $P \approx 2.0P_{\mathrm{th}}$ and $P \approx 3.2P_{\mathrm{th}}$, respectively. The mirror axis along which the image is flipped in one of the arms of the interferometer is highlighted in red. **d)-f)** Corresponding spatial coherence maps.

acteristics as well as the real space image above the lasing threshold. In Fig. 6.18 g), the emission spectra of a single VCSEL at excitation powers below and above the excitation threshold as well as an integrated spectrum of the entire interface of 30 VCSELs are presented. From these spectra, one can clearly observe that the lasing emission originates exclusively from the topological interface mode. Furthermore, at an excitation power of $P \approx P_{\mathrm{th}}$, the linewidth of 249 µeV of the integrated spectrum is on the same order of magnitude as the linewidth of 171 µeV of an individual VCSEL. Furthermore, this linewidth is smaller than the topological band gap, ensuring topological protection against scattering into bulk modes. Indeed, the emission observed in the real space image of the lasing mode that is displayed in Fig. 6.18 f) originates almost exclusively from the sites comprising the interface between the compressed and stretched domains of the lattice. The spectra extracted from the positions marked in Fig. 6.18 f) and presented in Fig. 6.18 h) further visualise that the variation between the emission of the individual lasers in on the order of the linewidth. This result is particularly important, as lasing with only small variations in energy between the individual emitters is the defining observable for injection locking and is a crucial prerequisite for coherent coupling.

The definitive property of a laser is the coherence of its emission. Therefore, Michelson interferometry with a prism in one arm of the interferometer, as introduced above, was performed. In Figs. 6.19 a)-c), Michelson interferograms recorded at excitation powers of $P \approx 1.6P_{\mathrm{th}}$, $P \approx 2.0P_{\mathrm{th}}$ and $P \approx 3.2P_{\mathrm{th}}$, respectively, are presented. For these measure-

ments, the sample was oriented such that the mirror axis is located at two corners of the hexagonal interface mode. With increasing distance to the mirror axis, the separation between superimposed lasers increases. Again, positions (1) and (2) correspond to superimposed emission from one VCSEL with itself and two VCSELs from opposite sides of the interface, respectively. The corresponding spatial coherence maps presented in Figs. 6.19 d)-f) reveal that interference fringes originating from the coherence of the lasing emission were observed along the entire interface of 30 lasers for excitation powers up to $P \approx 2.0 P_{\mathrm{th}}$. Even lasers on opposite sides of the interface emit with a fixed phase relation. Furthermore, the coherence length is considerably larger as compared to the previously studied sample presented in Fig. 6.16. This increase can be attributed to a combination of higher quality of the etching process, decreased spatial fluctuations of the potential environment due to the smaller interface size as well as enhanced coupling due to coherence along the entire closed loop of the interface. For even higher excitation powers, the lasing threshold for additional bulk modes is reached and the observed coherence length is reduced due to the multi-mode lasing emission.

Advancing from the demonstration of coherent emission along the entire interface of 30 VCSELs, the influence of topological protection on the lasing emission is elaborated. Following this objective, a CTI lattice with a weaker parameter variation, given by $v_{\mathrm{i}}^{\mathrm{c}} = 0.85$, $v_{\mathrm{e}}^{\mathrm{c}} = 1.00$, $v_{\mathrm{i}}^{\mathrm{s}} = 0.95$ and $v_{\mathrm{e}}^{\mathrm{s}} = 0.80$, and an unmodified honeycomb lattice on sample InFE2 were investigated. Due to the weaker parameter variation, the CTI lattice features smaller band gaps of 350 µeV and 420 µeV in the compressed and stretched domains, respectively, and thus provides less protection for the topological interface mode. For the honeycomb lattice, the lasing emission originates from topologically trivial bulk modes. In Figs. 6.20 a) and b), Michelson interferograms of the lasing emission from the CTI lattice with a weaker parameter variation as well as the unmodified honeycomb lattice, respectively, both excited with a hexagonal laser spot, are presented. The corresponding spatial coherence maps are depicted in Figs. 6.20 c) and d). In Fig. 6.20 e), an evaluation of the coherence length along the interface, starting at the mirror axis in points (1) and ending at points (2) where the emission from two VCSELs from opposite sides of the interface is superimposed, is presented. The coherence was averaged over the four available paths. While the coherence of the CTI lattice with the stronger parameter variation, introduced in Figs. 6.18 and 6.19, remains approximately constant along the entire interface, a fast decay of the coherence is observed for the bulk-mode lasing from the unmodified honeycomb lattice. As expected, the coherence length of the CTI lattice with a weaker parameter variation can be found in between. As a guide to the eye, a constant fit was added to the data corresponding to the CTI lattice with a stronger variation. The decay of coherence observed for the CTI lattice with the weaker variation as well as the

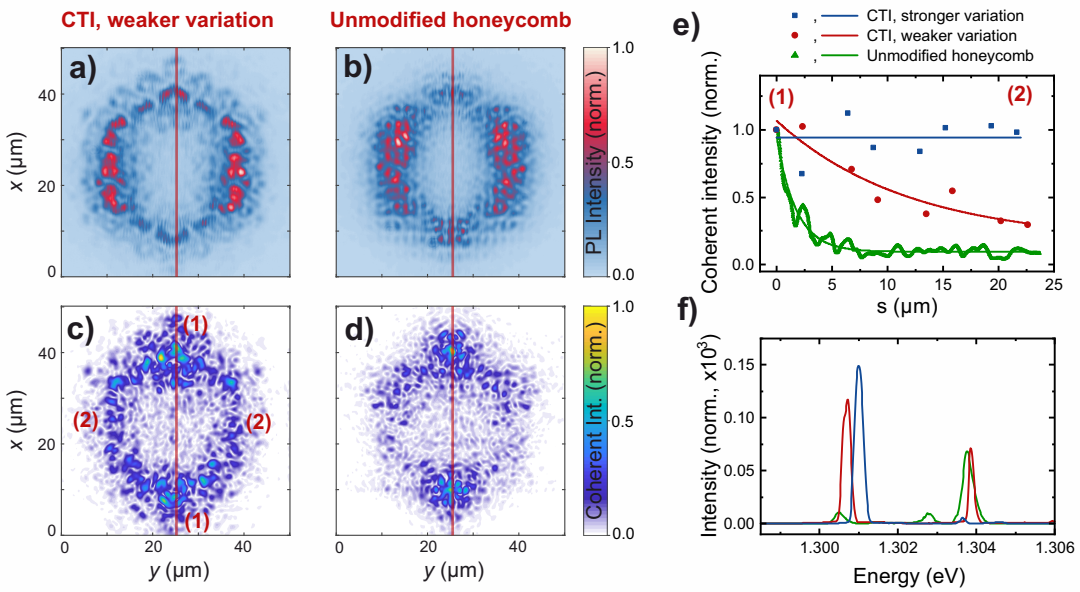

Figure 6.20: **a)-b)** Michelson interferograms of the lasing emission from a CTI lattice with a weaker parameter variation, given by $v_{\mathrm{i}}^{\mathrm{c}} = 0.85$, $v_{\mathrm{e}}^{\mathrm{c}} = 1.00$, $v_{\mathrm{i}}^{\mathrm{s}} = 0.95$ and $v_{\mathrm{e}}^{\mathrm{s}} = 0.80$, and an unmodified honeycomb lattice, respectively. **c)-d)** Corresponding spatial coherence maps. **e)-f)** Comparison of the coherence lengths and emission spectra, respectively, of two CTI lattices with different parameter variations as well as an unmodified honeycomb lattice, highlighting the influence of the topological protection on the lasing properties.

unmodified honeycomb lattice was reproduced by exponential fits with decay constants of 11.9 µm and 1.8 µm, respectively. To understand this result, an evaluation of the spectral composition of the lasing emission from the three lattices is presented in Fig. 6.20 f). Real space spectra and images extracted from the mode tomographies analysed to obtain this spectral comparison can be found in the appendix in Fig. A.10. While the CTI lattice features single-mode emission from the topological interface mode, the lasing emission transitions to multi-mode emission originating predominantly from P bulk modes for the CTI lattice with a weaker modulation and the unmodified honeycomb lattice.

The aim of the investigations presented in this section was to evaluate the suitability of using a propagating topological mode to couple individual lasers such that they emit as one coherent laser. These experiments were performed using VCSELs, as these lasers represent a mature technological platform commonly used in commercial products. After a systematic investigation and optimisation of the topological band gaps that were achieved in CTI lattices of VCSELs, selective lasing from the topological interface mode was realised and the coherence properties were demonstrated. Here, it is particularly important to note that a high degree of coherence along an interface mode with 30 sites

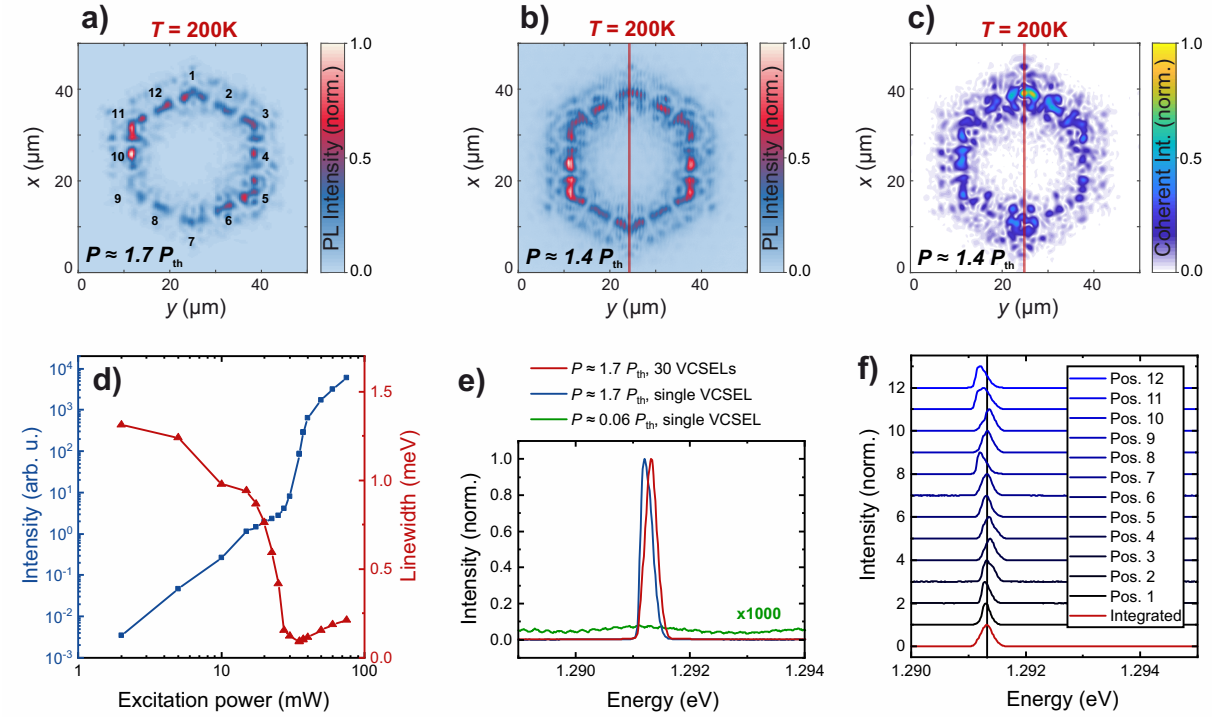

Figure 6.21: Measurements at an elevated temperature of $T = 200\,\mathrm{K}$. **a)** Real space image at the energy of the topological lasing mode. **b)** Michelson interferogram of the topological laser mode. **c)** Corresponding spatial coherence map. **d)** Input-output characteristic as well as linewidth. **e)** Emission spectra of a single VCSEL below and above the lasing threshold as well as the integrated spectrum of the full lasing interface. **f)** Spectral analysis of the spatial fluctuations. The positions at which the spectra were extracted are marked in a).

was achieved and the idea of using a propagating, topologically protected mode to ensure injection locking of an array of VCSELs was experimentally verified. Furthermore, the superior performance of this topologically protected mode with respect to bulk modes in an unmodified honeycobm lattice was demonstrated. This result therefore represents the first demonstration of a vertically emitting topological insulator laser array. A key advantage of this configuration compared to previously reported topological lasers [Bah+17; Ban+18] is the separation of the emission direction from the topologically protected propagation. This separation not only allows efficient and convenient collection of the lasing emission, but also overcomes the requirement of a precisely fixed emission wavelength. In contrast to previous realisations, the underlying mechanism evoking the topological protection does not rely on precisely matched phase differences and is therefore considerably less dependent on the emission wavelength.

To substantiate this aspect, the Michelson interferometry was repeated at an elevated temperature of 200 K, resulting in a shift of the emission energy by approximately 10 meV.

The resulting real space image, interference pattern as well as the spatial coherence map, input-output characteristic and spectral analysis are presented in Fig. 6.21. Again, single-mode lasing of the topological mode as well as interference fringes along the entire interface were observed. The fluctuations in intensity along the interface as well as the increased noise level in the spatial coherence map can, in part, be explained by a considerably lower stability of the sample position within the cryostat at this elevated temperature. It is, however, important to note that the linewidth of 247 µeV of the integrated spectrum along the full interface has not changed with respect to the measurements at a temperature of $T = 4\,\mathrm{K}$. As expected, the separation of the topological propagation from the emission direction and the use of a topologically non-trivial mode not relying on phase differences drastically reduced the dependence of the topological protection on the emission wavelength. Additionally, the coherence observed at an elevated temperature of $T = 200\,\mathrm{K}$ is very promising, as the samples investigated here were not optimised for room temperature operation, in particular under the consideration that VCSELs operating at room temperature are already commercially available. Furthermore, electrical injection of a micropillar lattice has already been demonstrated [Suc+18], allowing to envision commercial applications of topological insulator VCSELs arrays. The results presented in this section were published in reference [Dik+21] and were filed as patent application [Seg+21].

7 Engineering of polaritonic band structures

The band structure of a polariton lattice is determined by the geometry in which the pillars are arranged. To design a band structure with certain features it is therefore fruitful to think about possible lattice geometries. As introduced in section 2.3.3, there are five two-dimensional Bravais lattices, namely the oblique, square, rectangular, centred rectangular and hexagonal lattices. Starting from these lattices, further lattices were derived by increasing the number of sites within a unit cell, resulting for example in the Lieb, Honeycomb and Kagome lattices. These lattices already feature significantly more interesting band structures hosting Dirac cones and flatbands.

Additionally to Bravais lattices and their derived lattices, quasicrystals representing an ordered arrangement of sites without translational symmetry, such as the penrose tiling, offer the opportunity towards an entirely different approach of thinking about band structures. Research on quasicrystals started in the context of research on materials and their properties [She+84]. From there, the research field advanced towards artificial lattices where photonic, quasicrystalline structures were implemented [SS07] and connections between quasicrystals and topological physics were discovered [Kra+12; BRS16]. With the investigation of a one-dimensional Fibonacci chain, quasicrystals reached the field of polaritonics [Bab+17].

Next to designing entirely new lattice geometries, existing lattices can be modified through strain. At the centre of this development is strained graphene, where strain induced gauge fields act as magnetic fields for wave packets close to the Dirac points. Due to these gauge fields, the band structure is altered from the well-known graphene band structure to the characteristic Landau levels of the quantum Hall effect without the need for an actual magnetic field [PCP09; Lev+10; GKG10; Yan+12]. Starting from strained graphene, the concept of strain-induced gauge fields reached photonics, where actual physical strain is replaced by designing the lattice of waveguides or microresonators that constitute the lattice such that is represents a certain strain geometry [SH13; Rec+13b; Rec+13c].

Finally, the derived lattices introduced above offer another degree of freedom towards modifying the band structure, as the sites within each unit cell can be unbalanced by

equipping them with different eigenenergies. For the honeycomb lattice, this idea was first described by Semenoff in 1984 [Sem84]. As a band gap is opened at the Dirac points of an unbalanced honeycomb lattices, this research direction is closely related to the quantum valley Hall effect and was transferred to artificial lattices such as photonic lattices as well [Col+16]. In this chapter, the idea of unbalancing the sites within a unit cell is applied to polaritonic EnO lattices in the Lieb geometry in section 7.1 and honeycomb lattices in section 7.2.

7.1 Band gaps in unbalanced Lieb lattices

The aim of this section is to implement Lieb lattices with unbalanced eigenenergies of the sites within the unit cell as an additional degree of freedom to engineer the band structure. As the eigenenergies of the microtraps constituting a polariton lattice depend on the diameter of the traps, studying individual traps represents an ideal starting point towards an unbalanced Lieb lattice. In Figs. 7.1 a) and b), exemplary real space spectra of individual traps on sample Ga-EnO1 with diameters of $d = 2.0\,\mu\text{m}$ and $d = 6.0\,\mu\text{m}$ that were excited with a small, cw laser spot are presented. By comparing these two spectra one can clearly observe that the modes of the smaller trap are blue-shifted with respect to the larger trap. Furthermore, the energetic separation between the individual modes increases as expected from a potential well with a smaller size. The evaluation of the S mode position with respect to the diameter of the traps presented in Fig. 7.1 c) reveals that a significant variation of the energetic position of the S mode is achievable for traps with a diameter smaller than $d = 4.0\,\mu\text{m}$. Even though the traps that were investigated for this evaluation were located in close proximity on the wafer, the data was corrected for the MBE growth induced detuning gradient arising due to the radial shift of the photonic mode across the wafer. In a linear approximation, the energy of the S mode is shifted by 1.7 meV per micrometer for traps smaller than $d = 4.0\,\mu\text{m}$.
Based on this insight, unbalanced Lieb lattices on sample Ga-EnO1 located at a detuning of $\Delta_\text{E} \approx -7.6\,\text{meV}$ were investigated. In Figs. 7.2 a)-c), Fourier space spectra of Lieb lattices comprised of B and C sites with diameters of $d_\text{B} = d_\text{C} = 2.0\,\mu\text{m}$ and A sites with diameters of $d_\text{A} = 2.0\,\mu\text{m}$, $2.2\,\mu\text{m}$ and $2.4\,\mu\text{m}$, respectively, along the X-Γ-X direction are presented. The centre-to-centre distances between adjacent sites are $a = 2.00\,\mu\text{m}$, $1.98\,\mu\text{m}$ and $2.16\,\mu\text{m}$, respectively. In Figs. 7.2 d)-f), corresponding Fourier space spectra along the M-X-M direction, cutting through the intersection of the flatband with the dispersive bands at the Dirac point, are displayed. In these spectra a significant change of the band structure due to the unbalancing of the sites in the unit cell is observed, as band gaps of $E_\text{g} = 476\,\mu\text{eV}$ and $E_g = 636\,\mu\text{eV}$ open at the Dirac points of the lattices with A

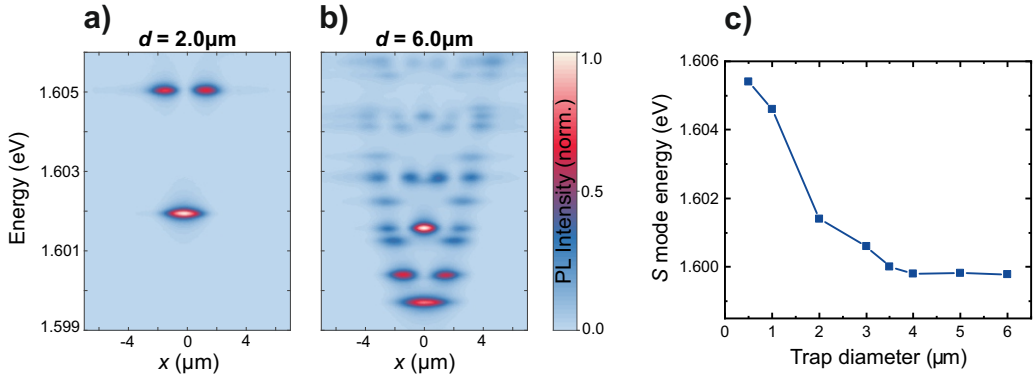

Figure 7.1: Real space spectra of individual EnO microtraps with diameters of $d = 2.0\,\mu m$ in **a)** and $d = 6.0\,\mu m$ in **b)**. **c)** Evaluation of the energetic position of the S mode of individual microtraps with respect to their diameter. The energies were corrected for the spatial detuning gradient due to the radial shift of the photonic mode across the wafer.

site diameters of $d_A = 2.2\,\mu m$ and $d_A = 2.4\,\mu m$, respectively. The size of these band gaps was determined analogously to the evaluation of the band gaps of crystalline topological insulator lattices that is described in the appendix in section A.4. In these unbalanced Lieb lattices, the coupling of the flatband to the dispersive bands is thus drastically changed, as it touches the anti-bonding S sub-band that hosts polaritons with a finite mass at a potential minimum instead of crossing a Dirac point hosting massless polaritons. The three-dimensional reconstructions depicted in Figs. 7.2 g)-i) further visualise the changes to the band structure. The data presented in Fig. 7.2 were reproduced by tight binding models including nearest and next-nearest neighbour coupling as well as the unbalanced eigenenergies in the unit cell. While the bonding S sub-band as well as the S flatband are accurately reproduced, deviations are observed for the anti-bonding S sub-band. These deviations demonstrate that the modal shape as well as the hybridisation with the P band cannot be fully accounted for with a tight binding model and motivate the future development of a Bloch mode description of unbalanced Lieb lattices.

In conclusion, a band gap as well as a drastic change of the coupling environment of the flatband was realised in EnO Lieb lattices by unbalancing the eigenenergies of the sites within the unit cell. These results represent the foundation for detailed future experiments on the coupling between flatbands and dispersive bands that is of crucial importance when envisioning to use flatbands for the distortion-free storage of information [GLN18]. Here, the EnO microcavity polariton platform is particularly suitable as it not only allows the precise engineering of the band structures but also the controlled excitation both in real and Fourier space based on the resonant excitation techniques presented in section 5.2.

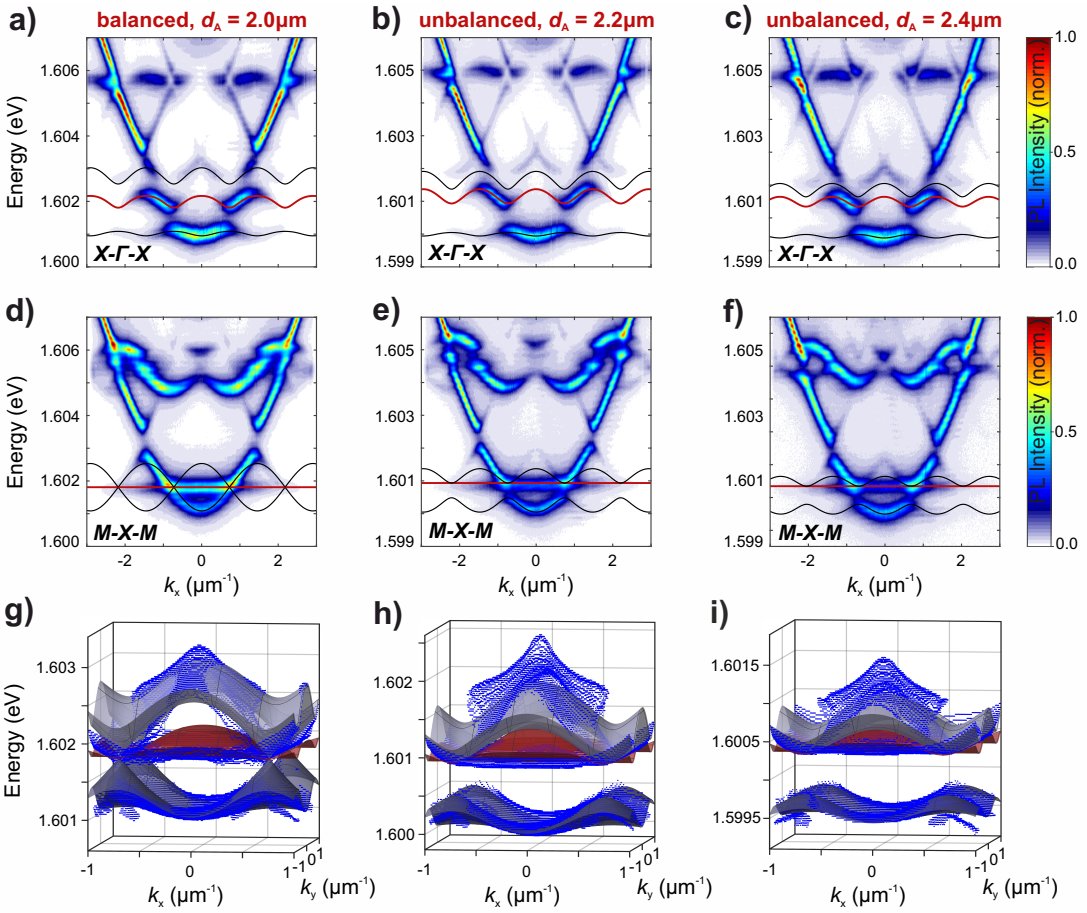

Figure 7.2: **a)-c)** Fourier space spectra along the X-Γ-X direction of Lieb lattices with trap diameters of the B and C sites of $d_B = d_C = 2.0\,\mu m$ and of the A sites of $d_A = 2.0\,\mu m$, $2.2\,\mu m$ and $2.4\,\mu m$, respectively. The data are reproduced by a tight binding model with the flatband highlighted in red. **d)-f)** Corresponding Fourier space spectra along the M-X-M direction, cutting through the intersection of the flatband at the Dirac cones in the M points. **g)-i)** Full band structure reconstruction from the hyperspectral imaging scan (blue data points) including a tight binding fit (surface plot) with the flatband highlighted in red.

7.2 Polariton quantum valley Hall effect

Analogously to the band gap that opens at the Dirac points of an unbalanced Lieb lattice and was demonstrated in the previous section, a band gap can be opened at the Dirac points of a honeycomb lattice by unbalancing the eigenenergies of the two sites of the unit cell. This effect is particularly interesting in the context of the quantum valley Hall effect that is based on describing the two valleys at the K and K' points as pseudospins. While the K and K' points are already inequivalent in a balanced honeycomb lattice, the band gap opened in an unbalanced honeycomb lattice is non-trivial when considering only one of the valleys and thus supports topological transport at domain interfaces. The quantum valley Hall effect was first studied for graphene [RTB07; DYN07; YDN08], where a band gap can be opened by stacking multiple layers of graphene on top of each other [Zha+09b; Liu+19]. In complementary approaches, silicene [Tah+13; Kim+14] as well as transition metal dichalcogenide (TMD) [Mak+14; Lun+19] monolayers have been considered for realisations of quantum valley Hall physics. It is important to note that the quantum valley Hall effect does not result in topological edge modes at the lattice edges, as valleys and valley pseudospins do not exist in vacuum. At a zigzag interface between two domains with permuted sites in the interface, however, a topological boundary exists [YYN09]. But, while lattices with different eigenenergies of the two sites of the unit cells can be realised with TMDs, an interface between two inverted lattices is not possible with these atomic lattices and thus motivates the development of artificial lattice simulators [BSM17; MXS19].

Building upon this background, polaritonic honeycomb lattices with trap diameters of $d_\mathrm{A} = 2.0\,\mu\mathrm{m}$ and $d_\mathrm{B} = 2.4\,\mu\mathrm{m}$ of the A and B sites of the unit cell were fabricated on sample Ga-EnO1 and excited with a large Gaussian, cw laser spot. The centre-to-centre distance of adjacent sites is $a = 2.0\,\mu\mathrm{m}$ and the investigated lattice is located at a detuning of $\Delta_\mathrm{E} = -3.5\,\mathrm{meV}$. Additionally, the lattice features a boundary to a domain with permuted sites in the unit cell, characterised by $d_\mathrm{A} = 2.4\,\mu\mathrm{m}$ and $d_\mathrm{B} = 2.0\,\mu\mathrm{m}$. Based on the results presented in the previous section, an easily observable band gap would be expected. However, for the given parameters, the band gap is too small to be observed in the Fourier spectrum along the K-Γ-K' direction presented in Fig. 7.3 a). This reduction of the effect of unbalancing the eigenenergies is most likely induced by a deformation of the modes due to the overlap between adjacent sites that compensates the difference in trap diameter and confinement of the individual traps. Even though the band gap appears to be smaller than the linewidth, it is worthwhile to study the real space spectrum across the boundary between the two domains of the lattice that is presented in Fig. 7.3 b). In this spectrum, a gap between the bonding and anti-bonding S sub-bands can be observed.

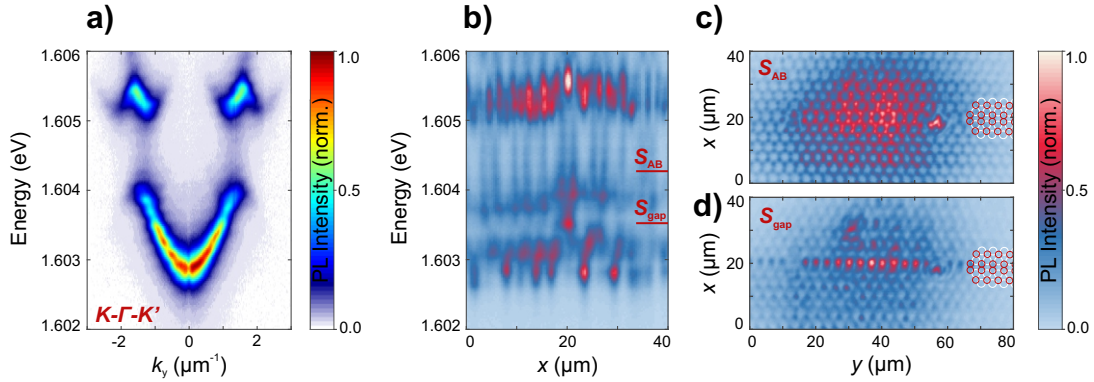

Figure 7.3: **a)** Fourier space spectrum along the K-Γ-K' direction of an unbalanced honeycomb lattice with trap diameters of $d_A = 2.0\,\mu m$ (red) and $d_B = 2.4\,\mu m$ (white). **b)** Real space spectrum perpendicular to the zigzag domain wall between two unbalanced honeycomb lattices with permuted sites in the unit cells. **c)-d)** Real space images of the anti-bonding S sub-band and the quantum valley Hall gap mode, respectively.

The size of this gap does not represent the size of the band gap. It is considerably larger, as the real space emission is convoluted with the polariton density distribution. As the highest occupation occurs at an energetic distance to the Dirac points, the gap is enhanced in a real space spectrum. Within this gap, a boundary mode at the interface of the two domains arises due to the quantum valley Hall mechanism. This observation is confirmed by the real space image of this gap mode presented in Fig. 7.3 d). The geometry of the lattice can be seen in the real space image of the anti-bonding S sub-band presented in Fig. 7.3 c), where additionally the interface between the two domains is highlighted by the lattice schematic consisting of red and white rings corresponding to traps with diameters of $d = 2.0\,\mu m$ and $d = 2.4\,\mu m$, respectively.

In summary, the quantum valley Hall boundary mode arising at the interface between two unbalanced honeycomb lattices with permuted sites of the unit cell was demonstrated. Even though the band gap induced by the unbalancing is still smaller than the polaritonic linewidth, this result opens the path towards future experiments on the polariton quantum valley Hall effect, as the gap size can be increased by increasing the distance between adjacent sites and increasing the size difference between the sites of the unit cell. The starting point presented here is particularly valuable in the context of a recent theoretical proposal by Bleu and co-workers [BMS18] who suggest to lock the winding of a propagating vortex to the valley index to realise true topological protection of the valley pseudospin.

8 Summary and outlook

The fascination of microcavity exciton-polaritons (polaritons) rests upon the combination of advanced technological control over both the III-V semiconductor material platform as well as the precise spectroscopic access to polaritonic states, which provide access to the investigation of open questions and complex phenomena due to the inherent nonlinearity and direct spectroscopic observables such as energy-resolved real and Fourier space information, pseudospin and coherence. The focus of this work was to advance the research area of polariton lattice simulators with a particular emphasis on their lasing properties. Following the brief introduction into the fundamental physics of polariton lattices in chapter 2, important aspects of the sample fabrication as well as the Fourier spectroscopy techniques used to investigate various features of these lattices were summarised in chapter 3. Here, the implementation of a spatial light modulator for advanced excitation schemes was presented.

At the foundation of this work is the capability to confine polaritons into micropillars or microtraps resulting in discrete energy levels. By arranging these pillars or traps into various lattice geometries and ensuring coupling between neighbouring sites, polaritonic band structures were engineered. In chapter 4, the formation of a band structure was visualised in detail by investigating ribbons of honeycomb lattices. Here, the transition of the discrete energy levels of a single chain of microtraps to the fully developed band structure of a honeycomb lattice was observed. This study allows to design the size of individual domains in more complicated lattice geometries such that a description using band structures becomes feasible, as it revealed that a width of just six unit cells is sufficient to reproduce all characteristic features of the S band of a honeycomb lattice. In particular in the context of potential technological applications in the realms of lasing, the laser-like, coherent emission from polariton microcavities that can be achieved through the excitation of polariton condensates is intriguing. The condensation process is significantly altered in a lattice potential environment when compared to a planar microcavity. Therefore, an investigation of the polariton condensation process in a lattice with respect to the characteristics of the excitation laser, the exciton-photon detuning as well as the reduced trap distance that represents a key design parameter for polaritonic lattices was performed. Based on the demonstration of polariton condensation into multiple bands,

the preferred condensation into a desired band was achieved by selecting the appropriate detuning. Additionally, a decreased condensation threshold in confined systems compared to a planar microcavity was revealed.

In chapter 5, the influence of the peculiar feature of flatbands arising in certain lattice geometries, such as the Lieb and Kagome lattices, on polaritons and polariton condensates was investigated. Deviations from a lattice simulator described by a tight binding model that is solely based on nearest neighbour coupling cause a remaining dispersiveness of the flatbands along certain directions of the Brillouin zone. Therefore, the influence of the reduced trap distance on the dispersiveness of the flatbands was investigated and precise technological control over the flatbands was demonstrated. As next-nearest neighbour coupling is reduced drastically by increasing the distance between the corresponding traps, increasing the reduced trap distance enables to tune the S flatbands of both Lieb and Kagome lattices from dispersive bands to flatbands with a bandwidth on the order of the polariton linewidth. Additionally to technological control over the band structures, the controlled excitation of large condensates, single compact localized state (CLS) condensates as well as the resonant excitation of polaritons in a Lieb flatband were demonstrated. Furthermore, selective condensation into flatbands was realised. This combination of technological and spectroscopic control illustrates the capabilities of polariton lattice simulators and was used to study the coherence of flatband polariton condensates. Here, the ability to tune the dispersiveness from a dispersive band to an almost perfect flatband in combination with the selectivity of the excitation is particularly valuable. By exciting large flatband condensates, the increasing degree of localisation to a CLS with decreasing dispersiveness was demonstrated by measurements of first order spatial coherence. Furthermore, the first order temporal coherence of CLS condensates was increased from $\tau_{\mathrm{coh}} = 68\,\mathrm{ps}$ for a dispersive flatband, a value typically achieved in high-quality microcavity samples, to a remarkable $\tau_{\mathrm{coh}} = 459\,\mathrm{ps}$ in a flatband with a dispersiveness below the polarion linewidth. Corresponding to this drastic increase of the first order coherence time, a decrease of the second order temporal coherence function from $g^{(2)}(\tau = 0) = 1.062$ to $g^{(2)}(0) = 1.035$ was observed. Next to laser-like, coherent emission, polariton condensates can form vortex lattices. In this work, two distinct vortex lattices that can form in polariton condensates in Kagome flatbands were revealed. Furthermore, chiral, superfluid edge transport was realised by breaking the spatial symmetry through a localised excitation spot. This chirality was related to a change in the vortex orientation at the edge of the lattice and thus opens the path towards further investigations of symmetry breaking and chiral superfluid transport in Kagome lattices.

Arguably the most influential concept in solid-state physics of the recent decades is the idea of topological order that has also provided a new degree of freedom to control the

propagation of light. Therefore, in chapter 6, the interplay of topologically non-trivial band structures with polaritons, polariton condensates and lasing was emphasised. Firstly, a two-dimensional exciton-polariton topological insulator based on a honeycomb lattice was realised. Here, a topologically non-trivial band gap was opened at the Dirac points through a combination of TE-TM splitting of the photonic mode and Zeeman splitting of the excitonic mode. While the band gap is too small compared to the linewidth to be observed in the linear regime, the excitation of polariton condensates allowed to observe the characteristic, topologically protected, chiral edge modes that are robust against scattering at defects as well as lattice corners. This result represents a valuable step towards the investigation of non-linear and non-Hermitian topological physics, based on the inherent gain and loss of microcavities as well as the ability of polaritons to interact with each other. Apart from fundamental interest, the field of topological photonics is driven by the search of potential technological applications, where one direction is to advance the development of lasers. In this work, the starting point towards studying topological lasing was the Su-Schrieffer-Heeger (SSH) model, since it combines a simple and well-understood geometry with a large topological gap. The coherence properties of the topological edge defect of an SSH chain was studied in detail, revealing a promising degree of second order temporal coherence of $g^{(2)}(0) = 1.07$ for a microlaser with a diameter of only $d = 3.5\,\mu\text{m}$. In the context of topological lasing, the idea of using a propagating, topologically protected mode to ensure coherent coupling of laser arrays is particularly promising. Here, a topologically non-trivial interface mode between the two distinct domains of the crystalline topological insulator (CTI) was realised. After establishing selective lasing from this mode, the coherence properties were studied and coherence of a full, hexagonal interface comprised of 30 vertical-cavity surface-emitting lasers (VCSELs) was demonstrated. This result thus represents the first demonstration of a topological insulator VCSEL array, combining the compact size and convenient light collection of vertically emitting lasers with an in-plane topological protection.

Finally, in chapter 7, an approach towards engineering the band structures of Lieb and honeycomb lattices by unbalancing the eigenenergies of the sites within each unit cell was presented. For Lieb lattices, this technique opens up a path towards controlling the coupling of a flatband to dispersive bands and could enable a detailed study of the influence of this coupling on the polariton flatband states. In an unbalanced honeycomb lattice, a quantum valley Hall boundary mode between two distinct, unbalanced honeycomb domains with permuted sites in the unit cells was demonstrated. This boundary mode could serve as the foundation for the realisation of a polariton quantum valley Hall effect with a truly topologically protected spin based on vortex charges. Modifying polariton lattices by unbalancing the eigenenergies of the sites that comprise a unit cell was thus identified as an additional, promising path for the future development of polariton lattice simulators.

In conclusion, the unique combination of an inherent non-linearity, extensive spectroscopic access and advanced fabrication techniques was used to advance microcavity polaritons as lattice simulators that combine technological applicability with access to open physical questions of fundamental interest. One of the most convincing directions towards technological applications is the development of new types of lasers based on the potentially low threshold of polariton lasers [Ima+96; Sch+13] or the coherent coupling of lasers based on topologically protected modes [Bah+17; Ban+18; Har+18]. While topological lasers are already highly exciting as photonic laser arrays based on coupled VCSELs, the recent progess in the development of polaritonic lattices based on new material platforms, such as perovskites and organics, may even bring room temperature, topological polariton lasing into consideration [Su+20; Dus+20; Pol+20].

From a fundamental perspective, lattice simulators provide access to a broad range of open questions. First of all, the research on flatbands offers exciting perspectives for subsequent studies of the coupling of flatbands to dispersive bands [GLN18], based on the controlled excitation of polariton wave packets at certain points in either the real or the Fourier spectrum. Furthermore, the interaction between multiple CLS condensates offers interesting open questions [Lon19].

For topologically non-trivial lattices, the realisation of a topologically protected quantum valley Hall state [BMS18], applying the concepts of Floquet theory to the polariton platform [GBL18] or investigating the topology of quasicrystals [BRS16] are just some examples of exciting ideas. When thinking even further ahead, it is worth remembering that the concept of topology is influencing large parts of solid-state physics that offer inspiration for future experiments based on the polariton platform. One example is the extension of topological classification from two to three dimensions. Here, the simplest, topologically non-trivial state is the Weyl point, which can be understood as an analogon of the Dirac point that arises in two-dimensional systems. The observation of Weyl points in electronic systems [Lv+15; Xu+15] inspired the development of photonic systems and resulted in the realisation of microwave [Lu+15] and photonic [Noh+17] implementations. Additionally to building three-dimensional structures, the concept of synthetic dimensions provides a path towards accessing the physics of three and even higher dimensions in lattices with two spatial dimensions. This approach is inspired by the ultra-cold atom community, where Thouless pump schemes [Tho83; Loh+18] as well as a spin modal space [Man+15; Stu+15] have been used, and was successfully transferred to coupled photonic waveguides [Zil+18; Lus+19]. This direction of research is particularly interesting as it provides access to higher dimensional effect beyond the three spatial dimensions and could provide inspiration for the development of experiments based on polariton lattices.

Another direction to advance research on topological insulators is based on the perspective that the Berry phase is a formalism describing the electric polarisation in crystals based on electric dipole moments, thus motivating a multipole expansion that results in higher order topological insulators [BBH17]. The topological edge and boundary modes in first order topological insulators are reduced by one dimension with respect to the lattice bulk, resulting for example in the one-dimensional edge states that are observed in two-dimensional lattices. Consequently, a second order, two-dimensional topological insulator features zero-dimensional corner modes which have already been realised in photonics [Noh+18b; Mit+19; Li+20]. In this context, polariton lattices could provide new insight for example on the coupling between corner modes through edge states [BML20]. Covering all of these future directions is the notion that the polariton lattice simulator platform features inherent non-linearities that are induced by inter-particle interactions as well as gain and loss. The latter is particularly interesting in the context of parity-time ($\mathcal{PT}$)-symmetric Hamiltonians. Generally, it was assumed that only hermitian Hamiltonians have real eigenvalues. However, Bender and Boettcher found that the same holds true for Hamiltonians that are $\mathcal{PT}$-symmetric [BB98]. Photonics is particularly suited for experimental realisations of such Hamiltonians, as parity and time symmetry translate into symmetries of the real and imaginary parts of the complex refractive index [Özd+19]. While $\mathcal{PT}$-symmetric Hamiltonians offer interesting open research questions in themselves, the combination with other phenomena, such as topological physics, enhances the impact even further [Wei+17].

When thinking even further ahead and following the ultra-cold atom community, bringing polariton lattice simulators to the realms of quantum mechanics represents a very promising path towards unexplored phenomena. Here, the on-chip nature of the polariton platform represents an important advantage. As a first step, a polariton blockade in a single micropillar has recently been demonstrated [VCC06; Del+19; Muñ+19]. While the reported degree of anti-bunching is still modest, further technological optimisation can be performed based on this first demonstration, until eventually quantum computing operations [GL20] or a lattice of coupled polariton micropillars each showing a polariton blockade could be envisioned. Another technological approach towards bringing polariton lattice simulators into the realms of quantum mechanics could rely on site-controlled quantum dots arranged such that there is one quantum dot in each site of the lattice [Sch+09]. Alternatively, an approach of realising a polariton qubit based on ring currents [Luk+18; Xue+21] could be implemented. Again, the combination with topological physics could help to protect quantum states as single photons could be transported in topologically protected modes [Bar+18; Bla+18; MGH18].

All of these ideas profit from the technological progress in both the fabrication of po-

lariton lattices as well as the spectroscopical access. Here, in particular the use of EnO lattices under resonant excitation in transmission geometry appears particularly promising. Throughout the development of the research field of polaritonics, experiments were performed at negative detunings with a large photonic fraction, as the smaller photonic linewidth in combination with the larger coupling and efficient relaxation processes simplify spectroscopic experiments. However, it is the excitonic component that differentiates polaritonics from photonics. Therefore, experiments under resonant excitation that do not depend on relaxation mechanisms but allow the precise excitation of wave packets at a certain position in the dispersion relation represents a powerful technique for future experiments. Furthermore, the active modulation of a lattice potential environment by exciting for example only one sublattice, which becomes feasible based on the implementation of an SLM, motivates to envision new research directions.

To conclude, the results presented in this work combined with the broad range of ideas for the future development of polariton lattice simulators leave little doubt that the capability of the polariton platform to provide extensive access to visualise complex physical phenomena will continue to draw fascination.

9 Zusammenfassung

Die Faszination von Exziton-Polaritonen (Polaritonen) basiert auf der einzigartigen Kombination aus technologischer Kontrolle über die III-V Halbleiterplattform und umfassendem spektroskopischen Zugang zu polaritonischen Zuständen, die aufgrund ihrer inhärenten Nichtlinearität und vielfältigen Observablen, wie zum Beispiel Real- und Fourierraumspektren, Pseudospin und Kohärenz, Zugang zu diversen offenen Fragen und komplexen physikalischen Phänomenen bieten. Im Fokus dieser Arbeit lag die Weiterentwicklung von Polaritongittern als Simulatoren für diverse physikalische Phänomene. Dabei wurde insbesondere die das kohärente, Laser-artige Licht, das von Polaritonkondensaten ausgesendet wird, untersucht. Die Arbeit beginnt mit einer kurzen Zusammenfassung der für das Verständnis relevanten physikalischen Grundlagen in Kapitel 2, gefolgt von einer Beschreibung der Probenherstellung sowie der spektroskopischen Methoden, die für die Untersuchung der polaritonischen Gitter verwendet wurden, in Kapitel 3. Hier wurde insbesondere die Implementierung eines *Spatial Light Modulators*[1] für die Erzeugung beliebig definierbarer Anregunsmuster präsentiert.

Diese Arbeit basiert auf der Fähigkeit, Einschlusspotentiale in Form von Mikrotürmchen oder Mikrofallen für Polaritonen zu erzeugen, die zu einem diskretisierten Modenspektrum führen. Wird nun ein Gitter aus solchen Türmchen oder Fallen hergestellt, führt die Kopplung zwischen benachbarten Gitterpositionen zur Ausbildung von Bandstrukturen. Die Ausbildung einer solchen Bandstruktur wurde in Kapitel 4 anhand von Streifen eines Honigwabengitters veranschaulicht. Dabei konnte der Übergang vom diskreten Energiespektrum einer eindimensionalen Kette bishin zur vollständig ausgebildeten Bandstruktur eines Honigwabengitters dargestellt werden. Diese systematische Untersuchung ermöglicht das gezielte Design neuer, komplizierterer Gittergeometrien, die aus verschiedenen Domänen bestehen, da gezeigt werden konnte, dass eine Domänengröße von sechs Einheitszellen ausreicht, um eine Bandstruktur zu erzeugen. Neben der Ausbildung von Bandstrukturen in Gittern ist das Phänomen der Polaritonkondensation, das zur Emission von kohärenter Strahlung führt, besonders spannend, da es in direktem Bezug zu möglichen technologischen Anwendungen als Laser steht. Da sich der Kondensationsprozess in einem Gitter grundsätzlich vom Kondensationsprozess in einer planaren

[1] engl.: Gerät zur räumlichen Modulation von Licht

Kavität unterscheidet, wurde dieser detailliert untersucht. Hierbei wurde insbesondere der Einfluss des Anregungslasers, der Verstimmung zwischen Exziton und Photon, sowie des reduzierten Fallenabstandes, der einen wichtigen Parameter im Design neuer Gitter darstellt, untersucht. Im Rahmen dieser Untersuchung konnte die Polaritonkondensation in mehrere Bänder nachgewiesen werden. Außerdem wurde selektive Kondensation in ein gewünschtes Band durch die Wahl einer geeigneten Verstimmung zwischen Exziton und Photon erreicht. Abschließend konnte eine Verringerung der Kondensationsschwelle in einem Gitter gegenüber einer planaren Kavität nachgewiesen werden.
Ein bemerkenswertes Phänomen, das zum Beispiel in den Bandstrukturen von Lieb- und Kagomegittern auftritt, sind Flachbänder, deren Einfluss auf Polaritonen und Polaritonkondensate, insbesondere in Bezug zu ihren Kohärenzeigenschaften, in Kapitel 5 untersucht wurde. Abweichungen von einem Gittersimulator, der sich mit einem *Tight Binding*[2] Modell, das nur Kopplung zwischen nächsten Nachbarn berücksichtigt, beschreiben lässt, führen dazu, dass Flachbänder entlang bestimmter Richtungen in der Brillouinzone dispersiv werden. Mit einer Untersuchung des Einflusses des reduzierten Fallenabstandes auf Flachbänder konnte technologische Kontrolle über diese Dispersivität gezeigt werden. Da die Kopplung zwischen übernächsten Nachbarn mit steigendem Abstand zwischen den Fallen stark abnimmt, lassen sich die Flachbänder in den S Bändern von Lieb- und Kagomegittern von dispersiven in nahezu perfekte Flachbänder, deren Bandbreite in der Größenordnung der polaritonischen Linienbreite liegt, überführen, indem der reduzierte Fallenabstand vergrößert wird. Zusätzlich zur technologischen Kontrolle über die Dispersivität der Flachbänder wurde die kontrollierte Anregung von großen Flachbandkondensaten, Kondensaten in einzelnen *Compact Localised States* (CLS)[3], sowie die resonante Anregung von Polaritonen in einem Lieb Flachband demonstriert. Insbesondere für das Flachband des Kagomegitters konnte selektive Kondensation realisiert werden. Diese Kombination aus technologischer und spektroskopischer Kontrolle verdeutlicht das Potential polaritonischer Gittersimulatoren. Aufbauend auf der Kontrolle über polaritonische Flachbänder wurde die Kohärenz von Flachbandkondensaten untersucht. In diesem Zusammenhang erwies sich die Kombination aus der Möglichkeit, die Dispersivität des Flachbandes zu beeinflussen, und der selektiven Kondensation als besonders wertvoll. Durch interferometrische Messungen an großen Flachbandkondensaten konnte gezeigt werden, dass sich die Kohärenz mit abnehmender Dispersivität des Flachbandes auf einen CLS lokalisiert. Außerdem konnte eine Steigerung der Kohärenzzeit von $\tau_{\mathrm{coh}} = 68\,\mathrm{ps}$, einem für hochwertige Mikrokavitäten typischen Wert, in einem dispersiven Flachband

[2] engl.: enge Bindung; Methode zur Berechnung von Bandstrukturen basierend auf stark gebundenen Zuständen
[3] engl.: kompakter, lokalisierter Zustand

zu beeindruckenden $\tau_{\mathrm{coh}} = 459\,\mathrm{ps}$ in einem Flachband, dessen Dispersivität kleiner als die polaritonische Linienbreite ist, gezeigt werden. Passend zu dieser deutlichen Steigerung der Kohärenzzeit erster Ordnung konnte eine Abnahmde der Kohärenzfunktion zweiter Ordnung von $g^{(2)}(\tau = 0) = 1.062$ zu $g^{(2)}(0) = 1.035$ beobachtet werden. Neben den mit einem Laser vergleichbaren Emissionseigenschaften können Polaritonkondensate Gitter aus Vortices ausbilden. Im Rahmen dieser Arbeit wurden zwei verschiedene Vortexgitter nachgewiesen. Außerdem konnte durch Symmetriebrechung mittels eines lokalisierten Anregungslasers chiraler, superfluider Randtransport realisiert werden. Diese Chiralität konnte mit einer Änderung der Vortexausrichtung am Rand des Gitters in Verbindung gebracht werden und motiviert daher weitere Untersuchungen zu Symmetriebrechung und chiralem, superfluidem Transport in Kagomegittern.

Das vermutlich einflussreichste Konzept in der Festkörperphysik der letzten Jahrzehnte ist die Idee einer topologischen Ordnung, die auch einen neuen Freiheitsgrad zur Kontrolle der Propagation von Licht bietet. Daher wurde in Kapitel 6 das Zusammenspiel aus topologisch nicht-trivialen Bandstrukturen und Polaritonen, Polarionkondensaten und Lasern untersucht. Zuerst wurde ein zweidimensionaler, polaritonischer, topologischer Isolator, der auf einem Honigwabengitter basiert, realisiert. Die topologisch nicht-triviale Bandlücke wurde durch eine Kombination aus einer Modenaufspaltung zwischen der transversal-elektrischen und der transversal-magnetischen Komponente der photonischen Mode sowie einer Zeeman-Aufspaltung der exzitonischen Mode geöffnet. Da die Bandlücke zu klein gegenüber der Linienbreite war, um sie im linearen Regime nachweisen zu können, wurden Polaritonkondensate angeregt. Mithilfe dieser Kondensate war es möglich, die charakteristischen, topologisch geschützten, chiralen Randmoden, die robust gegenüber Rückstreuung und Streuung an Defekten sowie den Ecken des Gitters sind, nachzuweisen. Dieses Ergebnis stellt einen wichtigen Schritt in der Untersuchung nicht-linearer und nicht-hermitischer, topologischer Systeme dar, da Mikrokavitäten eine intrinsische Nichtlinearität aufweisen und Polaritonen untereinander wechselwirken können. Neben dem fundamentalen Interesse wird das Feld der topologischen Photonik vor allem durch die Suche nach neuen technologischen Anwendungen vorangetrieben. Eine wichtige Forschungsrichtung ist dabei die Entwicklung neuer Laser. In dieser Arbeit war der Ausgangspunkt für die Untersuchung topologischer Laser das Su-Schrieffer-Heeger (SSH) Modell, da es eine einfache, gut verstandene Geometrie und eine große topologische Bandlücke bietet. Die Kohärenzeigenschaften des topologischen Randdefekts in SSH Ketten wurden detailliert untersucht und ein Grad zeitlicher Kohärenz zweiter Ordnung von $g^{(2)}(0) = 1.07$ erreicht. Für einen Mikrolaser mit einem Durchmesser von nur $d = 3.5\,\mu\mathrm{m}$ ist dies ein sehr gutes Ergebnis. Besonders vielversprechend in der Entwicklung topologischer Laser ist allerdings vor allem die kohärente Kopplung vieler Laser mithilfe einer propagierenden, topolo-

gisch geschützten Mode. Um diese Kopplung zu untersuchen wurde eine topologisch nichttriviale Mode an der Domänengrenze zwischen zwei kristallinen, topologischen Isolatoren implementiert. Nachdem selektive Laseremission aus dieser Mode erreicht wurde, wurden insbesondere die Kohärenzeigenschaften untersucht. Dabei konnte gezeigt werden, dass 30 vertikal emittierende Laser, die eine geschlossene, hexagonale Domänengrenze bilden, kohärent gekoppelt werden können. Dieser erste Nachweis eines topologisch geschützten Gitters aus gekoppelten, vertikal emittieren Lasern überzeugt vor allem durch die Kombination der kompakten Bauform und einfachen Bündelung der Laseremission vertikal emittierenden Laser mit dem topologischem Schutz der zwischen den Lasern propagierenden Mode.

Zuletzt wurde in Kapitel 7 untersucht, wie die Bandstrukturen von Lieb- und Honigwabengittern durch die Einführung eines Energieunterschiedes zwischen den Untergittern gezielt verändert werden können. In Liebgittern bietet diese Technologie einen Weg, die Kopplungsumgebung des Flachbandes drastisch zu ändern, da das Flachband nun nicht mehr einen Dirac-Punkt mit linearer Dispersion schneidet, sondern ein dispersives Band an einem Potentialminimum berührt. In Honigwabengittern konnte eine *Quantum Valley Hall*[4] Mode an der Grenzfläche zwischen zwei Domänen mit invertiertem Untergitter gezeigt werden. Diese Mode könnte die Basis für die Entwicklung eines Quantum Valley Hall Zustandes mit echtem topologischem Schutz auf der Basis von Vortizes bilden. Eine Variation der Eigenenergien der Untergitter stellt also einen vielversprechenden, weiteren Weg für zukünftige Experimente mit polaritonischen Gittersimulatoren dar.

[4]engl.: Effekt aus der Familie der Quantenhalleffekte, der auf dem Unterschied der K und K' Punkte des Honigwabengitters beruht

References

[Ada85] S. Adachi. GaAs, AlAs, and $Al_xGa_{1-x}As$: Material parameters for use in research and device applications. *Journal of Applied Physics* **58** (3), R1–R29 (1985).

[Adi+15] A. F. Adiyatullin et al. Temporally resolved second-order photon correlations of exciton-polariton Bose-Einstein condensate formation. *Applied Physics Letters* **107** (22), 221107 (2015).

[Adi+17] A. F. Adiyatullin et al. Periodic squeezing in a polariton Josephson junction. *Nature Communications* **8** (1), 1329 (2017).

[Aid+15] M. Aidelsburger et al. Measuring the Chern number of Hofstadter bands with ultracold bosonic atoms. *Nature Physics* **11** (2), 162 (2015).

[AGJ15] V. V. Albert, L. I. Glazman, and L. Jiang. Topological properties of linear circuit lattices. *Physical Review Letters* **114** (17), 173902 (2015).

[AAR12] I. L. Aleiner, B. L. Altshuler, and Y. G. Rubo. Radiative coupling and weak lasing of exciton-polariton condensates. *Physical Review B* **85** (12) (2012).

[Aly+20] S. Alyatkin et al. Optical Control of Couplings in Polariton Condensate Lattices. *Physical Review Letters* **124** (20), 207402 (2020).

[AC20] I. Amelio and I. Carusotto. Theory of the Coherence of Topological Lasers. *Physical Review X* **10** (4), 041060 (2020).

[Amo+09a] A. Amo et al. Collective fluid dynamics of a polariton condensate in a semiconductor microcavity. *Nature* **457** (7227), 291–295 (2009).

[Amo+11] A. Amo et al. Polariton superfluids reveal quantum hydrodynamic solitons. *Science* **332** (6034), 1167–1170 (2011).

[AB16] A. Amo and J. Bloch. Exciton-polaritons in lattices: A non-linear photonic simulator. *Comptes Rendus Physique* **17** (8), 934–945 (2016).

[Amo+09b] A. Amo et al. Superfluidity of polaritons in semiconductor microcavities. *Nature Physics* **5** (11), 805–810 (2009).

[AE15] A. Andrae and T. Edler. On Global Electricity Usage of Communication Technology: Trends to 2030. *Challenges* **6** (1), 117–157 (2015).

[Ang17] D. G. Angelakis, ed. *Quantum Simulations with Photons and Polaritons: Merging Quantum Optics with Condensed Matter Physics*. Quantum Science and Technology. Cham: Springer, 2017.

[AAM96] H. Aoki, M. Ando, and H. Matsumura. Hofstadter butterflies for flat bands. *Physical Review B* **54** (24), R17296–R17299 (1996).

[AHM10] V. Apaja, M. Hyrkäs, and M. Manninen. Flat bands, Dirac cones, and atom dynamics in an optical lattice. *Physical Review A* **82** (4), 646 (2010).

[AOP16] J. K. Asbóth, L. Oroszlány, and A. Pályi. *A short course on topological insulators: Band structure and edge states in one and two dimensions*. **919**. Lecture notes in physics. Cham et al.: Springer, 2016.

[AM12] N. W. Ashcroft and N. D. Mermin. *Solid state Physics*. Brooks/Cole Thomson Learning, 2012.

[Ask+13] A. Askitopoulos et al. Polariton condensation in an optically induced two-dimensional potential. *Physical Review B* **88** (4), 041308 (2013).

[Ask+16] A. Askitopoulos et al. Nonresonant optical control of a spinor polariton condensate. *Physical Review B* **93** (20), 205307 (2016).

[Ask+19] A. Askitopoulos et al. Giant increase of temporal coherence in optically trapped polariton condensate. *arXiv e-prints* 1911.08981 (2019).

[Ata+13] M. Atala et al. Direct measurement of the Zak phase in topological Bloch bands. *Nature Physics* **9** (12), 795–800 (2013).

[Bab+16] F. Baboux et al. Bosonic Condensation and Disorder-Induced Localization in a Flat Band. *Physical Review Letters* **116** (6), 066402 (2016).

[Bab+17] F. Baboux et al. Measuring topological invariants from generalized edge states in polaritonic quasicrystals. *Physical Review B* **95** (16), 161114 (2017).

[Bah+17] B. Bahari et al. Nonreciprocal lasing in topological cavities of arbitrary geometries. *Science* **358** (6363), 636–640 (2017).

[Baj+08] D. Bajoni et al. Polariton laser using single micropillar GaAs-GaAlAs semiconductor cavities. *Physical Review Letters* **100** (4), 047401 (2008).

[Bal+07] R. Balili et al. Bose-Einstein condensation of microcavity polaritons in a trap. *Science* **316** (5827), 1007–1010 (2007).

[Bal+13] D. Ballarini et al. All-optical polariton transistor. *Nature Communications* **4** (1), 1778 (2013).

[Bal+17] D. Ballarini et al. Macroscopic Two-Dimensional Polariton Condensates. *Physical Review Letters* **118** (21), 215301 (2017).

[Bal+20] D. Ballarini et al. Polaritonic Neuromorphic Computing Outperforms Linear Classifiers. *Nano letters* **20** (5), 3506–3512 (2020).

[BRS16] M. A. Bandres, M. C. Rechtsman, and M. Segev. Topological Photonic Quasicrystals: Fractal Topological Spectrum and Protected Transport. *Physical Review X* **6** (1), 011016 (2016).

[BS18] M. A. Bandres and M. Segev. Non-Hermitian Topological Systems. *Physics* **11** (1), 96 (2018).

[Ban+18] M. A. Bandres et al. Topological insulator laser: Experiments. *Science* **359** (6381), eaar4005 (2018).

[BML20] R. Banerjee, S. Mandal, and T. C. H. Liew. Coupling between Exciton-Polariton Corner Modes through Edge States. *Physical Review Letters* **124** (6), 063901 (2020).

[BB48] J. Bardeen and W. H. Brattain. The Transistor, A Semi-Conductor Triode. *Physical Review* **74** (2), 230–231 (1948).

[Bar+15] C.-E. Bardyn et al. Topological polaritons and excitons in garden-variety systems. *Physical Review B* **91** (16), 161413 (2015).

[Bar+16] C.-E. Bardyn et al. Chiral Bogoliubov excitations in nonlinear bosonic systems. *Physical Review B* **93** (2), 020502 (2016).

[Bar+18] S. Barik et al. A topological quantum optics interface. *Science* **359** (6376), 666–668 (2018).

[Bar+20] S. Barik et al. Chiral quantum optics using a topological resonator. *Physical Review B* **101** (20), 205303 (2020).

[Bau+00] J. J. Baumberg et al. Parametric oscillation in a vertical microcavity: A polariton condensate or micro-optical parametric oscillation. *Physical Review B* **62** (24), R16247–R16250 (2000).

[Bay+98] M. Bayer et al. Optical Modes in Photonic Molecules. *Physical Review Letters* **81** (12), 2582–2585 (1998).

[Bay+99] M. Bayer et al. Optical Demonstration of a Crystal Band Structure Formation. *Physical Review Letters* **83** (25), 5374–5377 (1999).

[BBH17] W. A. Benalcazar, B. A. Bernevig, and T. L. Hughes. Quantized electric multipole insulators. *Science* **357** (6346), 61–66 (2017).

[BB98] C. M. Bender and S. Boettcher. Real Spectra in Non-Hermitian Hamiltonians Having PT Symmetry. *Physical Review Letters* **80** (24), 5243–5246 (1998).

[BL13] E. J. Bergholtz and Z. Liu. Topological Flat Band Models and Fractional Chern Insulators. *International Journal of Modern Physics B* **27** (24), 1330017 (2013).

[Ber+17] N. G. Berloff et al. Realizing the classical XY Hamiltonian in polariton simulators. *Nature Materials* **16** (11), 1120 (2017).

[BH13] B. A. Bernevig and T. L. Hughes. *Topological insulators and topological superconductors*. Princeton: Princeton University Press, 2013.

[BHZ06] B. A. Bernevig, T. L. Hughes, and S.-C. Zhang. Quantum spin Hall effect and topological phase transition in HgTe quantum wells. *Science* **314** (5806), 1757–1761 (2006).

[Ber84] M. V. Berry. Quantal Phase Factors Accompanying Adiabatic Changes. *Proceedings of the Royal Society A: Mathematical, Physical and Engineering Sciences* **392** (1802), 45–57 (1984).

[Bha+13] P. Bhattacharya et al. Solid state electrically injected exciton-polariton laser. *Physical Review Letters* **110** (20), 206403 (2013).

[BM18] T. Bilitewski and R. Moessner. Disordered flat bands on the kagome lattice. *Physical Review B* **98** (23), 235109 (2018).

[Bir+00] P. Birch et al. A comparison of the iterative Fourier transform method and evolutionary algorithms for the design of diffractive optical elements. *Optics and Lasers in Engineering* **33** (6), 439–448 (2000).

[Bla+16] A. Blanco-Redondo et al. Topological Optical Waveguiding in Silicon and the Transition between Topological and Trivial Defect States. *Physical Review Letters* **116** (16), 163901 (2016).

[Bla+18] A. Blanco-Redondo et al. Topological protection of biphoton states. *Science* **362** (6414), 568–571 (2018).

[BMS18] O. Bleu, G. Malpuech, and D. D. Solnyshkov. Robust quantum valley Hall effect for vortices in an interacting bosonic quantum fluid. *Nature Communications* **9** (1), 3991 (2018).

[BSM16] O. Bleu, D. D. Solnyshkov, and G. Malpuech. Interacting quantum fluid in a polariton Chern insulator. *Physical Review B* **93** (8), 3 (2016).

[BSM17] O. Bleu, D. D. Solnyshkov, and G. Malpuech. Quantum valley Hall effect and perfect valley filter based on photonic analogs of transitional metal dichalcogenides. *Physical Review B* **95** (23), 235431 (2017).

[Ble+18] O. Bleu et al. Effective Theory of Nonadiabatic Quantum Evolution Based on the Quantum Geometric Tensor. *Physical Review Letters* **121** (2), 020401 (2018).

[Blo05] I. Bloch. Ultracold quantum gases in optical lattices. *Nature Physics* **1** (1), 23–30 (2005).

[BDZ08] I. Bloch, J. Dalibard, and W. Zwerger. Many-body physics with ultracold gases. *Reviews of Modern Physics* **80** (3), 885–964 (2008).

[Bod+14] J. D. Bodyfelt et al. Flatbands under correlated perturbations. *Physical Review Letters* **113** (23), 236403 (2014).

[Bos24] S. N. Bose. Plancks Gesetz und Lichtquantenhypothese. *Zeitschrift für Physik* **26** (1), 178–181 (1924).

[Bou+16] T. Boulier et al. Lattices of quantized vortices in polariton superfluids. *Comptes Rendus Physique* **17** (8), 893–907 (2016).

[Bow+17] D. Bowman et al. High-fidelity phase and amplitude control of phase-only computer generated holograms using conjugate gradient minimisation. *Optics express* **25** (10), 11692–11700 (2017).

[Bra+17] B. Bradlyn et al. Topological quantum chemistry. *Nature* **547** (7663), 298–305 (2017).

[BP09] H.-P. Breuer and F. Petruccione. *The theory of open quantum systems*. Oxford: Clarendon Press, 2009.

[Bro+17] S. Brodbeck et al. Experimental Verification of the Very Strong Coupling Regime in a GaAs Quantum Well Microcavity. *Physical Review Letters* **119** (2), 027401 (2017).

[Bro+13] M. A. Broome et al. Photonic boson sampling in a tunable circuit. *Science* **339** (6121), 794–798 (2013).

[But+02] L. V. Butov et al. Towards Bose-Einstein condensation of excitons in potential traps. *Nature* **417** (6884), 47–52 (2002).

[But+06] R. Butté et al. Room-temperature polariton luminescence from a bulk GaN microcavity. *Physical Review B* **73** (3), 033315 (2006).

[BKY14] T. Byrnes, N. Y. Kim, and Y. Yamamoto. Exciton-polariton condensates. *Nature Physics* **10** (11), 803–813 (2014).

[Cao+18a] Y. Cao et al. Correlated insulator behaviour at half-filling in magic-angle graphene superlattices. *Nature* **556** (7699), 80–84 (2018).

[Cao+18b] Y. Cao et al. Unconventional superconductivity in magic-angle graphene superlattices. *Nature* **556** (7699), 43–50 (2018).

[Car+19] N. Carlon Zambon et al. Optically controlling the emission chirality of microlasers. *Nature Photonics* **13** (4), 283 (2019).

[CC13] I. Carusotto and C. Ciuti. Quantum fluids of light. *Reviews of Modern Physics* **85** (1), 299 (2013).

[Cas+09] A. H. Castro Neto et al. The electronic properties of graphene. *Reviews of Modern Physics* **81** (1), 109–162 (2009).

[Cer+10] E. A. Cerda-Méndez et al. Polariton condensation in dynamic acoustic lattices. *Physical Review Letters* **105** (11), 116402 (2010).

[Che+14a] J. G. Checkelsky et al. Trajectory of the anomalous Hall effect towards the quantized state in a ferromagnetic topological insulator. *Nature Physics* **10** (10), 731–736 (2014).

[Che+14b] W.-J. Chen et al. Experimental realization of photonic topological insulator in a uniaxial metacrystal waveguide. *Nature Communications* **5** (1), 5782 (2014).

[CA75] A. Y. Cho and J. R. Arthur. Molecular beam epitaxy. *Progress in Solid State Chemistry* **10** (1), 157–191 (1975).

[CK03] D. S. Citrin and J. B. Khurgin. Microcavity effect on the electron-hole relative motion in semiconductor quantum wells. *Physical Review B* **68** (20), 3314 (2003).

[Col+16] M. J. Collins et al. Integrated optical Dirac physics via inversion symmetry breaking. *Physical Review A* **94** (6), 063827 (2016).

[CDS19] N. R. Cooper, J. Dalibard, and I. B. Spielman. Topological bands for ultracold atoms. *Reviews of Modern Physics* **91** (1), 015005 (2019).

[Dal+14] R. Dall et al. Creation of orbital angular momentum states with chiral polaritonic lenses. *Physical Review Letters* **113** (20), 200404 (2014).

[Das+02] G. Dasbach et al. Tailoring the polariton dispersion by optical confinement: Access to a manifold of elastic polariton pair scattering channels. *Physical Review B* **66** (20), 553 (2002).

[Del+07] G. Della Valle et al. Visualization of coherent destruction of tunneling in an optical double well system. *Physical Review Letters* **98** (26), 263601 (2007).

[DMV17] P. Delplace, J. B. Marston, and A. Venaille. Topological origin of equatorial waves. *Science* **358** (6366), 1075–1077 (2017).

[Del+19] A. Delteil et al. Towards polariton blockade of confined exciton-polaritons. *Nature Materials* **18** (3), 219–222 (2019).

[Dem13] W. Demtröder. *Experimentalphysik 2*. Berlin, Heidelberg: Springer, 2013.

[DHY10] H. Deng, H. Haug, and Y. Yamamoto. Exciton-polariton Bose-Einstein condensation. *Reviews of Modern Physics* **82** (2), 1489–1537 (2010).

[Den+02] H. Deng et al. Condensation of semiconductor microcavity exciton polaritons. *Science* **298** (5591), 199–202 (2002).

[Den+03] H. Deng et al. Polariton lasing vs. photon lasing in a semiconductor microcavity. *Proceedings of the National Academy of Sciences of the United States of America* **100** (26), 15318–15323 (2003).

[Den+07] H. Deng et al. Spatial coherence of a polariton condensate. *Physical Review Letters* **99** (12), 126403 (2007).

[DRM15] O. Derzhko, J. Richter, and M. Maksymenko. Strongly correlated flat-band systems: The route from Heisenberg spins to Hubbard electrons. *International Journal of Modern Physics B* **29** (12), 1530007 (2015).

[Dev06] B. Deveaud. *The Physics of Semiconductor Microcavities*. Wiley-VCH Verlag GmbH & Co. KGaA, 2006.

[Dev12] B. Deveaud-Plédran. On the condensation of polaritons. *Journal of the Optical Society of America B* **29** (2), A138 (2012).

[DCN10] Di Xiao, M.-C. Chang, and Q. Niu. Berry phase effects on electronic properties. *Reviews of Modern Physics* **82** (3), 1959–2007 (2010).

[DYN07] Di Xiao, W. Yao, and Q. Niu. Valley-contrasting physics in graphene: magnetic moment and topological transport. *Physical Review Letters* **99** (23), 236809 (2007).

[Die+16] F. Diebel et al. Conical Diffraction and Composite Lieb Bosons in Photonic Lattices. *Physical Review Letters* **116** (18), 183902 (2016).

[Dik+21] A. Dikopoltsev et al. Topological insulator vertical-cavity laser array. *Science* **373** (6562), 1514–1517 (2021).

[Dir28] P. A. M. Dirac. The Quantum Theory of the Electron. *Proceedings of the Royal Society of London. Series A* **117** (778), 610–624 (1928).

[Doa+05] T. D. Doan et al. Condensation kinetics of microcavity polaritons with scattering by phonons and polaritons. *Physical Review B* **72** (8), 085301 (2005).

[Don+17] J.-W. Dong et al. Valley photonic crystals for control of spin and topology. *Nature Materials* **16** (3), 298–302 (2017).

[Dro+17] R. Drost et al. Topological states in engineered atomic lattices. *Nature Physics* **13** (7), 668–671 (2017).

[Dus+20] M. Dusel et al. Room temperature organic exciton-polariton condensate in a lattice. *Nature Communications* **11** (1), 2863 (2020).

[Ein24] A. Einstein. Quantentheorie des einatomigen idealen Gases. *Verlag der Königlich-Preussischen Akademie der Wissenschaften* 261–267 (1924).

[El +06] O. El Daïf et al. Polariton quantum boxes in semiconductor microcavities. *Applied Physics Letters* **88** (6), 061105 (2006).

[Els03] V. Elser. Phase retrieval by iterated projections. *Journal of the Optical Society of America. A, Optics, image science, and vision* **20** (1), 40–55 (2003).

[Esq+14] P. Esquinazi et al. On the superconductivity of graphite interfaces. *JETP Letters* **100** (5), 336–339 (2014).

[FP97] C. Fabry and A. Pérot. Sur les franges des lames minces argentées et leur application à la mesure de petites épaisseurs d'air. *Annales de Chimie et de Physique* **12** (1), 459–501 (1897).

[FYF12] K. Fang, Z. Yu, and S. Fan. Realizing effective magnetic field for photons by controlling the phase of dynamic modulation. *Nature Photonics* **6** (11), 782–787 (2012).

[Far+08] A. Faraon et al. Coherent generation of non-classical light on a chip via photon-induced tunnelling and blockade. *Nature Physics* **4** (11), 859–863 (2008).

[Fed+19] Z. Fedorova Cherpakova et al. Limits of topological protection under local periodic driving. *Light: Science & Applications* **8** (1), 63 (2019).

[Fie78] J. R. Fienup. Reconstruction of an object from the modulus of its Fourier transform. *Optics letters* **3** (1), 27–29 (1978).

[Fie80] J. R. Fienup. Iterative Method Applied To Image Reconstruction And To Computer-Generated Holograms. *Optical Engineering* **19** (3), 193297 (1980).

[Fie82] J. R. Fienup. Phase retrieval algorithms: a comparison. *Applied optics* **21** (15), 2758–2769 (1982).

[Fis+14] J. Fischer et al. Spatial coherence properties of one dimensional exciton-polariton condensates. *Physical Review Letters* **113** (20), 203902 (2014).

[Fis+96] T. Fisher et al. Electro-optic tuning of vacuum Rabi coupling in semiconductor quantum microcavity structures. *Solid-State Electronics* **40** (1-8), 493–496 (1996).

[Flä+16] N. Fläschner et al. Experimental reconstruction of the Berry curvature in a Floquet Bloch band. *Science* **352** (6289), 1091–1094 (2016).

[FKA16] R. Fleury, A. B. Khanikaev, and A. Alù. Floquet topological insulators for sound. *Nature Communications* **7** 11744 (2016).

[Flo83] G. Floquet. Sur les équations différentielles linéaires à coefficients périodiques. *Annales scientifiques de l'École normale supérieure* **12** 47–88 (1883).

[Fre31] J. Frenkel. On the Transformation of light into Heat in Solids. I. *Physical Review* **37** (1), 17–44 (1931).

[Fuj+96] M. Fujita et al. Peculiar Localized State at Zigzag Graphite Edge. *Journal of the Physical Society of Japan* **65** (7), 1920–1923 (1996).

[Gal+12] M. Galbiati et al. Polariton condensation in photonic molecules. *Physical Review Letters* **108** (12), 126403 (2012).

[Gao+18] T. Gao et al. Controlled Ordering of Topological Charges in an Exciton-Polariton Chain. *Physical Review Letters* **121** (22), 225302 (2018).

[Gar+18] J. C. Gartside et al. Realization of ground state in artificial kagome spin ice via topological defect-driven magnetic writing. *Nature Nanotechnology* **13** (1), 53–58 (2018).

[GH12] A. L. Gaunt and Z. Hadzibabic. Robust digital holography for ultracold atom trapping. *Scientific Reports* **2** (1), 721 (2012).

[GBL18] R. Ge, W. Broer, and T. C. H. Liew. Floquet topological polaritons in semiconductor microcavities. *Physical Review B* **97** (19), 195305 (2018).

[GAN14] I. M. Georgescu, S. Ashhab, and F. Nori. Quantum simulation. *Reviews of Modern Physics* **86** (1), 153–185 (2014).

[Gér+96] J. M. Gérard et al. Quantum boxes as active probes for photonic microstructures: The pillar microcavity case. *Applied Physics Letters* **69** (4), 449–451 (1996).

[GS72] R. W. Gerchberg and W. O. Saxton. A Practical Algorithm for the Determination of Phase from Image and Diffraction Plane Pictures. *Optik* **35** (2), 237–246 (1972).

[Ges+14] J. Gessler et al. Electro optical tuning of Tamm-plasmon exciton-polaritons. *Applied Physics Letters* **105** (18), 181107 (2014).

[GM20] N. J. Ghimire and I. I. Mazin. Topology and correlations on the kagome lattice. *Nature Materials* **19** (2), 137–138 (2020).

[GL20] S. Ghosh and T. C. H. Liew. Quantum computing with exciton-polariton condensates. *npj Quantum Information* **6** (1), 1–6 (2020).

[Gia+20] A. Gianfrate et al. Measurement of the quantum geometric tensor and of the anomalous Hall drift. *Nature* **578** (7795), 381–385 (2020).

[Gla63a] R. J. Glauber. Coherent and Incoherent States of the Radiation Field. *Physical Review* **131** (6), 2766–2788 (1963).

[Gla63b] R. J. Glauber. The Quantum Theory of Optical Coherence. *Physical Review* **130** (6), 2529–2539 (1963).

[Gla07] R. J. Glauber. *Quantum theory of optical coherence: Selected papers and lectures*. Weinheim: Wiley-VCH, 2007.

[GLN18] C. Gneiting, Z. Li, and F. Nori. Lifetime of flatband states. *Physical Review B* **98** (13), 134203 (2018).

[Gob+19] V. Goblot et al. Nonlinear Polariton Fluids in a Flatband Reveal Discrete Gap Solitons. *Physical Review Letters* **123** (11), 113901 (2019).

[Gol11] D. H. Goldstein. *Polarized light*. CRC Press and Taylor & Francis Group, 2011.

[Goo17] J. W. Goodman. *Introduction to fourier optics*. Fourth edition. New York: W.H. Freeman Macmillan learning, 2017.

[Gor+18] M. A. Gorlach et al. Far-field probing of leaky topological states in all-dielectric metasurfaces. *Nature Communications* **9** (1), 909 (2018).

[GB16] T. Guillet and C. Brimont. Polariton condensates at room temperature. *Comptes Rendus Physique* **17** (8), 946–956 (2016).

[GKG10] F. Guinea, M. I. Katsnelson, and A. K. Geim. Energy gaps and a zero-field quantum Hall effect in graphene by strain engineering. *Nature Physics* **6** (1), 30 (2010).

[Gul+16] D. R. Gulevich et al. Kagome lattice from an exciton-polariton perspective. *Physical Review B* **94** (11), 115437 (2016).

[GLS15] C. Guo, S. Liu, and J. T. Sheridan. Iterative phase retrieval algorithms. I: optimization. *Applied optics* **54** (15), 4698–4708 (2015).

[Gut+98] T. Gutbrod et al. Weak and strong coupling of photons and excitons in photonic dots. *Physical Review B* **57** (16), 9950–9956 (1998).

[Guz+14] D. Guzmán-Silva et al. Experimental observation of bulk and edge transport in photonic Lieb lattices. *New Journal of Physics* **16** (6), 063061 (2014).

[HKA16] Y. Hadad, A. B. Khanikaev, and A. Alù. Self-induced topological transitions and edge states supported by nonlinear staggered potentials. *Physical Review B* **93** (15) (2016).

[Haf+13] M. Hafezi et al. Imaging topological edge states in silicon photonics. *Nature Photonics* **7** (12), 1001–1005 (2013).

[Haf+11] M. Hafezi et al. Robust optical delay lines with topological protection. *Nature Physics* **7** (11), 907 (2011).

[Hal88] F. D. M. Haldane. Model for a Quantum Hall Effect without Landau Levels: Condensed-Matter Realization of the "Parity Anomaly". *Physical Review Letters* **61** (18), 2015 (1988).

[HR08] F. D. M. Haldane and S. Raghu. Possible realization of directional optical waveguides in photonic crystals with broken time-reversal symmetry. *Physical Review Letters* **100** (1), 013904 (2008).

[HT56] R. Hanbury Brown and R. Q. TWISS. Correlation between Photons in two Coherent Beams of Light. *Nature* **177** (4497), 27–29 (1956).

[Har+18] G. Harari et al. Topological insulator laser: Theory. *Science* **359** (6381), eaar4003 (2018).

[Har+20] T. H. Harder et al. Exciton-polaritons in flatland: Controlling flatband properties in a Lieb lattice. *Physical Review B* **102** (12), 121302 (2020).

[Har+21a] T. H. Harder et al. Coherent Topological Polariton Laser. *ACS Photonics* **8** (5), 1377–1384 (2021).

[Har+21b] T. H. Harder et al. Kagome Flatbands for Coherent Exciton-Polariton Lasing. *ACS Photonics* **8** (11), 3193–3200 (2021).

[HR06] S. Haroche and J.-M. Raimond, eds. *Exploring the quantum: Atoms, cavities and photons*. Oxford graduate texts. Oxford and New York: Oxford University Press, 2006.

[HK10] M. Z. Hasan and C. L. Kane. Colloquium: Topological insulators. *Reviews of Modern Physics* **82** (4), 3045–3067 (2010).

[Hau+12] H. Haug et al. Temporal first- and second-order correlations in a polariton condensate. *Physical Review B* **85** (20), 205310 (2012).

[Hel+20] T. Helbig et al. Generalized bulk–boundary correspondence in non-Hermitian topolectrical circuits. *Nature Physics* **16** (7), 747–750 (2020).

[Hel+19] T. Helbig et al. Band structure engineering and reconstruction in electric circuit networks. *Physical Review B* **99** (16), 161114 (2019).

[Hen+07] K. Hennessy et al. Quantum nature of a strongly coupled single quantum dot-cavity system. *Nature* **445** (7130), 896–899 (2007).

[HS13] M. A. Herman and H. Sitter. *Molecular Beam Epitaxy: Fundamentals and Current Status*. Springer, 2013.

[Hof+19] T. Hofmann et al. Chiral Voltage Propagation and Calibration in a Topolectrical Chern Circuit. *Physical Review Letters* **122** (24), 247702 (2019).

[Hoh67] P. C. Hohenberg. Existence of Long-Range Order in One and Two Dimensions. *Physical Review* **158** (2), 383–386 (1967).

[Hol21] H. Holzer. *Die Berechnung der Drehschwingungen und ihre Anwendung im Maschinenbau*. Springer, 1921.

[Hop58] J. J. Hopfield. Theory of the Contribution of Excitons to the Complex Dielectric Constant of Crystals. *Physical Review* **112** (5), 1555–1567 (1958).

[Hub16] S. D. Huber. Topological mechanics. *Nature Physics* **12** (7), 621–623 (2016).

[Igl+14] V. I. Iglovikov et al. Superconducting transitions in flat-band systems. *Physical Review B* **90** (9), 094506 (2014).

[Ima+96] A. Imamoglu et al. Nonequilibrium condensates and lasers without inversion: Exciton-polariton lasers. *Physical Review A* **53** (6), 4250–4253 (1996).

[Imh+18] S. Imhof et al. Topolectrical-circuit realization of topological corner modes. *Nature Physics* **14** (9), 925–929 (2018).

[Int14] Intergovernmental Panel on Climate Change. *Climate Change 2014: Synthesis Report. Contribution of Working Groups I, II and III to the Fifth Assessment Report of the Intergovernmental Panel on Climate Change*. Geneva, Switzerland: IPCC, 2014.

[Iof20] Ioffe Physico-Technical Institute. *New Semiconductor Materials. Characteristics and Properties*. 2020. URL: `http://www.matprop.ru/` (visited on 03/09/2020).

[Jac+14] T. Jacqmin et al. Direct observation of Dirac cones and a flatband in a honeycomb lattice for polaritons. *Physical Review Letters* **112** (11), 116402 (2014).

[JC63] E. T. Jaynes and F. W. Cummings. Comparison of quantum and semiclassical radiation theories with application to the beam maser. *Proceedings of the IEEE* **51** (1), 89–109 (1963).

[St-+17] P. St-Jean et al. Lasing in topological edge states of a one-dimensional lattice. *Nature Photonics* **11** (10), 651 (2017).

[Jin+94] R. Jin et al. Photon-number correlations near the threshold of microcavity lasers in the weak-coupling regime. *Physical Review A* **49** (5), 4038–4042 (1994).

[Jon18] N. Jones. How to stop data centres from gobbling up the world's electricity. *Nature* **561** (7722), 163–166 (2018).

[Jot+14] G. Jotzu et al. Experimental realization of the topological Haldane model with ultracold fermions. *Nature* **515** (7526), 237–240 (2014).

[Kah60] D. Kahng. Silicon-silicon dioxide field induced surface devices. *the Solid State Device Research Conf., Pittsburgh, PA. June 1960* (1960).

[KM05a] C. L. Kane and E. J. Mele. Quantum Spin Hall Effect in Graphene. *Physical Review Letters* **95** (22), 226801 (2005).

[KM05b] C. L. Kane and E. J. Mele. Z_2 topological order and the quantum spin Hall effect. *Physical Review Letters* **95** (14), 146802 (2005).

[Kan+20] M. Kang et al. Dirac fermions and flat bands in the ideal kagome metal FeSn. *Nature Materials* **19** (2), 163–169 (2020).

[KS16] Y. V. Kartashov and D. V. Skryabin. Modulational instability and solitary waves in polariton topological insulators. *Optica* **3** (11), 1228 (2016).

[KS17a] Y. V. Kartashov and D. V. Skryabin. Bistable Topological Insulator with Exciton-Polaritons. *Physical Review Letters* **119** (25), 253904 (2017).

[KS19] Y. V. Kartashov and D. V. Skryabin. Two-Dimensional Topological Polariton Laser. *Physical Review Letters* **122** (8), 083902 (2019).

[Kar+15] T. Karzig et al. Topological Polaritons. *Physical Review X* **5** (3), 031001 (2015).

[Kas+06] J. Kasprzak et al. Bose-Einstein condensation of exciton polaritons. *Nature* **443** (7110), 409–414 (2006).

[Kas+08] J. Kasprzak et al. Second-order time correlations within a polariton Bose-Einstein condensate in a CdTe microcavity. *Physical Review Letters* **100** (6), 067402 (2008).

[Kav10] A. V. Kavokin. Exciton-polaritons in microcavities: Recent discoveries and perspectives. *physica status solidi (b)* **247** (8), 1898–1906 (2010).

[KMG05] A. V. Kavokin, G. Malpuech, and M. Glazov. Optical Spin Hall Effect. *Physical Review Letters* **95** (13), 136601 (2005).

[Kav+17] A. V. Kavokin et al. *Microcavities*. **21**. Oxford University Press, 2017.

[Kav+04] K. V. Kavokin et al. Quantum theory of spin dynamics of exciton-polaritons in microcavities. *Physical Review Letters* **92** (1), 017401 (2004).

[Ket04] V. Kettunen. Review of iterative Fourier-transform algorithms for beam shaping applications. *Optical Engineering* **43** (11), 2549 (2004).

[Ket+04] V. Kettunen et al. Diffractive elements designed to suppress unwanted zeroth order due to surface depth error. *Journal of Modern Optics* **51** (14), 2111–2123 (2004).

[KS17b] A. B. Khanikaev and G. Shvets. Two-dimensional topological photonics. *Nature Photonics* **11** (12), 763–773 (2017).

[Kha+13] A. B. Khanikaev et al. Photonic topological insulators. *Nature Materials* **12** (3), 233–239 (2013).

[Kha+15] A. B. Khanikaev et al. Topologically robust sound propagation in an angular-momentum-biased graphene-like resonator lattice. *Nature Communications* **6** (1), 8260 (2015).

[Khi34] A. Khintchine. Korrelationstheorie der stationären stochastischen Prozesse. *Mathematische Annalen* **109** 604–615 (1934).

[Khu01] J. B. Khurgin. Excitonic radius in the cavity polariton in the regime of very strong coupling. *Solid State Communications* **117** (5), 307–310 (2001).

[Kih94] T. Kihara. Stokes parameters measurement of light over a wide wavelength range by judicious choice of azimuthal settings of quarter-wave plate and linear polarizer. *Optics Communications* **110** (5-6), 529–532 (1994).

[Kim+11] N. Y. Kim et al. Dynamical d-wave condensation of exciton–polaritons in a two-dimensional square-lattice potential. *Nature Physics* **7** (9), 681–686 (2011).

[Kim+16] S. Kim et al. Coherent Polariton Laser. *Physical Review X* **6** (1), 011026 (2016).

[Kim+14] Y. Kim et al. Topological domain walls and quantum valley Hall effects in silicene. *Physical Review B* **89** (8), 085429 (2014).

[Kit05] C. Kittel. *Introduction to solid state physics*. 8. ed. Hoboken, NJ: Wiley, 2005.

[Kla+18] M. Klaas et al. Evolution of Temporal Coherence in Confined Exciton-Polariton Condensates. *Physical Review Letters* **120** (1), 017401 (2018).

[Kla+19] M. Klaas et al. Nonresonant spin selection methods and polarization control in exciton-polariton condensates. *Physical Review B* **99** (11), 10 (2019).

[Kle29] O. Klein. Die Reflexion von Elektronen an einem Potentialsprung nach der relativistischen Dynamik von Dirac. *Zeitschrift für Physik* **53** (3-4), 157–165 (1929).

[Kle+17] S. Klembt et al. Polariton condensation in S - and P -flatbands in a two-dimensional Lieb lattice. *Applied Physics Letters* **111** (23), 231102 (2017).

[Kle+18] S. Klembt et al. Exciton-polariton topological insulator. *Nature* **562** (7728), 552–556 (2018).

[Kli12] C. F. Klingshirn. *Semiconductor Optics*. Fourth Edition. New York: Springer, 2012.

[KDP80] K. v. Klitzing, G. Dorda, and M. Pepper. New Method for High-Accuracy Determination of the Fine-Structure Constant Based on Quantized Hall Resistance. *Physical Review Letters* **45** (6), 494–497 (1980).

[Knu03] M. Knupfer. Exciton binding energies in organic semiconductors. *Applied Physics A* **77** (5), 623–626 (2003).

[Kön+07] M. König et al. Quantum spin hall insulator state in HgTe quantum wells. *Science* **318** (5851), 766–770 (2007).

[Kot+01] R. Kotlyar et al. Zeeman spin splittings in semiconductor nanostructures. *Physical Review B* **63** (8), 1284 (2001).

[Kra+12] Y. E. Kraus et al. Topological States and adiabatic pumping in quasicrystals. *Physical Review Letters* **109** (10), 106402 (2012).

[Kri+06] D. N. Krizhanovskii et al. Dominant effect of polariton-polariton interactions on the coherence of the microcavity optical parametric oscillator. *Physical Review Letters* **97** (9), 097402 (2006).

[Kri+09] D. N. Krizhanovskii et al. Coexisting nonequilibrium condensates with long-range spatial coherence in semiconductor microcavities. *Physical Review B* **80** (4), 045317 (2009).

[Kru+19] S. Kruk et al. Nonlinear light generation in topological nanostructures. *Nature Nanotechnology* **14** (2), 126–130 (2019).

[LMM11] C. Lacroix, P. Mendels, and F. Mila. *Introduction to Frustrated Magnetism.* **164**. Berlin, Heidelberg: Springer, 2011.

[Lag+08] K. G. Lagoudakis et al. Quantized vortices in an exciton–polariton condensate. *Nature Physics* **4** (9), 706–710 (2008).

[Lag+09] K. G. Lagoudakis et al. Observation of half-quantum vortices in an exciton-polariton condensate. *Science* **326** (5955), 974–976 (2009).

[Lag+10] K. G. Lagoudakis et al. Coherent oscillations in an exciton-polariton Josephson junction. *Physical Review Letters* **105** (12), 120403 (2010).

[Lag+03] P. G. Lagoudakis et al. Electron-polariton scattering in semiconductor microcavities. *Physical Review Letters* **90** (20), 206401 (2003).

[Lai+07] C. W. Lai et al. Coherent zero-state and pi-state in an exciton-polariton condensate array. *Nature* **450** (7169), 529–532 (2007).

[Lan+18] L.-J. Lang et al. Effects of non-Hermiticity on Su-Schrieffer-Heeger defect states. *Physical Review B* **98** (9), 467 (2018).

[Lan+07] W. Langbein et al. Polarization beats in ballistic propagation of exciton-polaritons in microcavities. *Physical Review B* **75** (7), 3851 (2007).

[Lea+06] J. Leach et al. Interactive approach to optical tweezers control. *Applied optics* **45** (5), 897–903 (2006).

[Lee+18] C. H. Lee et al. Topolectrical Circuits. *Communications Physics* **1** (1), 39 (2018).

[Ler+17] G. Lerario et al. Room-temperature superfluidity in a polariton condensate. *Nature Physics* **13** (9), 837 (2017).

[Leu+20] T.-H. Leung et al. Interaction-Enhanced Group Velocity of Bosons in the Flat Band of an Optical Kagome Lattice. *Physical Review Letters* **125** (13), 133001 (2020).

[Lev+10] N. Levy et al. Strain-induced pseudo-magnetic fields greater than 300 tesla in graphene nanobubbles. *Science* **329** (5991), 544–547 (2010).

[Ley+07] C. Leyder et al. Observation of the optical spin Hall effect. *Nature Physics* **3** (9), 628–631 (2007).

[LAF18] D. Leykam, A. Andreanov, and S. Flach. Artificial flat band systems: from lattice models to experiments. *Advances in Physics: X* **3** (1), 1473052 (2018).

[LF18] D. Leykam and S. Flach. Perspective: Photonic flatbands. *APL Photonics* **3** (7), 070901 (2018).

[Li+18a] C. Li et al. Lieb polariton topological insulators. *Physical Review B* **97** (8), 081103 (2018).

[Li+20] M. Li et al. Higher-order topological states in photonic kagome crystals with long-range interactions. *Nature Photonics* **14** (2), 89–94 (2020).

[LC19] R. Li and L. Cao. Progress in Phase Calibration for Liquid Crystal Spatial Light Modulators. *Applied Sciences* **9** (10), 2012 (2019).

[Li+18b] Z. Li et al. Realization of flat band with possible nontrivial topology in electronic Kagome lattice. *Science Advances* **4** (11), eaau4511 (2018).

[Lid+98] D. G. Lidzey et al. Strong exciton–photon coupling in an organic semiconductor microcavity. *Nature* **395** (6697), 53 (1998).

[Lid+99] D. G. Lidzey et al. Room Temperature Polariton Emission from Strongly Coupled Organic Semiconductor Microcavities. *Physical Review Letters* **82** (16), 3316–3319 (1999).

[Lie89] E. H. Lieb. Two theorems on the Hubbard model. *Physical Review Letters* **62** (10), 1201–1204 (1989).

[Lie18] S. Lieu. Topological phases in the non-Hermitian Su-Schrieffer-Heeger model. *Physical Review B* **97** (4), 045106 (2018).

[LKS07] T. C. H. Liew, A. V. Kavokin, and I. A. Shelykh. Excitation of vortices in semiconductor microcavities. *Physical Review B* **75** (24), 1174 (2007).

[Lim+06] M. M. de Lima et al. Phonon-induced polariton superlattices. *Physical Review Letters* **97** (4), 045501 (2006).

[Lin+20] Z. Lin et al. Dirac fermions in antiferromagnetic FeSn kagome lattices with combined space inversion and time-reversal symmetry. *Physical Review B* **102** (15), 155103 (2020).

[LRG11] N. H. Lindner, G. Refael, and V. Galitski. Floquet topological insulator in semiconductor quantum wells. *Nature Physics* **7** (6), 490–495 (2011).

[LT02] J. S. Liu and M. R. Taghizadeh. Iterative algorithm for the design of diffractive phase elements for laser beam shaping. *Optics letters* **27** (16), 1463–1465 (2002).

[Liu+19] J. Liu et al. Quantum Valley Hall Effect, Orbital Magnetism, and Anomalous Hall Effect in Twisted Multilayer Graphene Systems. *Physical Review X* **9** (3), 031021 (2019).

[Loh+18] M. Lohse et al. Exploring 4D quantum Hall physics with a 2D topological charge pump. *Nature* **553** (7686), 55–58 (2018).

[Lon09] S. Longhi. Quantum-optical analogies using photonic structures. *Laser & Photonics Reviews* **3** (3), 243–261 (2009).

[Lon19] S. Longhi. Photonic flat-band laser. *Optics letters* **44** (2), 287–290 (2019).

[Lov+08] A. P. D. Love et al. Intrinsic Decoherence Mechanisms in the Microcavity Polariton Condensate. *Physical Review Letters* **101** (6), 067404 (2008).

[LJS14] L. Lu, J. D. Joannopoulos, and M. Soljačić. Topological photonics. *Nature Photonics* **8** (11), 821 (2014).

[LJS16] L. Lu, J. D. Joannopoulos, and M. Soljačić. Topological states in photonic systems. *Nature Physics* **12** (7), 626–629 (2016).

[Lu+15] L. Lu et al. TOPOLOGICAL MATTER. Experimental observation of Weyl points. *Science* **349** (6248), 622–624 (2015).

[Luk+18] V. A. Lukoshkin et al. Persistent circular currents of exciton-polaritons in cylindrical pillar microcavities. *Physical Review B* **97** (19), 195149 (2018).

[Lum+13] Y. Lumer et al. Self-localized states in photonic topological insulators. *Physical Review Letters* **111** (24), 243905 (2013).

[Lun+19] N. Lundt et al. Optical valley Hall effect for highly valley-coherent exciton-polaritons in an atomically thin semiconductor. *Nature Nanotechnology* **14** (8), 770–775 (2019).

[Lus+19] E. Lustig et al. Photonic topological insulator in synthetic dimensions. *Nature* **567** (7748), 356–360 (2019).

[Lv+15] B. Q. Lv et al. Experimental Discovery of Weyl Semimetal TaAs. *Physical Review X* **5** (3), 031013 (2015).

[Ma+20a] J. Ma et al. Direct Observation of Flatband Loop States Arising from Nontrivial Real-Space Topology. *Physical Review Letters* **124** (18), 183901 (2020).

[MXS19] J. Ma, X. Xi, and X. Sun. Topological Photonic Integrated Circuits Based on Valley Kink States. *Laser & Photonics Reviews* **13** (12), 1900087 (2019).

[Ma+19] L. Ma et al. Orbital degrees of freedom in artificial electron lattices on a metal surface. *Physical Review B* **99** (20), 205403 (2019).

[MS16] T. Ma and G. Shvets. All-Si valley-Hall photonic topological insulator. *New Journal of Physics* **18** (2), 025012 (2016).

[Ma+20b] X. Ma et al. Chiral condensates in a polariton hexagonal ring. *Optics Letters* **45** (20), 5700–5703 (2020).

[Mac92] L. Mach. Über einen Interferenzrefraktor. *Zeitschrift für Instrumentenkunde* **12** (1), 89–93 (1892).

[Mac+17] L. J. Maczewsky et al. Observation of photonic anomalous Floquet topological insulators. *Nature Communications* **8** (1), 13756 (2017).

[Mac+20a] L. J. Maczewsky et al. Fermionic time-reversal symmetry in a photonic topological insulator. *Nature Materials* **19** (8), 855–860 (2020).

[Mac+20b] L. J. Maczewsky et al. Nonlinearity-induced photonic topological insulator. *Science* **370** (6517), 701–704 (2020).

[MAS93] M. Z. Maialle, E. A. d. Andrada e Silva, and L. J. Sham. Exciton spin dynamics in quantum wells. *Physical Review B* **47** (23), 15776–15788 (1993).

[Mai+17] W. Maimaiti et al. Compact localized states and flat-band generators in one dimension. *Physical Review B* **95** (11), 115135 (2017).

[Mak+14] K. F. Mak et al. Valleytronics. The valley Hall effect in MoS_2 transistors. *Science* **344** (6191), 1489–1492 (2014).

[Mal+03] G. Malpuech et al. Polariton laser: thermodynamics and quantum kinetic theory. *Semiconductor Science and Technology* **18** (10), S395–S404 (2003).

[Man+15] M. Mancini et al. Observation of chiral edge states with neutral fermions in synthetic Hall ribbons. *Science* **349** (6255), 1510–1513 (2015).

[MGL19] S. Mandal, R. Ge, and T. C. H. Liew. Antichiral edge states in an exciton polariton strip. *Physical Review B* **99** (11) (2019).

[Mar+18] D. Marchenko et al. Extremely flat band in bilayer graphene. *Science Advances* **4** (11), eaau0059 (2018).

[Mas+12] N. Masumoto et al. Exciton–polariton condensates with flat bands in a two-dimensional kagome lattice. *New Journal of Physics* **14** (6), 065002 (2012).

[Max65] J. C. Maxwell. A Dynamical Theory of the Electromagnetic Field. *Philosophical Transactions of the Royal Society of London* **155** (1), 459–512 (1865).

[Mek03] M. Mekata. Kagome: The Story of the Basketweave Lattice. *Physics Today* **56** (2), 12–13 (2003).

[Mic+11] S. Michaelis de Vasconcellos et al. Spatial, spectral, and polarization properties of coupled micropillar cavities. *Applied Physics Letters* **99** (10), 101103 (2011).

[MM87] A. A. Michelson and E. W. Morley. On the Relative Motion of the Earth and the Luminiferous Ether. *American Journal of Science* **34** (203), 333–345 (1887).

[Mie91] A. Mielke. Ferromagnetic ground states for the Hubbard model on line graphs. *Journal of Physics A: Mathematical and General* **24** (2), L73 (1991).

[Mie92] A. Mielke. Exact ground states for the Hubbard model on the Kagome lattice. *Journal of Physics A: Mathematical and General* **25** (16), 4335 (1992).

[MT93] A. Mielke and H. Tasaki. Ferromagnetism in the Hubbard model: Examples from models with degenerate single-electron ground states. *Communications in Mathematical Physics* **158** (2), 341–371 (1993).

[MEB07] G. Milewski, D. Engström, and J. Bengtsson. Diffractive optical elements designed for highly precise far-field generation in the presence of artifacts typical for pixelated spatial light modulators. *Applied optics* **46** (1), 95–105 (2007).

[Mil+15] M. Milićević et al. Edge states in polariton honeycomb lattices. *2D Materials* **2** (3), 034012 (2015).

[Mil+17] M. Milićević et al. Orbital Edge States in a Photonic Honeycomb Lattice. *Physical Review Letters* **118** (10), 107403 (2017).

[Mil+19] M. Milićević et al. Type-III and Tilted Dirac Cones Emerging from Flat Bands in Photonic Orbital Graphene. *Physical Review X* **9** (3), 031010 (2019).

[Mil+18] M. Milićević et al. Lasing in optically induced gap states in photonic graphene. *SciPost Physics* **5** (6), 64 (2018).

[Min+06] H. Min et al. Intrinsic and Rashba spin-orbit interactions in graphene sheets. *Physical Review B* **74** (16), 165310 (2006).

[Mit+14] S. Mittal et al. Topologically robust transport of photons in a synthetic gauge field. *Physical Review Letters* **113** (8), 087403 (2014).

[MDH18] S. Mittal, W. DeGottardi, and M. Hafezi. Topological Photonic Systems. *Optics and Photonics News* **29** (5), 36 (2018).

[MGH18] S. Mittal, E. A. Goldschmidt, and M. Hafezi. A topological source of quantum light. *Nature* **561** (7724), 502–506 (2018).

[Mit+16] S. Mittal et al. Measurement of topological invariants in a 2D photonic system. *Nature Photonics* **10** (3), 180–183 (2016).

[Mit+19] S. Mittal et al. Photonic quadrupole topological phases. *Nature Photonics* **13** (1), 692–696 (2019).

[Moo06] G. E. Moore. Cramming more components onto integrated circuits, Reprinted from Electronics, volume 38, number 8, April 19, 1965, pp.114 ff. *IEEE Solid-State Circuits Society Newsletter* **11** (3), 33–35 (2006).

[MKW15] S. H. Mousavi, A. B. Khanikaev, and Z. Wang. Topologically protected elastic waves in phononic metamaterials. *Nature Communications* **6** (1), 8682 (2015).

[Muk+15] S. Mukherjee et al. Observation of a Localized Flat-Band State in a Photonic Lieb Lattice. *Physical Review Letters* **114** (24), 245504 (2015).

[Muk+17] S. Mukherjee et al. Experimental observation of anomalous topological edge modes in a slowly driven photonic lattice. *Nature Communications* **8** (1), 13918 (2017).

[Muñ+19] G. Muñoz-Matutano et al. Emergence of quantum correlations from interacting fibre-cavity polaritons. *Nature Materials* **18** (3), 213–218 (2019).

[Nak05] M. Nakahara. *Geometry, topology, and physics*. 2. ed., repr. Graduate student series in physics. Bristol: Inst. of Physics Publishing, 2005.

[Nak+12] Y. Nakata et al. Observation of flat band for terahertz spoof plasmons in a metallic kagomé lattice. *Physical Review B* **85** (20), 205128 (2012).

[NSM15] A. Nalitov, D. Solnyshkov, and G. Malpuech. Polariton Z Topological Insulator. *Physical Review Letters* **114** (11), 116401 (2015).

[Nal+15] A. Nalitov et al. Spin-Orbit Coupling and the Optical Spin Hall Effect in Photonic Graphene. *Physical Review Letters* **114** (2), 026803 (2015).

[Nam+76] S. B. Nam et al. Free-exciton energy spectrum in GaAs. *Physical Review B* **13** (2), 761–767 (1976).

[Nar+09] G. Nardin et al. Probability density optical tomography of confined quasiparticles in a semiconductor microcavity. *Applied Physics Letters* **94** (18), 181103 (2009).

[Nar+11] G. Nardin et al. Hydrodynamic nucleation of quantized vortex pairs in a polariton quantum fluid. *Nature Physics* **7** (8), 635–641 (2011).

[Nas+89] K. J. Nash et al. Diamagnetism as a probe of exciton localization in quantum wells. *Physical Review B* **39** (15), 10943–10954 (1989).

[Nas+15] L. M. Nash et al. Topological mechanics of gyroscopic metamaterials. *Proceedings of the National Academy of Sciences of the United States of America* **112** (47), 14495–14500 (2015).

[Nin+15] J. Ningyuan et al. Time- and Site-Resolved Dynamics in a Topological Circuit. *Physical Review X* **5** (2), 021031 (2015).

[Nix+13] M. Nixon et al. Observing geometric frustration with thousands of coupled lasers. *Physical Review Letters* **110** (18), 184102 (2013).

[Noh+17] J. Noh et al. Experimental observation of optical Weyl points and Fermi arc-like surface states. *Nature Physics* **13** (6), 611–617 (2017).

[Noh+18a] J. Noh et al. Observation of Photonic Topological Valley Hall Edge States. *Physical Review Letters* **120** (6), 063902 (2018).

[Noh+18b] J. Noh et al. Topological protection of photonic mid-gap defect modes. *Nature Photonics* **12** (7), 408 (2018).

[Nov+07] K. S. Novoselov et al. Room-temperature quantum Hall effect in graphene. *Science* **315** (5817), 1379 (2007).

[Oha+16] H. Ohadi et al. Nontrivial Phase Coupling in Polariton Multiplets. *Physical Review X* **6** (3), 031032 (2016).

[Oha+17] H. Ohadi et al. Spin Order and Phase Transitions in Chains of Polariton Condensates. *Physical Review Letters* **119** (6), 067401 (2017).

[Oha+18] H. Ohadi et al. Synchronization crossover of polariton condensates in weakly disordered lattices. *Physical Review B* **97** (19), 195109 (2018).

[OA09] T. Oka and H. Aoki. Photovoltaic Hall effect in graphene. *Physical Review B* **79** (8), 081406 (2009).

[Ota+18] Y. Ota et al. Topological photonic crystal nanocavity laser. *Communications Physics* **1** (1), 1–8 (2018).

[Ota+20] Y. Ota et al. Active topological photonics. *Nanophotonics* **9** (3), 547–567 (2020).

[Oza+17] H. Ozawa et al. Interaction-Driven Shift and Distortion of a Flat Band in an Optical Lieb Lattice. *Physical Review Letters* **118** (17), 175301 (2017).

[Oza+19] T. Ozawa et al. Topological photonics. *Reviews of Modern Physics* **91** (1), 634 (2019).

[Özd+19] Ş. K. Özdemir et al. Parity-time symmetry and exceptional points in photonics. *Nature Materials* **18** (8), 783–798 (2019).

[PD07] D. Palima and V. R. Daria. Holographic projection of arbitrary light patterns with a suppressed zero-order beam. *Applied optics* **46** (20), 4197–4201 (2007).

[Pan+19] H. Pan et al. Two-kind boson mixture honeycomb Hamiltonian of Bloch exciton-polaritons. *Physical Review B* **99** (4), 045302 (2019).

[Pan+21] R. Panico et al. Dynamics of a Vortex Lattice in an Expanding Polariton Quantum Fluid. *Physical Review Letters* **127** (4), 047401 (2021).

[Pan+99] G. Panzarini et al. Exciton-light coupling in single and coupled semiconductor microcavities: Polariton dispersion and polarization splitting. *Physical Review B* **59** (7), 5082 (1999).

[PRS13] S. A. Parameswaran, R. Roy, and S. L. Sondhi. Fractional quantum Hall physics in topological flat bands. *Comptes Rendus Physique* **14** (9-10), 816–839 (2013).

[Par+18] M. Parto et al. Edge-Mode Lasing in 1D Topological Active Arrays. *Physical Review Letters* **120** (11), 113901 (2018).

[PD08] M. Pasienski and B. Demarco. A high-accuracy algorithm for designing arbitrary holographic atom traps. *Optics express* **16** (3), 2176–2190 (2008).

[Pel+07] O. Peleg et al. Conical diffraction and gap solitons in honeycomb photonic lattices. *Physical Review Letters* **98** (10), 103901 (2007).

[PCP09] V. M. Pereira, A. H. Castro Neto, and N. M. R. Peres. Tight-binding approach to uniaxial strain in graphene. *Physical Review B* **80** (4), 045401 (2009).

[Per+21] N. Pernet et al. Topological gap solitons in a 1D non-Hermitian lattice. *arXiv e-prints* 2101.01038 (2021).

[Per+05] M. Perrin et al. Polariton relaxation in semiconductor microcavities: Efficiency of electron-polariton scattering. *Physical Review B* **72** (7), 075340 (2005).

[Pet+05] E. Peter et al. Exciton-photon strong-coupling regime for a single quantum dot embedded in a microcavity. *Physical Review Letters* **95** (6), 067401 (2005).

[Pic+20] L. Pickup et al. Synthetic band-structure engineering in polariton crystals with non-Hermitian topological phases. *Nature Communications* **11** (1), 4431 (2020).

[Pie+21] M. Pieczarka et al. Topological phase transition in an all-optical exciton-polariton lattice. *Optica* **8** (8), 1084 (2021).

[PB71] G. E. Pikus and G. L. Bir. Exchange interaction in excitons in semiconductors. *Soviet Physics JETP* **33** (1), 195–208 (1971).

[PS03] L. P. Pitaevskij and S. Stringari. *Bose-Einstein condensation*. Repr. **116**. Oxford science publications. Oxford: Clarendon Press, 2003.

[Plo+14] Y. Plotnik et al. Observation of unconventional edge states in 'photonic graphene'. *Nature Materials* **13** (1), 57–62 (2014).

[Pol+17] C. Poli et al. Partial chiral symmetry-breaking as a route to spectrally isolated topological defect states in two-dimensional artificial materials. *2D Materials* **4** (2), 025008 (2017).

[Pol+20] L. Polimeno et al. Observation of Two Thresholds Leading to Polariton Condensation in 2D Hybrid Perovskites. *Advanced Optical Materials* **8** (16), 2000176 (2020).

[Pol+13] M. Polini et al. Artificial honeycomb lattices for electrons, atoms and photons. *Nature Nanotechnology* **8** (9), 625–633 (2013).

[Pol17] M. Polyanskiy. *Refractive index database*. 2017. URL: `https://refractiveindex.info` (visited on 08/16/2017).

[PT03] D. Porras and C. Tejedor. Linewidth of a polariton laser: Theoretical analysis of self-interaction effects. *Physical Review B* **67** (16), 1547 (2003).

[Pre+07] D. Press et al. Photon antibunching from a single quantum-dot-microcavity system in the strong coupling regime. *Physical Review Letters* **98** (11), 117402 (2007).

[Pus+20] A. A. Pushkina et al. Comprehensive model and performance optimization of phase-only spatial light modulators. *Measurement Science and Technology* **31** (12), 125202 (2020).

[QZ11] X.-L. Qi and S.-C. Zhang. Topological insulators and superconductors. *Reviews of Modern Physics* **83** (4), 1057–1110 (2011).

[Rac18] S. Rachel. Interacting topological insulators: a review. *Reports on progress in physics. Physical Society (Great Britain)* **81** (11), 116501 (2018).

[RH08] S. Raghu and F. D. M. Haldane. Analogs of quantum-Hall-effect edge states in photonic crystals. *Physical Review A* **78** (3), 247 (2008).

[Rah+11] A. Rahimi-Iman et al. Zeeman splitting and diamagnetic shift of spatially confined quantum-well exciton polaritons in an external magnetic field. *Physical Review B* **84** (16), 165325 (2011).

[Ram94] A. P. Ramirez. Strongly Geometrically Frustrated Magnets. *Annual Review of Materials Science* **24** (1), 453–480 (1994).

[Rec+13a] M. C. Rechtsman et al. Photonic Floquet topological insulators. *Nature* **496** (7444), 196–200 (2013).

[Rec+13b] M. C. Rechtsman et al. Strain-induced pseudomagnetic field and photonic Landau levels in dielectric structures. *Nature Photonics* **7** (2), 153–158 (2013).

[Rec+13c] M. C. Rechtsman et al. Topological creation and destruction of edge states in photonic graphene. *Physical Review Letters* **111** (10), 103901 (2013).

[RL13] S. Reichelt and N. Leister. Computational hologram synthesis and representation on spatial light modulators for real-time 3D holographic imaging. *Journal of Physics: Conference Series* **415** (1), 012038 (2013).

[Rei+04] J. P. Reithmaier et al. Strong coupling in a single quantum dot-semiconductor microcavity system. *Nature* **432** (7014), 197–200 (2004).

[Ric19] M. Richard. Free-fall of photons in a planar optical cavity. *Journal of Physics Communications* **3** (4), 045007 (2019).

[Ric+05] M. Richard et al. Spontaneous coherent phase transition of polaritons in CdTe microcavities. *Physical review letters* **94** (18), 187401 (2005).

[Rou+11] G. Roumpos et al. Single vortex–antivortex pair in an exciton-polariton condensate. *Nature Physics* **7** (2), 129–133 (2011).

[Rou+17] J.-G. Rousset et al. Magnetic field effect on the lasing threshold of a semimagnetic polariton condensate. *Physical Review B* **96** (12), 125403 (2017).

[RL09] M. S. Rudner and L. S. Levitov. Topological transition in a non-Hermitian quantum walk. *Physical Review Letters* **102** (6), 065703 (2009).

[Rud+13] M. S. Rudner et al. Anomalous Edge States and the Bulk-Edge Correspondence for Periodically Driven Two-Dimensional Systems. *Physical Review X* **3** (3), 031005 (2013).

[RTB07] A. Rycerz, J. Tworzydło, and C. W. J. Beenakker. Valley filter and valley valve in graphene. *Nature Physics* **3** (3), 172–175 (2007).

[RH02] S. Ryu and Y. Hatsugai. Topological origin of zero-energy edge states in particle-hole symmetric systems. *Physical Review Letters* **89** (7), 077002 (2002).

[Sab+01] M. Saba et al. High-temperature ultrafast polariton parametric amplification in semiconductor microcavities. *Nature* **414** (6865), 731–735 (2001).

[SDD98] R. Saito, G. Dresselhaus, and M. S. Dresselhaus. *Physical properties of carbon nanotubes*. London: Imperial College Press, 1998.

[Sal+15] V. G. Sala et al. Spin-Orbit Coupling for Photons and Polaritons in Microstructures. *Physical Review X* **5** (1), 011034 (2015).

[ST91] B. E. A. Saleh and M. C. Teich. *Fundamentals of photonics*. A Wiley-Interscience publication. New York: Wiley, 1991.

[San+10] D. Sanvitto et al. Persistent currents and quantized vortices in a polariton superfluid. *Nature Physics* **6** (7), 527–533 (2010).

[Sch+09] C. Schneider et al. Single site-controlled In(Ga)As/GaAs quantum dots: growth, properties and device integration. *Nanotechnology* **20** (43), 434012 (2009).

[Sch+16] C. Schneider et al. Exciton-polariton trapping and potential landscape engineering. *Reports on Progress in Physics* **80** (1), 016503 (2016).

[Sch+13] C. Schneider et al. An electrically pumped polariton laser. *Nature* **497** (7449), 348–352 (2013).

[Sch13] H. Schomerus. Topologically protected midgap states in complex photonic lattices. *Optics letters* **38** (11), 1912–1914 (2013).

[SH13] H. Schomerus and N. Y. Halpern. Parity anomaly and Landau-level lasing in strained photonic honeycomb lattices. *Physical Review Letters* **110** (1), 013903 (2013).

[Seg+21] M. Segev et al. Topologic Insulator Surface Emitting Laser System. *International Patent Application* (PCT/IL2021/050489) (2021).

[Sem84] G. W. Semenoff. Condensed-Matter Simulation of a Three-Dimensional Anomaly. *Physical Review Letters* **53** (26), 2449–2452 (1984).

[SWS05] P. Senthilkumaran, F. Wyrowski, and H. Schimmel. Vortex Stagnation problem in iterative Fourier transform algorithms. *Optics and Lasers in Engineering* **43** (1), 43–56 (2005).

[Sha+19] M. I. Shalaev et al. Robust topologically protected transport in photonic crystals at telecommunication wavelengths. *Nature Nanotechnology* **14** (1), 31 (2019).

[She+84] D. Shechtman et al. Metallic Phase with Long-Range Orientational Order and No Translational Symmetry. *Physical Review Letters* **53** (20), 1951–1953 (1984).

[She+09] I. A. Shelykh et al. Polariton polarization-sensitive phenomena in planar semiconductor microcavities. *Semiconductor Science and Technology* **25** (1), 013001 (2009).

[She+10] R. Shen et al. Single Dirac cone with a flat band touching on line-centered-square optical lattices. *Physical Review B* **81** (4) (2010).

[SLL17] H. Sigurdsson, G. Li, and T. C. H. Liew. Spontaneous and superfluid chiral edge states in exciton-polariton condensates. *Physical Review B* **96** (11), 115453 (2017).

[Sin+15] I. S. Sinev et al. Mapping plasmonic topological states at the nanoscale. *Nanoscale* **7** (28), 11904–11908 (2015).

[SFW98] M. S. Skolnick, T. A. Fisher, and D. M. Whittaker. Strong coupling phenomena in quantum microcavity structures. *Semiconductor Science and Technology* **13** (7), 645–669 (1998).

[Slo+17a] A. Slobozhanyuk et al. Three-dimensional all-dielectric photonic topological insulator. *Nature Photonics* **11** (2), 130 (2017).

[Slo+17b] M. R. Slot et al. Experimental realization and characterization of an electronic Lieb lattice. *Nature Physics* **13** (7), 672–676 (2017).

[Smi+20] D. Smirnova et al. Nonlinear topological photonics. *Applied Physics Reviews* **7** (2), 021306 (2020).

[SNM16] D. Solnyshkov, A. Nalitov, and G. Malpuech. Kibble-Zurek Mechanism in Topologically Nontrivial Zigzag Chains of Polariton Micropillars. *Physical Review Letters* **116** (4), 046402 (2016).

[SBM18] D. D. Solnyshkov, O. Bleu, and G. Malpuech. Topological optical isolator based on polariton graphene. *Applied Physics Letters* **112** (3), 031106 (2018).

[Spa+12] R. Spano et al. Coherence properties of exciton polariton OPO condensates in one and two dimensions. *New Journal of Physics* **14** (7), 075018 (2012).

[Spr+13] J. B. Spring et al. Boson sampling on a photonic chip. *Science* **339** (6121), 798–801 (2013).

[Ste+21] A. Stegmaier et al. Topological Defect Engineering and PT Symmetry in Non-Hermitian Electrical Circuits. *Physical Review Letters* **126** (21), 215302 (2021).

[SS07] W. Steurer and D. Sutter-Widmer. Photonic and phononic quasicrystals. *Journal of Physics D: Applied Physics* **40** (13), R229–R247 (2007).

[Sto52] G. G. Stokes. On the composition and resolution of streams of polarized light from different sources. *Transactions of the Cambridge Philosophical Society* (9), 399 (1852).

[Stu+15] B. K. Stuhl et al. Visualizing edge states with an atomic Bose gas in the quantum Hall regime. *Science* **349** (6255), 1514–1518 (2015).

[Su+20] R. Su et al. Observation of exciton polariton condensation in a perovskite lattice at room temperature. *Nature Physics* **16** (3), 301–306 (2020).

[SSH79] W. P. Su, J. R. Schrieffer, and A. J. Heeger. Solitons in Polyacetylene. *Physical Review Letters* **42** (25), 1698 (1979).

[Suc+18] H. Suchomel et al. Platform for Electrically Pumped Polariton Simulators and Topological Lasers. *Physical Review Letters* **121** (25), 257402 (2018).

[Sun+18] M. Sun et al. Excitation of localized condensates in the flat band of the exciton-polariton Lieb lattice. *Physical Review B* **98** (16), 161204 (2018).

[Sun+20] S. Sun et al. Designing Kagome Lattice from Potassium Atoms on Phosphorus-Gold Surface Alloy. *Nano letters* **20** (7), 5583–5589 (2020).

[SH15] R. Süsstrunk and S. D. Huber. Observation of phononic helical edge states in a mechanical topological insulator. *Science* **349** (6243), 47–50 (2015).

[Sut86] B. Sutherland. Localization of electronic wave functions due to local topology. *Physical Review B* **34** (8), 5208–5211 (1986).

[Syo51] I. Syozi. Statistics of Kagome Lattice. *Progress of Theoretical Physics* **6** (3), 306–308 (1951).

[SN10] A. Szameit and S. Nolte. Discrete optics in femtosecond-laser-written photonic structures. *Journal of Physics B: Atomic, Molecular and Optical Physics* **43** (16), 163001 (2010).

[Sza+06] A. Szameit et al. Two-dimensional soliton in cubic fs laser written waveguide arrays in fused silica. *Optics express* **14** (13), 6055–6062 (2006).

[Tah+13] M. Tahir et al. Quantum spin/valley Hall effect and topological insulator phase transitions in silicene. *Applied Physics Letters* **102** (16), 162412 (2013).

[Tai+15] S. Taie et al. Coherent driving and freezing of bosonic matter wave in an optical Lieb lattice. *Science Advances* **1** (10), e1500854 (2015).

[Tan+96] H. H. Tan et al. Large energy shifts in GaAs–AlGaAs quantum wells by proton irradiation–induced intermixing. *Applied Physics Letters* **68** (17), 2401–2403 (1996).

[Tan+13] D. Tanese et al. Polariton condensation in solitonic gap states in a one-dimensional periodic potential. *Nature Communications* **4** (1), 1749 (2013).

[Tas08] H. Tasaki. Hubbard model and the origin of ferromagnetism. *The European Physical Journal B* **64** (3), 365–372 (2008).

[Tas92] H. Tasaki. Ferromagnetism in the Hubbard models with degenerate single-electron ground states. *Physical Review Letters* **69** (10), 1608 (1992).

[Taw+04] T. Tawara et al. Cavity polaritons in InGaN microcavities at room temperature. *Physical Review Letters* **92** (25), 256402 (2004).

[Tho83] D. J. Thouless. Quantization of particle transport. *Physical Review B* **27** (10), 6083 (1983).

[Tho+82] D. J. Thouless et al. Quantized Hall Conductance in a Two-Dimensional Periodic Potential. *Physical Review Letters* **49** (6), 405 (1982).

[Til+13] M. Tillmann et al. Experimental boson sampling. *Nature Photonics* **7** (7), 540–544 (2013).

[TS12] V. Timofeev and D. Sanvitto. *Exciton Polaritons in Microcavities: New Frontiers*. **172**. Springer, 2012.

[Tis+05] J. R. Tischler et al. Strong coupling in a microcavity LED. *Physical Review Letters* **95** (3), 036401 (2005).

[Töp+21] J. D. Töpfer et al. Engineering spatial coherence in lattices of polariton condensates. *Optica* **8** (1), 106 (2021).

[Tos+12a] G. Tosi et al. Geometrically locked vortex lattices in semiconductor quantum fluids. *Nature Communications* **3** 1243 (2012).

[Tos+12b] G. Tosi et al. Sculpting oscillators with light within a nonlinear quantum fluid. *Nature Physics* **8** (3), 190–194 (2012).

[Tsi+08] S. I. Tsintzos et al. A GaAs polariton light-emitting diode operating near room temperature. *Nature* **453** (7193), 372–375 (2008).

[Vah03] K. J. Vahala. Optical microcavities. *Nature* **424** (6950), 839–846 (2003).

[VCC06] A. Verger, C. Ciuti, and I. Carusotto. Polariton quantum blockade in a photonic dot. *Physical Review B* **73** (19), 193306 (2006).

[Vic+15] R. A. Vicencio et al. Observation of Localized States in Lieb Photonic Lattices. *Physical Review Letters* **114** (24), 245503 (2015).

[VMD98] J. Vidal, R. Mosseri, and B. Douçot. Aharonov-Bohm Cages in Two-Dimensional Structures. *Physical Review Letters* **81** (26), 5888–5891 (1998).

[Vol18] G. E. Volovik. Graphite, Graphene, and the Flat Band Superconductivity. *JETP Letters* **107** (8), 516–517 (2018).

[Wal47] P. R. Wallace. The Band Theory of Graphite. *Physical Review* **71** (9), 622–634 (1947).

[Wan+08] Z. Wang et al. Reflection-free one-way edge modes in a gyromagnetic photonic crystal. *Physical Review Letters* **100** (1), 013905 (2008).

[Wan+09] Z. Wang et al. Observation of unidirectional backscattering-immune topological electromagnetic states. *Nature* **461** (7265), 772–775 (2009).

[Wan37] G. H. Wannier. The Structure of Electronic Excitation Levels in Insulating Crystals. *Physical Review* **52** (3), 191–197 (1937).

[Wei+20] S. Weidemann et al. Topological funneling of light. *Science* **368** (6488), 311–314 (2020).

[Wei+17] S. Weimann et al. Topologically protected bound states in photonic parity-time-symmetric crystals. *Nature Materials* **16** (4), 433–438 (2017).

[Wei+92] C. Weisbuch et al. Observation of the coupled exciton-photon mode splitting in a semiconductor quantum microcavity. *Physical Review Letters* **69** (23), 3314–3317 (1992).

[Wen95] X.-G. Wen. Topological orders and edge excitations in fractional quantum Hall states. *Advances in Physics* **44** (5), 405–473 (1995).

[Whi+18] C. E. Whittaker et al. Exciton Polaritons in a Two-Dimensional Lieb Lattice with Spin-Orbit Coupling. *Physical Review Letters* **120** (9), 097401 (2018).

[Whi+19] C. E. Whittaker et al. Effect of photonic spin-orbit coupling on the topological edge modes of a Su-Schrieffer-Heeger chain. *Physical Review B* **99** (8), 081402 (2019).

[WE09] D. M. Whittaker and P. R. Eastham. Coherence properties of the microcavity polariton condensate. *Europhysics Letters (EPL)* **87** (2), 27002 (2009).

[Wie30] N. Wiener. Generalized harmonic analysis. *Acta Mathematica* **55** (0), 117–258 (1930).

[Wim+94] T. Wimbauer et al. Zeeman splitting of the excitonic recombination in In_xGa_{1-x} As/GaAs single quantum wells. *Physical Review B* **50** (12), 8889–8892 (1994).

[Win+16] K. Winkler et al. Collective state transitions of exciton-polaritons loaded into a periodic potential. *Physical Review B* **93** (12), 121303 (2016).

[Win+15] K. Winkler et al. A polariton condensate in a photonic crystal potential landscape. *New Journal of Physics* **17** (2), 023001 (2015).

[WC10] M. Wouters and I. Carusotto. Superfluidity and critical velocities in nonequilibrium Bose-Einstein condensates. *Physical Review Letters* **105** (2), 020602 (2010).

[WD08] C. Wu and S. Das Sarma. px,y -orbital counterpart of graphene: Cold atoms in the honeycomb optical lattice. *Physical Review B* **77** (23), 738 (2008).

[WCT15] L. Wu, S. Cheng, and S. Tao. Simultaneous shaping of amplitude and phase of light in the entire output plane with a phase-only hologram. *Scientific Reports* **5** (1), 15426 (2015).

[WH15] L.-H. Wu and X. Hu. Scheme for Achieving a Topological Photonic Crystal by Using Dielectric Material. *Physical Review Letters* **114** (22), 223901 (2015).

[Xia+16] S. Xia et al. Demonstration of flat-band image transmission in optically induced Lieb photonic lattices. *Optics letters* **41** (7), 1435–1438 (2016).

[Xu+20] H. Xu et al. Universal Self-Correcting Computing with Disordered Exciton-Polariton Neural Networks. *Physical Review Applied* **13** (6), 064074 (2020).

[Xu+15] S.-Y. Xu et al. Discovery of a Weyl fermion semimetal and topological Fermi arcs. *Science* **349** (6248), 613–617 (2015).

[Xue+21] Y. Xue et al. Split-ring polariton condensates as macroscopic two-level quantum systems. *Physical Review Research* **3** (1), 013099 (2021).

[XC04] X. Xun and R. W. Cohn. Phase calibration of spatially nonuniform spatial light modulators. *Applied optics* **43** (35), 6400–6406 (2004).

[Yan+12] H. Yan et al. Observation of Landau-level-like quantization at 77 K along a strained-induced graphene ridge. *Physical Review B* **85** (3), 035422 (2012).

[YW15] D.-K. Yang and S.-T. Wu. *Fundamentals of liquid crystal devices*. 2. ed. Wiley-SID series in display technology. Chichester: Wiley, 2015.

[Yan+15] Z. Yang et al. Topological acoustics. *Physical Review Letters* **114** (11), 114301 (2015).

[YDN08] W. Yao, Di Xiao, and Q. Niu. Valley-dependent optoelectronics from inversion symmetry breaking. *Physical Review B* **77** (23), 235406 (2008).

[YYN09] W. Yao, S. A. Yang, and Q. Niu. Edge states in graphene: from gapped flat-band to gapless chiral modes. *Physical Review Letters* **102** (9), 096801 (2009).

[Yao+07] Y. Yao et al. Spin-orbit gap of graphene: First-principles calculations. *Physical Review B* **75** (4), 041401 (2007).

[Yos+04] T. Yoshie et al. Vacuum Rabi splitting with a single quantum dot in a photonic crystal nanocavity. *Nature* **432** (7014), 200–203 (2004).

[YC10] P. Y. Yu and M. Cardona. *Fundamentals of Semiconductors*. Berlin, Heidelberg: Springer Berlin Heidelberg, 2010.

[Yu+10] R. Yu et al. Quantized anomalous Hall effect in magnetic topological insulators. *Science* **329** (5987), 61–64 (2010).

[Yu03] S. Yu. *Analysis and design of vertical cavity surface emitting lasers*. Wiley-Interscience, 2003.

[Yu+19] X. Yu et al. Strong Coupling in Microcavity Structures: Principle, Design, and Practical Application. *Laser & Photonics Reviews* **13** (1), 1800219 (2019).

[Yve+17] S. Yves et al. Crystalline metamaterials for topological properties at subwavelength scales. *Nature Communications* **8** (1), 16023 (2017).

[Zak89] J. Zak. Berry's phase for energy bands in solids. *Physical Review Letters* **62** (23), 2747–2750 (1989).

[Zas+19] A. V. Zasedatelev et al. A room-temperature organic polariton transistor. *Nature Photonics* **13** (6), 378–383 (2019).

[Zee97] P. Zeeman. The Effect of Magnetisation on the Nature of Light Emitted by a Substance. *Nature* **55** (1424), 347 (1897).

[Zeh91] L. Zehnder. Ein neuer Interferenzrefraktor. *Zeitschrift für Instrumentenkunde* **11** 275–285 (1891).

[Zeu+15] J. M. Zeuner et al. Observation of a Topological Transition in the Bulk of a Non-Hermitian System. *Physical Review Letters* **115** (4), 040402 (2015).

[Zha+14] B. Zhang et al. Zero-dimensional polariton laser in a subwavelength grating-based vertical microcavity. *Light: Science & Applications* **3** (1), e135–e135 (2014).

[ZWZ19] C. Zhang, Y. Wang, and W. Zhang. Topological phase transition with p orbitals in the exciton-polariton honeycomb lattice. *Journal of Physics: Condensed Matter* **31** (33), 335403 (2019).

[Zha+09a] H. Zhang et al. Elimination of a zero-order beam induced by a pixelated spatial light modulator for holographic projection. *Applied optics* **48** (30), 5834–5841 (2009).

[Zha+09b] Y. Zhang et al. Direct observation of a widely tunable bandgap in bilayer graphene. *Nature* **459** (7248), 820–823 (2009).

[Zhu+16] W. Zhu et al. Interaction-Driven Spontaneous Quantum Hall Effect on a Kagome Lattice. *Physical Review Letters* **117** (9), 096402 (2016).

[Zil+18] O. Zilberberg et al. Photonic topological boundary pumping as a probe of 4D quantum Hall physics. *Nature* **553** (7686), 59 (2018).

[Zon+16] Y. Zong et al. Observation of localized flat-band states in Kagome photonic lattices. *Optics express* **24** (8), 8877–8885 (2016).

A Appendix

A.1 Microcavity basic characterisation

In Figs. A.1, A.2, A.3, A.4 and A.5, the measurements performed to evaluate the basic parameters of the microcavities presented in table 3.1 are displayed.

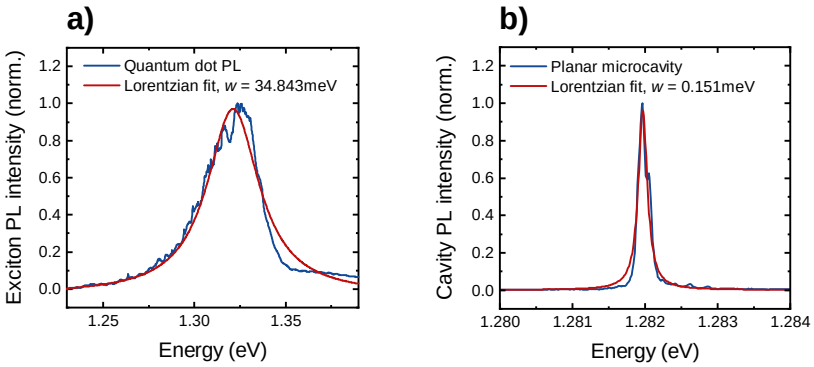

Figure A.1: Characterisation measurements for sample **In-FE1**. **a)** Photoluminescence spectrum of the quantum dot ensemble. **b)** Photoluminescence spectrum of the photonic cavity mode obtained to evaluate the Q factor.

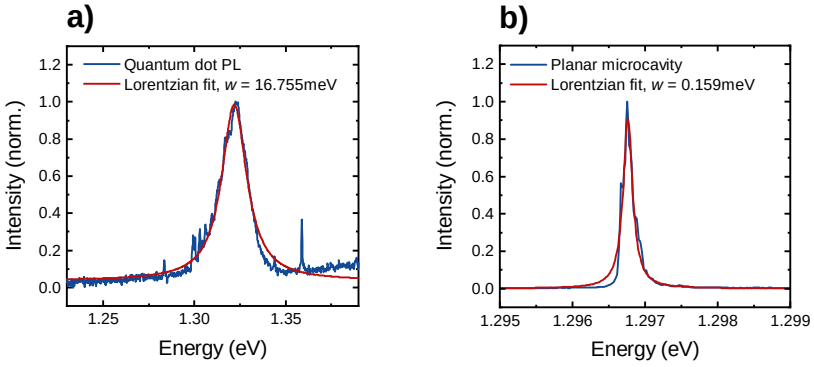

Figure A.2: Characterisation measurements for sample **In-FE2**. **a)** Photoluminescence spectrum of the quantum dot ensemble. **b)** Photoluminescence spectrum of the photonic cavity mode obtained to evaluate the Q factor.

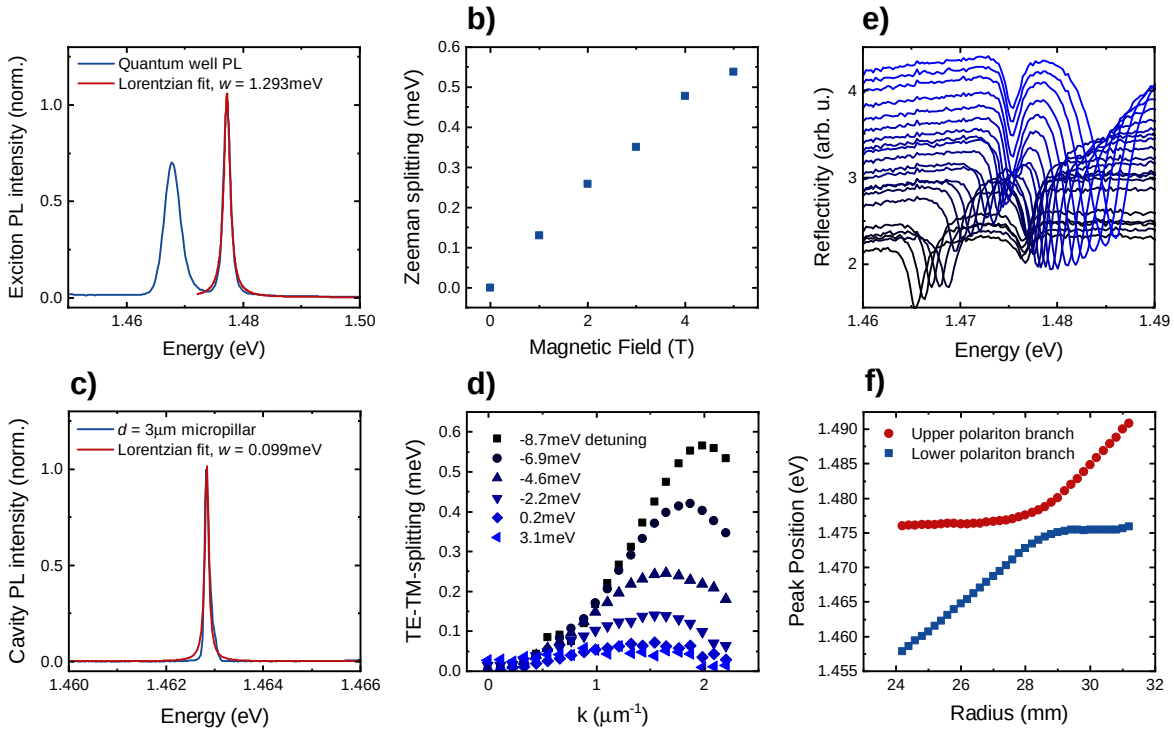

Figure A.3: Characterisation measurements for sample **In-HE1**. **a)** Photoluminescence spectrum of the bare quantum wells. To obtain this spectrum, all but two mirror pairs were removed from a piece of microcavity by etching. **b)** Zeeman splitting of the bare quantum wells. **c)** Photoluminescence spectrum of a far negatively detuned, single polariton micropillar with a diameter of $d = 3.0\,\mu\text{m}$ obtained to evaluate the Q factor. **d)** TE-TM splitting of the planar cavity resonance, evaluated for a range of detunings. **e)** White light reflection measurements for a range of detunings visualising the anti-crossing behaviour due to strong coupling between exciton and photon. For better visibility, approximately 20 mirror pairs were removed from the top distributed Bragg reflector (DBR) by etching. **f)** Evaluation of the reflectivity minima of the measurements in e) highlighting the strong coupling.

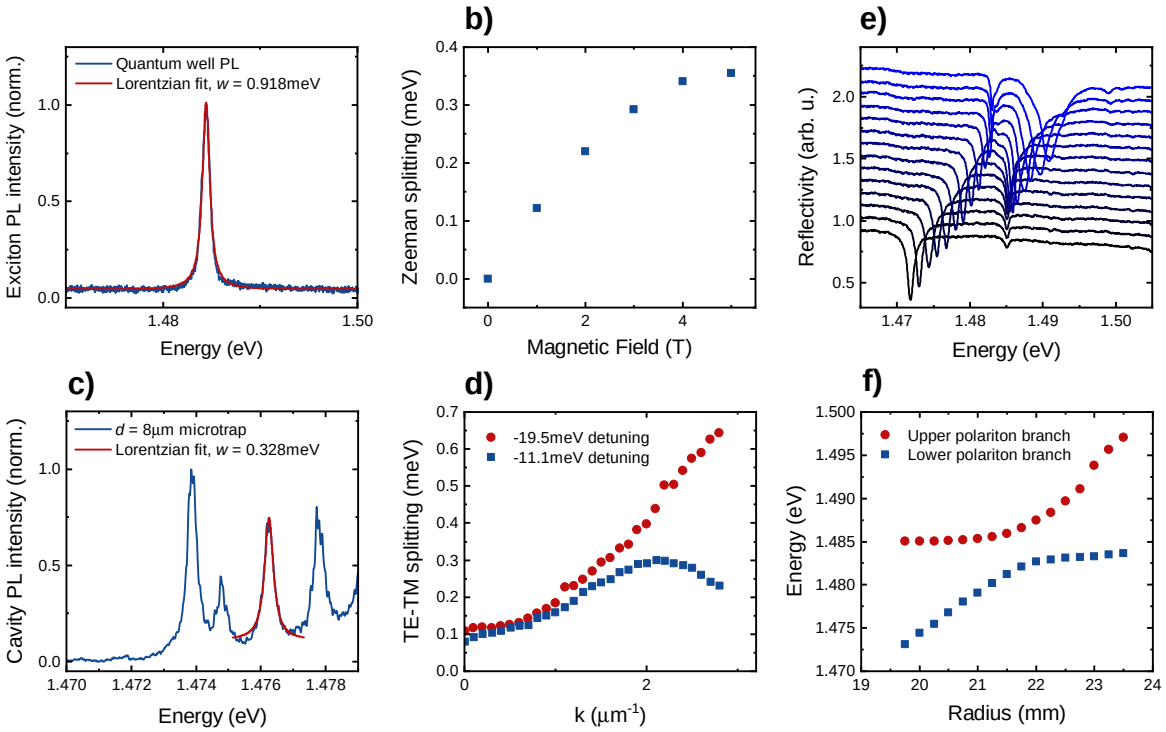

Figure A.4: Characterisation measurements for sample **In-EnO1**. **a)** Photoluminescence spectrum of the bare quantum wells. To obtain this spectrum, all but two mirror pairs were removed from a piece of microcavity by etching. **b)** Zeeman splitting of the bare quantum wells. **c)** Photoluminescence spectrum of a far negatively detuned, single polariton microtrap with a diameter of $d = 8.0\,\mu\text{m}$ obtained to evaluate the Q factor. **d)** TE-TM splitting of the planar cavity resonance, evaluated for two detunings. **e)** White light reflection measurements for a range of detunings visualising the anti-crossing behaviour due to strong coupling between exciton and photon. For better visibility, approximately 20 mirror pairs were removed from the top DBR by etching. **f)** Evaluation of the reflectivity minima of the measurements in e) highlighting the strong coupling.

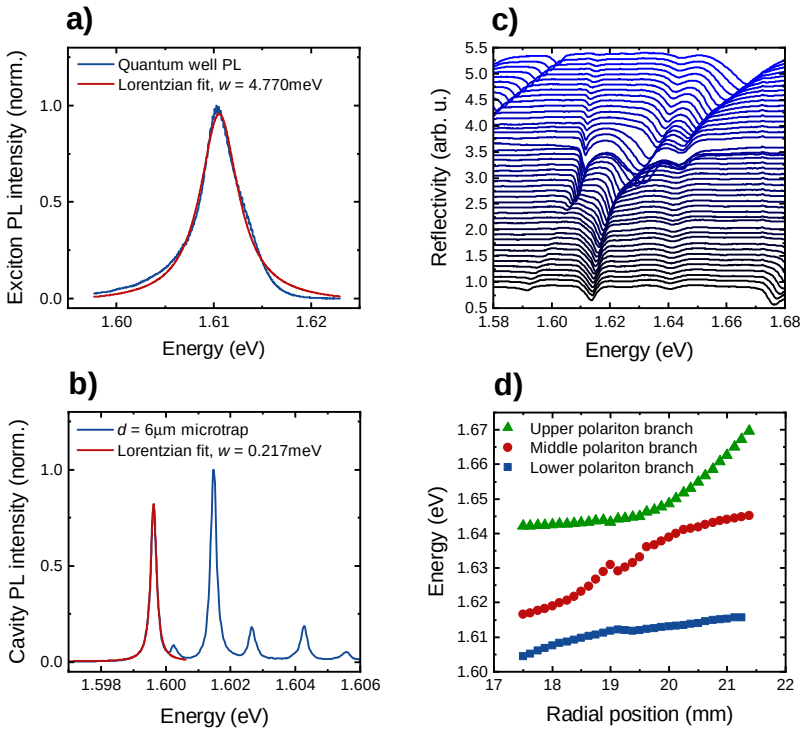

Figure A.5: Characterisation measurements for sample **Ga-EnO1**. **a)** Photoluminescence spectrum of the bare quantum wells. To obtain this spectrum, all but two mirror pairs were removed from a piece of microcavity by etching. **b)** Photoluminescence spectrum of a far negatively detuned, single polariton microtrap with a diameter of $d = 6.0\,\mu\text{m}$ obtained to evaluate the Q factor. **c)** White light reflection measurements for a range of detunings visualising the anti-crossing behaviour due to strong coupling between exciton and photon. For better visibility, approximately 20 mirror pairs were removed from the top DBR by etching. **f)** Evaluation of the reflectivity minima of the measurements in e) highlighting the strong coupling.

A.2 Back side polishing process

To prepare a sample for excitation in transmission geometry, the back side needs to be polished. A schematic of this process is depicted in Fig. A.6. First, the sample is cleaned using acetone and isopropyl alcohol. To be able to mount the sample without damaging the surface, a layer of poly(methyl methacrylate) (PMMA) is spin coated onto the top of the sample and hardened by heating the sample to 165 °C. Next, the sample is glued upside-down to a disc using wax and mounted to the vacuum holder of the lapping machine. The polishing process is performed using a lapping plate with an abrasive consisting of aluminium oxide powder with a grain size of 1 µm in a sodium hypochloride solution. Finally, the wax and the PMMA are removed using Ecoclear-OCON 178 and isopropyl alcohol, respectively.

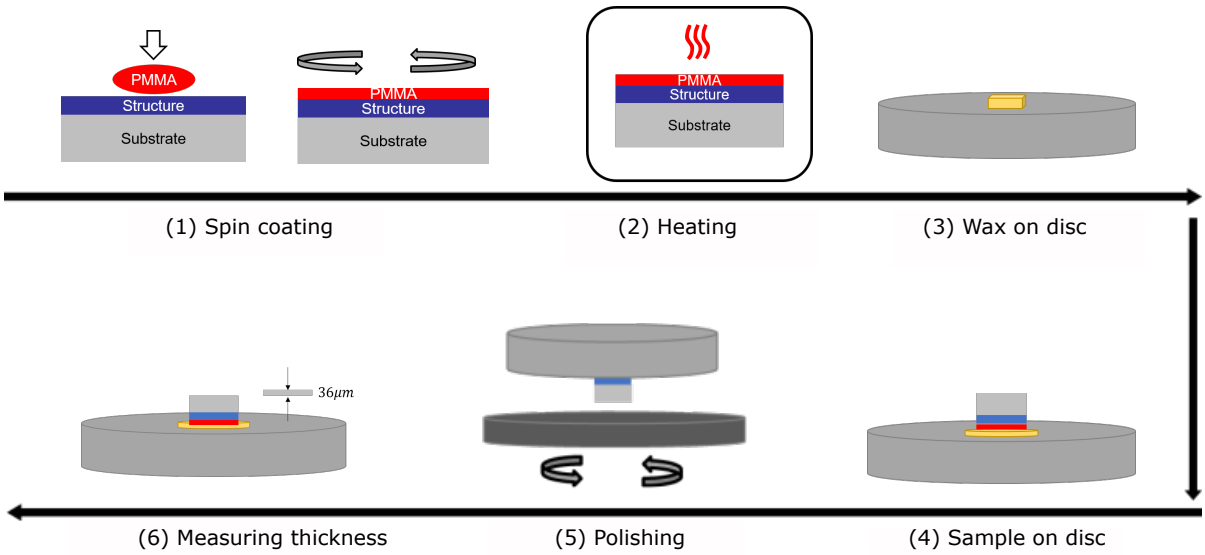

Figure A.6: Schematic of the back side polishing process used to prepare samples for resonant excitation in transmission geometry.

A.3 Polariton condensation threshold in Kagome flatbands

In Fig. A.7, the pulsed laser, excitation power dependent measurements performed to determine the threshold of polariton condensation in single, compact localised states (CLSs) of Kagome lattices with reduced trap distances of $v = 0.95$, 1.00 and 1.05 are presented. These measurements correspond to the second order temporal correlation measurements that are presented in Fig. 5.12.

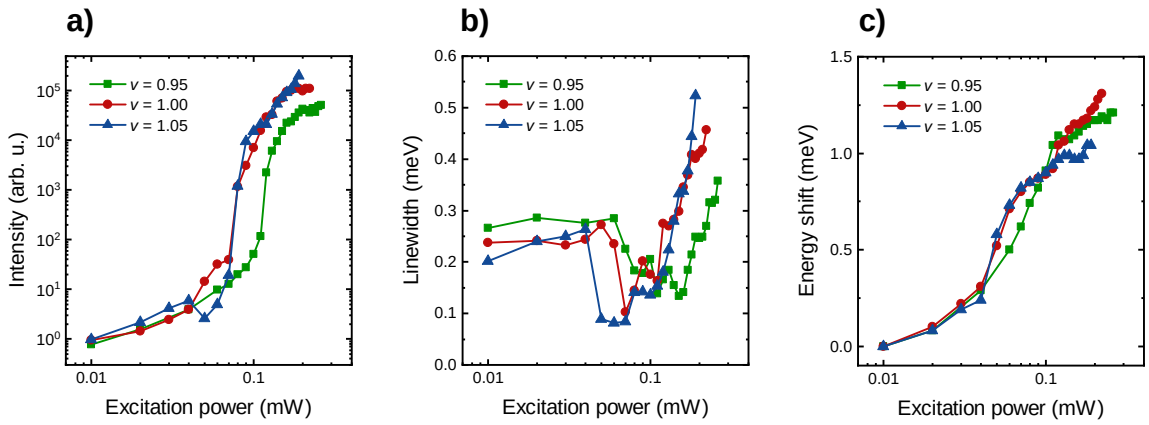

Figure A.7: a)-c) Input-output characteristics, linewidth and energetic blueshift, respectively, of polariton condensation in a single compact localised state (CLS) in Kagome lattices with reduced trap distances of $v = 0.95$, 1.00 and 1.05.

A.4 Band gap evaluation

In this section, the method used to evaluate the band gaps of crystalline topological insulator (CTI) lattices is elaborated using a stretched CTI lattice with pillar diameters of $d = 2.5\,\mu\text{m}$ that are arranged in lattice variation $L3$. First, the Fourier space image at the energy of the Dirac points of the underlying honeycomb lattice that is depicted in Fig. A.8 a) is obtained from a hyperspectral imaging scan. Using this scan, the Fourier space spectrum that represents a cross section along the K-Γ-K' direction and is displayed in Fig. A.8 b) is selected. From this spectrum, line spectra within wave vector intervals that correspond to the band gaps at the K and K' points are extracted and fitted with Lorentzian peak profiles. An exemplary line spectrum including the fit is presented in Fig. A.8 c). The peak positions of these fits represent a reconstruction of the band structure at the Dirac points and can be approximated by a parabolic fit, as is depicted in Fig. A.8 d). Finally, the size of the band gap is evaluated from the two parabolas. One prevailing contribution to the error of this analysis is the choice of the correct cross section that is limited by the scan resolution. Additionally, imperfections in the lattice itself and uncertainties of the band gap evaluation add to the error and can be estimated by considering the difference between the band gaps that are obtained for the K and K' points.

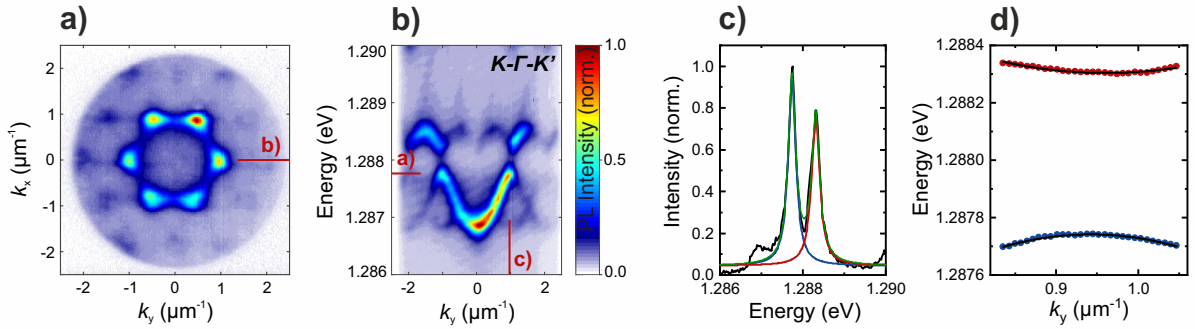

Figure A.8: **a)** Fourier space image at the energy of the Dirac points of a stretched CTI lattice with pillar diameters of $d = 2.5\,\mu\text{m}$, arranged in lattice variation $L3$. **b)** Corresponding Fourier space spectrum along the K-Γ-K' direction. **c)** Exemplary line spectrum through the band gap with a double Lorentzian fit. **d)** Band reconstruction obtained from Lorentzian fits of multiple line spectra around the K' point including parabolic fits.

A.5 Optical and scanning electron microscopy images of a crystalline topological insulator interface

In this section, optical as well as electron microscopy images that visualise the lattice geometry of the topological interface comprised of 30 VCSELs that is introduced in Fig. 6.18 are presented.

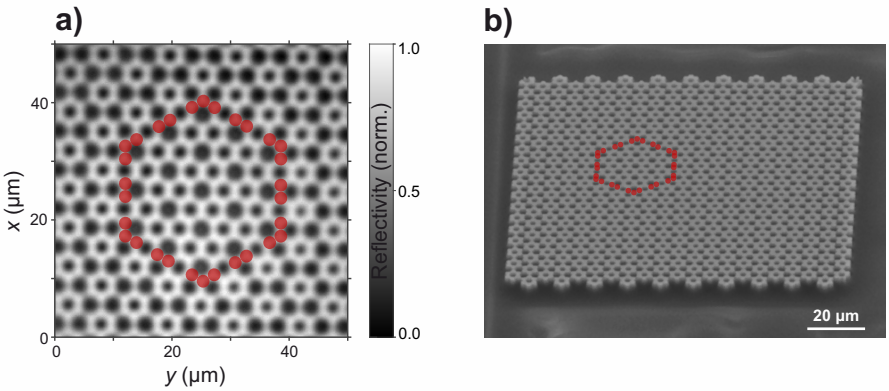

Figure A.9: Optical microscopy image in **a)** as well as scanning electron microscopy image in **b)** of a topological interface, highlighted in red, between a stretched and a compressed domain of a CTI.

A.6 Spectral comparison of the crystalline topological insulator lasing mode

In this section, mode tomographies above the lasing threshold of a CTI lattice with a weaker parameter variation and an unmodified honeycomb lattice, corresponding to the comparison of the coherence properties as well as emission spectra presented in Fig. 6.20, are depicted.

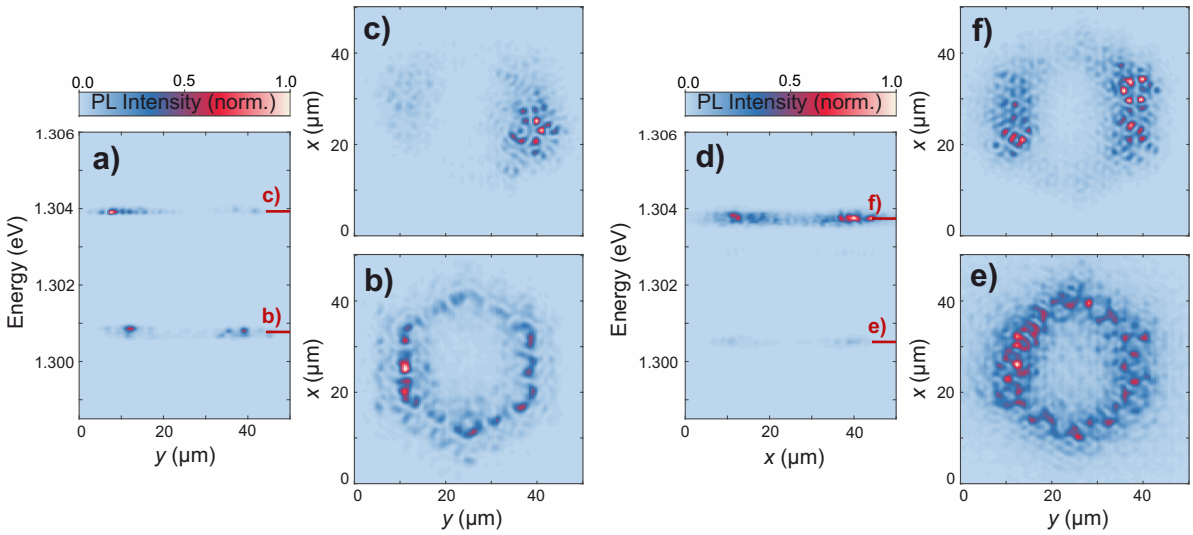

Figure A.10: **a)** Real space spectrum obtained on the CTI lattice with a weaker parameter variation, corresponding to Fig. 6.20. **b)-c)** Real space images of the topological interface lasing mode as well as the lasing emission from a P bulk mode. **d)-f)** Analogous mode tomography obtained on an unmodified honeycomb lattice featuring lasing emission from bulk modes in the S and P bands.

B Abbreviations

APD	avalanche photo diode
BEC	Bose-Einstein condensate
BKT	Berezinskii-Kosterlitz-Thouless
CCD	charge coupled device
CLS	compact localized state
cw	continuous wave
DBR	distributed Bragg reflector
EnO	etch-and-overgrowth
FFT	fast Fourier transform
GS	Gerchberg-Saxton
HBT	Hanbury Brown-Twiss
IFFT	inverse fast Fourier transform
LCAO	linear combination of atomic orbitals
LED	light emitting diode
LP	lower polariton branch
MBE	molecular beam epitaxy
MOSFET	metal-oxide-semiconductor field-effect-transistor
MP	mirror pair
MRAF	mixed-region amplitude freedom
NA	numerical aperture

OD optical density

PID proportional–integral–derivative

PL photoluminescence

PMMA poly(methyl methacrylate)

polariton exciton-polariton

QD quantum dot

QW quantum well

SLM spatial light modulator

SSH Su-Schrieffer-Heeger

CTI crystalline topological insulator

TE transverse electric

TM transverse magnetic

TMD transition metal dichalcogenide

UP upper polariton branch

VCSEL vertical-cavity surface-emitting laser

Publications of the author

Publications and patents as part of this work

T. H. Harder, O. A. Egorov, C. Krause, J. Beierlein, P. Gagel, M. Emmerling, C. Schneider, U. Peschel, S. Höfling and S. Klembt. Kagome Flatbands for Coherent Exciton-Polariton Lasing. *ACS Photonics* **8** (11), 3193-3200 (2021).

A. Dikopoltsev[1], **T. H. Harder**[1], E. Lustig, O. A. Egorov, J. Beierlein, A. Wolf, Y. Lumer, M. Emmerling, C. Schneider, S. Höfling, M. Segev and S. Klembt. Topological insulator vertically-emitting laser. *Science* **373** (6562), 1514-1517 (2021).

M. Segev, S. Höfling, S. Klembt, A. Dikopoltsev, **T. H. Harder**, E. Lustig, Y. Lumer. Topologic insulator surface emitting laser system. *International patent application*, No. PCT/IL2021/050489, April 27$^{\text{th}}$, 2020.

T. H. Harder, M. Sun, O. A. Egorov, I. Vakulchyk, J. Beierlein, P. Gagel, M. Emmerling, C. Schneider, U. Peschel, I. G. Savenko, S. Klembt and Sven Höfling. Coherent topological polariton laser. *ACS Photonics* **8** (5), 1377-1384 (2021).

T. H. Harder, O. A. Egorov, J. Beierlein, P. Gagel, J. Michl, M. Emmerling, C. Schneider, U. Peschel, S. Höfling and S. Klembt. Exciton-polaritons in flatland: Controlling flatband properties in a Lieb lattice. *Physical Review B* **102** (12), 121302(R) (2020).

S. Klembt[1], **T. H. Harder**[1], O. A. Egorov, K. Winkler, R. Ge, M. A. Bandres, M. Emmerling, L. Worschech, T. C. H. Liew, M. Segev, C. Schneider and S. Höfling. Exciton-polariton topological insulator. *Nature* **562** (7728), 552-556 (2018).

[1]These authors contributed equally

Further publications

P. Gagel, **T. H. Harder**, S. Betzold, O. A. Egorov, J. Beierlein, H. Suchomel, M. Emmerling, A. Wolf, U. Peschel, S. Höfling, C. Schneider and S. Klembt. Electro-optical Switching of a Topological Polariton Laser. *ACS Photonics* **9** (2), 405-412 (2022).

T. H. Harder, S. Höfling and S. Klembt. Topologischer Laser mit vertikalen Resonatoren. *Physik in unserer Zeit* **53** (1), 6-7 (2022).

M. Dusel, S. Betzold, **T. H. Harder**, M. Emmerling, J. Ohmer, U. Fischer, R. Thomale, C. Schneider, S. Höfling and S. Klembt. Room-Temperature Topological Polariton Laser in an Organic Lattice. *Nano Letters* **21** (15), 6398-6405 (2021).

C. Anton-Solanas, M. Waldherr, M. Klaas, H. Suchomel, **T. H. Harder**, H. Cai, E. Sedov, S. Klembt, A. V. Kavokin, S. Tongay, K. Watanabe, T. Taniguchi, S. Höfling and C. Schneider. Bosonic condensation of exciton–polaritons in an atomically thin crystal. *Nature Materials* **20** (1), 1233-1239 (2021).

J. Beierlein, O. A. Egorov, **T. H. Harder**, P. Gagel, M. Emmerling, C. Schneider, S. Höfling, U. Peschel and S. Klembt. Bloch Oscillations of Hybrid Light-Matter Particles in a Waveguide Array. *Advanced Optical Materials* **9** (13), 2100126 (2021).

J. Beierlein, E. Rozas, O. A. Egorov, M. Klaas, A. Yulin, H. Suchomel, **T. H. Harder**, M. Emmerling, M. D. Martín, I. A. Shelykh, C. Schneider, U. Peschel, L. Viña, S. Höfling and S. Klembt. Propagative Oscillations in Codirectional Polariton Waveguide Couplers. *Physical Review Letters* **126** (7), 075302 (2021).

S. J. Gonçalves, J. Weis, S. China, H. Evangelista, **T. H. Harder**, S. Müller, M. Sampaio, A. Laskin, M. K. Gilles and R. H. M. Godoi. Photochemical reactions on aerosols at West Antarctica: A molecular case-study of nitrate formation among sea salt aerosols. *Science of The Total Environment* **758** (1), 143586 (2020).

S. Gerhardt, M. Deppisch, S. Betzold, **T. H. Harder**, T. C. H. Liew, A. Predojević, S. Höfling and C. Schneider. Polarization-dependent light-matter coupling and highly indistinguishable resonant fluorescence photons from quantum dot-micropillar cavities with elliptical cross-section. *Physical Review B* **100** (11), 115305 (2019).

M. Klaas, O. A. Egorov, T. C. H. Liew, A. Nalitov, V. Marković, H. Suchomel, **T. H. Harder**, S. Betzold, E. A. Ostrovskaya, A. Kavokin, S. Klembt, S. Höfling and C. Schneider. Nonresonant spin selection methods and polarization control in exciton-polariton condensates. *Physical Review B* **99** (11), 115303 (2019).

M. Klaas, J. Beierlein, E. Rozas, S. Klembt, H. Suchomel, **T. H. Harder**, K. Winkler, M. Emmerling, H. Flayac, M. D. Martín, L. Viña, S. Höfling and C. Schneider. Counter-directional polariton coupler. *Applied Physics Letters* **114** (6), 061102 (2019).

S. Klembt, **T. H. Harder** and S. Höfling. Topologischer Isolator aus Licht und Materie. *Physik in unserer Zeit* **50** (1), 11-12 (2019).

H. Suchomel, S. Klembt, **T. H. Harder**, M. Klaas, O. A. Egorov, K. Winkler, M. Emmerling, R. Thomale, S. Höfling and C. Schneider. Platform for Electrically Pumped Polariton Simulators and Topological Lasers. *Physical Review Letters* **121** (25), 257402 (2018).

S. China, S. M. Burrows, B. Wang, **T. H. Harder**, J. Weis, M. Tanarhte, L. V. Rizzo, J. Brito, G. G. Cirino, P.-L. Ma, J. Cliff, P. Artaxo, M. K. Gilles and A. Laskin. Fungal spores as a source of sodium salt particles in the Amazon basin. *Nature Communications* **9** (1), 4793 (2018).

S. Klembt, **T. H. Harder**, O. A. Egorov, K. Winkler, H. Suchomel, J. Beierlein, M. Emmerling, C. Schneider and S. Höfling. Polariton condensation in S- and P-flatbands in a two-dimensional Lieb lattice. *Applied Physics Letters* **111** (23), 231102 (2017).

M. Fraund, D. Q. Pham, D. Bonanno, **T. H. Harder**, B. Wang, J. Brito, S. S. de Sá, S. Carbone, S. China, P. Artaxo, S. T. Martin, C. Pöhlker, M. O. Andreae, A. Laskin, M. K. Gilles and R. C. Moffet. Elemental Mixing State of Aerosol Particles Collected in Central Amazonia during GoAmazon2014/15. *Atmosphere* **8** (9), 173 (2017).

N. Lundt, P. Nagler, A. Nalitov, S. Klembt, M. Wurdack, S. Stoll, **T. H. Harder**, S. Betzold, V. Baumann, A. V. Kavokin, C. Schüller, T. Korn, S. Höfling and C. Schneider. Valley polarized relaxation and upconversion luminescence from Tamm-plasmon trion–polaritons with a $MoSe_2$ monolayer. *2D Materials* **4** (2), 025096 (2017).

A. P. Bateman, Z. Gong, **T. H. Harder**, S. S. de Sá, B. Wang, P. Castillo, S. China, Y. Liu, R. E. O'Brien, B. B. Palm, H.-W. Shiu, G. G. Cirino, R. Thalman, K. Adachi, M. L. Alexander, P. Artaxo, A. K. Bertram, P. R. Buseck, M. K. Gilles, J. L. Jimenez, A. Laskin, A. O. Manzi, A. Sedlacek, R. A. F. Souza, J. Wang, R. Zaveri and S. T. Martin. Anthropogenic influences on the physical state of submicron particulate matter over a tropical forest. *Atmospheric Chemistry and Physics* **17** (3), 1759–1773 (2017).

B. Wang, D. A. Knopf, S. China, B. W. Arey, **T. H. Harder**, M. K. Gilles and A. Laskin. Direct observation of ice nucleation events on individual atmospheric particles. *Physical Chemistry Chemical Physics* **18** (43), 29721-29731 (2016).

B. Wang, **T. H. Harder**, S. T. Kelly, D. S. Piens, S. China, L. Kovarik, M. Keiluweit, B. W. Arey, M. K. Gilles and A. Laskin. Airborne soil organic particles generated by precipitation. *Nature Geoscience* **9** (6), 433-437 (2016).

D. S. Piens, S. T. Kelly, **T. H. Harder**, M. D. Petters, R. E. O'Brien, B. Wang, K. Teske, P. Dowell, A. Laskin and M. K. Gilles. Measuring Mass-Based Hygroscopicity of Atmospheric Particles through in Situ Imaging. *Environmental Science & Technology* **50** (10), 5172-5180 (2016).

Acknowledgements

This work would not have been possible without the outstanding help of multiple people. I would therefore like to thank

- my supervisor Prof. Dr. Sebastian Klembt for guidance and numerous discussions.
- Prof. Dr. Sven Höfling for providing the opportunity to join the Chair for Applied Physics.
- Johannes Beierlein for never giving up on implementing the most advanced lattices in ECP, always enjoying a discussion and being a great friend.
- Dr. Tobias Huber for his patience in teaching me how to service a laser.
- the Bachelor students Cedric Schmitt and Constantin Krause for their motivation and efforts to understand and advance the field of microcavity lattices.
- Philipp Gagel, Karol Winkler, Holger Suchomel and Dr. Christian Schneider for providing excellent microcavity samples.
- Monika Emmerling and Adriana Wolf for their dedication to reach outstanding lithography and etching results.
- Adriana Wolf and Johannes Michl for implementing the back side polishing process.
- Dr. Oleg Egorov and Prof. Dr. Ulf Peschel for inspiring discussions and theoretical support on the peculiarities of polaritons.
- Alex Dikopoltsev, Eran Lustig, Dr. Miguel Bandres and Prof. Dr. Mordechai (Moti) Segev for sharing their outstanding expertise on topology and topological lasing.
- Meng Sun, Ihor Vakulchyk and Prof. Dr. Ivan Savenko for fruitful discussions and simulations on flatbands.
- Dr. Rong-Chun Ge and Prof Dr. Timothy Liew for theoretical support on polariton topological insulators.

- Tobias Helbig, Tobias Hofmann, Alexander Stegmaier and Prof. Dr. Ronny Thomale for open-minded discussions on interlinking various research fields of topology.
- Michael Fraser for his theoretical support on vortices and transport of superfluids in Kagome lattices.
- Cornelius Ziga for providing a dependable supply of liquid Helium.
- Johannes Beierlein for proof-reading this work.
- Oliver Iff for his assistance in dealing with the countless IT-support requests.
- Thorsten Feichtner for 3D-printing an outstanding model of a polariton topological insulator
- Simon Betzold and Johannes Beierlein for providing a never-ending supply of coffee.
- the entire team at TEP for the pleasant working atmosphere .
- the Elitenetzwerk Bayern for funding my work.
- the German Academic Scholarship Foundation for intellectual distractions and providing a space for discussions on all kinds of topics.
- my friends and family for supporting me throughout this work.